

Electron Scattering from an Almost Free Neutron in Deuterium

Nathan Kidd Baillie

Burke, Virginia

B.S. Physics, Mary Washington College, 2002  
M.S. Physics, The College of William and Mary, 2004

A Dissertation presented to the Graduate Faculty  
of the College of William and Mary in Candidacy for the Degree of  
Doctor of Philosophy

Department of Physics

The College of William and Mary  
January 2010

© Copyright by Nathan Kidd Baillie 2010  
All Rights Reserved

## APPROVAL PAGE

This Dissertation is submitted in partial fulfillment of  
the requirements for the degree of  
Doctor of Philosophy

---

Nathan Kidd Baillie

Approved by the Committee, July, 2009

---

Committee Chair  
Professor Keith Griffioen, Physics  
The College of William and Mary

---

Professor David Armstrong, Physics  
The College of William and Mary

---

Professor Carl Carlson, Physics  
The College of William and Mary

---

Dr. Howard Fenker  
Jefferson Laboratory

---

Professor Sebastian Kuhn, Physics  
Old Dominion University

## ABSTRACT PAGE

The Barely Off-Shell Nucleon Structure (BoNuS) experiment measured electron scattering from neutrons bound in deuterium nuclei at Jefferson Lab's Hall B with the intent of obtaining the ratio  $F_2^n / F_2^p$  at high Bjorken  $x$ . The  $F_2^n$  structure function is difficult to obtain due to nature's lack of a free neutron target. Previous experiments have measured inclusive scattering from atomic nuclei, but extracting  $F_2^n$  from these data requires knowledge of inclusive scattering from the proton and corrections for nucleon binding and Fermi motion. In BoNuS we restrict our analysis to neutron scattering events tagged by a backward-going low-energy recoil proton. This selects loosely bound neutrons that are nearly on their mass-shell and have few final state interactions with the recoil proton. The recoil protons were detected in a Radial Time Projection Chamber (RTPC) using gas electron multipliers (GEMs) in a cylindrical geometry around the target. The production data were taken at three beam energies: 2.140 GeV, 4.223 GeV and 5.262 GeV with an additional set of calibration data taken at 1.099 GeV. The kinematic coverage includes the invariant mass,  $W$ , from the quasi-elastic peak up to 3.0 GeV and momentum transfer,  $Q^2$ , from 0.2 GeV<sup>2</sup> up to approximately 3.0 GeV<sup>2</sup>. The final experimental observations presented here are the *tagged / untagged* cross section ratios, corrected for a number of physical processes and backgrounds. The ratio enables us to ignore many complications arising from a typical absolute cross section measurement. An extraction of  $F_2^n / F_2^p$  for  $x$  up to 0.75 is made and compared with previous data. These data are important because they can provide a model independent measurement of neutron structure.

## **DEDICATION**

This document is dedicated to my two favorite people, my little brother Joel and my sweet wife Karen. They inspire and delight me everyday and my life has been supremely enriched by their presence. I am so thankful for you and I love you both a heart full.

# Contents

|  |           |
|--|-----------|
| <b>ACKNOWLEDGEMENTS</b>                                      | <b>iv</b> |
| <b>LIST OF FIGURES</b>                                       | <b>vi</b> |
| <b>LIST OF TABLES</b>  | <b>x</b>  |
| <b>1 INTRODUCTION</b>  | <b>1</b>  |
| <b>2 FORMALISM</b>   | <b>4</b>  |
| 2.1 Introduction . . . . .                                   | 4         |
| 2.2 Kinematics of Electron Scattering . . . . .              | 4         |
| 2.3 Deep Inelastic Scattering . . . . .                      | 6         |
| 2.4 The Quark-Parton Model . . . . .                         | 8         |
| 2.5 Quantum Chromodynamics . . . . .                         | 11        |
| 2.6 Nucleon Structure Function Ratio $F_2^n/F_2^p$ . . . . . | 12        |
| 2.7 Bound Nucleon Structure . . . . .                        | 16        |
| 2.7.1 Nuclear Effects . . . . .                              | 16        |
| 2.7.2 Spectator Tagging . . . . .                            | 17        |
| 2.8 Backgrounds . . . . .                                    | 19        |
| 2.8.1 Target Fragmentation . . . . .                         | 20        |
| 2.8.2 Off-shell Corrections . . . . .                        | 21        |
| 2.8.3 Final State Interactions . . . . .                     | 22        |
| 2.9 Analysis Objectives . . . . .                            | 23        |
| <b>3 PRE-EXISTING EXPERIMENTAL APPARATUS</b>                 | <b>27</b> |
| 3.1 Continuous Electron Beam Accelerator Facility . . . . .  | 27        |
| 3.2 CEBAF Large Acceptance Spectrometer . . . . .            | 27        |
| 3.2.1 Torus Magnet . . . . .                                 | 31        |
| 3.2.2 Drift Chambers . . . . .                               | 31        |
| 3.2.3 Cherenkov Counters . . . . .                           | 35        |
| 3.2.4 Scintillation Counters . . . . .                       | 38        |
| 3.2.5 Electromagnetic Calorimeter . . . . .                  | 41        |
| 3.3 Solenoid Magnet . . . . .                                | 44        |
| <b>4 NEW EXPERIMENTAL APPARATUS</b>                          | <b>48</b> |
| 4.1 Radial Time Projection Chamber . . . . .                 | 48        |
| 4.1.1 Design Motivations and Constraints . . . . .           | 48        |
| 4.1.2 Gas Electron Multipliers . . . . .                     | 51        |
| 4.1.3 Prototypes . . . . .                                   | 54        |
| 4.1.4 Production Chamber . . . . .                           | 59        |
| 4.1.5 High Voltage Divider Circuit . . . . .                 | 62        |
| 4.1.6 Analog and Readout Electronics . . . . .               | 63        |
| 4.2 Target Straw . . . . .                                   | 67        |

|          |  |            |
|----------|--|------------|
| <b>5</b> | <b>DATA PROCESSING</b>   | <b>71</b>  |
| 5.1      | RTPC Track Reconstruction . . . . .                                    | 71         |
| 5.1.1    | Determining Local $\vec{E}$ and $\vec{B}$ . . . . .                    | 72         |
| 5.1.2    | MAGBOLTZ . . . . .   | 75         |
| 5.1.3    | Drift Electron Paths . . . . .   | 81         |
| 5.1.4    | Offset Corrections . . . . .   | 87         |
| 5.1.5    | Reconstructing Hits . . . . .  | 89         |
| 5.1.6    | Chain Linking . . . . .  | 94         |
| 5.1.7    | Helix Fitting . . . . .  | 97         |
| 5.1.8    | Track Parameters . . . . .   | 100        |
| 5.2      | RTPC Calibration . . . . .   | 105        |
| 5.2.1    | Electron Drift Velocity . . . . .                                      | 105        |
| 5.2.2    | Channel by Channel Gain Parameters . . . . .                           | 109        |
| 5.3      | Data File Selection . . . . .  | 119        |
| 5.3.1    | Electrons per Charge Measured . . . . .                                | 119        |
| 5.3.2    | High Mass ( $A > 1$ ) Background in the RTPC . . . . .                 | 119        |
| 5.4      | Electron Identification in CLAS . . . . .                              | 122        |
| 5.4.1    | Cherenkov Detector Fiducial Cuts . . . . .                             | 122        |
| 5.4.2    | Electromagnetic Calorimeter Cuts . . . . .                             | 127        |
| 5.4.3    | Solenoid $\theta - z$ Cut . . . . .                                    | 128        |
| 5.5      | RTPC Proton Identification . . . . .                                   | 128        |
| 5.5.1    | Timing Cuts . . . . .  | 128        |
| 5.5.2    | Vertex Cut and Background Subtraction . . . . .                        | 136        |
| 5.5.3    | $dQ/dx$ vs. $p/z$ Cut . . . . .  | 138        |
| 5.5.4    | Other RTPC Track Quality Cuts . . . . .                                | 140        |
| 5.6      | Corrections . . . . .  | 141        |
| 5.6.1    | Electron Momentum, Angle, and Vertex . . . . .                         | 141        |
| 5.6.2    | RTPC Simulation and Proton Energy Loss Correction . . . . .            | 146        |
| 5.6.3    | Radiative Corrections . . . . .  | 153        |
| 5.6.4    | Acceptance and Efficiency . . . . .                                    | 157        |
| 5.6.5    | Pion and Charge Symmetric Background Contamination . . . . .           | 161        |
| <b>6</b> | <b>RESULTS AND CONCLUSIONS</b>   | <b>167</b> |
| 6.1      | Introduction . . . . .   | 167        |
| 6.2      | Structure Function Ratio Extraction . . . . .                          | 167        |
| 6.3      | Error Estimation . . . . .   | 170        |
| 6.4      | Ratios ( $F_2^n/F_2^d$ , $F_2^n/F_2^p$ , $d/u$ ) and $F_2^n$ . . . . . | 170        |
| 6.5      | Conclusion and Summary . . . . .                                       | 172        |
|          | <b>BIBLIOGRAPHY</b>  | <b>194</b> |

## ACKNOWLEDGEMENTS

To begin, I humbly thank and appreciate the steadfast support and guidance of my patient and wise advisor, Keith Griffioen. His advice and expertise played a key role in my success throughout my graduate career. He first gave me the opportunity to work at SLAC for a summer, kindly funded my attendance of many enriching conferences, and patiently guided me through the rough waters of this research project. There were many days when his even-temper provided me with reassurance during stressful times and I consider myself very lucky to have had him along for this ride.

I would like to especially acknowledge Howard Fenker for the role that he played as my mentor for the many years that we have been involved with the BoNuS experiment. From that first day in the summer of 2003 setting up the “clean room” lab, to our long days of detector development, to his currently ongoing guidance and extremely helpful suggestions during the analysis phase. I am certainly grateful for his willingness to share his expertise through every stage. It has become my professional goal to one day be a detector expert near the level that he has attained.

My fellow BoNuS graduate students deserve my utmost thanks. Thank you Jixie Zhang, Slava Tkachenko, and Narbe Kalantarians for the valuable work that you performed during these many years. I certainly would not have been able to do this without you guys and I appreciate your constant efforts.

There are many other people I would like to thank for their gracious support and helpfulness in one way or another: Stephen Bueltmann, Sebastian Kuhn, Thia Keppel, Eric Christy, Peter Bosted, Vladas Tvaskis, Dipangkar Dutta, Chandana Jayalath, Sucheta Jawalker, Gabriel and Ioana Niculescu, Michael Ispiriyan, Jason Novick, Rob Fersch, Cornel Butuceanu, Stepan Stepanyan, Gail Dodge, Rolf Ent, Wally Melnitchouk, Julie Roche, Marc Vanderhaegen, Steve Christo, Peter Bradshaw, Josh Evans, The Hall-B engineering crew (especially Jill Gram), and John Domingo.

I want to thank my dissertation committee: Carl Carlson (W&M), David Armstrong (W&M), Sebastian Kuhn (ODU), Howard Fenker (Jefferson Lab), and Keith Griffioen (W&M) for the crucial role that you've played in this process.

I'd like to thank my undergraduate physics professors at Mary Washington College, Bulent Atalay and George King, III. They helped spark my interest in physics and gave me the foundation for my graduate experience.

I must express gratitude to my entire supportive family and my parents, Larry and Becky Baillie, especially. I could not ask for better role models or sincere friends. You have been there for me every step of the way and I will always remember it.

My wife Karen deserves a massive amount of credit for the number of ways that she contributed to this endeavor. She has always provided me with a great deal of perspective and tried to instill in me a "can-do" attitude when things seemed bleak. Not only did she handle all aspects of our day-to-day lives so that I could focus exclusively on finishing graduate school, but as a fellow physicist, she was able to give me valuable comments and observations as she helped to edit the entire thesis. She is an amazing woman with a huge heart and the value of her support to me cannot be overstated.

## List of Figures

|      |   |    |
|------|---|----|
| 2.1  | Diagram of inclusive lepton-nucleon scattering . . . . .                            | 5  |
| 2.2  | A compilation of $F_2^p$ data from the PDG . . . . .                                | 9  |
| 2.3  | Quark distributions versus $x$ . . . . .  | 13 |
| 2.4  | A SLAC measurement of $F_2^n / F_2^p$ . . . . .                                     | 15 |
| 2.5  | A schematic of the EMC effect . . . . .   | 16 |
| 2.6  | A calculation of Target Fragmentation effects . . . . .                             | 20 |
| 2.7  | Comparing bound and free neutron structure functions . . . . .                      | 22 |
| 2.8  | Comparing bound and free neutron structure functions . . . . .                      | 23 |
| 2.9  | Comparing bound and free neutron structure functions . . . . .                      | 24 |
| 2.10 | The effect of final state interactions on the spectral function . . . . .           | 25 |
| 2.11 | The effect of final state interactions on the spectral function . . . . .           | 26 |
|      |   |    |
| 3.1  | A schematic of CEBAF . . . . .  | 28 |
| 3.2  | A schematic of the CLAS detector . . . . .  | 28 |
| 3.3  | A parallel cross-section of CLAS . . . . .  | 29 |
| 3.4  | A perpendicular cross-section of CLAS . . . . .                                     | 30 |
| 3.5  | A schematic of the magnetic field of the torus . . . . .                            | 30 |
| 3.6  | The magnetic field vectors of the torus . . . . .                                   | 32 |
| 3.7  | The CLAS drift chambers . . . . .   | 32 |
| 3.8  | Tracking in the CLAS drift chambers . . . . .                                       | 34 |
| 3.9  | Result of the final drift chamber calibration . . . . .                             | 35 |
| 3.10 | Result of the final drift chamber calibration . . . . .                             | 36 |
| 3.11 | Drift chamber residuals pre-alignment . . . . .                                     | 36 |
| 3.12 | Drift chamber residuals post-alignment . . . . .                                    | 37 |
| 3.13 | The CLAS Cherenkov Counter . . . . .  | 38 |
| 3.14 | The CLAS Scintillation Counter . . . . .  | 39 |
| 3.15 | Time-of-flight resolution . . . . .   | 40 |
| 3.16 | Time-of-flight resolution . . . . .   | 40 |
| 3.17 | The CLAS Electromagnetic Calorimeter . . . . .                                      | 41 |
| 3.18 | Position reconstruction in the EC . . . . .   | 42 |
| 3.19 | Timing calibration in the RC . . . . .  | 43 |
| 3.20 | A schematic of the solenoid magnet . . . . .  | 44 |
| 3.21 | The Møller electron simulation showing the $\theta$ coverage. . . . .               | 45 |
| 3.22 | Møller electron distribution in the $r$ vs. $z$ plane . . . . .                     | 45 |
| 3.23 | The solenoid field strength versus $z$ . . . . .                                    | 47 |
|      |   |    |
| 4.1  | A schematic diagram of a TPC . . . . .  | 49 |
| 4.2  | Sampling of space points in a TPC . . . . .   | 50 |
| 4.3  | A typical GEM foil imaged with an electron microscope. . . . .                      | 52 |
| 4.4  | The typical energy resolution of a GEM-based TPC. . . . .                           | 53 |
| 4.5  | A schematic representation of each layer in a standard triple GEM detector. . . . . | 53 |
| 4.6  | The effective gain vs the voltage across the GEM foils. . . . .                     | 54 |
| 4.7  | An electric field map surrounding a GEM foil . . . . .                              | 55 |
| 4.8  | A photograph of a custom GEM foil. . . . .  | 55 |
| 4.9  | A cross sectional view of the flat prototype Triple GEM TPC . . . . .               | 56 |
| 4.10 | Exploded diagram of the 105 degree prototype . . . . .                              | 57 |
| 4.11 | Flat and Curved GEM x-ray energy distributions . . . . .                            | 58 |

|      |  |     |
|------|--|-----|
| 4.12 | A schematic and a photograph of the production RTPC . . . . .                              | 59  |
| 4.13 | Lorentz angle and drift velocity for different field configurations . . . . .              | 61  |
| 4.14 | The RTPC high voltage circuit . . . . .  | 62  |
| 4.15 | Pad layout in the production RTPC . . . . .  | 64  |
| 4.16 | A preamp and receiver schematic . . . . .  | 65  |
| 4.17 | A photograph of the RTPC . . . . .   | 66  |
| 4.18 | ALTRO chip block diagram. . . . .  | 67  |
| 4.19 | A mechanical drawing of the gas target cell . . . . .                                      | 68  |
| 4.20 | A schematic of the full gas circuit for the RTPC-target system . . . . .                   | 69  |
|      |  |     |
| 5.1  | A diagram describing the linear interpolation procedure . . . . .                          | 74  |
| 5.2  | Solenoid magnetic field vectors . . . . .  | 76  |
| 5.3  | A typical MAGBOLTZ simulation result . . . . .   | 77  |
| 5.4  | Radial and azimuthal drift velocities versus $r$ . . . . .                                 | 79  |
| 5.5  | The dependence of the radial and azimuthal drift velocity on $z$ for a given $r$ . . . . . | 80  |
| 5.6  | Lorentz angle, position vectors, deflection angle . . . . .                                | 81  |
| 5.7  | Two drift electron paths at different $z$ . . . . .  | 83  |
| 5.8  | Azimuthal angle covered by drift electrons versus $t$ . . . . .                            | 85  |
| 5.9  | Radial coordinate of drift electrons versus $t$ . . . . .                                  | 86  |
| 5.10 | The $\phi$ offset versus $z$ for RTPC left . . . . .                                       | 90  |
| 5.11 | The time offset versus $z$ for RTPC left . . . . .   | 90  |
| 5.12 | Determining the proper time coordinate . . . . .   | 92  |
| 5.13 | Determining the reconstructed $\phi$ coordinate . . . . .                                  | 92  |
| 5.14 | A sample RTPC track . . . . .  | 93  |
| 5.15 | The distance that each point is separated from other link candidates . . . . .             | 95  |
| 5.16 | $\Delta z$ 's dependence on the chain link separation cut . . . . .                        | 96  |
| 5.17 | The number of points in a chain vs $\Delta z$ . . . . .                                    | 97  |
| 5.18 | Track fits in two different coordinate spaces . . . . .                                    | 101 |
| 5.19 | Hit residuals after initial helix fit . . . . .  | 102 |
| 5.20 | The slope and offset of the beam position as a function of run number . . . . .            | 102 |
| 5.21 | How to find the CLAS beamline using elastic events . . . . .                               | 103 |
| 5.22 | A typical "in-time" RTPC track seen looking upstream . . . . .                             | 105 |
| 5.23 | The electron track projected into the RTPC . . . . .                                       | 108 |
| 5.24 | Comparing $\Delta z$ before and after RTPC drift velocity calibrations. . . . .            | 110 |
| 5.25 | Comparing $\Delta\theta$ before and after RTPC drift velocity calibrations. . . . .        | 110 |
| 5.26 | Comparing $\Delta\phi$ before and after RTPC drift velocity calibrations. . . . .          | 111 |
| 5.27 | Comparing $edist$ before and after RTPC drift velocity calibrations. . . . .               | 111 |
| 5.28 | Comparing $sdist$ before and after RTPC drift velocity calibrations . . . . .              | 112 |
| 5.29 | $dQ/dx$ vs. $p/z$ before RTPC gain calibrations . . . . .                                  | 113 |
| 5.30 | The channel gain constants in two separate data runs . . . . .                             | 114 |
| 5.31 | The difference between two sets of gain constants . . . . .                                | 115 |
| 5.32 | The number of times a given pad was used on a track in a typical run . . . . .             | 116 |
| 5.33 | $dQ/dx$ vs. $p/z$ after RTPC gain calibrations . . . . .                                   | 117 |
| 5.34 | $dQ/dx$ vs. $p/z$ after RTPC gain calibrations for a deuterium data set . . . . .          | 118 |
| 5.35 | The ratio of the number of good scattered electrons to the total charge . . . . .          | 120 |
| 5.36 | RTPC particles which pass the golden track cuts and the $dQ/dx$ cut . . . . .              | 121 |
| 5.37 | RTPC particles which pass the golden track cuts but fail the $dQ/dx$ cut . . . . .         | 122 |
| 5.38 | Ten times the number of photoelectrons vs. the $p$ of the particle . . . . .               | 123 |
| 5.39 | Number of photoelectrons vs. $cc_{c2}$ for negative particles . . . . .                    | 124 |
| 5.40 | The result of the CC fiducial cut . . . . .  | 125 |
| 5.41 | The result of the CC fiducial cut . . . . .  | 126 |

|      |  |     |
|------|--|-----|
| 5.42 | The result of the Osipenko cuts . . . . .  | 127 |
| 5.43 | Energy deposit in the EC . . . . .   | 129 |
| 5.44 | Energy deposit in the EC . . . . .   | 130 |
| 5.45 | The <i>edist</i> cut . . . . .   | 132 |
| 5.46 | The <i>sdist</i> cut . . . . .   | 133 |
| 5.47 | The track <i>edist</i> versus <i>sdist</i> . . . . .   | 134 |
| 5.48 | The track parameters <i>edist</i> versus <i>sdist</i> - color scale represents the $\langle \Delta z \rangle$ . . . . .              | 135 |
| 5.49 | The $z$ of the RTPC particle vs. the $z$ of the CLAS electron . . . . .  | 136 |
| 5.50 | The difference in $z$ between the electron vertex and the spectator proton vertex . . . . .  | 137 |
| 5.51 | Ratio of measured/predicted $dQ/dx$ for a few sample runs . . . . .  | 139 |
| 5.52 | The peak mean and width from the gaussian fit for the entire experiment . . . . .  | 140 |
| 5.53 | The measured/expected $dQ/dx$ in bins of particle momentum . . . . .   | 141 |
| 5.54 | Comparing RTPC particles which pass/fail the PID cuts . . . . .  | 142 |
| 5.55 | The $\chi^2$ distribution of RTPC tracks . . . . .   | 143 |
| 5.56 | Radius of curvature of RTPC tracks . . . . .   | 143 |
| 5.57 | Number of unique pads used in an RTPC track . . . . .  | 144 |
| 5.58 | The result of the electron momentum corrections . . . . .  | 145 |
| 5.59 | Electron energy loss correction results . . . . .  | 146 |
| 5.60 | Proton energy loss through the RTPC . . . . .  | 148 |
| 5.61 | RTPC momentum correction from simulation . . . . .   | 149 |
| 5.62 | Spectator momentum distributions after various cuts . . . . .  | 150 |
| 5.63 | Simulation results for exclusive channel . . . . .   | 151 |
| 5.64 | Empirical spectator momentum correction . . . . .  | 152 |
| 5.65 | Empirical versus simulated momentum corrections . . . . .  | 154 |
| 5.66 | Radiative corrections . . . . .  | 155 |
| 5.67 | Radiation length . . . . .   | 156 |
| 5.68 | Radiative correction super ratio . . . . .   | 158 |
| 5.69 | Radiative correction super ratio . . . . .   | 159 |
| 5.70 | Acceptance corrections using data/model . . . . .  | 160 |
| 5.71 | Normalization of <i>tagged/untagged</i> ratio . . . . .  | 161 |
| 5.72 | Pion contamination correction . . . . .  | 163 |
| 5.73 | Pair symmetric background correction . . . . .   | 164 |
| 5.74 | Pion contamination correction . . . . .  | 165 |
| 5.75 | Pair symmetric background correction . . . . .   | 166 |
| 6.1  | <i>tagged</i> and <i>untagged</i> samples versus $W^*$ and $W$ . . . . .   | 168 |
| 6.2  | Invariant mass and momentum transfer coverage . . . . .  | 169 |
| 6.3  | The ratio $F_2^n/F_2^p$ versus $x$ . . . . .   | 174 |
| 6.4  | The ratio of $d/u$ extracted from the nucleon structure function ratio . . . . .   | 175 |
| 6.5  | $F_2^n/F_2^d$ , $F_2^n/F_2^p$ , and $F_2^n$ vs. $W$ and $x$ at $Q^2 = 0.65 - 0.77 \text{ GeV}^2$ , $E = 4.223 \text{ GeV}$ . . . . . | 176 |
| 6.6  | Same as Fig. 6.5 but at $0.77 < Q^2 < 0.92 \text{ GeV}^2$ . . . . .  | 177 |
| 6.7  | Same as Fig. 6.5 but at $0.92 < Q^2 < 1.10 \text{ GeV}^2$ . . . . .  | 178 |
| 6.8  | Same as Fig. 6.5 but at $1.10 < Q^2 < 1.31 \text{ GeV}^2$ . . . . .  | 179 |
| 6.9  | Same as Fig. 6.5 but at $1.31 < Q^2 < 1.56 \text{ GeV}^2$ . . . . .  | 180 |
| 6.10 | Same as Fig. 6.5 but at $1.56 < Q^2 < 1.87 \text{ GeV}^2$ . . . . .  | 181 |
| 6.11 | Same as Fig. 6.5 but at $1.87 < Q^2 < 2.23 \text{ GeV}^2$ . . . . .  | 182 |
| 6.12 | Same as Fig. 6.5 but at $2.23 < Q^2 < 2.66 \text{ GeV}^2$ . . . . .  | 183 |
| 6.13 | Same as Fig. 6.5 but at $2.66 < Q^2 < 3.17 \text{ GeV}^2$ . . . . .  | 184 |
| 6.14 | $F_2^n/F_2^d$ , $F_2^n/F_2^p$ , and $F_2^n$ vs. $W$ and $x$ at $Q^2 = 0.92 - 1.10 \text{ GeV}^2$ , $E = 5.262 \text{ GeV}$ . . . . . | 185 |
| 6.15 | Same as Fig. 6.14 but at $1.10 < Q^2 < 1.31 \text{ GeV}^2$ . . . . .   | 186 |
| 6.16 | Same as Fig. 6.14 but at $1.31 < Q^2 < 1.56 \text{ GeV}^2$ . . . . .   | 187 |

|      |  |     |
|------|--|-----|
| 6.17 | Same as Fig. 6.14 but at $1.56 < Q^2 < 1.87 \text{ GeV}^2$ . | 188 |
| 6.18 | Same as Fig. 6.14 but at $1.87 < Q^2 < 2.23 \text{ GeV}^2$ . | 189 |
| 6.19 | Same as Fig. 6.14 but at $2.23 < Q^2 < 2.66 \text{ GeV}^2$ . | 190 |
| 6.20 | Same as Fig. 6.14 but at $2.66 < Q^2 < 3.17 \text{ GeV}^2$ . | 191 |
| 6.21 | Same as Fig. 6.14 but at $3.17 < Q^2 < 3.79 \text{ GeV}^2$ . | 192 |
| 6.22 | Same as Fig. 6.14 but at $3.79 < Q^2 < 4.52 \text{ GeV}^2$ . | 193 |

## List of Tables

|     |   |     |
|-----|---|-----|
| 3.1 | Critical dimensions of the DVCS solenoid. . . . .                       | 46  |
| 4.1 | Electric fields in the RTPC . . . . .                                   | 64  |
| 5.1 | Final Drift Electron Path Parameters . . . . .                          | 87  |
| 5.2 | Final Offset Parameters for RTPC Left . . . . .                         | 88  |
| 5.3 | Final Offset Parameters for RTPC Right . . . . .                        | 89  |
| 5.4 | Raw triggers and the number which pass the good electron cuts . . . . . | 131 |
| 6.1 | The total systematic error on the ratio $F_2^n/F_2^p$ . . . . .         | 171 |

# Chapter 1

## INTRODUCTION

The main components of the atomic nucleus, which carry 99.9% of any visible object's mass, are called protons and neutrons. Together, they are known as "nucleons". Experiments that took place in the 1960's at the Stanford Linear Accelerator Center (SLAC) demonstrated that the nucleon could be described as a cluster of even smaller objects. The structure of the nucleons can be mostly described in terms of two elementary components, spin-1/2 particles known as quarks and spin-1 gauge bosons called gluons. Each nucleon is made up of three valence quarks which communicate with each other via the exchange of gluons, the carriers of the strong nuclear force. Each quark has one of three possible "colors" by which it couples to the gluons. The theory of this interaction is called Quantum Chromodynamics (QCD). In this theory, the gluons can also interact with each other or they can split into quark-antiquark pairs, which can radiate their own gluons, forming a "sea" of tangled virtual particles surrounding the valence quarks.

There are six species of quarks, named up, down, strange, charm, bottom and top ( $u, d, s, c, b, t$ ), in order of increasing mass. The heaviest three of these types of quark, or flavors, are usually of no importance when discussing nucleon structure because their relatively large mass suppress their appearance in the nucleon wave function. The valence quark flavors of the proton are ( $uud$ ), whereas the neutron has up and down quarks interchanged ( $ddu$ ).

One can learn about how the quarks and gluons distribute themselves within the nucleon by bombarding it with high energy leptons and trying to make sense of the resulting debris. An analogy is firing bullets at a bag of steel balls in front of a wall, then attempting to learn something about the size and shape of the balls by studying the hole patterns that the bullets made on the wall behind the bag. In practice, one can learn a great deal about the struck nucleon just by measuring the scattering angle and energy of the outgoing lepton - this is known as inclusive scattering and it is the fundamental process analyzed in this project.

Inclusive scattering from a free proton is simple - just fill the target with hydrogen. However,

nature has not blessed us with a corresponding free neutron target. An unbound neutron is only stable for 15 min, on average, before the weak interaction causes it to beta decay into a proton, an electron and a neutrino. Luckily, there is an abundance of neutrons tied up in nuclei, but further complications are introduced when dealing with a bound system. The nucleus used in this experiment is the deuteron, because it is, after all, the simplest bound state.

One can make sure that the lepton (in the case of this experiment, the electron) interacted with only the neutron by detecting a proton which was a spectator to the reaction. The initial state of the neutron can be inferred from the spectator that recoils away from the vertex. This technique is known as spectator tagging and the framework for this mechanism has been developed in the theoretical literature for many decades.

The experimental data accumulated for this analysis was obtained in 2005 by the Barely Off-shell Nucleon Structure Collaboration (BoNuS) as part of the CEBAF Large Acceptance Spectrometer (CLAS) Collaboration at Jefferson Lab. Polarized electrons were scattered from an unpolarized deuterium target in Experimental Hall B, but the electron polarization is irrelevant to this analysis project. The scattered electrons were detected by the CLAS detector and the spectator protons were measured by a novel slow proton detector known as the BoNuS Radial Time Projection Chamber (BoNuS RTPC). The production data were taken at three beam energies: 2.140 GeV, 4.223 GeV and 5.262 GeV with an additional set of calibration data taken at 1.099 GeV. The kinematic coverage includes the final state invariant mass,  $W$ , from the quasi-elastic peak up to 3.0 GeV and momentum transfer,  $Q^2$ , from 0.2 GeV<sup>2</sup> up to approximately 3.0 GeV<sup>2</sup>.

The following topics are discussed in this thesis:

- Chapter 2: Outlines the physics motivations and particular measurements which the experiment performed.
- Chapter 3: Discusses the standard experimental apparatus which was already in place prior to the BoNuS experiment.
- Chapter 4: Describes in detail the design, development, and construction of the BoNuS RTPC and the target straw.
- Chapter 5: Details the BoNuS RTPC track reconstruction and the remainder of the data analysis procedures.

- Chapter 6: Presents the first physics results and includes a summary and conclusion statement.

# Chapter 2

## FORMALISM

### 2.1 Introduction

The nucleon is a composite object that can be described by the wavefunctions of its constituents. We know from quantum field theory that the quarks and gluons inside a hadron can interact in several ways. Gluons can split into quark-antiquark pairs that can subsequently interact with the other valence or sea quarks or radiate gluons. Furthermore, the laws of non-Abelian gauge theory also allow the gluons to interact with one another. Clearly, this complexity of a hadron requires specific tools and terminology to describe its structure in a comprehensible way. One of the primary probes we have to investigate the QCD structure of the nucleon is electron scattering. The formalism presented in this chapter follows closely that of Refs. [1] and [2].

### 2.2 Kinematics of Electron Scattering

A detailed “photograph” of the nucleon can be taken by measuring the four-momentum of electrons which have been scattered after exchanging a virtual photon with the nucleon. The resolution of the picture is determined by the momentum of the exchanged boson. Higher exchanged momentum corresponds to smaller wavelength of the probe, giving access to smaller structures within the larger object. Fig. 2.1 depicts the lowest order (Born) approximation of the inclusive lepton-nucleon interaction. An incident electron enters the picture with energy,  $E$ , four-momentum  $k = (E, \vec{k})$  and exits at an angle  $\theta$  with respect to the initial direction and final four-momentum  $k' = (E', \vec{k}')$  after transferring some energy via a virtual photon. The energy transferred from the lepton to the nucleon is equal to the energy of the virtual photon,  $\gamma^*$ , and is given in Lorentz invariant form by

$$\nu = \frac{p \cdot q}{M} \tag{2.1}$$

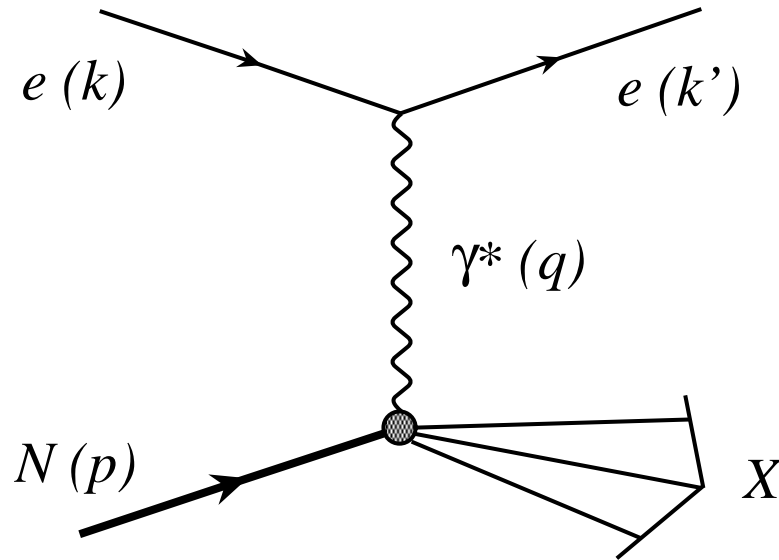


Figure 2.1: The kinematics of inclusive lepton-nucleon scattering in the Born approximation (one photon exchange). The four-momenta of the electrons ( $e$ ), the virtual photon ( $\gamma^*$ ) and the nucleon target ( $N$ ) are given in parenthesis.

where  $p$  is the four-momentum of the struck nucleon,  $q$  is the four-momentum of the virtual photon and  $M$  is the nucleon mass. It can be shown that the energy transfer in the labframe is  $\nu = E - E'$ . The degree of virtuality is  $q^2 = \nu^2 - \vec{q}^2$  and we make the definition

$$Q^2 \equiv -q^2 \approx 4EE' \sin^2 \frac{\theta}{2}. \quad (2.2)$$

This quantity,  $Q^2$ , is a measure of the virtual photon's inverse wavelength. The invariant mass squared of the recoiling hadronic system ( $X$  in Fig. 2.1) is related to  $Q^2$  and  $\nu$  by,

$$W^2 = (p + q)^2 = M^2 + 2M\nu - Q^2. \quad (2.3)$$

When the incident electron excites the nucleon into a resonance state,  $W$  is the mass of the excited resonance. Below  $W = 2.0$  GeV, the so-called resonance region, is characterized by clear peaks, when scattering from a free nucleon.

Two more useful Lorentz invariants are the dimensionless Bjorken scaling variable,  $x$  (more on the interpretation of this quantity in the next section), and the fraction of the beam energy

carried by the virtual photon,  $y$ , which are given by,

$$x = \frac{Q^2}{2p \cdot q} = \frac{Q^2}{2M\nu}, \quad (2.4)$$

$$y = \frac{p \cdot q}{p \cdot k} = \frac{\nu}{E}. \quad (2.5)$$

We can rewrite Eq. 2.3 in terms of  $x$ ,  $W^2 = M^2 + Q^2(1 - x)/x$  and see immediately for the special case of elastic scattering (when  $W = M$ ) that  $x = 1$  and  $Q^2 = 2M\nu$ .

## 2.3 Deep Inelastic Scattering

Traditionally,  $Q^2 > 1.0 \text{ GeV}^2$  and  $W > 2.0 \text{ GeV}$  defines the deep inelastic scattering (DIS) region. Here, no more discernable resonance peaks exist because the number of resonances per unit energy and their widths increase to a level where they can no longer be separated. Also, the virtual photon resolution is sufficient to scatter incoherently from individual quarks in the nucleon. Thus, the large momentum transfer enables us to directly probe the substructure of the nucleon.

We can express the doubly-differential cross section for scattering unpolarized leptons from unpolarized nucleon targets as

$$\frac{d^2\sigma}{d\Omega dE'} = \frac{\alpha^2}{Q^4} \frac{E'}{E} L_{\mu\nu} W^{\mu\nu}, \quad (2.6)$$

where  $\alpha$  is the fine-structure constant,  $d\Omega$  is the solid angle into which the lepton is scattered in the lab frame, and  $L_{\mu\nu}$  and  $W^{\mu\nu}$  are the leptonic and hadronic tensors, respectively. When summed and averaged over spins, the leptonic tensor can be written as

$$L_{\mu\nu} = 2(k_\mu k'_\nu + k'_\mu k_\nu - g_{\mu\nu} k \cdot k') \quad (2.7)$$

and is directly calculable from the rules of Quantum Electrodynamics (QED). The hadronic tensor, on the other hand, is a general way of parameterizing a complex system that we cannot

calculate from first principles. Anti-symmetric contributions to this term cancel out in the contraction with the leptonic tensor so we can write  $W^{\mu\nu}$  containing two independent structures

$$W^{\mu\nu} = W_1(\nu, Q^2) \left( \frac{q^\mu q^\nu}{q^2} - g^{\mu\nu} \right) + \frac{W_2(\nu, Q^2)}{M^2} \left( p^\mu + \frac{p \cdot q}{q^2} q^\mu \right) \left( p^\nu + \frac{p \cdot q}{q^2} q^\nu \right) \quad (2.8)$$

where  $W_1$  and  $W_2$  are inelastic structure functions of the Lorentz scalar variables  $q^2$  and  $\nu$  that parameterize our ignorance of nucleon structure. We can now contract the tensors in Eqs. 2.7 and 2.8 and combine with Eq. 2.6 to find the following form for the cross section:

$$\frac{d^2\sigma}{d\Omega dE'} = \sigma_{\text{Mott}} \left( 2W_1(\nu, Q^2) \tan^2 \frac{\theta}{2} + W_2(\nu, Q^2) \right). \quad (2.9)$$

The Mott cross section,  $\sigma_{\text{Mott}}$ , describes relativistic electron scattering from a spinless point particle in a Coulomb field,

$$\sigma_{\text{Mott}} = \frac{4\alpha^2 E'^2}{Q^4} \cos^2 \frac{\theta}{2}. \quad (2.10)$$

Two independent structure functions exist in Eq. 2.9 because the total photoabsorption cross section can be split into independent portions, transverse (helicity  $\lambda = \pm 1$ ) and longitudinal ( $\lambda = 0$ ). If we take the virtual photon as moving along the z-axis it has polarization vectors,

$$\lambda = \pm 1 : \epsilon_\pm = \mp \sqrt{\frac{1}{2}} (0; 1, \pm i, 0), \quad (2.11)$$

$$\lambda = 0 : \epsilon_0 = \frac{1}{\sqrt{Q^2}} (\sqrt{Q^2 + \nu^2}; 0, 0, \nu). \quad (2.12)$$

and the total cross sections for the interaction of polarized photons on unpolarized nucleons becomes

$$\sigma_\lambda^{\text{tot}} = \frac{4\pi^2\alpha}{K} \epsilon_\lambda^{\mu*} \epsilon_\lambda^\nu W_{\mu\nu}, \quad (2.13)$$

where  $K$  is the incident flux of photons. Since we are dealing with the virtual photon case ( $Q^2 \neq 0$ ),  $K$  is somewhat arbitrary and we choose the Hand convention to make the definition

$$K = \frac{W^2 - M^2}{2M} = \nu(1 - x). \quad (2.14)$$

Now the differential cross section can be expressed in terms of  $\sigma_T$  and  $\sigma_L$ , the transverse and

longitudinal cross sections

$$\sigma \equiv \frac{d^2\sigma}{d\Omega dE'} = \Gamma(\sigma_T + \epsilon\sigma_L) \quad (2.15)$$

where  $\Gamma$  is the flux of transverse virtual photons,

$$\Gamma = \frac{\alpha}{2\pi^2 Q^2} \frac{E'}{E} \frac{K}{1-\epsilon} \quad (2.16)$$

and the ratio of virtual photon polarizations given by

$$\epsilon = \left[ 1 + 2 \left( 1 + \frac{\nu^2}{Q^2} \right) \tan^2 \frac{\theta}{2} \right]^{-1}. \quad (2.17)$$

The components of the total virtual photoabsorption cross section can be found by contracting the polarization vectors of Eqs. 2.11 and 2.12 with  $W^{\mu\nu}$  from Eq. 2.8

$$\sigma_T \equiv \frac{1}{2}(\sigma_+^{\text{tot}} + \sigma_-^{\text{tot}}) = \frac{4\pi^2\alpha}{K} W_1(\nu, Q^2) \quad (2.18)$$

$$\sigma_L \equiv \sigma_0^{\text{tot}} = \frac{4\pi^2\alpha}{K} \left[ \left( 1 + \frac{\nu^2}{Q^2} \right) W_2(\nu, Q^2) + W_1(\nu, Q^2) \right]. \quad (2.19)$$

Finally, the photon polarization cross section ratio,  $R$ , turns out to be a useful quantity,

$$R \equiv \frac{\sigma_L}{\sigma_T} = \frac{W_2}{W_1} \left( 1 + \frac{\nu^2}{Q^2} \right) - 1. \quad (2.20)$$

## 2.4 The Quark-Parton Model

We know that  $W_1$  and  $W_2$  are scalar functions of  $\nu$  and  $Q^2$  [3] but Bjorken predicted that in the deep inelastic regime the structure functions would be independent of  $\nu$  and  $Q^2$  but dependent on their ratio,  $x$ , the famous scaling variable which carries Bjorken's name [4].

$$MW_1(\nu, Q^2) \rightarrow F_1(x); \quad Q^2 \rightarrow \infty, \nu \rightarrow \infty$$

$$\nu W_2(\nu, Q^2) \rightarrow F_2(x) \quad (2.21)$$

Fig. 2.2 depicts how, at moderate  $x$ ,  $F_2^p$  is independent of  $Q^2$  over four orders of magnitude, leading to the conclusion that inelastic electron-proton scattering is equivalent to incoherent

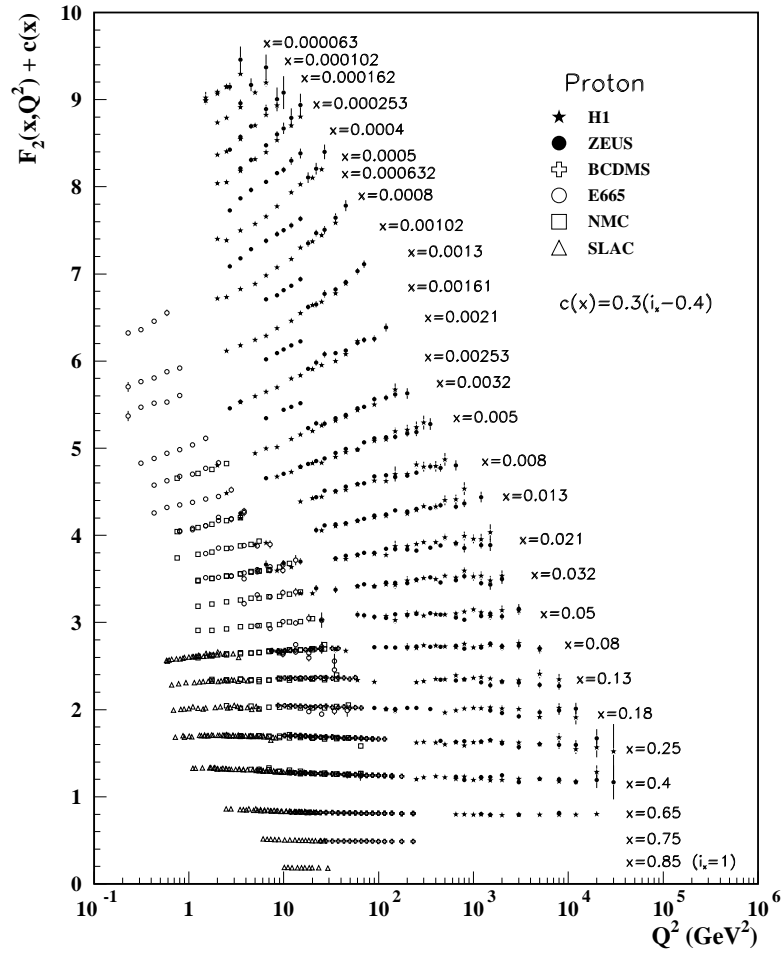


Figure 2.2: The Particle Data Group's compilation of the proton's structure function,  $F_2$  plus an  $x$  dependent offset to visually separate the data [5].

elastic scattering from point-like “partons” within the nucleon. QCD scaling violations ( $F_2$  increasing with  $Q^2$  at very low  $x$  and decreasing with  $Q^2$  at high  $x$ ) do occur and are described in Sec. 2.5.

The Quark-Parton Model (QPM) was formulated by Feynman, Bjorken and Paschos [4] to describe the early deep inelastic scattering data. The structure functions are Lorentz invariants and therefore remain unchanged under a boost to the infinite-momentum frame ( $|p| \rightarrow \infty$ ). In this frame the interaction between the substructure of partons is a direct analogy with the nuclear impulse approximation, i.e. the electron interacts so quickly with one parton that the others do not have time to react. The model also makes the assumptions that the partons have no internal electromagnetic structure and have a negligible mass in the Bjorken limit ( $\nu, Q^2 \rightarrow$

$\infty$ ,  $x$  fixed). The structure functions in the QPM can be written as the sum over quark and antiquark distribution functions

$$F_1(x) = \frac{1}{2} \sum_i e_i^2 f_i(x)$$

$$F_2(x) = x \sum_i e_i^2 f_i(x) = 2xF_1(x) \quad (2.22)$$

where  $f_i(x)$  are the Parton Distribution Functions (PDFs) and can be defined as the probability to find a quark of flavor  $i$ , electric charge  $e_i$  and momentum fraction  $x$  in the proton. The relationship between  $F_1$  and  $F_2$  in Eq. 2.22 is known as the Callan-Gross Relation [6]. The differential cross section from Eq. 2.9 can be rewritten in terms of the dimensionless  $F_1$  and  $F_2$  structure functions as

$$\frac{d^2\sigma}{d\Omega dE'} = \sigma_{\text{Mott}} \left( \frac{2}{M} F_1(x, Q^2) \tan^2 \frac{\theta}{2} + \frac{1}{\nu} F_2(x, Q^2) \right), \quad (2.23)$$

and we can also express the structure functions in terms of  $\sigma_T$  and  $\sigma_L$

$$F_1(x, Q^2) = \frac{K}{4\pi^2\alpha} M \sigma_T(x, Q^2), \quad (2.24)$$

$$F_2(x, Q^2) = \frac{K}{4\pi^2\alpha} \frac{\nu}{(1 + \nu^2/Q^2)} [\sigma_T(x, Q^2) + \sigma_L(x, Q^2)]. \quad (2.25)$$

The ratio  $R$  can also written in terms of  $F_1$  and  $F_2$  as

$$R = \frac{F_2}{2xF_1} \left( 1 + \frac{4M^2x^2}{Q^2} \right) - 1. \quad (2.26)$$

So we can now see that knowledge of  $R$  and a measurement of differential cross section can lead to an extraction of  $F_2$  from inclusive electron scattering,

$$F_2 = \frac{\sigma}{\sigma_{\text{Mott}}} \nu \epsilon \frac{1 + R}{1 + \epsilon R} \quad (2.27)$$

where  $\sigma$  is given by Eq. 2.15.

## 2.5 Quantum Chromodynamics

The theory of strong interactions is known as Quantum Chromodynamics and it can be used to describe the scaling violations seen in Fig. 2.2. In this framework, quarks carry color (Red, Green or Blue) which is exchanged via bicolored, massless bosons called gluons which have spin 1. Similar rules to those of QED can be applied to the quark-gluon interaction with the replacement of the fine structure constant with the strong coupling constant ( $\alpha \rightarrow \alpha_s$ ) and the further complication that gluons may interact with each other since they carry color. At short distances,  $\alpha_s$  is small enough that color interactions can be calculated using a perturbative approach. The PDFs in Eq. 2.22, for example, take on a logarithmic dependence on  $Q^2$  as a consequence of the fact that electron scattering from a quark cannot be separated from the process where a soft gluon is also radiated. As  $Q^2$  increases we see more of the  $q\bar{q}$  pairs and gluons that make up the nucleon. When a high  $x$  quark radiates a gluon, the momentum fraction carried by the gluons increases and  $F_2$  will decrease with increasing  $Q^2$ . On the other hand, the sea quarks dominate the momentum at low  $x$ , causing  $F_2$  to increase with increasing  $Q^2$  [7].

Perturbative QCD (pQCD) can be used to evolve the structure functions from one  $Q^2$  to another  $Q^2$  using the Dokshitzer-Gribov-Lipatov-Altarelli-Parisi (DGLAP) equations [8] [9] [10]. The singlet DGLAP equations, for a single type of quark with distribution  $f_i(x, Q^2)$  and gluon distribution  $g(x, Q^2)dx$ , are

$$\begin{aligned} \frac{\partial}{\partial \ln Q^2} f_i(x, Q^2) &= \frac{\alpha_s(Q^2)}{2\pi} \int_x^1 \frac{dy}{y} \left( P_{qq}\left(\frac{x}{y}\right) f_i(y, Q^2) + P_{qg}\left(\frac{x}{y}\right) g(y, Q^2) \right) \\ \frac{\partial}{\partial \ln Q^2} g(x, Q^2) &= \frac{\alpha_s(Q^2)}{2\pi} \int_x^1 \frac{dy}{y} \left( P_{gq}\left(\frac{x}{y}\right) f_i(y, Q^2) + P_{gg}\left(\frac{x}{y}\right) g(y, Q^2) \right) \end{aligned} \quad (2.28)$$

The splitting functions do not depend on  $i$  and are defined as:

$$P_{g \rightarrow q}\left(\frac{x}{y}\right) \equiv P_{qg}\left(\frac{x}{y}\right) \quad (2.29)$$

with similar definitions for the splitting of quarks to gluons, quarks to quarks and gluons to gluons. Once the PDFs are known at some scale, they can be calculated at any other scale, provided that leading order (LO) pQCD applies (LO isn't good enough, however, in the DIS

region).

The DGLAP equations at LO are not enough to fully describe scaling violations. The splitting functions in Eq. 2.29 can be expanded in a Taylor series to include next to leading order (NLO) and next to next to leading order (NNLO) terms. These terms include further complication by adding more gluon lines (one gluon exchange between the struck quark and the spectator quarks, for example).

Power corrections of the form  $(1/Q^2)^n$  are known as the “higher-twist” corrections. The structure function  $F_2$  can be parameterized in the following way, if one defines a leading twist structure function,  $F_2^{LT}$ :

$$F_2(x, Q^2) = F_2^{LT}(x, Q^2) \left( 1 + \frac{C(x)}{Q^2} + \dots \right) \quad (2.30)$$

where the coefficient function  $C(x)$  is the strength of the twist-four term. The weakly logarithmic dependence on  $Q^2$  has been folded into the leading twist structure function, usually NLO or NNLO in  $F_2^{LT}$ . The number of twist terms needed in the calculation to properly describe the data on nucleon targets remains an open question.

## 2.6 Nucleon Structure Function Ratio $F_2^n / F_2^p$

Measurements of the inelastic structure functions at high  $Q^2$  tell us about the quark substructure of the nucleon. If we consider the nucleon to be made up of  $(u, d, s)$  quarks we find the sums in Eq. 2.22 become

$$\begin{aligned} \frac{F_2^p(x)}{x} &= (2/3)^2 [u^p(x) + \bar{u}^p(x)] + (1/3)^2 [d^p(x) + \bar{d}^p(x)] + (1/3)^2 [s^p(x) + \bar{s}^p(x)] \\ \frac{F_2^n(x)}{x} &= (2/3)^2 [u^n(x) + \bar{u}^n(x)] + (1/3)^2 [d^n(x) + \bar{d}^n(x)] + (1/3)^2 [s^n(x) + \bar{s}^n(x)]. \end{aligned} \quad (2.31)$$

Isospin symmetry suggests that the quark distributions are invariant when simultaneously interchanging down and up quarks and  $p \leftrightarrow n$  ( $u^p(x) = d^n(x) \equiv u(x)$ ,  $d^p(x) = u^n(x) \equiv d(x)$ ). We assume that the nucleons have identical strange quark distributions  $s^p(x) = s^n(x) \equiv s(x)$ .

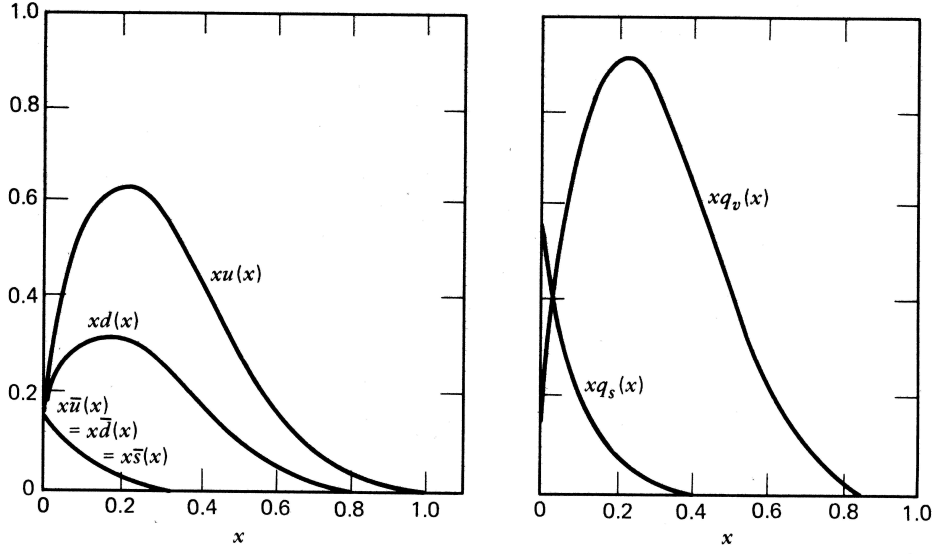


Figure 2.3: The quark structure function distributions, as a function of Bjorken  $x$ , extracted from DIS data. The right hand figure shows the separated valence and sea quark distributions (From Ref. [1]).

Now, we can take the ratio of  $F_2$  for the neutron and proton

$$\frac{F_2^n}{F_2^p} = \frac{u(x) + \bar{u}(x) + s(x) + \bar{s}(x) + 4[d(x) + \bar{d}(x)]}{4[u(x) + \bar{u}(x)] + s(x) + \bar{s}(x) + d(x) + \bar{d}(x)} \quad (2.32)$$

If we neglect the antiquark and strange PDFs and make the assumption that strong vacuum polarization does not introduce a nucleon dependent difference in the sea quark distributions the  $F_2$  ratio becomes:

$$\frac{F_2^n}{F_2^p} \approx \frac{1 + 4d/u}{4 + d/u} \quad (2.33)$$

and is expected to be true at high  $x$  where there are no sea quarks. At low  $x$  the structure function ratio should be close to unity because the sea quarks dominate the distribution and the sea in the proton and neutron is indistinguishable. Fig. 2.3 shows that the sea quarks carry a smaller percentage of the nucleon momentum than the valence quarks and can therefore be neglected as  $x \rightarrow 1$ .

If we lived in a universe where exact SU(6) symmetry held, the  $u$  and  $d$  quarks in the proton would be identical (aside from their charge and flavor), leading the nucleon and  $\Delta$  isobar to be

degenerate in mass. The wave function of the proton polarized in the  $+z$  direction would be [2]:

$$p \uparrow = \frac{1}{\sqrt{2}} u \uparrow (ud)_{S=0} + \frac{1}{\sqrt{18}} u \uparrow (ud)_{S=1} \quad (2.34)$$

$$- \frac{1}{3} u \downarrow (ud)_{S=1} - \frac{1}{3} d \uparrow (uu)_{S=1} \quad (2.35)$$

$$- \frac{\sqrt{2}}{3} d \downarrow (uu)_{S=1}, \quad (2.36)$$

where the subscript  $S$  represents the total spin of the two-quark (diquark) component. The valence quark distributions of the proton would simply follow the rule  $u_v(x) = 2d_v(x)$  for all  $x$  and the following ratio would be constant for all  $x$ ,

$$\frac{F_2^n}{F_2^p} = \frac{2}{3}, \quad \frac{d}{u} = \frac{1}{2} \quad [\text{SU}(6) \text{ symmetry}] \quad (2.37)$$

However, SU(6) symmetry does not hold in nature as evidenced by the non-zero difference between the quark masses, etc. The symmetry has been theorized to be broken because of the suppression of the diquark configuration with  $S = 1$  relative to the  $S = 0$  configuration in Eq. 2.36 [11] [12] [13]. This behavior has been built into many phenomenological fits to the PDFs (see [14], for example) but it has never been tested extensively. The apparent  $d$  quark suppression is also explained by Isgur [15] [16] as arising from one-gluon exchange dominating the color hyperfine interaction between quarks which are spectators to the deep inelastic collision. In the case where  $F_2^p$  is given by a single  $u$  quark distribution (as  $x \rightarrow 1$ ), the ratios become:

$$\frac{F_2^n}{F_2^p} \rightarrow \frac{1}{4}, \quad \frac{d}{u} \rightarrow 0 \quad [S = 0 \text{ dominant}] \quad (2.38)$$

Another prediction, based on pQCD, is that the valence wave function that dominates is the  $S_z = 0$  diquark spin projection. That is, scattering from a quark anti-aligned from the nucleon is suppressed by a factor of  $(1-x)$  less than the other, aligned state. This suggestion that the same spin orientation state dominates initially came from Farrar and Jackson [17] but a similar result has been put forth by Brodsky [18] using a hard gluon exchange model based on quark-counting rules. Both predictions lead to a non-vanishing  $d/u$  ratio:

$$\frac{F_2^n}{F_2^p} \rightarrow \frac{3}{7}, \quad \frac{d}{u} \rightarrow \frac{1}{5} \quad [S_z = 0 \text{ dominant}] \quad (2.39)$$

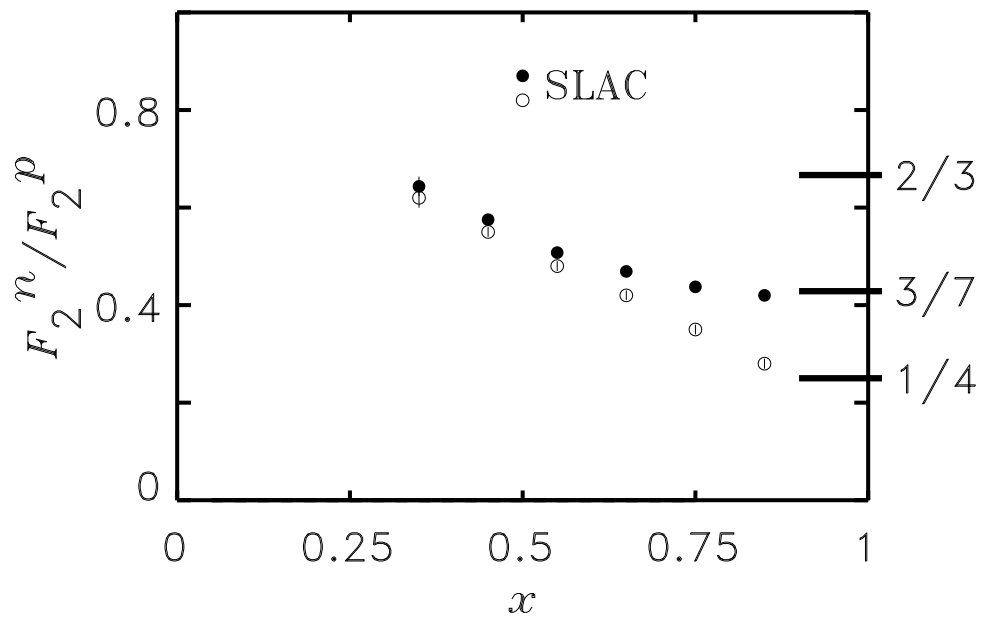


Figure 2.4: The high- $x$  behavior of  $F_2^n / F_2^p$  extracted from SLAC data ([20] and [21]). The same data converge to different theoretical predictions as  $x \rightarrow 1$  if analyzed with (full circles) and without off-shell corrections [19].

Melnitchouk and Thomas [19] have taken binding, Fermi motion and nucleon off-shellness corrections into account when analyzing SLAC data from proton and deuteron targets in the experiments E139 [20] and E140 [21]. The effect of the different prescriptions for the nuclear corrections can be seen in Fig. 2.4. The inclusion of model corrections does make the ratio data appear to trend towards  $3/7$ , but this model-dependent method is not ideal and relies on an uncertain extrapolation to  $x \rightarrow 1$ . Any method of extracting the nucleon structure function ratio at high  $x$  from bound nucleon targets will have an uncertainty on the degree of corrections which need to be applied to account for binding effects and the existence of the EMC effect in the deuteron (see Section 2.7.1 for more on this phenomenon). A technique which will allow a measurement of  $F_2^n$  on a free nucleon is necessary to answer this question once and for all.

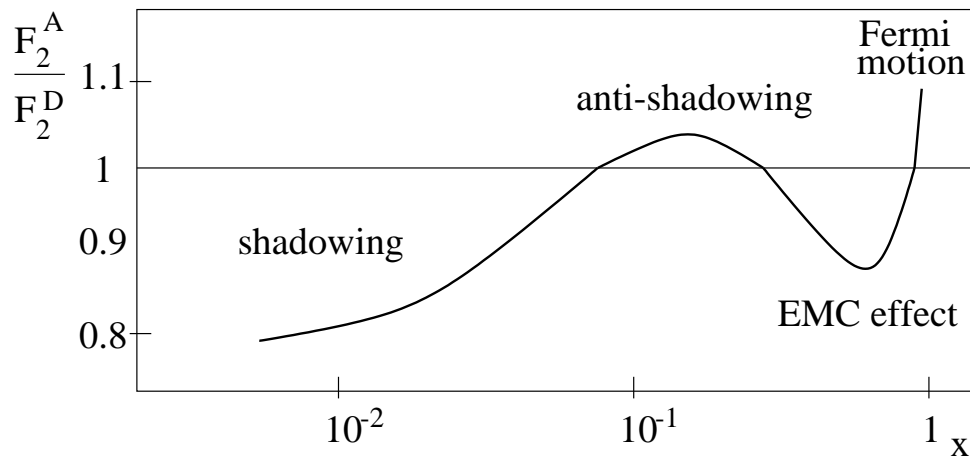


Figure 2.5: A schematic depiction of the deviation of structure function ratios from unity when using different nuclear targets.

## 2.7 Bound Nucleon Structure

### 2.7.1 Nuclear Effects

When DIS experiments first started it was thought that the choice of nuclear target did not matter because the energy scale of DIS (GeV) is much larger than the scale of nuclear binding energies (MeV). However, a great surprise was found when the European Muon Collaboration (EMC) at CERN discovered that the ratio  $R_A = F_2^A / F_2^D$  is not unity for all  $x$  [22]. This leads to the conclusion that quark distributions are different for bound and free nucleons. Furthermore,  $R_A$  is greater than unity at some values of  $x$  and less than unity at others. These regions are depicted in Fig. 2.5 and are known as the shadowing region ( $x < 0.1$ ), anti-shadowing ( $0.1 < x < 0.2$ ), the EMC effect ( $0.2 < x < 0.8$ ), and finally at  $x > 0.8$  the deviation is thought to be due to Fermi motion. There are a large number of approaches and models trying to explain this complicated behavior. An excellent review of these is found in Ref. [23]. A few of the approaches are summarized here without detailed explanations:

- $x$  Rescaling - The effective nucleon mass in nuclei is lower than the free nucleon. This is one explanation for the anti-shadowing effect.
- Pion Enhancement - The nucleon-nucleon interaction enhances the pion field in the nucleus, increasing with mass number  $A$ . This theory attempts to describe anti-shadowing and the EMC effect but it has been mostly ruled out by other data.

- $Q^2$  Rescaling Model - There is an increase in the quark confinement scale in the nucleus versus the free nucleon. Only the EMC effect has been explained by this model.
- Nucleon Swelling - A larger bound nucleon radius will compress the quark momentum distribution and decrease the measured value of  $F_2^A$ .
- Cluster Model - A dense nucleus with tightly packed nucleons is treated as a collection of multi-valence quark bags. This theory has successfully described the EMC effect in iron.

An interesting model to explain the EMC effect at  $x > 0.3$  is put forth by Frankfurt and Strikman [24]. The color screening model for the suppression of point-like configurations (PLC) in bound nucleons predicts deviations from unity of the ratio  $R_n$  of more than 5%. In this model one attributes most or all of the EMC effect to a medium modification of the internal structure of the bound nucleon, and little of the effect to mechanisms such as nuclear binding. The PLC suppression prediction to the nucleon structure function ratio is shown together with the results of this experiment in the final chapter.

## 2.7.2 Spectator Tagging

Our aim in this experiment is to extract the nucleon structure function ratio without extreme model dependence at high  $x$ . One way to realize this goal is spectator tagging — that is, by measuring  $d(e, e' p_s)X$  where the electron and spectator proton are detected and the spectator is assumed to have played no role in the electron-neutron interaction. Sec. 2.8 discusses for which spectator kinematic range this technique is valid. For now we briefly present the theoretical framework of spectator tagging.

Deep inelastic scattering from the deuteron is approached most simply from the nuclear impulse approximation [25]. Consider the case of one nucleon on its mass shell and the other off shell — this is known in the literature as the Covariant Instant-Form Approach. In this approximation the deuteron hadronic tensor can be written as

$$W_D^{\mu\nu}(P, p_s, q) \approx S^{IF}(P, p_s) W_N^{\mu\nu(eff)}(p_s, q) \quad (2.40)$$

where  $P$ ,  $p_s$  and  $q$  are the four-momenta of the deuteron, the spectator nucleon and the virtual photon, respectively. The spectral function in this approximation,  $S^{IF}$ , is the probability of

detecting a spectator with the given kinematics and can be written as

$$S^{IF}(\alpha_s, p_T^s) = (2 - \alpha_s) \frac{E_s M_D}{2(M_D - E_s)} |\psi_D(\alpha_s, p_T^s)|^2. \quad (2.41)$$

The definition for the light-cone momentum fraction of the spectator nucleon is made here,  $\alpha_s = \frac{E_s - p_z^s}{M}$ , as well as the four-momentum of the spectator,  $p_s = (E_s, p_T^s, p_z^s)$ , with  $\hat{z}$  defined in the same direction as the momentum transfer. The mass of the deuteron is  $M_D$  and its non-relativistic wave function is represented by  $\psi_D$ . The spectral function is normalized such that

$$\int d^2 p_T^s \frac{d\alpha_s}{\alpha_s} S^{IF}(\alpha_s, p_T^s) = 1. \quad (2.42)$$

The effective (that is, bound) nucleon hadronic tensor is defined as the following and can be compared with the free nucleon tensor in Eq. 2.8:

$$W_N^{\mu\nu(eff)} = -\left(g_{\mu\nu} + \frac{q_\mu q_\nu}{Q^2}\right) F_{1N}^{(eff)}\left(\frac{x}{2 - \alpha_s}, p^2, Q^2\right) + \dots \quad (2.43)$$

in which the effective nucleon structure function  $F_{1N}^{(eff)}$  depends on the momentum fraction  $x/(2 - \alpha_s)$ , the virtuality  $p^2$  of the bound nucleon and  $Q^2$ . The virtuality can be expressed as the following function of the transverse momentum,  $p_T$ , of the interacting nucleon, which is equal and opposite to that of the spectator:

$$p^2 = -\frac{2p_T^2 + (2 - \alpha_s)M^2}{\alpha_s} + \frac{1}{2}(2 - \alpha_s)M_D^2 \quad (2.44)$$

Now, if we go to the light-cone approach where both nucleons are on their mass shell but off the light-cone energy shell, the instant form spectral function is replaced with the following expression for the deuterium momentum distribution:

$$S^{LC}(\alpha_s, p_T) = \frac{\sqrt{M^2 + \mathbf{k}^2}}{2 - \alpha_s} |\psi_D(k)|^2 \quad (2.45)$$

and we have the definition

$$k \equiv |\mathbf{k}| = \sqrt{\frac{M^2 + p_T^2}{\alpha_s(2 - \alpha_s)} - M^2}. \quad (2.46)$$

The spectator approximation assumes that the recoil proton is on its mass shell when the

electron strikes the neutron and does not gain any energy or momentum. After the interaction takes place on its sister nucleon, the spectator travels off with unchanged momentum. The differential cross section can now be written (when the spectator kinematics are in the region where final state interactions are small — see Section 2.8.3):

$$\frac{d\sigma}{dx dW^2 d(\log \alpha_s) d^2 \mathbf{p}_T} = \frac{2\alpha_{\text{em}}^2}{Q^4} (1-y) S(\alpha_s, p_T) F_2^{n(\text{eff})} \left( \frac{x}{2-\alpha_s}, p_T, Q^2 \right). \quad (2.47)$$

In the limit where  $p^2 \rightarrow M^2$  and  $\alpha_s \rightarrow 1$  the effective neutron structure function  $F_2^{n(\text{eff})}(W^2, Q^2, p^2) \rightarrow F_2^n(W^2, Q^2, M^2) \equiv F_2^n(x, Q^2)$ , which is the free neutron structure function.

We can also redefine the standard  $x$ ,  $y$ , and  $W$  in terms of our new spectator kinematics. These expressions are the proper ones to use for scattering from a moving neutron inside of the deuteron:

$$\begin{aligned} x^* &= \frac{Q^2}{2p_n^\mu q_\mu} \approx \frac{Q^2}{2M\nu(2-\alpha_s)} = \frac{x}{2-\alpha_s} \\ y^* &= \frac{p_n^\mu q_\mu}{p_n^\mu k_\mu} \approx y \\ W^{*2} &= (p_n^\mu + q^\mu)^2 \approx M^{*2} - Q^2 + 2M\nu(2-\alpha_s) \end{aligned} \quad (2.48)$$

where  $q^\mu = (\nu, \mathbf{q})$  is the usual momentum transfer four-vector,  $k^\mu = (E, 0, 0, E)$  is the momentum four vector of the incoming electron,  $p_n^\mu = (M_D - E_s, -\mathbf{p}_s)$ . Also, the off-shell mass of the bound nucleon is given by  $M^{*2} = (M_D - E_s)^2 - p_s^2$ , defining the degree to which the struck neutron is off-shell. Now that we've made these crucial definitions, the next section will discuss how to select spectator kinematics which lead to the best approximation of scattering from a free neutron.

## 2.8 Backgrounds

It is intuitively obvious that selecting a proton with backward kinematics with respect to the direction of momentum transfer will minimize the final state interactions (FSIs). If the proton were not a spectator in the electron-neutron interaction, some momentum would be transferred and it would be kicked forward. Restriction of the spectator momentum to small values not

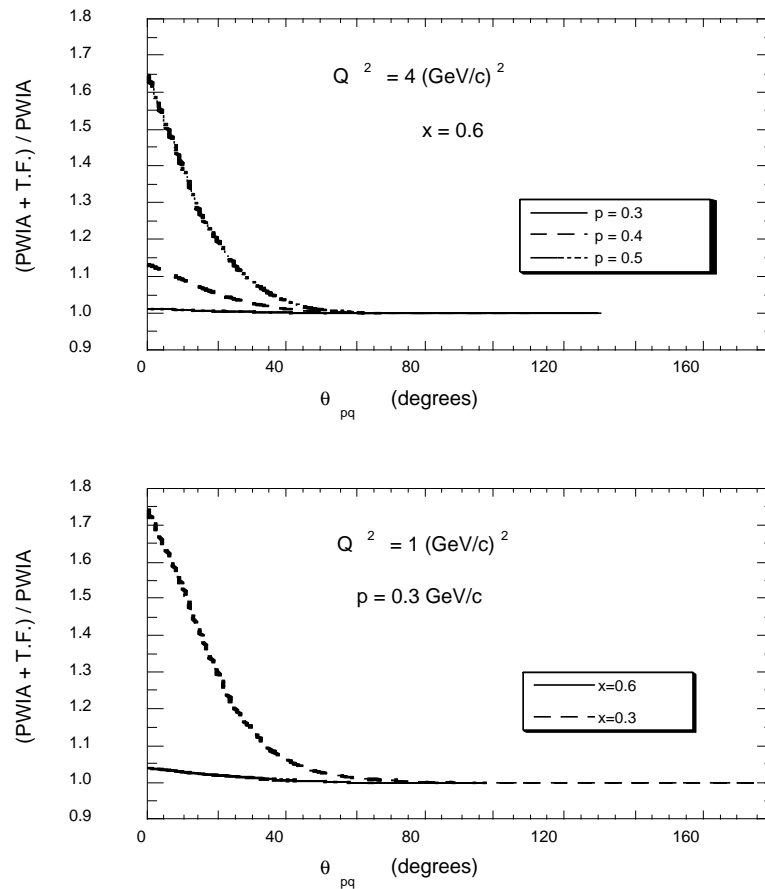


Figure 2.6: The ratio of the plane wave impulse approximation calculation of DIS from the deuteron with and without target fragmentation as a function of the angle between the spectator proton and the momentum transfer [26]. In this figure  $p = p_s$ , the magnitude of the spectator momentum.

only ensures that the interaction took place on a loosely bound deuteron (quasi-free nucleon constituents), but this requirement also puts the scattering event in a region where FSIs are thought to be small. This section will briefly outline the range of spectator momentum,  $p_s$ , and angle,  $\theta_{pq}$ , with respect to the direction of momentum transfer  $\vec{q}$  to choose so that target fragmentation, FSIs and off-shell corrections are as small as possible.

### 2.8.1 Target Fragmentation

A low momentum proton can be produced by the hadronic debris of the struck neutron. These protons from direct quark to proton fragmentation are in the direction of the  $q$  vector and a simple requirement that detected spectator protons are ejected at a backward angle will serve

to suppress this background.

This conclusion is supported by Fig. 2.6 which shows the ratio of the calculated contribution of the plane wave impulse approximation (PWIA) including a model for target fragmentation to the PWIA without the effects [26]. It is clear that for  $\theta_{pq} > 90^\circ$  target fragmentation is negligible and independent of  $p_s$ ,  $x$ , and  $Q^2$ .

## 2.8.2 Off-shell Corrections

If the neutron structure function measured in the bound deuteron system is to be the best approximation to the free structure function, the amount which it is off the mass shell must be minimized. It is impossible in a real experiment for the difference  $p^2 - M^2 = 0$  because the spectator would not leave the target. An evaluation of how much the neutron's off-shellness matters in the spectator approach is therefore necessary.

In the spectator model of Ref. [27], the effective neutron structure function from Eq. 2.47 is described in terms of a nucleon-quark-diquark interaction. The model is constrained by fitting to proton and deuteron structure function data and the dependence on the virtuality of the off-shell neutron is investigated. The ratio of the off-shell to on-shell neutron structure functions,  $R_n = F_2^{n(eff)} / F_2^{n(free)}$ , is plotted in Fig. 2.7 as a function of spectator proton momentum for different values of  $x$ . When  $p_s$  is below 100 MeV/c, regardless of the value of  $x$ ,  $R_n$  is within 1% of unity.

Another theoretical model found in Refs. [28] and [29] describes the scattering from a bound nucleon in terms of a relativistic quark spectral function. Here, the way the structure function of the bound nucleon deviates from the free nucleon is dependent on the spectator diquark system, the bound nucleon momentum, and the binding energy. Again, at low values of  $p_s$ ,  $R_n$  approaches 1.0. In this model the ratio's dependence on  $x$  is negligible. This behavior is witnessed in Fig. 2.8.

A third model using an instant form approach can be found in Ref. [30]. Here a shifted energy transfer,  $\nu \rightarrow \bar{\nu}$ , which depends on the degree of off-shellness, relates the bound and free structure functions. The shift in  $\nu$  will cause a corresponding shift in  $x$  and  $Q^2$  where the structure function is evaluated. The ratio of the calculation of the structure functions in the PWIA with and without these off-shell effects is shown in Fig. 2.9. In this model, at  $p_s = 100$

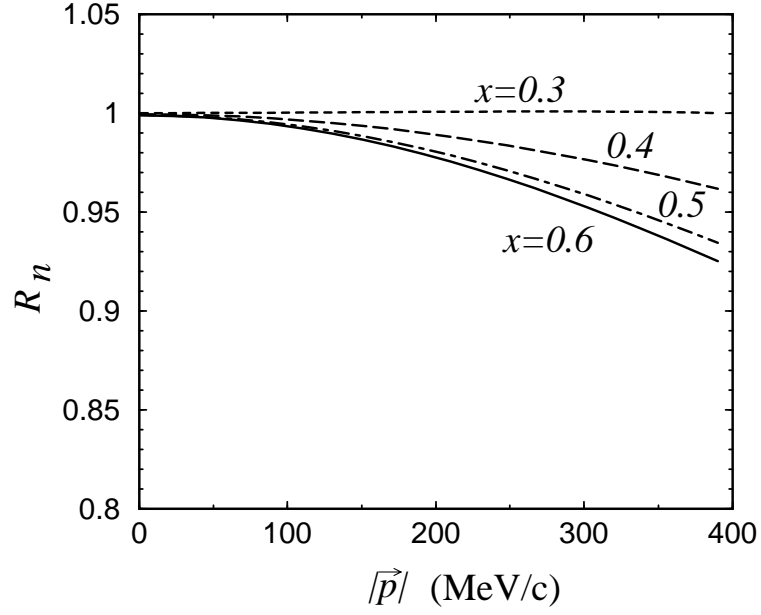


Figure 2.7: The bound to free ratio ( $R_n \equiv F_2^{n(eff)}/F_2^{n(free)}$ ) of neutron structure functions, as a function of spectator momentum from Ref. [27].

MeV/c the ratio is almost exactly unity, independent even of  $\theta_{pq}$ .

### 2.8.3 Final State Interactions

There are no nuclear scattering experiments, other than elastic scattering, which are completely immune to FSIs, but again, there are spectator kinematics where the effect of the spectator proton rescattering from the deep inelastic debris is mitigated. In the distorted wave impulse approximation, treated in Ref. [25], the deuteron spectral function, with an estimate for FSIs taken into account ( $eD \rightarrow epn$ ), is compared to the normal spectral function. It can be seen in Fig. 2.10 that as the spectator's transverse momentum with respect to the momentum transfer,  $p_T \rightarrow 0$  and  $\alpha_s < 1.5$ , the FSI effects contribute less than 5% to the difference between the spectral function calculations.

Another theoretical picture of the impact that FSIs have on the spectral function comes from Ref. [31] where the authors evaluated  $S^{FSI}$  within a hadronization model. An effective cross section describing the probability that a backward spectator will interact with the hadronic debris from DIS is developed in this framework. The effective rescattering cross section is logarithmically dependent on time and momentum transfer, but a constant cross section similar to the

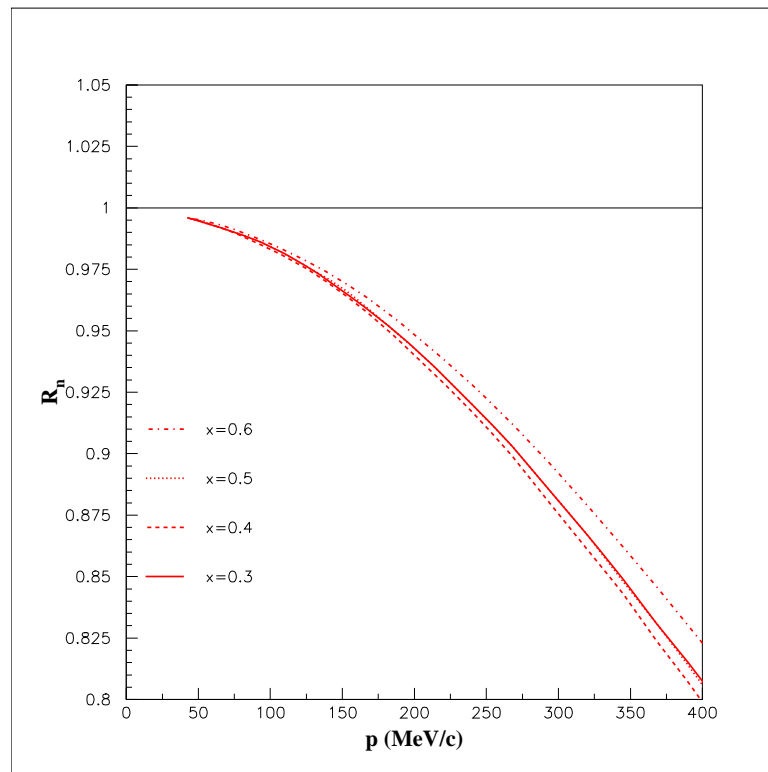


Figure 2.8: The ratio  $R_n \equiv F_2^{n(eff)} / F_2^{n(free)}$  of the bound to free neutron structure functions, as a function of the spectator proton momentum, in the relativistic quark spectral function model of Refs. [28] and [29]. Note that this result is largely independent of  $x$ .

total hadronic cross section was also considered. The ratio of spectral functions calculated with and without the contribution of FSIs in PWIA can be seen in Fig. 2.11. No matter what model for the rescattering probability,  $\sigma_{eff}$ , is used, if the spectator momentum is kept at or below 100 MeV/c for  $\theta_{pq} > 110^\circ$ , the FSIs play little role in determining the proper spectral function.

## 2.9 Analysis Objectives

In light of the theoretical predictions from Sec. 2.8 concerning the range in spectator proton kinematics which reduce background effects and best reproduce the free neutron structure function, this analysis will make a cut of  $p_s < 100$  MeV/c and  $\theta_{pq} > 100^\circ$ . Protons which pass these cuts (as well as all the other quality cuts discussed in Chapter 5) will be known as Very Important Protons or VIPs. Unless otherwise noted, all reports of physics data should be

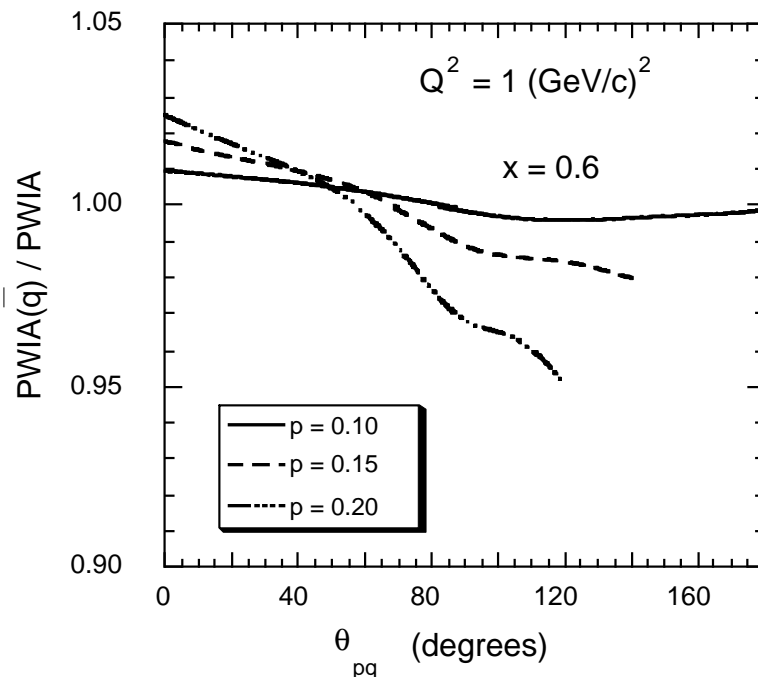


Figure 2.9: Ratio of bound to free nucleon structure functions versus  $\theta_{pq}$ , calculated in the plane wave impulse approximation with (PWIA( $\bar{q}$ )) and without (PWIA) off shell effects in the model of Ref. [30]. The spectator proton momentum  $p$  is in units of GeV/c.

assumed to be extracted from events that had a VIP in coincidence with the scattered electron.

The structure function ratios presented in this document is not extracted from the measurement of absolute cross sections. Instead, the ratios of events *tagged* by the semi-inclusive reaction  $d(e, e'p_s)X$  to *untagged* inclusive events,  $d(e, e')X$ , in the same data set are reported. In this way, the factors that are crucial to the measurement of a cross section (electron acceptance, integrated beam charge, electron tracking efficiencies, computer live time, and target thickness) will largely cancel out in the ratio since these factors are common to numerator and denominator. Also, many systematic errors are eliminated in the ratio, but there are still factors which will need to be addressed for the spectator proton and they will also be discussed in Chapter 5.

An extraction of the largely model-independent nucleon structure function ratio ( $F_2^n / F_2^p$ ) will be presented as a function of  $x$  and compared to the results of different prescriptions for the nuclear corrections.

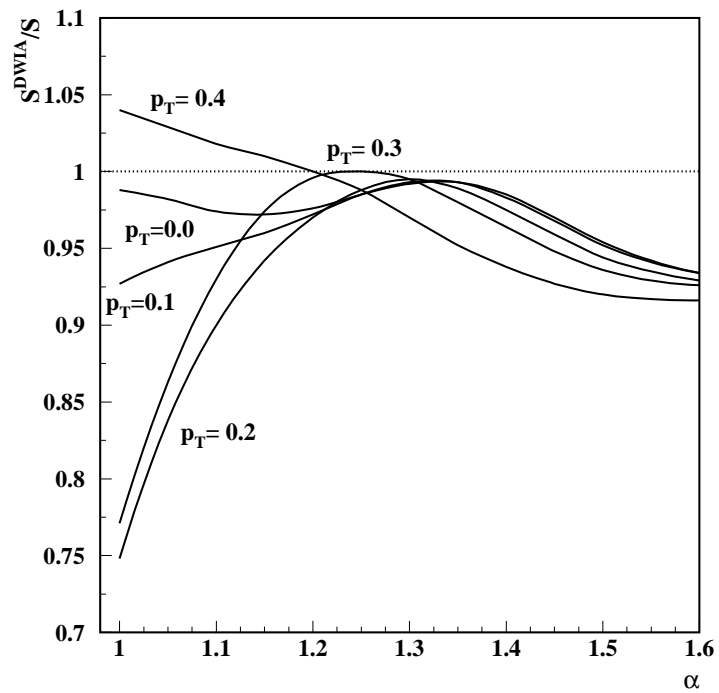


Figure 2.10: Spectral function calculated with ( $S^{DWIA}$ ) and without ( $S$ ) FSI effects within the DWIA [25]. The curves correspond to different values of the spectator proton transverse momentum  $p_T$  (in GeV/c).

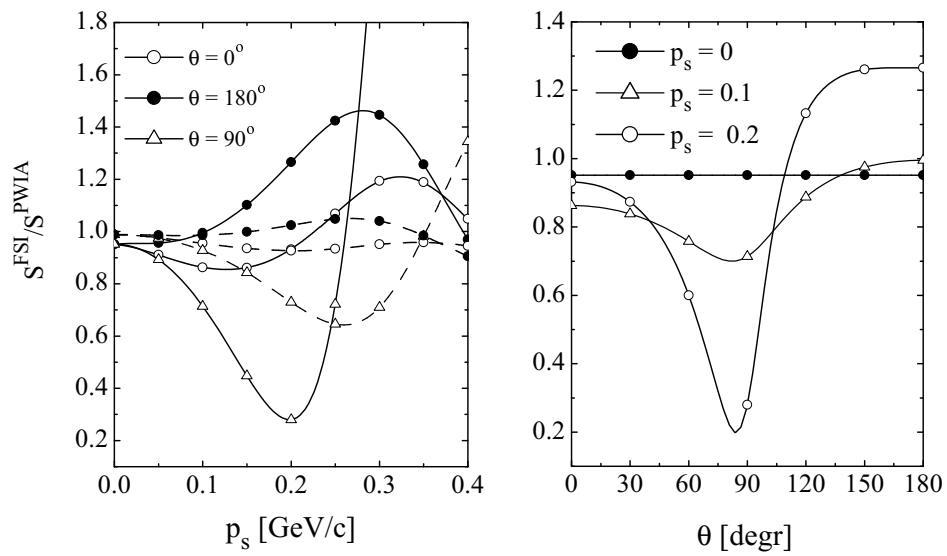


Figure 2.11: The spectator momentum and angular dependence of the ratio  $S^{FSI}/S^{PWIA}$  from [31], for DIS kinematics  $Q^2 = 5 \text{ GeV}^2$  and  $x = 0.2$ . Left panel: dependence on spectator momentum, using a functional form for  $\sigma_{eff}$  (solid), and a constant  $\sigma_{eff} = 20 \text{ mb}$  (dashed). Right panel: dependence on the labframe angle between the spectator proton and the virtual photon direction.

# Chapter 3

## PRE-EXISTING EXPERIMENTAL APPARATUS

### 3.1 Continuous Electron Beam Accelerator Facility

Jefferson Laboratory is home to the superconducting radiofrequency (RF) Continuous Electron Beam Accelerator Facility (CEBAF) [32]. The machine was built in the early 1990's as a tool for researchers in nuclear and particle physics. The facility consists of two antiparallel linear accelerators linked by nine recirculation beam lines. Simultaneous delivery to three end stations is possible with currents up to  $300 \mu\text{A}$  and longitudinal beam polarizations up to  $\approx 85\%$ . The consistency of the beam's delivered momentum is superb with a relative momentum spread of only a few times  $10^{-5}$ . The main components of the accelerator can be seen in Fig. 3.1. A 100 kV photoelectron gun injects 45 MeV electrons in 1497 MHz RF modulated 3 pC charge bunches. These electrons are then fed into two 600 MeV linear accelerators (RF cryomodules). The cryomodules have an average field gradient of 7.5 MeV/m and operate at a temperature of 2 K. The RF separator splits the beam into three 499 MHz beams for the experimental halls. Recirculation arcs magnetically steer the beam up to 5 times around the racetrack, kicking the electrons up in energy by 1-1.2 GeV per pass. The current delivered to Hall-B must be reduced because the drift chambers can only handle 100 nA before incurring multiple high voltage breakdowns in Region 1 (more details later in this chapter). During the BoNuS run period the current was between 30-60 nA.

### 3.2 CEBAF Large Acceptance Spectrometer

Jefferson Lab's Experimental Hall B houses the CEBAF Large Acceptance Spectrometer (CLAS). This special spectrometer differs from other detectors at Jefferson Lab in that it can detect particles in close to  $2\pi$  steradians. In the following discussion  $\theta$  refers to the polar angle and  $\phi$  is the azimuthal angle with respect to the electron beam direction. CLAS is a combination of six

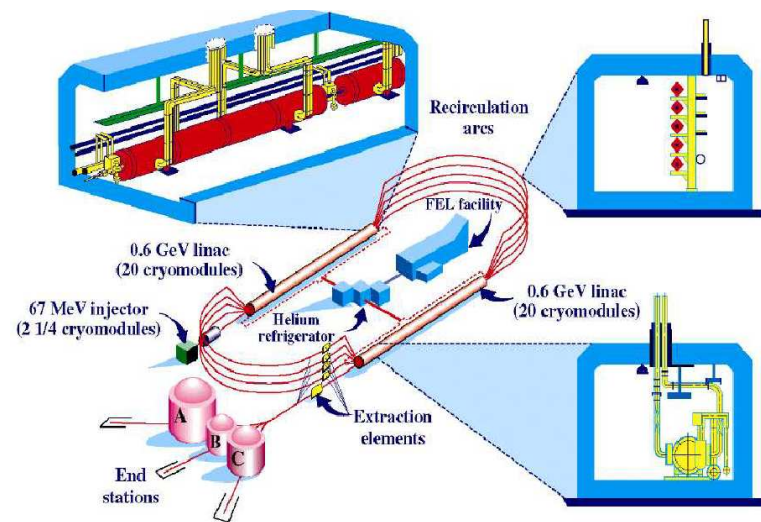


Figure 3.1: A depiction of the Continuous Electron Beam Accelerator Facility showing the location of each component in the racetrack.

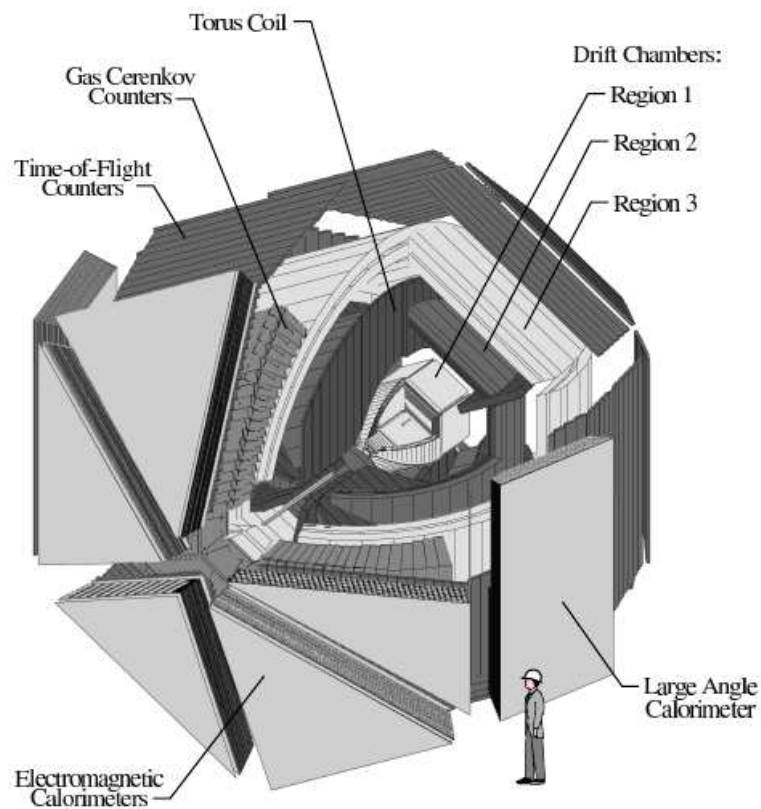


Figure 3.2: The CLAS detector shown with a portion removed so that the inside may be clearly viewed. The beam travels down the central axis of the detector cluster in this image from upper right to lower left.

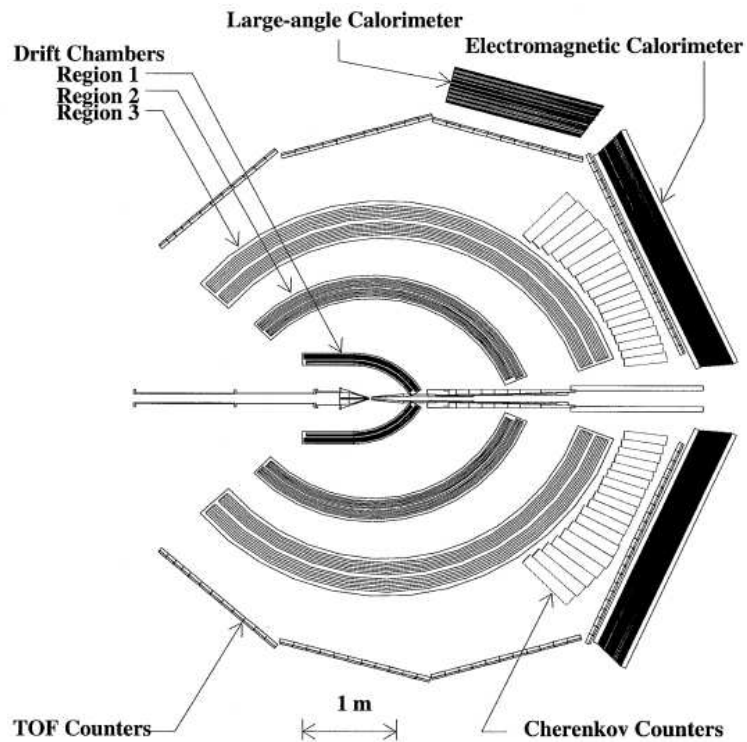


Figure 3.3: A cross-sectional view of the CLAS detector sliced parallel to the beamline.

identical spectrometers rotated about  $\phi$  in  $60^\circ$  increments (Fig. 3.2). Figs. 3.3 and 3.4 show cross sections of the entire spectrometer taken parallel and perpendicular to the beamline, respectively. In between the sectors are the coils of a torus magnet. Each sector contains three layers of drift chambers (DC) and one plane of time-of-flight (TOF) scintillators covering the full polar range  $8^\circ < \theta < 142^\circ$ . The forward region ( $8^\circ < \theta < 45^\circ$ ) of each sector is instrumented with a Cherenkov counter (CC) and an Electromagnetic Calorimeter (EC).

The four main detector subsystems require off-line calibration. A standardized procedure for each calibration has been in place for many years. The TOF [33] and DC [34] calibrations are performed by an assigned person from each rungroup, whereas the EC and CC [35] calibrations are more straightforward, and they can be completed quickly by detector experts. A cursory discussion of the design and performance of each component follows, along with the calibration procedures. The myriad of detector details are discussed in depth in the references.

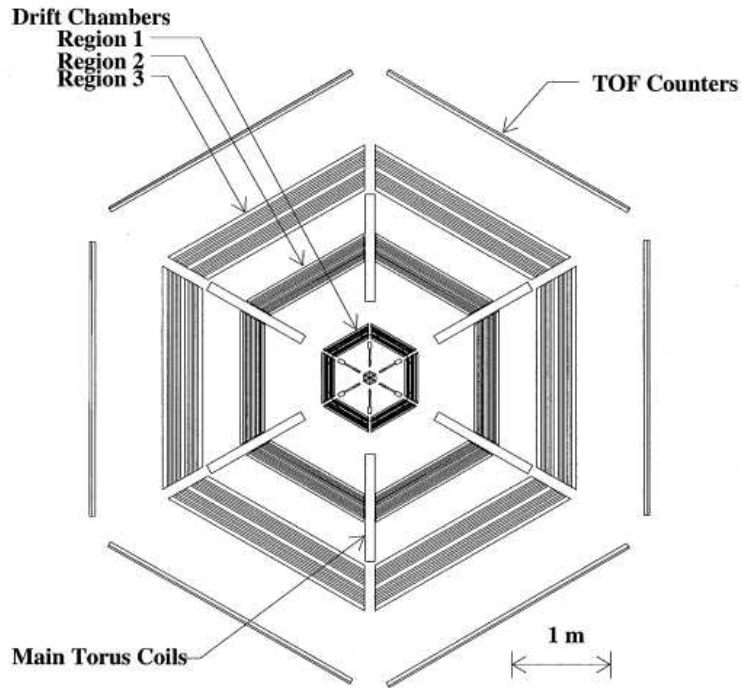


Figure 3.4: A cross-sectional view of the CLAS detector sliced perpendicular to the beamline.

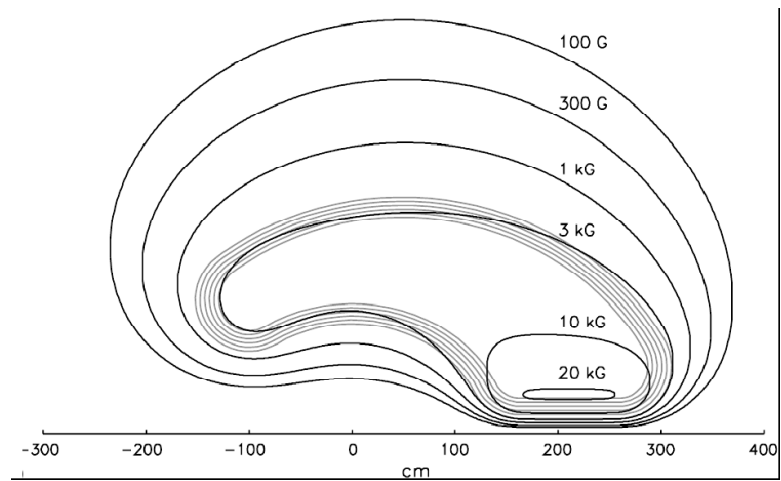


Figure 3.5: Lines of constant magnetic field in the center of the area between two torus coils. The outline of the coils is also shown as a multiple-lined "kidney bean".

### 3.2.1 Torus Magnet

After the beam interacts with the target material, scattered electrons and other charged particles are bent by a magnetic field in order to determine their momentum by the curvature of their trajectories. The field is produced by six superconducting coils arranged in a toroidal geometry. There is no iron in the coils so the field can be calculated simply from the current in the coils [36]. The entire magnet has a 5 m diameter and is approximately 5 m in length. Each segment has a kidney bean shape (Fig. 3.5), the six sectors together produce an azimuthal magnetic field which is most uniform at the midlines between the coils. Clearly the field vectors become larger and less regular near the coils themselves (Fig. 3.6), but there is no tracking volume at the coils or in the projected volume behind them. A good field map within the tracking volume is necessary to produce accurate momentum measurements. The highest field value is  $2.5 \text{ T} \cdot \text{m}$  at a current of 3860 A and forward angles. The  $\int \mathbf{B} \cdot d\mathbf{l}$  drops off to  $0.6 \text{ T} \cdot \text{m}$  at  $90^\circ$ . The particles can be bent towards or away from the beam axis to sweep low-angle particles into or out of the detector acceptance. In the area at the very center between two coils, there is no deflection in  $\phi$ . Some small  $\phi$  deflection does occur for tracks not on the center line. For During BoNuS the current was set at 1500 A when the electron beam was 1 or 2 GeV and 2250 A for 4 and 5 GeV. This gave us an electron momentum resolution of about 1%, after calibration. The various tracking and energy measuring devices naturally fall into a six segment geometry around the six coils. Each section is identical, only rotated  $60^\circ$  in  $\phi$ . Subsequently, there are six blind spots in  $\phi$  where the coils are mounted, covering  $\Delta\phi \sim 20^\circ$  each.

### 3.2.2 Drift Chambers

The first detector elements encountered by the final state particles are the drift chambers [37]. Each of the six sectors has three drift chambers at increasingly larger radial distances from the beam line, for a total of 18 separate drift chambers. The wire direction is perpendicular to the bend plane. The chambers can track particles with a polar angular range from  $\theta = 8\text{--}142^\circ$  and momentum  $> 200 \text{ MeV}/c$ . The design resolution goals were 0.5% for momentum and 2 mrad for the scattering angle. Region 1 (R1) is in the area of smallest field and closest to the target. Region 2 (R2) is in the middle of the coils where the highest field and azimuthal displacement occurs. Region 3 (R3) lies outside of the torus magnet. Fig. 3.7 shows the positions of the

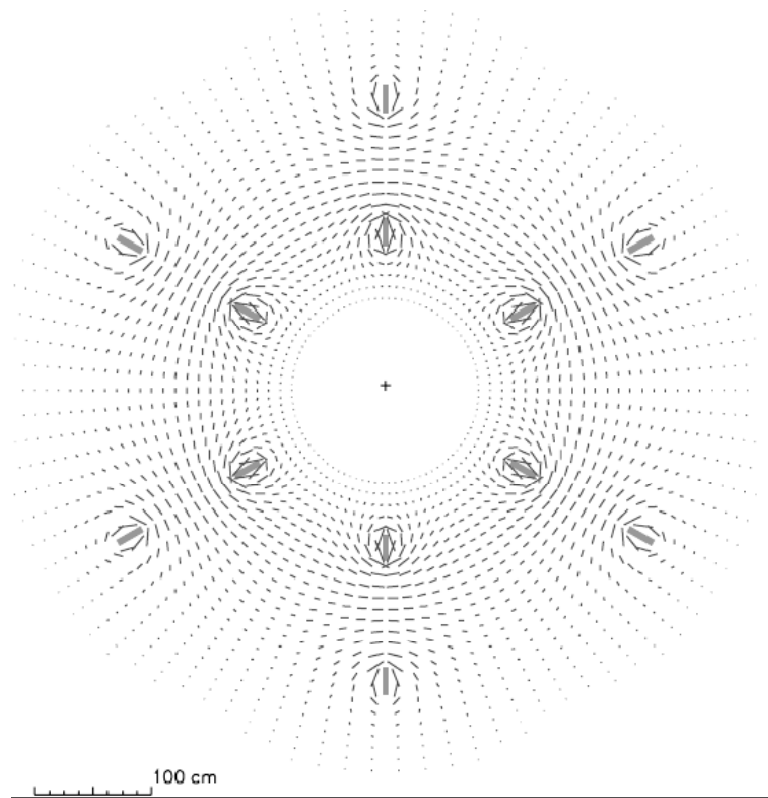


Figure 3.6: Magnetic field vectors for the CLAS toroid viewed transverse to the beam. The cross section is taken at the nominal CLAS target position. A larger line segment indicates a stronger relative field at that point.

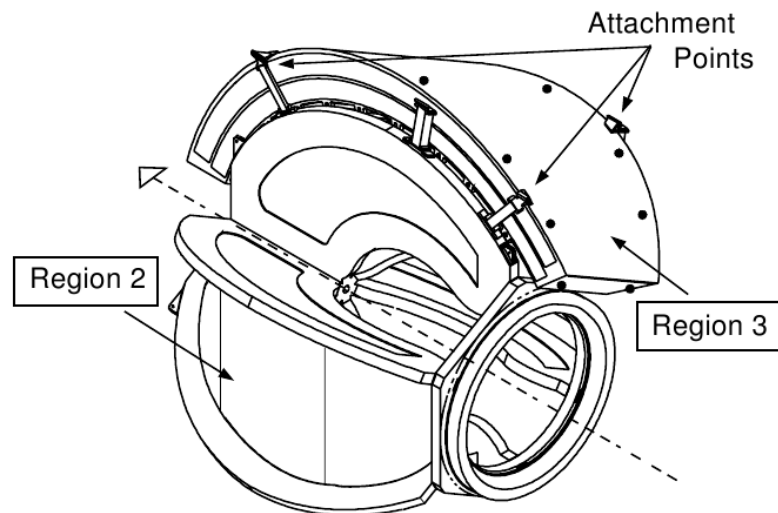


Figure 3.7: An R2 chamber and an R3 chamber shown in their installed positions on the torus cryostat. The R1 chambers are not shown. For the R3 chamber the three attachment points are indicated [36].

chambers with respect to the torus cryostat. The tracks are measured at three points to an accuracy of  $100 \mu\text{m}$  in the bend plane (containing the beam line) and  $1 \text{ mm}$  perpendicular to the bend plane. The amount of material is  $< 0.01$  radiation length in the tracking region. Each chamber is divided into two superlayers in order to obtain track redundancy and increase pattern recognition. One superlayer has wires axial to the magnetic field and the other has its wires tilted at  $6^\circ$ . There are six layers of drift cells in each superlayer (except the first superlayer of R1 which has only four). The cells are hexagonal in shape and there are 35,000 in all. Fig. 3.8 shows a typical track pattern. A signal wire lies at the midpoint of each hexagon with field wires at the vertices. There are guard wires at the edges of the chambers held at a high voltage intended to mimic an infinite grid of drift cells. The gas gain is a few times  $10^4$  and the electric field at the surface of the sense wires is  $\approx 280 \text{ kV/cm}$ . To minimize cathode deposits, the field at the surface of the field wires is  $< 20 \text{ kV/cm}$ . The drift chambers are filled with a typical ionization detector gas mixture of Argon- $\text{CO}_2$  in a 9:1 ratio that provides a saturated drift velocity of  $4 \text{ cm}/\mu\text{s}$ .

The drift time for each channel must be known in order to optimize position resolution in the drift chambers. Environmental conditions in the experimental hall, such as atmospheric pressure, humidity, etc., change the drift chamber gas properties. The drift time can also depend on the particle's entrance angle and velocity and the local magnetic field. Once a reference time is measured in the scintillation counters, the TDC time on the sense wires can be compared to the reference value and parameterized according to the following equation,

$$x(t) = v_0 t + \eta \left( \frac{t}{t_{max}} \right)^q + \kappa \left( \frac{t}{t_{max}} \right)^p \quad (3.1)$$

where  $t_{max}$  is the maximum drift time and  $v_0$  is the value for the saturated drift velocity near  $t = 0$ . The parameters  $\eta$ ,  $q$ ,  $\kappa$ , and  $p$  are determined by minimizing

$$\chi^2 = \frac{|x(t) - x_{path}|^2}{\sigma_{path}^2} \quad (3.2)$$

where  $x_{path}$  and  $\sigma_{path}$  are the distance of closest approach (DOCA) from the sense wire along the path and the error on this quantity, respectively. The quality of the calibration is measured via the spatial residual ( $|x(t) - x_{path}|$ ) where the lower the value, the better. The calculated

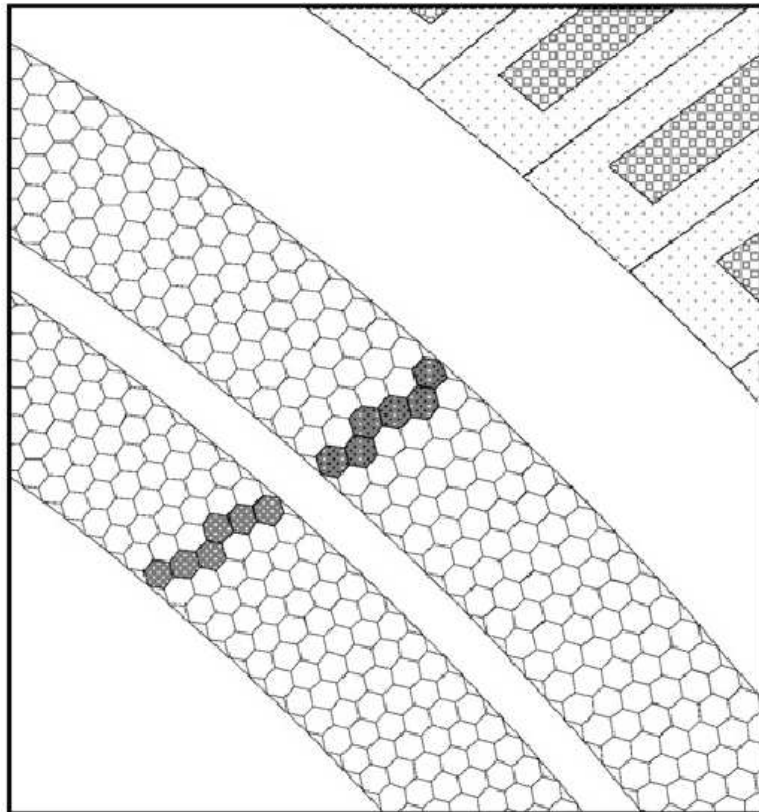


Figure 3.8: A track in two superlayers of a R3 sector. Sense wires are located at the center of each hexagon and field wires are at the vertices. There is no physical component along the edges of each hexagon, which simply show the outline of the individual tracking volumes.

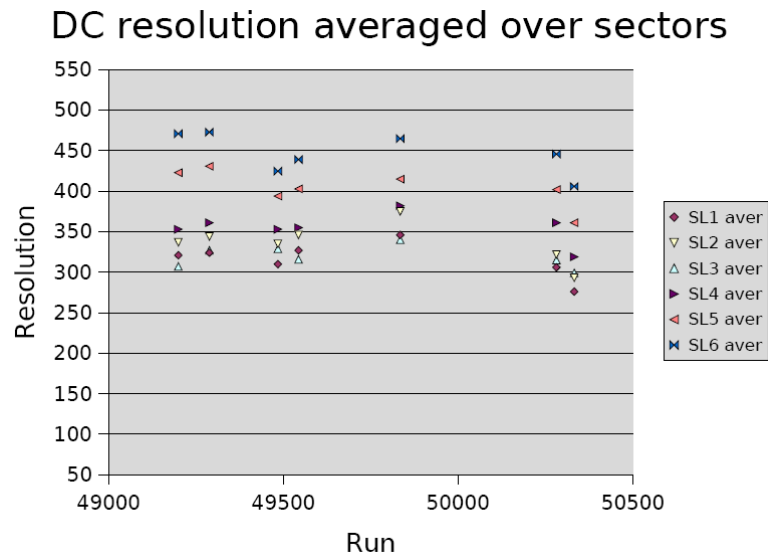


Figure 3.9: A sample of the final result for the calibration of the drift chambers. The resolution is shown in units of  $\mu\text{m}$ .

value  $x(t)$  can be found via Eq. 3.1 and a sample of the resolution of the residuals for our experiment can be found in Figs. 3.9 and 3.10. We obtained an average residual width between 250-500  $\mu\text{m}$  for all sectors.

The CLAS Region 1 drift chambers were pulled out for maintenance before the BoNuS run period. An alignment procedure needed to be implemented in order for the mean residual per layer to fall on zero. To take into account the new wire positions, the drift chamber position in the software was manually adjusted, then an automatic alignment script was executed on the altered results to optimize the new residuals. A comparison between the graphs in the upper left corner of Fig. 3.11 and Fig. 3.12 shows that this procedure was successful in reducing the mean of the residuals in Region 1 by making them more consistent with zero.

### 3.2.3 Cherenkov Counters

After passing through the drift chambers, a charged particle ( $\theta < 45^\circ$ ) encounters the Cherenkov counters (CC) [38]. The main purpose of the CC is to separate pions from electrons. The amount of material that particles must pass through before reaching the outer scintillators and calorimeters must be minimized in order to mitigate absorption and creation of secondaries.

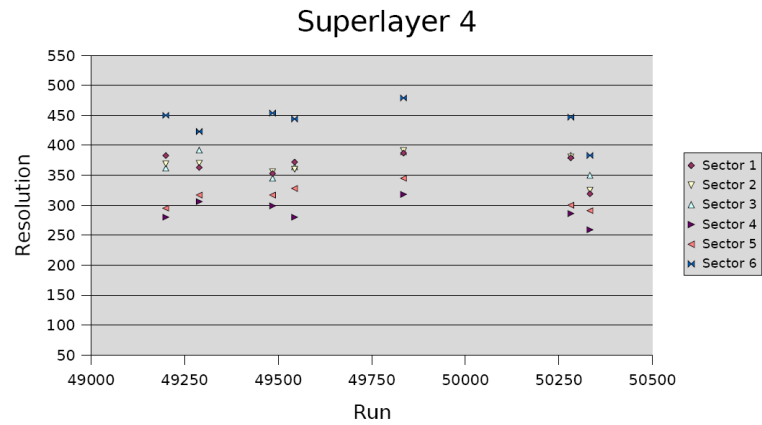


Figure 3.10: An example of the DC calibration result for super layer 4 of each sector. The resolution is shown in units of  $\mu\text{m}$ .

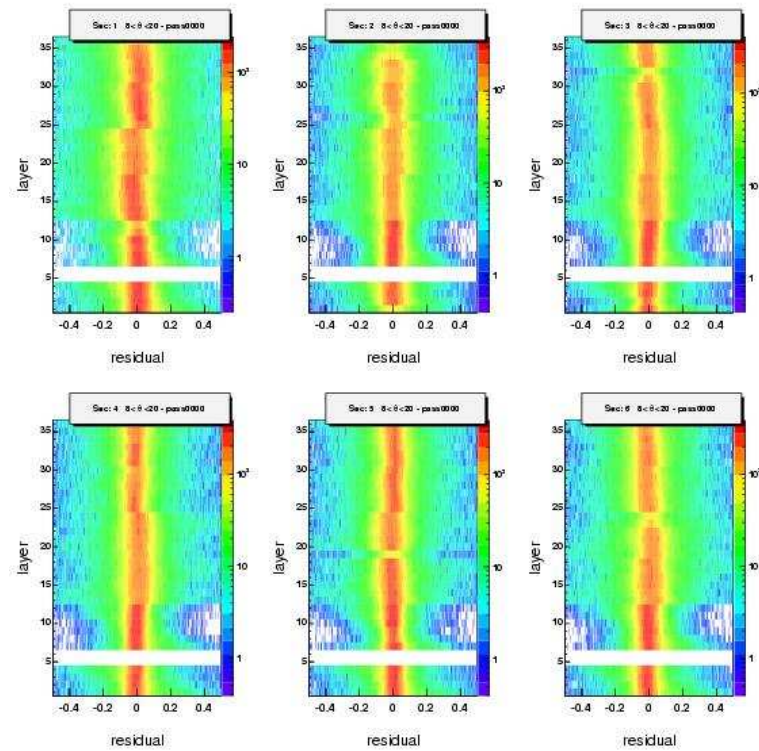


Figure 3.11: Residuals (in mm) for each super layer, by sector, before alignment. Note that the worst is Sector 1 because it was pulled out for maintenance before the BoNuS run period.

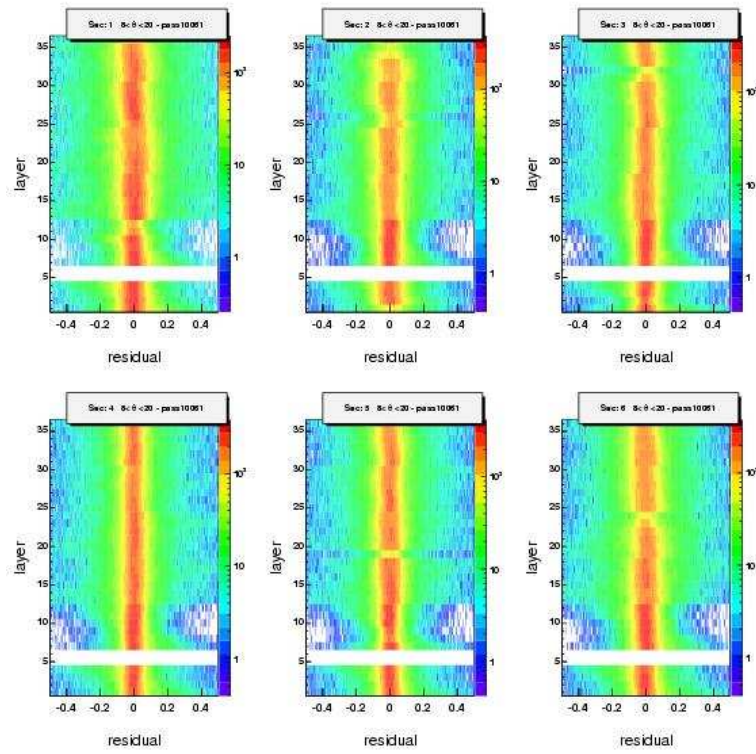


Figure 3.12: Residuals (in mm) for each super layer, by sector, after the alignment procedure. Note that Sector 1 has vastly improved (compare with Fig. 3.11).

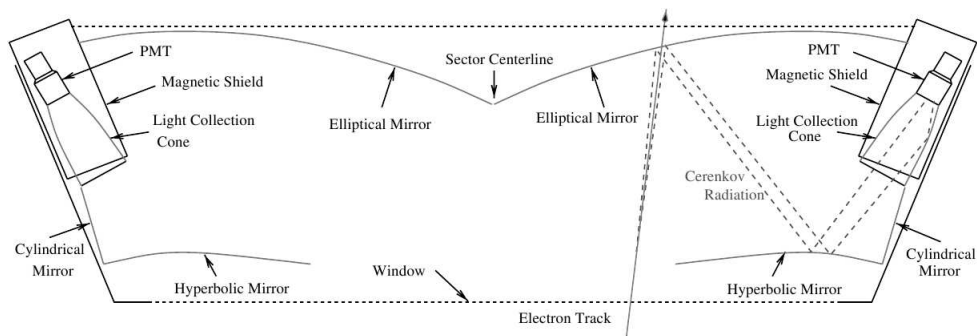


Figure 3.13: An optical diagram of the CLAS Cherenkov Counter. Cherenkov light is focused via a mirror system into shielded PMTs.

Furthermore, multiple scattering must be minimized because it degrades the energy or momentum resolution. The CC consists of 216 Cherenkov light collection modules (18 regions of  $\theta$ , 12 subsectors in  $\phi$ ). Elliptical, cylindrical and hyperbolic mirrors serve to focus the photons into the photomultiplier tubes (PMTs) (Fig. 3.13). The PMTs lie in  $\phi$  regions which are in the shadow cast by the torus to minimize direct particles hitting the photocathode of the PMT. Since the PMTs are located in the fringe field of the torus magnet, they are enclosed in magnetic shielding. The PMTs are sensitive to as little as one photoelectron. The efficiency of the CC drops off near its geometrical boundaries. Therefore, the final analysis makes fiducial cuts on the regions of high CC efficiency for electrons (see Sec. 5.4.1).

### 3.2.4 Scintillation Counters

An array of scintillators and PMTs make up the CLAS Time-of-Flight (TOF) system [39]. This module is mainly responsible for particle identification using tracking information from the drift chambers in conjunction with high-resolution time of flight measurements. The system is capable of separation of pions and kaons up to momentum of 2 GeV/c. Each scintillation counter (SC) covers  $1.5^\circ$  in polar scattering angle. The forward counters are 15 cm wide and the large angle counters are 22 cm wide. The counter length varies from 32 to 445 cm. A time resolution of  $\sigma = 120$  ps at small angles and 250 ps at angles  $> 90^\circ$  is possible after calibration. The TOF counters operate in a high rate environment produced by luminosities above  $10^{34}\text{cm}^{-2}\text{s}^{-1}$ . The average rate per scintillator is approx 100 kHz. Light guides, PMTs, voltage dividers and cables are located further from the beamline than the torus coils and the Region 3 drift chambers and

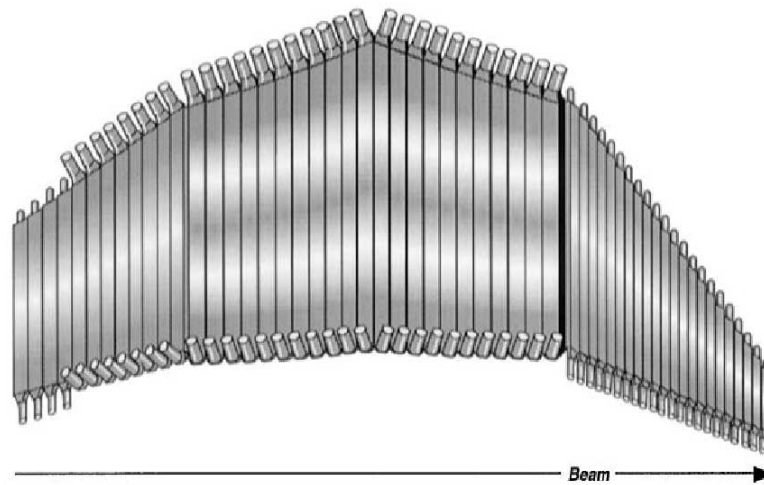


Figure 3.14: One sector of time-of-flight scintillation counters. The vertical rectangles are the scintillator bars and the tubes at the end represent the readout PMTs.

lie in the shadow of the coils to shield them from scattered particles. The active area consists of 5.08 cm thick Bicron BC-408 scintillators. The thickness was chosen to give a large enough signal to separate minimum-ionizing particles from background. The fiducial volume covers  $206 \text{ m}^2$  and the PMTs are magnetically shielded.

A good resolution in the TOF timing was obtained for our run period. The width of the distribution of the difference between the expected time of arrival of the trigger electron to the SC and the actual time recorded by the SC was reduced to an acceptable value. To calculate the expected arrival time, the electron is tracked to the target and associated with its proper beam bunch via a time stamp in the data stream derived from the RF signal. Fig. 3.15 shows that the achieved TOF resolution for this experiment was 150 ps, which is similar to the value that other run periods have obtained and is generally considered to be acceptable. Fig. 3.16 shows that the sample mean value distribution as a function of run number for the time offset between the RF signal time and the measured time is less than 20 ps over the range, again within accepted limits.

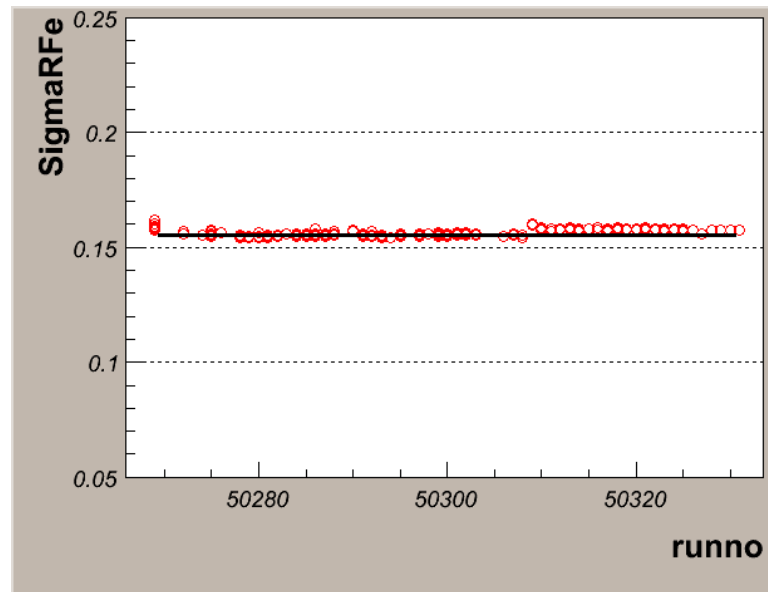


Figure 3.15: The TOF resolution in nanoseconds for a sample of the run period. Each red circle represents one subrun.

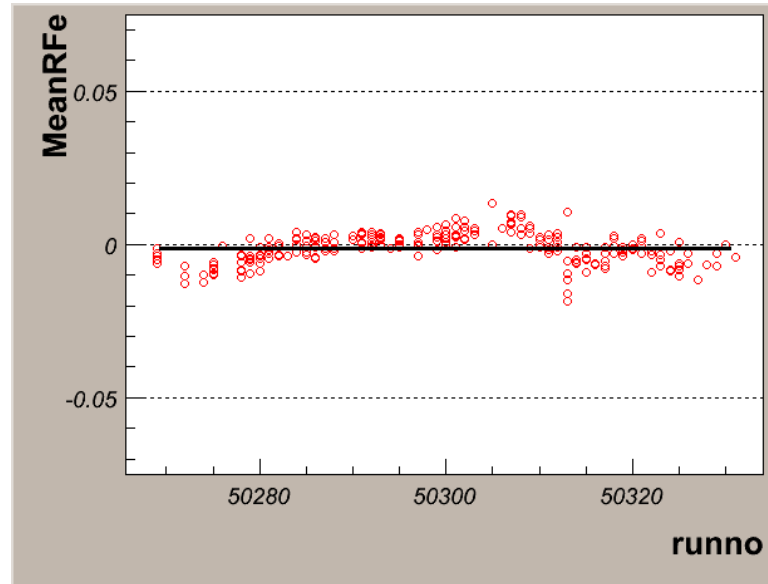


Figure 3.16: The mean time offset between the expected and measured times for electrons in nanoseconds for a sample of the run period. Each red circle represents one subrun.

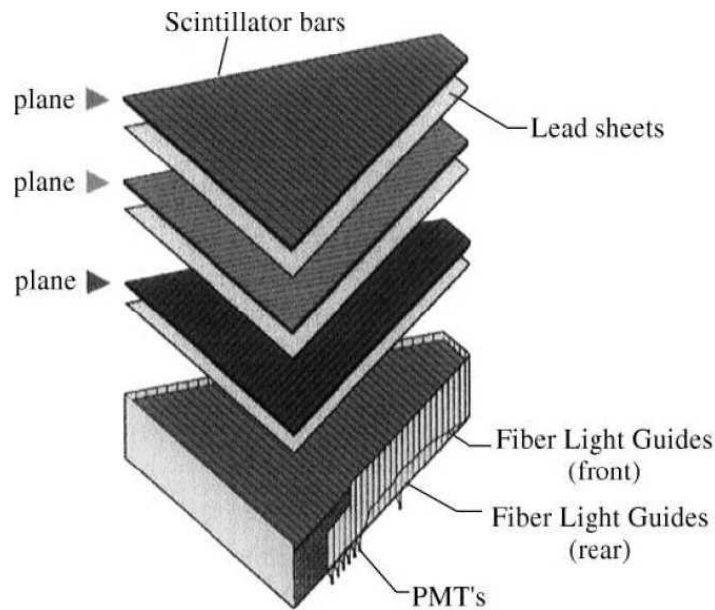


Figure 3.17: Exploded view of one sector of the electromagnetic calorimeter. The strip orientation of the U, V, and W planes can be clearly viewed.

### 3.2.5 Electromagnetic Calorimeter

The electromagnetic calorimeter's (EC) main function in BoNuS was to provide an electron for momenta above 0.5 GeV/c and  $\theta$  range from  $10^\circ$  to  $45^\circ$  [40]. The EC hardware consists of 39 alternating layers of scintillator strips and lead sheets with a total thickness of 39 cm and 8.4 cm, respectively (Fig. 3.17). Each sector is in the shape of an equilateral triangle and they are oriented in a flower pattern around the beam line. Each scintillator layer has 36 individual strips parallel to one side of the triangle. The strip orientation is rotated  $120^\circ$  from layer to layer (labeled U, V and W) to provide stereo information on the location of the shower and each layer is further divided into five inner and eight outer sections where the inner sections are the closest to the beamline. A typical reconstructed event in the EC can be seen in Fig. 3.18. The target EC energy resolution is  $\sigma/E \leq 0.1/\sqrt{E(\text{GeV})}$  with a position resolution of  $\delta r \approx 2$  cm at 1 GeV. Separation of pions from electrons is correct 99% of the time, with proper cuts on energy deposit on the inner and outer portions of the detectors. The entire background of pions could be removed from the electron sample, but too many good electrons would be lost. The EC timing calibration is performed after a reliable calibration exists for the TOF counters. The final result of this calibration is shown in Fig. 3.19.

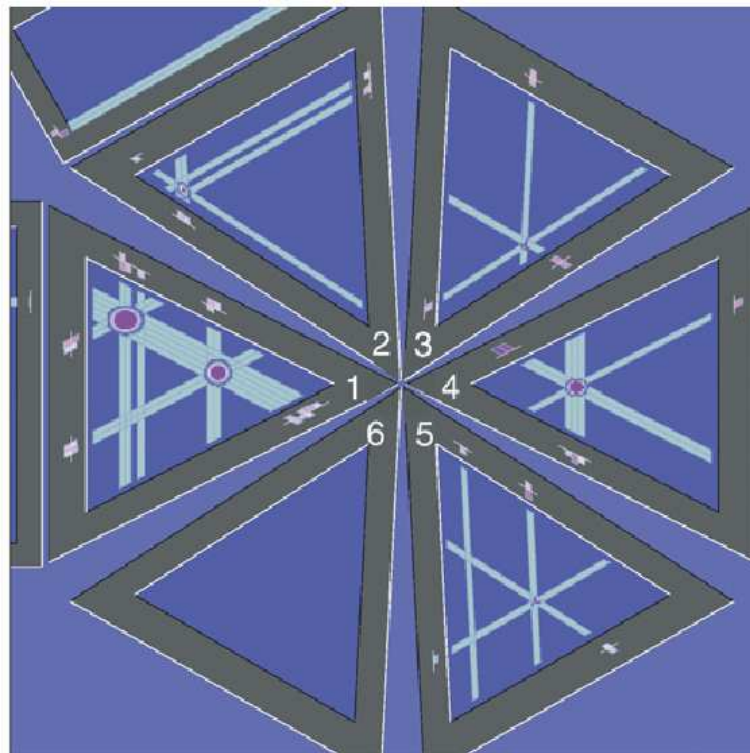


Figure 3.18: A typical image showing the position determination of energy deposited in the electromagnetic calorimeter. Each scintillator by itself does not locate the electron along its length, but the U, V, and W planes together triangulate the electron's position.

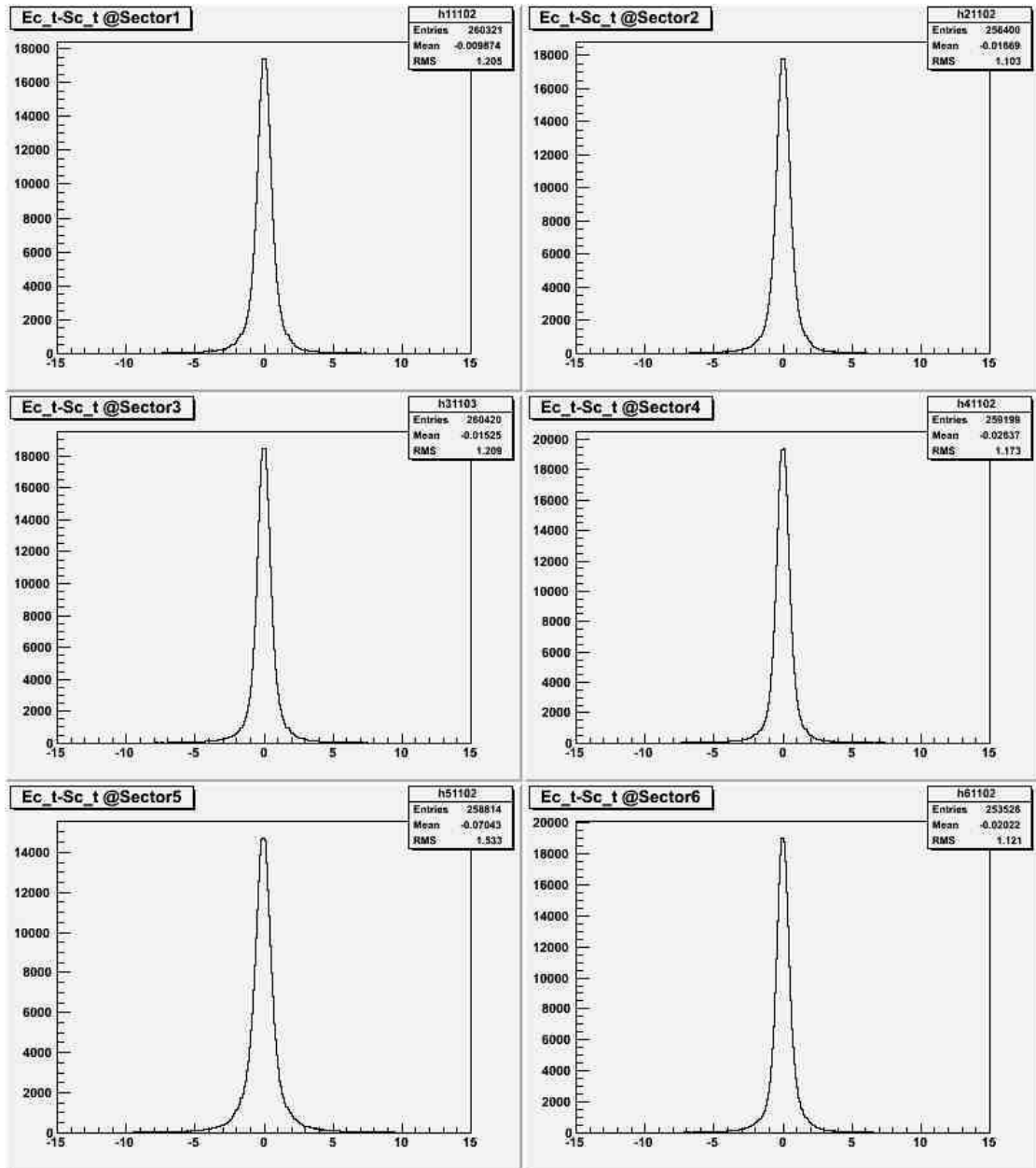


Figure 3.19: The final timing calibration for the EC. Each sector's time measurement is compared with the already calibrated TOF value. The horizontal axis is in units of nanoseconds.

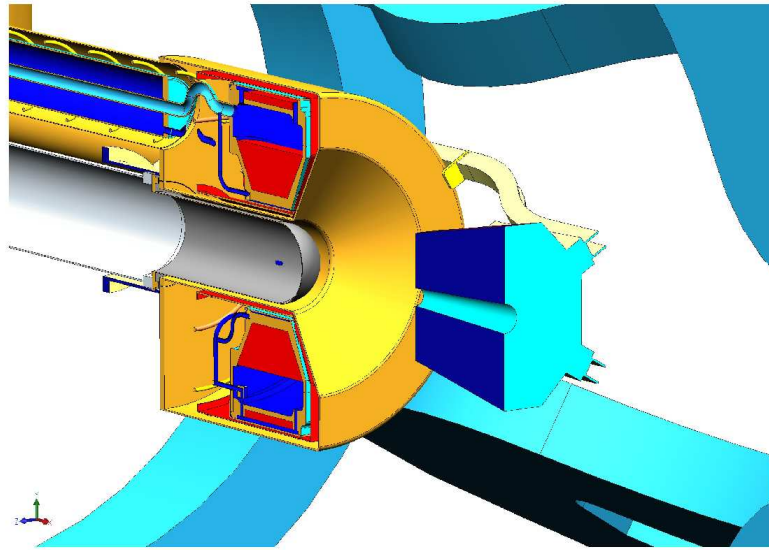


Figure 3.20: A schematic of the DVCS solenoid. The stainless steel shell is in yellow, the coils are in red, and the blue inside the shell is the liquid helium. The inner calorimeter is shown downstream of the magnet (not used for this experiment) and the torus magnet coils are shown in blue in the background.

### 3.3 Solenoid Magnet

A superconducting solenoid magnet with a stainless steel shell was constructed for an experiment in the CLAS run period just prior to BoNuS, known as DVCS. This magnet was able to provide the BoNuS detector adequate shielding from Møller electrons (when electrons from the beam knock out orbital electrons in the target gas) and provide enough curvature in the  $x - y$  plane to enable momentum determination of low energy protons. According to our simulations, all Møller electrons below 20 MeV/c will curl up before reaching the RTPC's tracking area (Fig. 3.21) and will remain within  $5^\circ$  of the z-axis (Fig 3.22).

The total field strength is 4.7 T at the center point when running at a nominal design current of 534 A. The currents running through the torus and the solenoid are in series with the power supply unit for safety reasons. The solenoid's fringe field does not cause a great perturbation in the CLAS torus field. A liquid helium cooling bath at a temperature of 4.3 K surrounds the magnet's coils, where the main coil has a field of 6.9 T field at the wires. Fig. 3.20 shows the cryogenic flow around the coils. See Table 3.1 for the critical dimensions of the CLAS-DVCS magnet.

We ran the magnet at 84% of maximum current for the bulk of our data taking, resulting

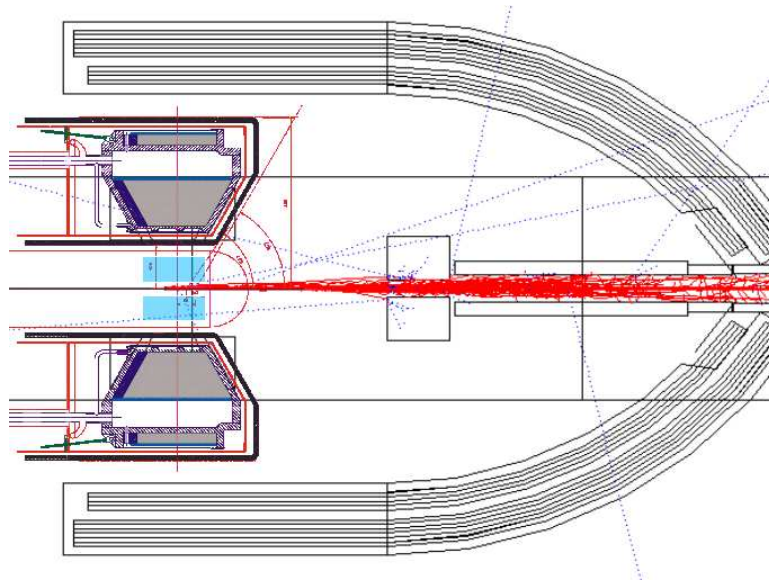


Figure 3.21: Simulation showing the  $\theta$  extent of Møller electrons. The RTPC sensitive region is shown as two light blue rectangles below and above the red Møller tracks. The Møller electrons are shown as red tracks and are contained within a volume downstream of the magnet. The R1 drift chambers are also visible to show that they are not in a region with a high flux of Møllers.

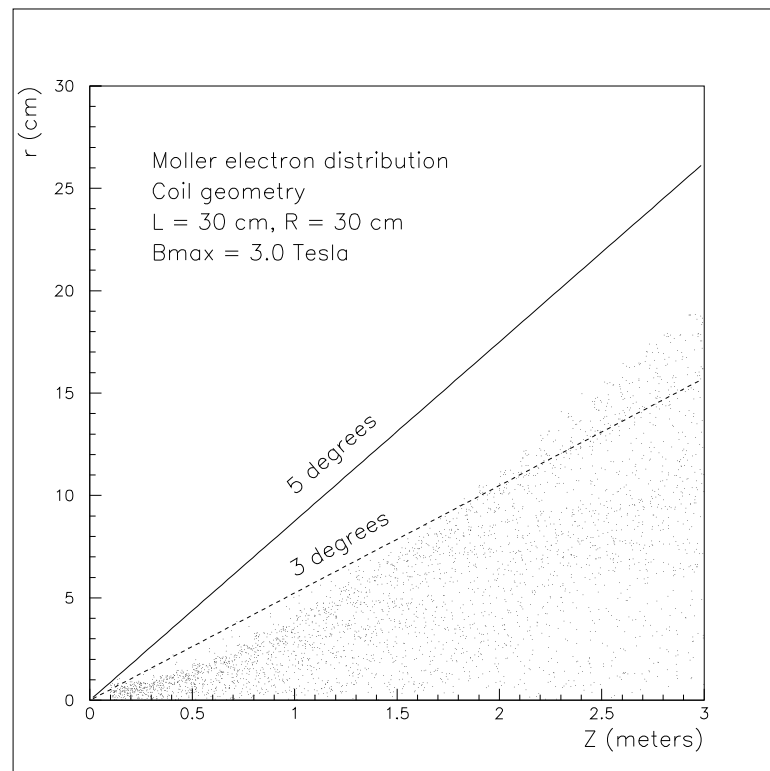


Figure 3.22: Møller electron distribution in the  $r$  vs.  $z$  plane. Our experiment ran with a higher solenoid field so that Møller electrons were contained within  $\theta$  of  $3^\circ$ .

|                        |           |
|------------------------|-----------|
| Aperture diameter      | 270 mm    |
| External diameter      | 910 mm    |
| Magnet length          | 910 mm    |
| Total length           | 2776 mm   |
| Total height           | 1661 mm   |
| Total width            | 1143 mm   |
| Cold mass at 4 K       | 700 kg    |
| Cold mass at 50 K      | 200 kg    |
| Total mass             | 1500 kg   |
| Liquid helium capacity | 65 litres |

Table 3.1: Critical dimensions of the DVCS solenoid.

in a field strength of 3.96 T at the center of the RTPC. In the RTPC's sensitive volume, the axial component of the field,  $B_z$ , ranges from 3.3 - 4.1 T, with the maximum value occurring at the largest radius in the  $x - y$  plane perpendicular to the central axis of the magnet. The radial component,  $B_r$ , ranges from 0 to 0.4 T and also increasing with radial distance away from the central axis. This non-negligible radial component of the field's effect on the overall field direction can be seen in Fig. 5.2.

According to a recent measurement of the field map, the longitudinal component  $B_z$  is in excellent agreement with what was expected from calculations. The relative error between the measured and the theoretical fields is about 0.5% [41]. Fig 3.23 shows how the field falls off with distance away from the center of the magnet.

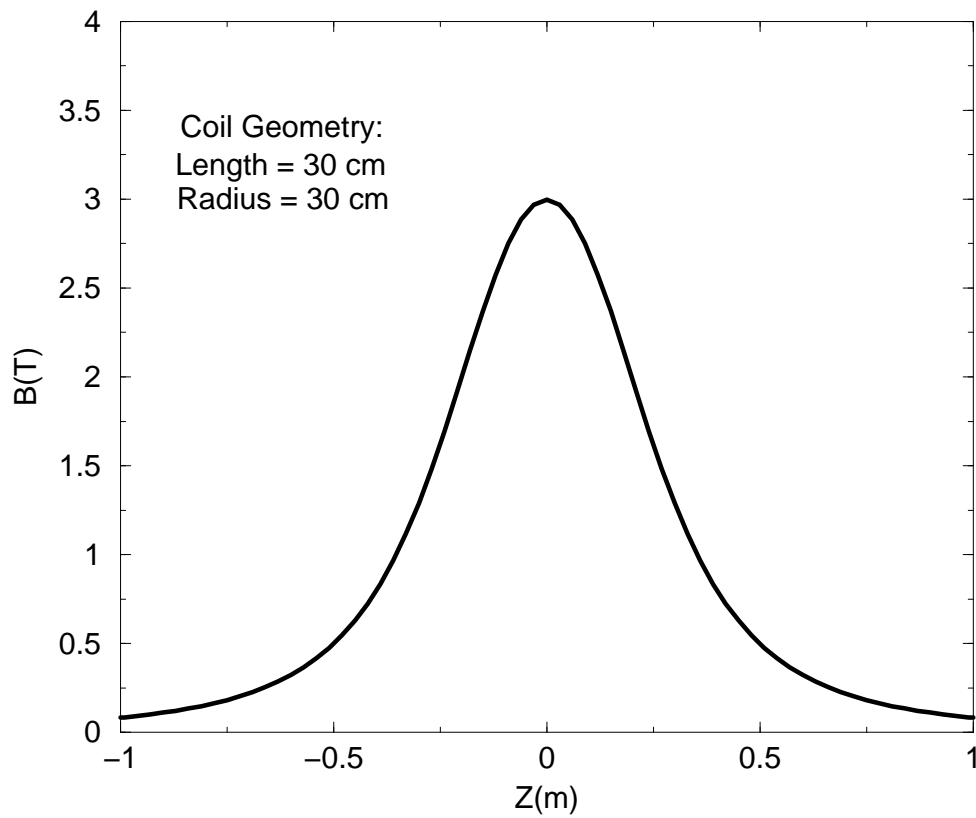


Figure 3.23: Solenoid field strength vs  $z$ . The magnitude scales linearly with current, but the shape of the distribution remains the same for all current settings.

# Chapter 4

## NEW EXPERIMENTAL APPARATUS

There were two new pieces of equipment which were custom-built for the BoNuS experiment, a Gas Electron Multiplier (GEM) based Radial Time Projection Chamber (RTPC) and a spiral wound target straw. The RTPC was conceived by detector expert Howard Fenker for the detection of low-momentum protons which are ejected from the target at backward angles with respect to the beamline. The Kapton<sup>®</sup>-walled target was designed, tested, and fabricated by Hall B's target expert, Steve Christo. The target held gaseous elements at various pressures, up to 7.5 atmospheres. This chapter will describe the design and construction of these two crucial, novel components.

### 4.1 Radial Time Projection Chamber

#### 4.1.1 Design Motivations and Constraints

The dominant factors that influenced the design of the RTPC were the solenoid magnet's size and field map and the nature of the low momentum protons. The entire detector, fully instrumented, needed to fit within the bore of the solenoid and also be made thin enough so that "Very Important Protons" (VIPs) would not come to a stop before reaching the sensitive volume.

A Time Projection Chamber (TPC) was chosen for the BoNuS experiment because of its natural advantages over other tracking devices. The first TPCs were invented in the late 1970s at Lawrence Berkeley Laboratory [43]. They used anode wires with endcap readout strips for the signal amplification and collection (Fig. 4.1). TPCs are routinely used in collider experiments to measure 3D particle tracks in high-rate environments. A TPC, like a bubble chamber, can simultaneously make measurements of the track and specific energy loss,  $dE/dx$ , of many particles. The TPC has been referred to as an *electronic bubble chamber* due to its fast, all digital readout [42].

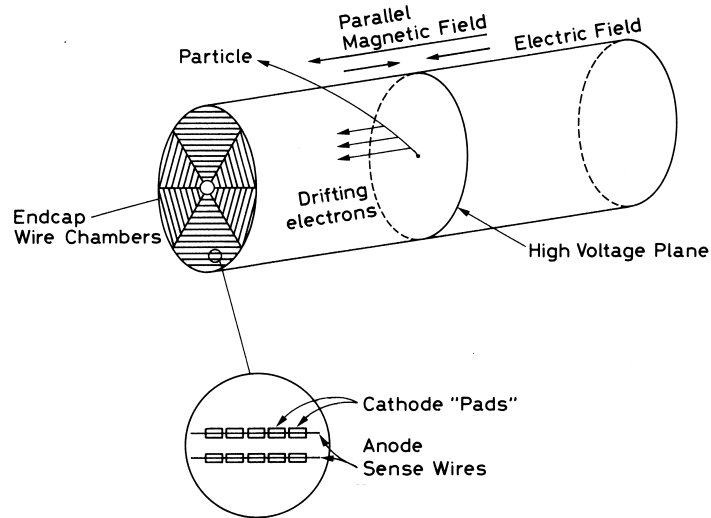


Figure 4.1: Schematic diagram of a Time Projection Chamber from Ref. [42].

TPCs measure the path of the track at many points, which leads to excellent position and momentum resolution (Fig. 4.2). Furthermore the timing resolution enables precise measurement of the energy deposited in each volume element (voxel) so that particle identification can be achieved. Conventional cylindrical TPC's are constructed so that the electric field, the magnetic field, and the central axis are parallel. This simple configuration causes ionization electrons to travel in straight lines at a constant speed. The cathode lies at one end of the cylinder in a plane perpendicular to the central axis with amplification and readout occurring on the opposite end.

There are two reasons why the conventional TPC was not ideal for the BoNuS experiment. (1) The forward scattered electrons would encounter a large amount of material on the downstream endcap of the TPC. This excess energy loss in dead material before the electron tracking system (CLAS) is not preferable. (2) The magnetic field produced by the solenoid has a non-negligible radial component which becomes larger at either end of the magnet. A significant number of electrons would never be collected because they would be steered into the walls of an axial-drift TPC in this field. Instead, a radial-drift TPC was chosen in which electrons travel along paths of constant  $z$  but varying  $r$  and  $\phi$ . The RTPC consists of a series of nested coaxial cylinders, each layer serving a different purpose. Details about the final detector design and construction follows in Sec. 4.1.4.

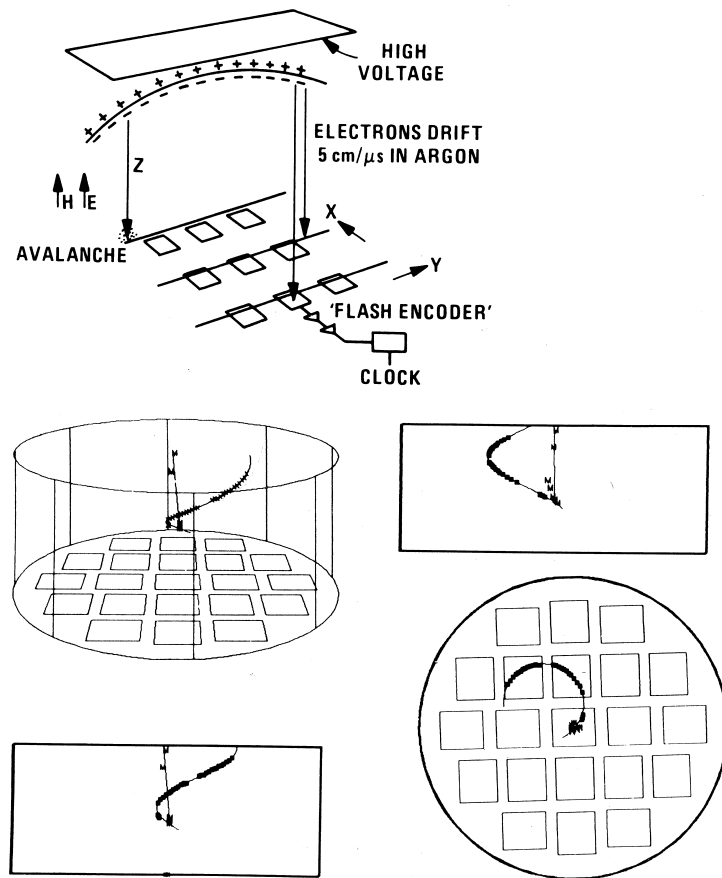


Figure 4.2: Top figure: Sampling the space points on a particle's trajectory with a TPC. Bottom four figures: Various views of a muon's decay into a positron. The signal is registered on readout pads represented by boxes on the bottom of the cylindrical volume. The muon is marked by a  $M$  [42].

Multi-Wire Proportional Chambers (MWPC) located at the endcaps of typical TPCs need relatively massive components to keep wire tension. These large components were not practical for this experiment given the diameter of the solenoid and the need to minimize the energy loss of particles in the detector. A further complication with the MWPC implementation is the production of a significant number of positive ions from avalanches drifting back towards the cathode. Over time, these ions can accumulate to the point where a distortion of the drift field occurs. Typically, this ion backdrift is prevented by the placement of a grid at ground potential, just before the anode wires, to capture the ions before they can wreak havoc in the sensitive volume.

#### 4.1.2 Gas Electron Multipliers

Micro-pattern gas gain elements such as MicroMegas and Gas Electron Multipliers (GEMs) [44] were invented in the mid-1990s as another option for the avalanche stage of a TPC. The GEM is a composite sheet of material consisting of a thin layer of insulator (typically Kapton<sup>®</sup> at 50  $\mu\text{m}$  thick) sandwiched between two thin ( $\sim 5 \mu\text{m}$ ) layers of metal (typically copper) as can be seen in the electron microscope picture in Fig. 4.3. The mesh is chemically etched in the foil which contains 50  $\mu\text{m}$  diameter holes with a pitch of some 100  $\mu\text{m}$  and a double-conical cross section. Other cross sections are possible (cylindrical, single-conical) but double-conical provides the best insulation between electrodes because of the longer distance that an electrical discharge would have to travel. Each hole serves as an amplification element for the drift electrons with a gas-gain per foil on the order of 100. The separation of the multiplication and readout regions further reduces the occurrence of discharges.

GEMs in particular provide an elegant solution to our problem for a number of reasons. The thin foil can easily be curved into a half cylinder, however it was a challenge to keep them wrinkle free during construction (see Sec. 4.1.4 for more details). GEMs dictate no preferred readout shape or orientation because they have a uniform surface over which amplification can occur. Furthermore, positive ion backdrift, which can be 20-30% in a typical MWPC, is a few percent or less in a GEM-based detector [45]. The thin GEM foil mesh provides minimal energy loss for scattered particles. A typical x-ray spectrum in a Single-GEM detector can be seen in Fig. 4.4. Our GEM detector marked the first attempt to use GEMs at Jefferson Lab and the first

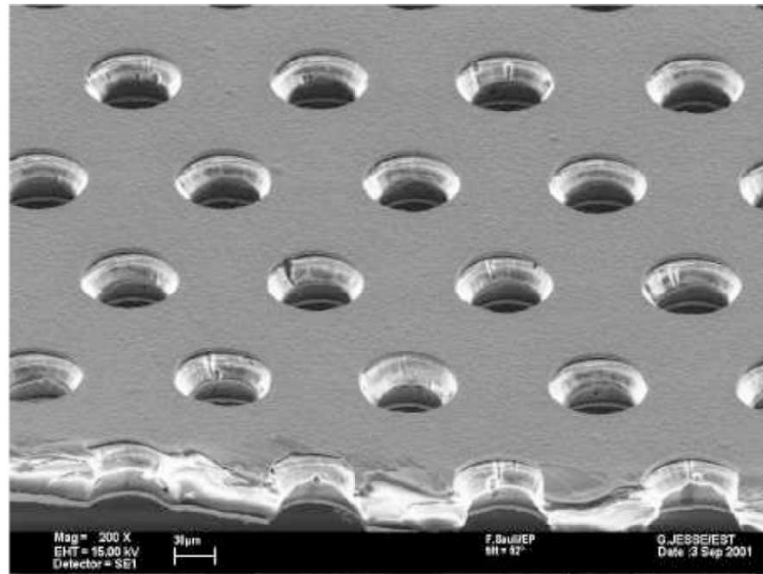


Figure 4.3: A typical GEM foil imaged with an electron microscope. The picture is roughly 400  $\mu$ m across.

attempt anywhere to use curved GEMs, although the CERN group which invented GEMs has long been aware of the ability to use them in a non-planar geometry [46, 47]. The Triple-GEM (TGEM) configuration (see Fig. 4.5 for a typical chamber layout) consists of three cascaded GEM foils and can be operated at a much lower voltage than a double GEM for a given gain (Fig. 4.6). This further reduces the occurrence of discharges.

Custom GEMs were produced for our experiment by the Tech-Etch corporation (Tech-Etch, Inc., 45 Aldrin Road, Plymouth, MA, USA.), and have an active area covering 20 cm  $\times$  17 cm. These GEMs were produced to the industry standard for the double-conical hole model. The double-conical cross section is produced by under-etching the polymer to produce the hour-glass shape in Fig. 4.7. The inner copper layer of each GEM is divided into four electrically isolated 5 cm  $\times$  17 cm regions to reduce the energy stored in any single high-voltage element (Fig. 4.8). The procedure that was followed to ensure rudimentary quality control for the GEMs included the following steps: First each GEM was rinsed with ethanol and blown dry (from one side only to prevent particulates from being blown back into the holes) with compressed nitrogen to remove the significant dust and contaminants that had accumulated on the surfaces during shipping and handling. Secondly, a custom box with high voltage clip leads on temporary frames and constant nitrogen flow was built to dry the foils overnight. Finally, high voltage was

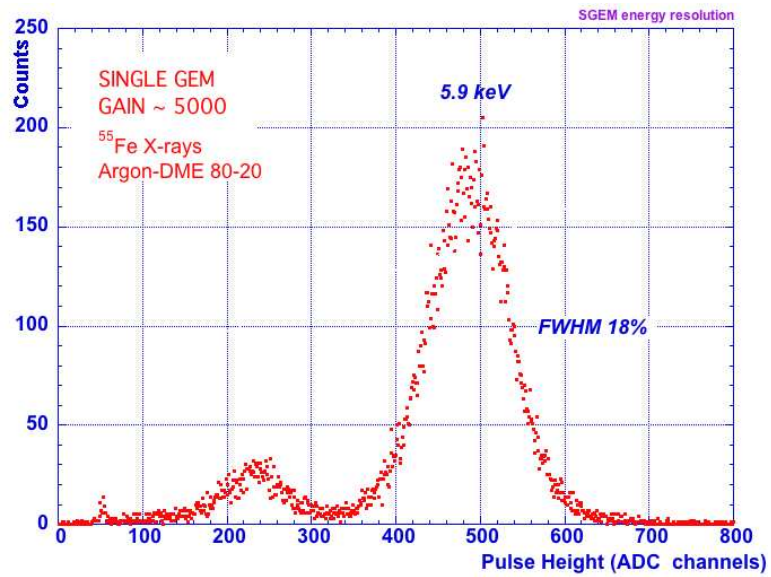


Figure 4.4: The typical energy resolution of a GEM-based TPC. The small bump at 225 is the Argon escape peak [48].

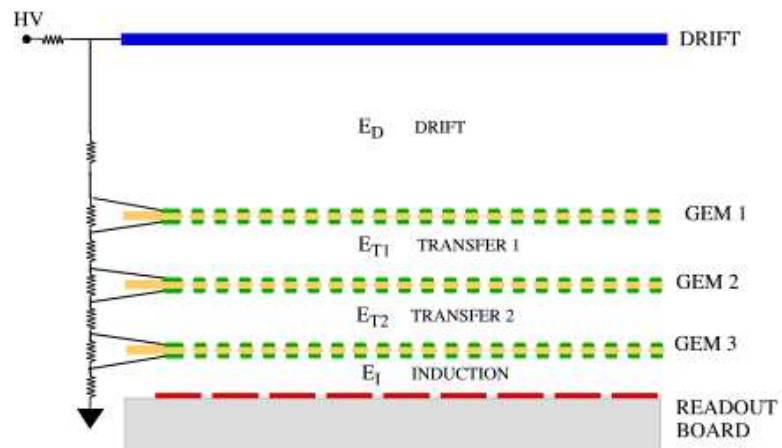


Figure 4.5: A schematic representation of each layer in a standard triple GEM detector.

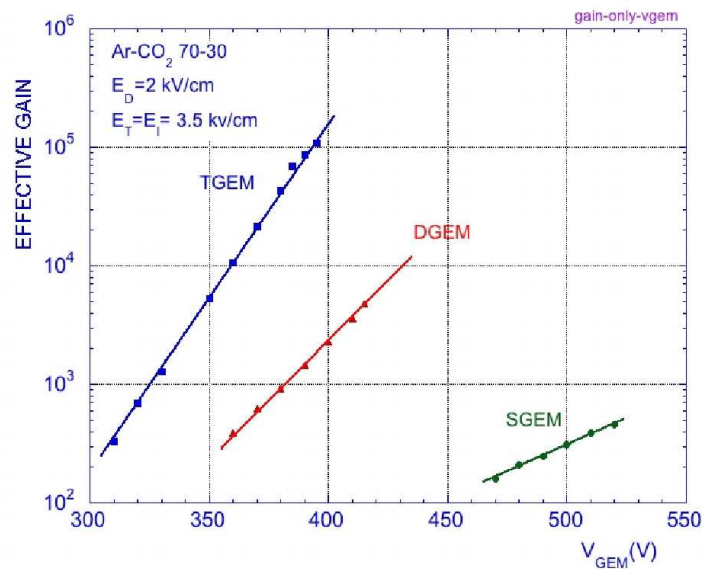


Figure 4.6: The effective gain vs the voltage across the GEM foils for three different TPCs. These are data taken by CERN's Gas Detector Development Group [48].

applied to each GEM, starting as high as possible depending on the side-to-side resistance. Typically the resistance began at a few  $M\Omega$  then gradually increased as the liquid between the holes evaporated or the tiny wisps of copper still connecting the sides were “burned” away. This “burning” process normally took a few hours and was declared finished when the leakage current was less than  $1 \mu A$  at 300 volts. About 90% of the GEMs passed this quality test.

### 4.1.3 Prototypes

The preparation for the BoNuS physics run included the construction of two main prototype detectors. The first prototype, a small flat GEM device, was built in order to give our group experience working with GEMs. Double-conical and cylindrical GEMs were tested while varying the number GEM layers between 1 and 3. The second prototype was the first ever TPC to use GEMs in any geometry other than planar. The final operating conditions for the physics run were determined using this prototype.

The flat prototype (Fig. 4.9) used for most of our early testing consisted of a  $5 \mu m$  thick aluminized-mylar entrance window, a  $5 \mu m$  thick aluminized-mylar cathode, a 19.1 mm thick tracking region, and three double-conical holed GEMs of dimension  $10 \text{ cm} \times 10 \text{ cm}$  from the

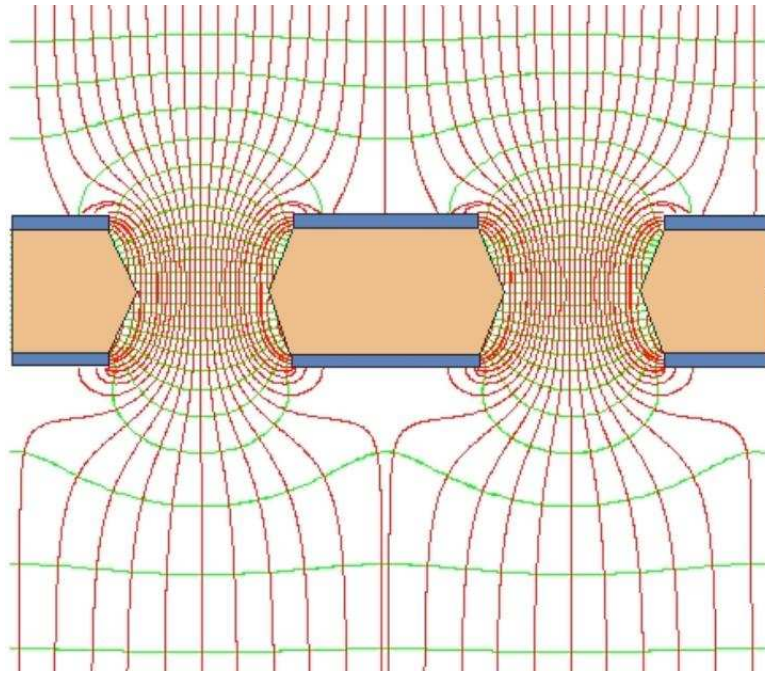


Figure 4.7: An electric field map surrounding a GEM foil as generated by GARFIELD [49]. The electric field lines are in red and the equipotential lines are in green.

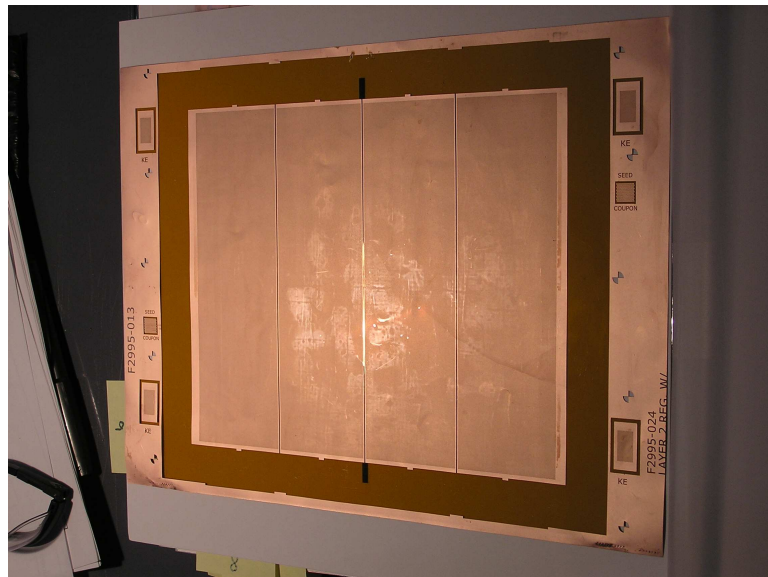


Figure 4.8: A custom 20 cm  $\times$  17 cm GEM foil, manufactured for this experiment by Tech-Etch. Fingerprints are clearly visible on the surface.

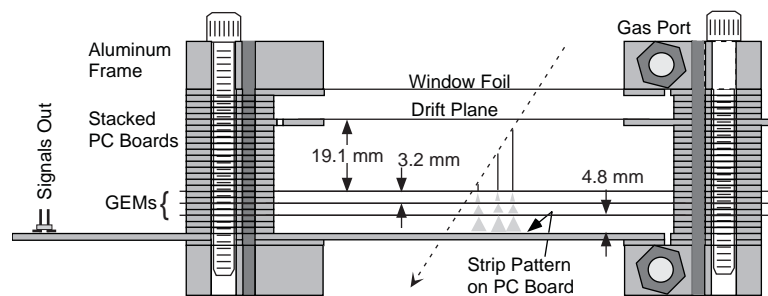


Figure 4.9: A cross sectional view of the flat prototype Triple GEM TPC

3M corporation. Charge collection was provided by a PC board with 2.5 mm wide strips. In our early studies, a typical, non-flammable drift gas (a mixture of 80% Argon and 20%  $\text{CO}_2$ ) was chosen so that experience could be gained using a TPC without the extra complications of using the flammable dimethylether (DME). The construction and usage of this device also gave us experience in handling GEMs for the first time. This prototype was used to successfully track low momentum protons at the Triangle Universities Nuclear Laboratory (TUNL, Durham, NC) research facility. TUNL's tandem accelerator shot  $\sim 137$  MeV/c protons at a gold-plated tungsten wire. Protons scattered at  $90^\circ$  were focused by a collimator onto the entrance window of the detector and their resulting signals were clearly distinguishable from those of minimum ionizing particles.

One important lesson that was learned in the construction of this prototype was that a cathode sheet made from  $50 \mu\text{m}$  of Kapton<sup>®</sup> will not hold 5 kV potential difference between two layers of copper on either side. All attempts to do this failed because a conductive path emerged along the edge of the copper cladding. This breakdown showed that the edge effects of the electric field were too severe. For this prototype, and for all the subsequent detectors outlined in this document, the cathode and the ground plane were separated by a gap flushed with drift gas. The cathodes and ground planes in all of our detectors are  $6.4 \mu\text{m}$  thick sheets of mylar coated with 35 nm of aluminum (a.k.a. aluminized mylar).

In order to test the performance of curved GEMs, a curved prototype covering  $\sim 1/8$  of the final  $\phi$  coverage but with equal curvature to the final detector was fabricated (Fig. 4.10). The radial length of the prototype tracking region was only 2 cm because the cathode was placed at a radius of 40 mm instead of the final design radius of 30 mm. The GEMs and the padboard readout layer were placed at identical radii to the final detector at  $r = 60, 63, 66,$  and  $69$  mm

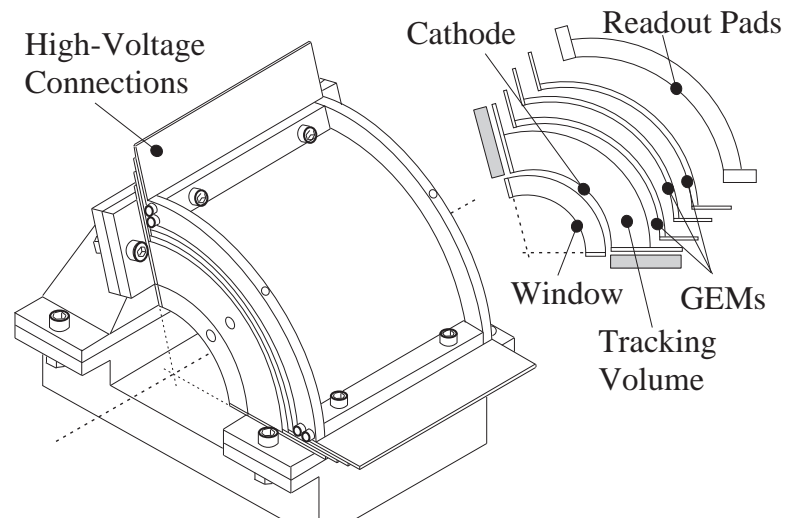


Figure 4.10: Exploded diagram of the 105 degree prototype

for GEM1, GEM2, GEM3 and the padboard, respectively. The span of  $105^\circ$  in azimuthal angle was determined by the available GEM dimension of  $10\text{ cm} \times 10\text{ cm}$ . The inner window (ground plane) was placed at 25.4 mm. The support frames were made of Ultem<sup>®</sup> instead of PC board. Like its flat predecessor, this prototype was tested using heavily ionizing protons ejected from the TUNL proton beam. This device marked the first time in history that curved GEMs were used for tracking. The signals were used to fine-tune the tracking software that would later be put into the production tracking package. A comparison between the pulse-height spectra from a  $^{55}\text{Fe}$  X-ray source using both the curved-GEM RTPC and the planar-GEM test are provided for comparison in Fig. 4.11. These data were taken using different GEM and chamber designs, and slightly different electronics. It is clear from the figure that GEMs retain their basic functionality after being formed into semi-cylinders.

Extensive tests were made to investigate the curved GEMs gas-gain dependence on high-voltage history (“charge-up”) and flux of ionizing radiation (“rate-dependence”). These two phenomena have been documented by other researchers testing flat GEMs and our curved GEMs also exhibited these behaviors. Ref [50] includes the details of the efforts to quantify the gain stability and other lessons learned from the prototype studies. In the end, three practices were adopted to make sure that these effects would not degrade the quality of our data. (1) The detector high voltage was turned on at least 30 minutes prior to data taking to minimize

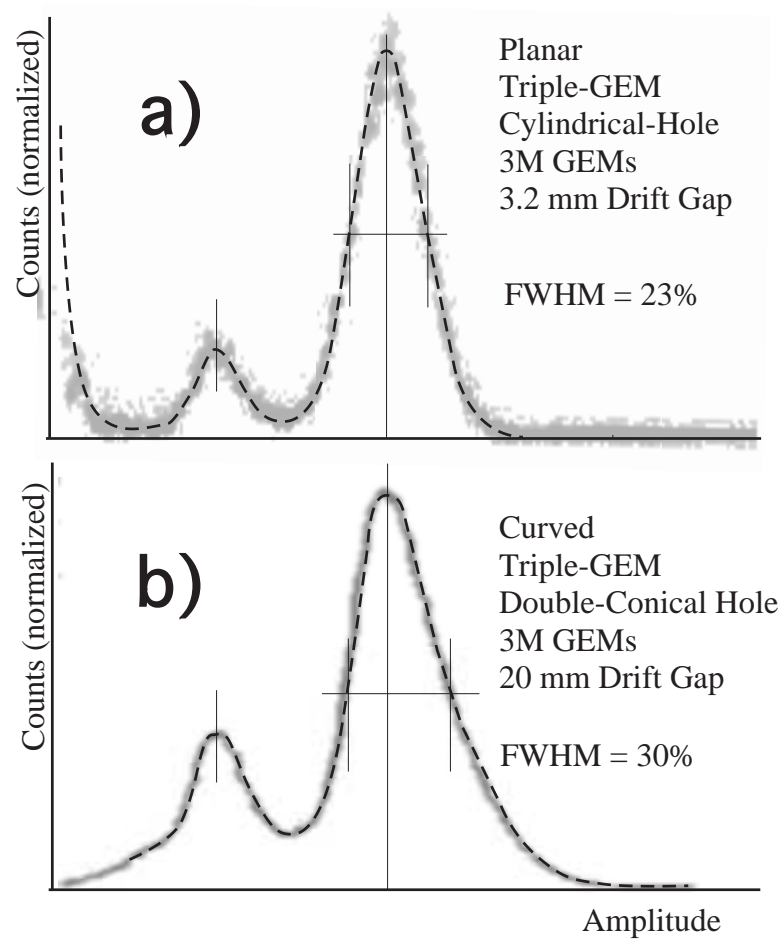


Figure 4.11: (a) Flat GEM chamber x-ray energy distribution. (b) Curved GEM chamber x-ray energy distribution.

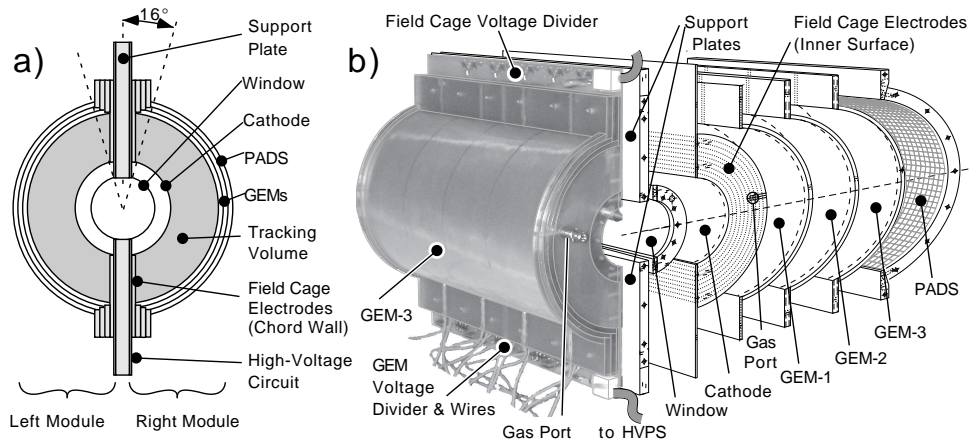


Figure 4.12: (a) A cross section of the RTPC taken on a plane perpendicular to the beam axis. (b) A photograph of the RTPC's left section without the padboard layer and an exploded diagram of the right section.

the “charge-up” effect. (2) Significant changes in beam intensity were noted and the data were monitored to ensure the RTPC's operational stability. (3) The data were monitored for needed adjustments of the gain calibration resulting from long-term drifts or environmental changes. Details on the handling of these effects can be found in Sec. 5.2.

#### 4.1.4 Production Chamber

Our group's experience with the fabrication and construction of the prototype detector modules laid the foundation for the successful realization of the production RTPC. As before, the final mechanical components had to be small and lightweight to increase the acceptance for spectator particles. In addition, they had to minimize the amount of background, yet be rigid enough to support the GEMs and the associated electronics. Fig. 4.12 contains a detailed picture of the final detector design. The device is actually two identical modules with rotational symmetry about  $180^\circ$ , spanning 200 mm in  $z$ . Each half has, in order of increasing radial distance from the target:

1. An aluminized mylar ground window, 20 mm away from the central axis, attached to the inside of a frame with a 10 mm radial thickness.
2. An aluminized mylar cathode attached at a 30 mm radius to the inside of a frame that defines the tracking region. The endcap walls of these frames are lined with the field

cage. These printed circuit board (PCB) frames extend beyond the next layers.

3. Three GEM sheets, each attached to the inside of 3 mm thick Ultem<sup>®</sup> frames.
4. A readout board with charge collection pads on the inside surface and 100 preamps with 16 channels each on the outside.
5. A voltage divider circuit for the field cage on the top (in Fig. 4.12b) and for the GEMs on the bottom (in Fig. 4.12b) support plates. These positions are inverted for the right chamber half.

The foundation of each detector half is made up of two vertical support planes running along the top and bottom. Each layer is screwed down on each end to these plates and the plates are finally bolted together to form the complete detector. Only the tension from the screws holds the layers together, therefore room temperature vulcanizable (RTV) silicone coats the cracks between the frames to create the gas-seal. The prefabricated frame pieces were held together on a custom mandrel while the epoxy at each junction cured. The GEMs were also placed on the mandrel while being epoxied to the frames, however they were not stretched during this process and some were deformed during the final assembly. None of the wrinkles introduced were larger than a few millimeters but this issue must be addressed during the next generation of BoNuS-like detectors in order to improve tracking resolution and energy resolution.

The drift electrons produced near the walls of the drift region need to be collected. If the electric field lines ended on the walls, clearly the collection efficiency at the edges would fall to zero. To mimic the field lines of an infinite cylinder, conductive rings were placed in a racetrack on the end arcs and the chord walls at voltages that would be present at the center strip radius in a radial field.

The drift gas chosen for the RTPC is a mixture of high purity helium and DME in a ratio of 80/20. Helium was chosen as the carrier gas because it has a low density and therefore minimizes the energy loss of slow protons. DME, as a quencher, has an acceptable Lorentz angle between  $20^\circ$  and  $30^\circ$  for our configuration. This mixture makes for a slow gas but the benefit of a reduced Lorentz angle offsets the timing drawbacks. Fig. 4.13 shows a sample of how the Lorentz angle and drift velocity components vary with the electric and magnetic fields present in the RTPC. More about the drift properties of our chosen gas-electromagnetic system follows in Sec. 5.1.3.

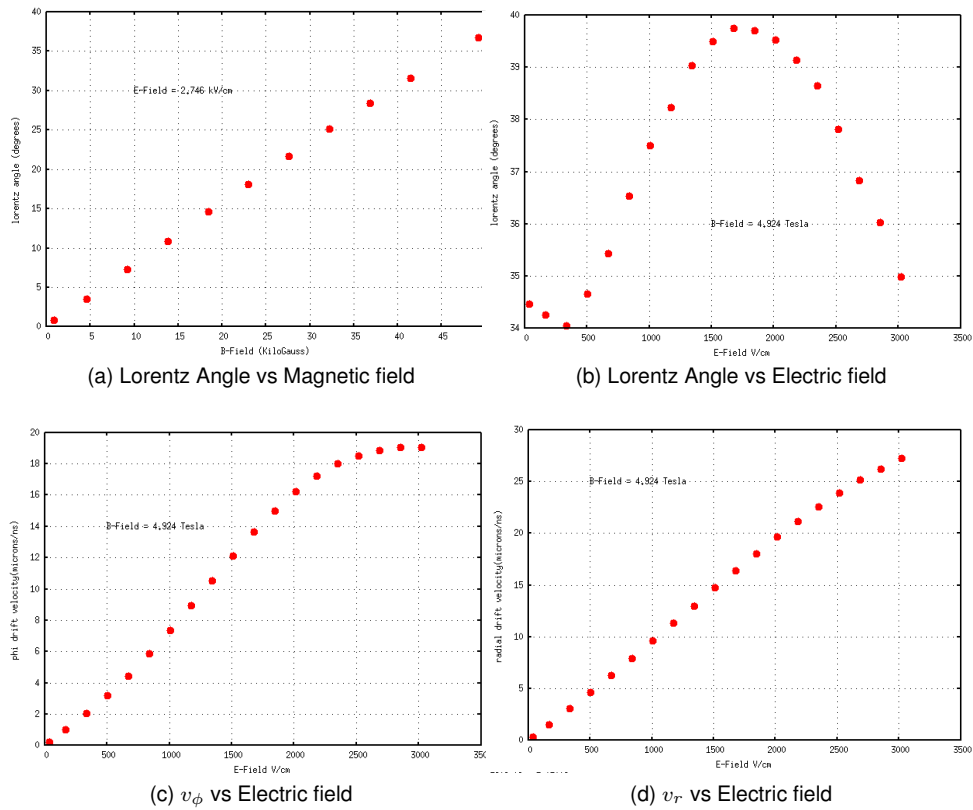


Figure 4.13: Simulated results from the program MAGBOLTZ showing in (a) and (b) the Lorentz angle's dependence on magnetic and electric fields in the RTPC. Shown in (c) and (d) are the radial and azimuthal components of the drift velocity depend on the electric field at a constant magnetic field.

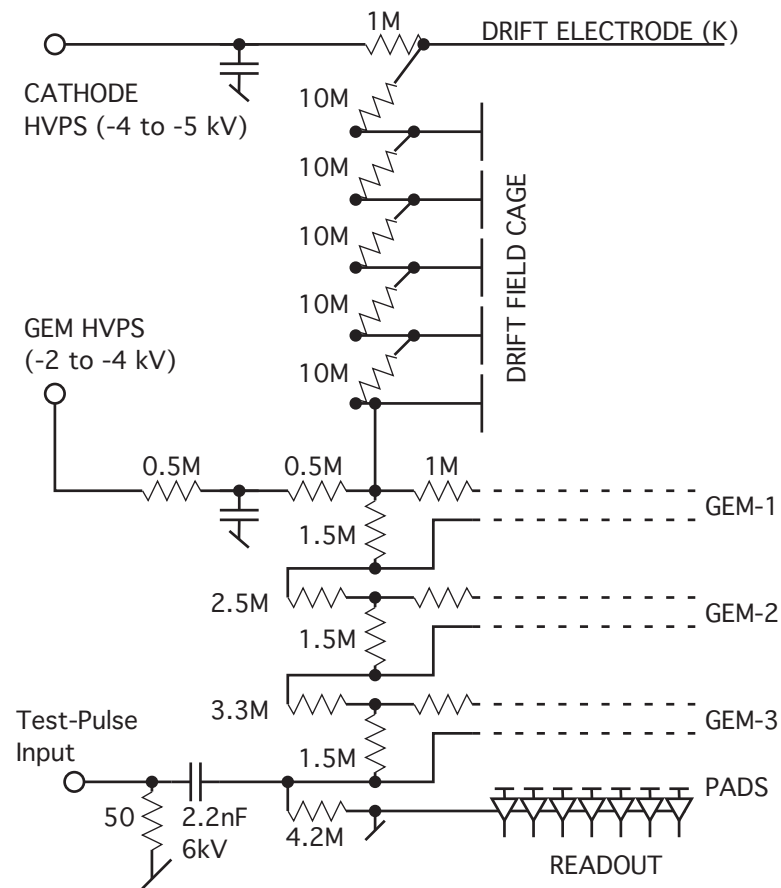


Figure 4.14: The bichannel high voltage circuit used for all the TPC devices. The resistor values shown are just an example of one setup. The real values were within 10% of the example.

#### 4.1.5 High Voltage Divider Circuit

Fig. 4.14 depicts the type of simple divider circuit in use for all of the detector setups described in this chapter. This circuit needed all of its high voltage components to shutdown immediately upon the detection of an overcurrent. A modification was made to the circuit described in Ref [51] so that the electric field in the drift region could be controlled independently from the fields existing in the amplification, transfer, and induction regions. Full detection efficiency for charges deposited in the drift gap is achieved with a relatively low electric field ( $\approx 0.5$  kV/cm) between the cathode and the first GEM foil.

Current-limiting resistors were placed on each segment of the GEM in order to impose an upper limit on the amount of current that can pass through the GEM electrodes to prevent damage to the GEMs during the inevitable short-circuits. Resistors were required whose values

would not drift at the applied voltages and temperatures (sufficient power rating). The Ohmite Slim-Mox<sup>®</sup> series (Ohmite Mfg. Co., Rolling Meadows, IL, USA) resistors rated at 1 W were used in the GEM divider chain. The resistor values shown in Fig. 4.14 are typical, not necessarily the final ones for the production chamber. The real values were within 10% of the example.

Kirchoff's junction and loop rules are needed to calculate the potential difference between the cathode and the first GEM as well as the voltage drop across each GEM and between GEMs. In the following equations,  $V_K$  and  $V_G$  as the cathode and GEM circuit's high voltage power supply settings, respectively,  $R_1$  is the cathode circuit's current limiter,  $R_2$  is the GEM circuit's current limiter, and  $R_K$  and  $R_G$  are the sum of the field cage and GEM resistors, respectively. It can be shown that the exact values for the currents flowing in the cathode ( $I_K$ ) and GEM ( $I_G$ ) circuits are

$$\begin{aligned} I_K &= \frac{V_K - V_G + \frac{V_G R_2}{R_G + R_2}}{R_2 - \frac{R_2^2}{R_G + R_2} + R_K + R_1} \\ I_G &= \frac{I_K R_2 + V_G}{R_G + R_2} \end{aligned} \quad (4.1)$$

Table 4.1 shows the electric fields in each region of the detector. Two different settings on each chamber half were used during the run period - one setting specifically tuned for the detection of spectator protons and one setting with the gain turned up so that minimum ionizing particles would leave a distinguishable track. No more than 1% of the channels exceeded 50% of full-scale in the ALTRO digitizers (i.e. 512 ADC units) in order to avoid non-linearities in the digitization of the charge.

#### 4.1.6 Analog and Readout Electronics

The pad-board at ground potential containing 3200 charge collection elements is the final surface inside the detector volume. The pad layout shown in Fig. 4.15 was etched into a thin PC board with a thickness of 380  $\mu\text{m}$ . Each pad is electrically connected to the opposite side of the board with traces leading to a standard commercial connector pattern. In order to freeze in the proper curvature, the board was mounted onto a tube with the correct curvature and baked in an oven at 120° for a few hours. The brick pattern in Fig. 4.15 ensures that all tracks with  $\theta$

Table 4.1: Electric fields in the RTPC during running of the experiment. The table unit is kV/cm. The values are very close approximations to the actual fields (the small Kirchoff correction is not applied).

| Detector Region | Heavily Ionizing Tracks |       | Minimum Ionizing Tracks |       |
|-----------------|-------------------------|-------|-------------------------|-------|
|                 | Left                    | Right | Left                    | Right |
| <Drift>         | 0.56                    | 0.56  | 0.57                    | 0.57  |
| GEM-1           | 57.6                    | 55.8  | 65.1                    | 63.6  |
| Transfer-1      | 1.63                    | 1.51  | 1.85                    | 1.72  |
| GEM-2           | 57.6                    | 54.7  | 65.1                    | 62.4  |
| Transfer-2      | 2.17                    | 1.99  | 2.45                    | 2.27  |
| GEM-3           | 59.1                    | 54.6  | 66.9                    | 62.3  |
| Induction       | 2.80                    | 2.53  | 3.17                    | 2.88  |

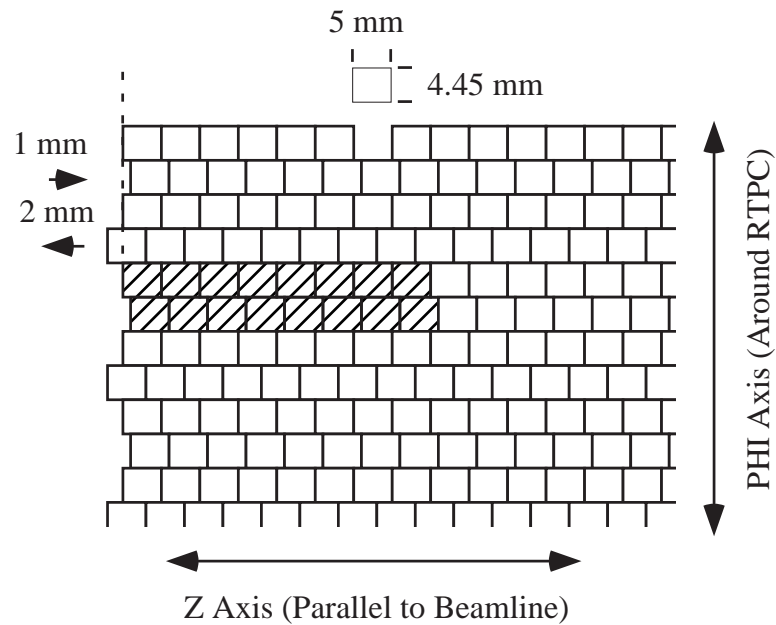


Figure 4.15: Pad layout in the production RTPC. In all, there are 40 rows and 40 columns of pads per detector half. The shaded region of the figure shows a group of pads read out by the same preamp. There are 5 columns and 20 rows of preamps per detector half.

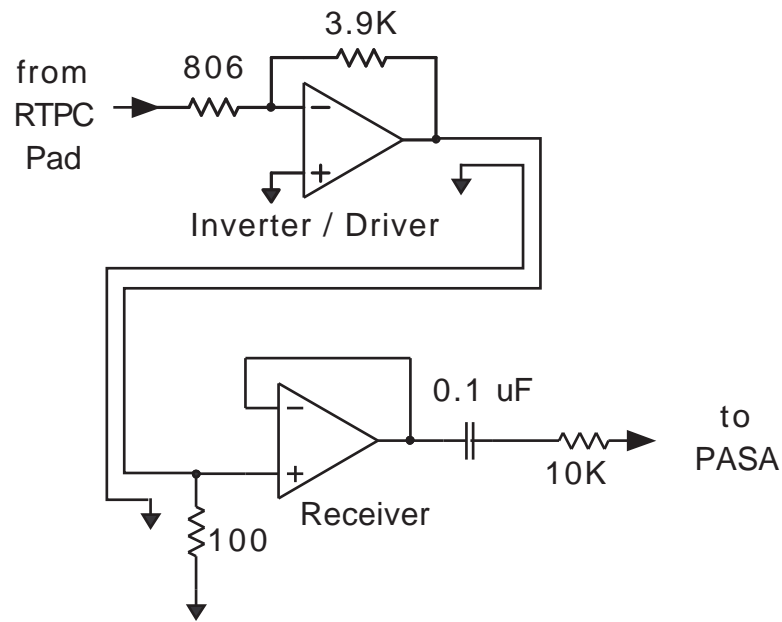


Figure 4.16: A preamp and receiver schematic showing the circuit attached to each channel.

between  $87.5^\circ$  and  $92.5^\circ$  are not assigned  $\theta = 90^\circ$ .

Each connector carries sixteen pad signals and four ground connections and supports a pre-amplifier card. There are 200 cards for the entire RTPC, 100 per side. A schematic for one channel preamplifier is shown in Fig. 4.16 and the fully instrumented detector is shown in Fig. 4.17. The circuit is stable against oscillation and is capable of driving the signals across a 6-m long, 0.635-mm pitch ribbon cable to a low-impedance receiver circuit in an upstream crate (also visible in Fig. 4.17). Because the preamplifier uses low-power components, it is possible to provide its supply voltages as well as sixteen ground and signal connections on each 34-conductor cable. Signals are received at the far end of the ribbons by buffer amplifiers built on 128-channel  $23\text{ cm} \times 33\text{ cm}$  PCBs (the receiver cards) and converted to a format which can be fed into the ALTRO chip.

The ALTRO (ALICE TPC Read Out) chip is a mixed-signal integrated circuit designed to be the main digitizing element for the readout electronics of gas detectors. It was originally conceived and optimized for the TPC of the ALICE experiment at the CERN LHC [52]. In one single chip, the analog signals from 16 channels are digitized, processed, compressed, and stored in a multi-event memory. After digitization, a pipelined Data Processor (see the block diagram of the chip's circuitry in Fig. 4.18) is able to remove a wide range of perturbations from the signal.

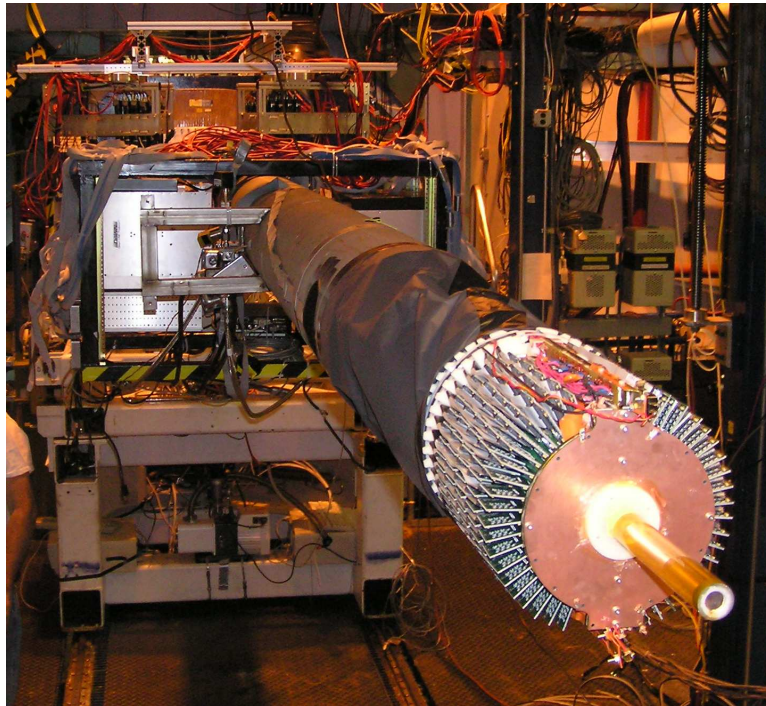


Figure 4.17: The fully instrumented RTPC on the end of the boom, just before insertion into the bore of the solenoid.

These fluctuations are related to the non-ideal behavior of the detector, temperature variation of the electronics, environmental noise, etc. The Data Processor is able to suppress the pulse tail within  $1 \mu\text{s}$  after the peak, thereby narrowing the pulses to improve their identification. For a time sample to be included in the recorded data, either it or one of its close neighbors must exceed the threshold value (5 ADC counts). If the sample passes this cut, the offset value (16 or 20, depending on the run period) is subtracted from it and eventually all non-negative results are written to the data file. Eventually, each data packet is marked with a time stamp and size so that the original data can be reconstructed afterwards and stored in the multi-event memory.

The BoNuS data recorded for each event consist of the TDC times (114 ns samples) and ADC amplitudes (10 bits) of all TPC pad signals above threshold. The data are stored in two separate BOS data banks [53], one for each TPC half. The time period extends from  $1.7 \mu\text{s}$  before to  $9.7 \mu\text{s}$  after a CLAS trigger. The CLAS trigger time defines the RTPC's  $T_0$ . The location of this trigger time in each channel's individual window is crucial when later converting hit time into spatial position. The interval is about 1.5 times the maximum drift time in the RTPC, large enough to record an entire "in-time" track but also to accept many accidentals - charge

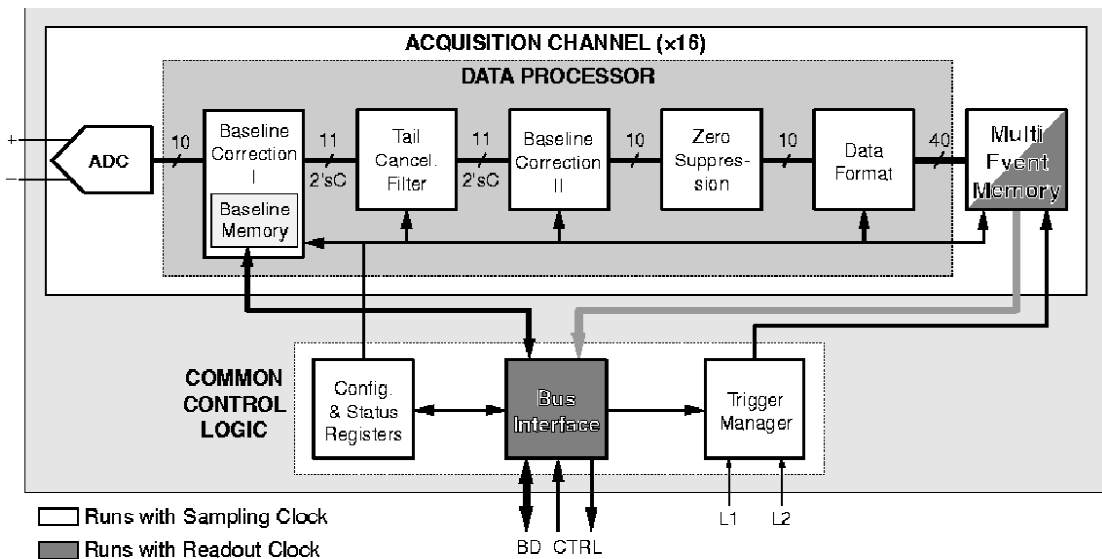


Figure 4.18: ALTRO chip block diagram.

which is not correlated with the CLAS trigger and needs to be removed from the sample.

## 4.2 Target Straw

The target material could not be made of a solid or liquid because the spectator protons would not have enough energy to escape. For this reason, a gaseous target cell was chosen which could withstand the required pressure. The cell was made of spiral wound, Kapton<sup>®</sup> foil with a thickness of 50  $\mu\text{m}$ . Most of the spectator proton's energy loss is in the target walls, which sets the lower detectable proton momentum limit. The full length of the straw is 280 mm, including 15  $\mu\text{m}$  thick aluminum window caps at either end. An aluminum collar covers the first 47 mm of upstream target length (Fig. 4.19) in order to shield the RTPC from protons coming from upstream. Similarly, the target extends 39.5 mm beyond the furthest downstream target acceptance to minimize the amount of background from the target endcap. The cell was inserted after the two chamber halves were bolted together. A helium bag surrounded the portion of the target which was downstream of the RTPC. This bag had a diameter of 25.4 mm and extended 100 mm past the RTPC. Its purpose was to minimize background in CLAS.

Deuterium was the target gas for the bulk of our data. However, we also used helium and hydrogen targets for the purposes of calibration (see Chapter 5 for a complete description of



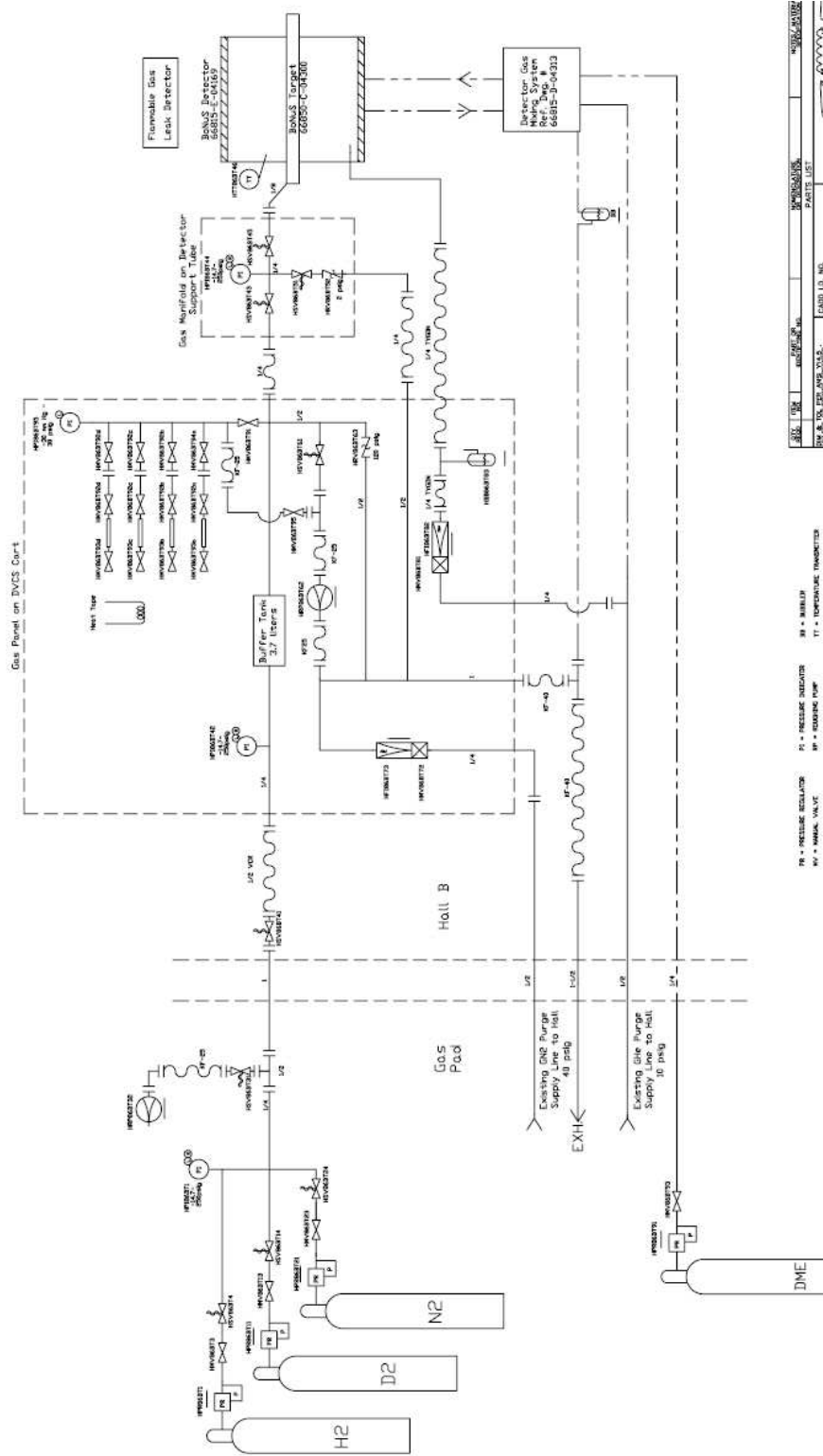


Figure 4.20: A detailed schematic of the full gas circuit for the RTPC-target system. The actual gas bottles are located in Hall-B's gas yard.

these procedures). The cell was held at a pressure of 100 psi to obtain the highest luminosity possible without blowing up the target. An extra volume of target gas (3.7 liters) was attached to the straw to minimize the amount of helium contamination from the RTPC's buffer gas. In this way, any contamination of the target from helium diffusion into the cell would be spread out over a large volume. The gas was completely flushed and refilled an average of every 80 runs and after every target change. Since the target pressure could not go below 14.7 psi (or 1 atm) without the target straw collapsing, it was filled and emptied twice between target gas changes to ensure minimal contamination. We also recharged the target when the pressure fell below 90 psi. Fig. 4.20 depicts the entire target gas system as well as the gas circuit for the RTPC volume.

# Chapter 5

## DATA PROCESSING

### 5.1 RTPC Track Reconstruction

The BoNuS RTPC readout system consists of 3200 charge collection pads, each having 100 possible time bins in which to register a signal. Some of these hits may be eliminated as candidates belonging to a good track because they are outside of the physical area where a particle may travel. The first step towards the goal of clustering these hits together and identifying VIP tracks is to have some knowledge of the paths on which ionization electrons travel before reaching the amplification and readout stages of the RTPC. The electric and magnetic fields in our configuration are neither parallel nor strictly perpendicular throughout the chamber volume giving us a challenging problem in track reconstruction. We must have a proper description of the electron drift velocity vectors before an attempt is even made to describe a particle track.

There exists a standard program called MAGBOLTZ [54] which takes as inputs the drift gas elements and mixture, the gas temperature and pressure, and the electric and magnetic field vectors. The program then outputs the components of the drift velocity vector in  $\mu\text{m}/\text{ns}$  with respect to the direction of the electric field. After finding the drift velocity vectors for an adequate number of chamber positions there were two paths we could have taken. The first was to use the program GARFIELD [49] that handles the simulation of two and three-dimensional drift chambers. GARFIELD uses commercial software to handle 3D magnetic fields, for which we did not have a license. With this in mind, the second approach we have taken, which circumvents the use of proprietary software, by writing our own code to determine approximations to the electron paths.

Using a parameterization of the electric and magnetic fields, and the composition of the gas, MAGBOLTZ was used to predict the drift velocity vector components at given points in the RTPC. Our own code then read the resulting spatial grid and simulated the trajectory of an ionization electron through the tracking region that terminates at the center of each pad. In the

end, we have generated a properly curved electron “path”, or “road”, for each pad, which was used to create a function that converts an observed signal into a reconstructed space point

$$P_{xyz} = P_{xyz}(I, t_{TDC}; V_{cathode}, V_{GEM}, R_{gas}) \quad (5.1)$$

where  $I$  is the pad number,  $t_{TDC}$  is the time (in ALTRO units) at which a signal was recorded,  $V_{cathode}$  and  $V_{GEM}$  are the RTPC operating voltages, and  $R_{gas}$  is the fraction of helium in the gas mixture. Ideally, the drift paths for the experiment would depend only on  $I$  and  $t_{TDC}$ . However, we ran with different electric field settings depending on the type of run (production or calibration) and we had an imperfect knowledge of the gas mixture (more on this later), which led us to include the other three parameters. Effective values for the extra parameters were determined that provided the best agreement with the data.

This section details the procedures used to turn the output of MAGBOLTZ into a reliable set of equations that convert the time at which a signal arrives on a pad into the coordinate which locates the point in the tracking region where the ionization occurred. The section goes on to explain how the hits are linked into a likely swath of charge left in the helium/DME mixture from a VIP and the subsequent track fitting. A description of the final extraction of the VIP’s position of liberation from the target and the momentum it carried both inside the initial state nucleus and after finally reaching the sensitive RTPC volume is made.

### 5.1.1 Determining Local $\vec{E}$ and $\vec{B}$

Three of the physical quantities that MAGBOLTZ requires to determine drift velocities are the  $\vec{E}$  and  $\vec{B}$  field magnitudes and the angle between them at a given space point. The field cage described in Chapter 4, which defines the boundaries of the drift regions, was designed to mimic the electric field gradient of two concentric infinite cylinders. Therefore we considered the  $\vec{E}$  field as purely radial, which falls off like  $1/r$  according to the familiar formula,

$$E(r) = \frac{V}{r \ln \frac{b}{a}}, \quad (5.2)$$

where  $V$  is the potential difference between the two cylinders,  $r$  is the perpendicular distance from the central axis, and  $b$  and  $a$  are the radii of the cylinders with  $b > a$ . In the RTPC we have

4 distinct regions where the electric field needs to be determined, the drift, transfer 1, transfer 2, and induction gaps. The drift gap is between the cathode ( $a = 30$  mm) and the first GEM ( $b = 60$  mm). Transfer gap 1 is between the first ( $a = 60$  mm) and second ( $b = 63$  mm) GEMs. Transfer gap 2 is between the second ( $a = 63$  mm) and third ( $b = 66$  mm) GEMs. And finally the induction gap is between the third GEM ( $a = 66$  mm) and the pad surface ( $b = 69$  mm). We must use Kirchoff's circuit law as described in Chapter 4.1.5 to determine the exact potential across each region. The electric field in the drift region varies with  $r$  from 800 V/cm to 400 V/cm, according to Eq. 5.2. In the first and second transfer regions and the induction region it averages 1650, 2200, and 2800 V/cm, respectively.

The corresponding magnetic field strength and direction must be read from a field map provided to us by the CLAS-DVCS group who built the solenoid at Saclay. The map gives the  $r, \phi, z$  components of the magnetic field in 0.5 cm steps from  $0 \leq r \leq 7$  cm and  $0 \leq z \leq 10$  cm, for a total of  $15 \times 21 = 315$  measurements. Fig. 5.2 shows the magnetic field vectors overlaid on a schematic of the different RTPC regions. A linear interpolation of this map was necessary to accommodate the finer grid on which we chose to run MAGBOLTZ.

To find the magnitude of  $\vec{B}$  at a particular point,  $(r_B, z_B)$ , that is not specifically on the field map, we first define a point on the map as  $\vec{B}(r_i, z_j) \equiv B_{ij}$  and find the values for  $i$  and  $j$  for which  $r_i < r_B < r_{i+1}$  and  $z_j < z_B < z_{j+1}$  (Fig. 5.1). Now we can write

$$r_B = \frac{nr_{i+1} + (N - n)r_i}{N} \quad (5.3)$$

as a weighted average of  $n$  parts  $r_{i+1}$  and  $N - n$  parts  $r_i$ . Replacing  $n$  and  $N$  by the fractional weighting  $t = n/N$ ,

$$r_B = tr_{i+1} + (1 - t)r_i \quad (5.4)$$

and therefore

$$t = \frac{r_B - r_i}{r_{i+1} - r_i}. \quad (5.5)$$

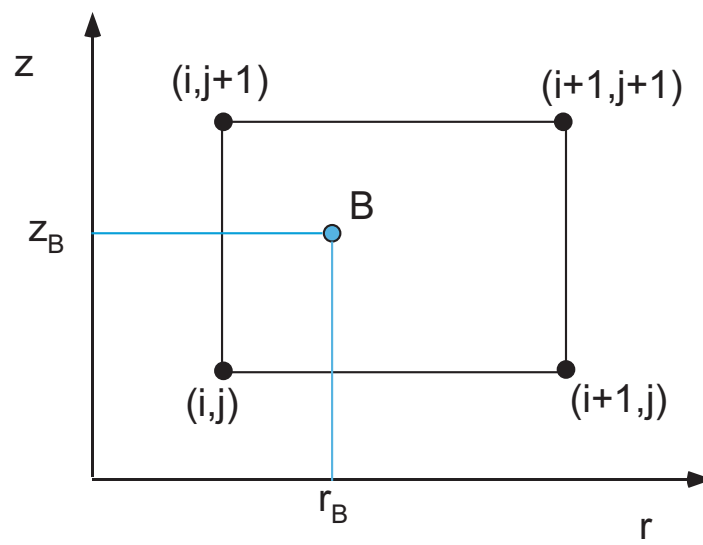


Figure 5.1: Two-dimensional interpolation procedure showing the grid points surrounding the particular  $(r, z)$  point where the magnetic field value needs to be evaluated.

Similarly for  $z_B$ ,

$$u = \frac{z_B - z_j}{z_{j+1} - z_j}. \quad (5.6)$$

We can now find the value of  $\vec{B}(r_B, z_B)$  by the formula,

$$\vec{B}(r_B, z_B) = (1-t)(1-u)B_{ij} + (t)(1-u)B_{i+1,j} + (1-t)(u)B_{i,j+1} + (t)(u)B_{i+1,j+1}. \quad (5.7)$$

The angle,  $\alpha$ , between the purely radial electric field vector and the magnetic field vector which lies in the  $r - z$  plane is simply  $\alpha = 90^\circ - \arctan(B_r/B_z)$ . We find that  $\alpha > 80^\circ$  throughout the sensitive regions of the RTPC.

### 5.1.2 MAGBOLTZ

MAGBOLTZ [54] is a Monte Carlo simulation of electron drift and diffusion in counting gases under the influence of electric and magnetic fields. MAGBOLTZ solves the Boltzmann transport equation using an energy distribution expansion up to the third Legendre polynomial. The calculated Lorentz angles (the angle by which particles moving in an electric field are deflected due to the effect of a magnetic field) are typically within  $1^\circ$  of the experimentally determined values (Fig. 5.3).

The collision types involved in the Monte Carlo integration include elastic and inelastic, attachment, ionizing and super-elastic. An analytic description of the electron's motion is used to speed up the calculation. The formalism of this description starts by assuming a magnetic field,  $B$ , along the  $x$ -axis and an electric field,  $E$ , at an angle  $\alpha$  in the  $x - z$  plane. The cyclotron frequency is given by the well known formula  $\omega = eB/m$  where  $e$  and  $m$  are the electron's charge and mass, respectively. The turning angle,  $\Omega$  in the magnetic field in a time,  $\delta t$ , between collisions is  $\Omega = \omega\delta t$ .

The electron starts with initial position  $(x_0, y_0, z_0)$  and velocity  $(v_{x0}, v_{y0}, v_{z0})$ , and propagates to a final position  $(x_1, y_1, z_1)$  and velocity  $(v_{x1}, v_{y1}, v_{z1})$  in a time  $\delta t$ . The analytic equations of

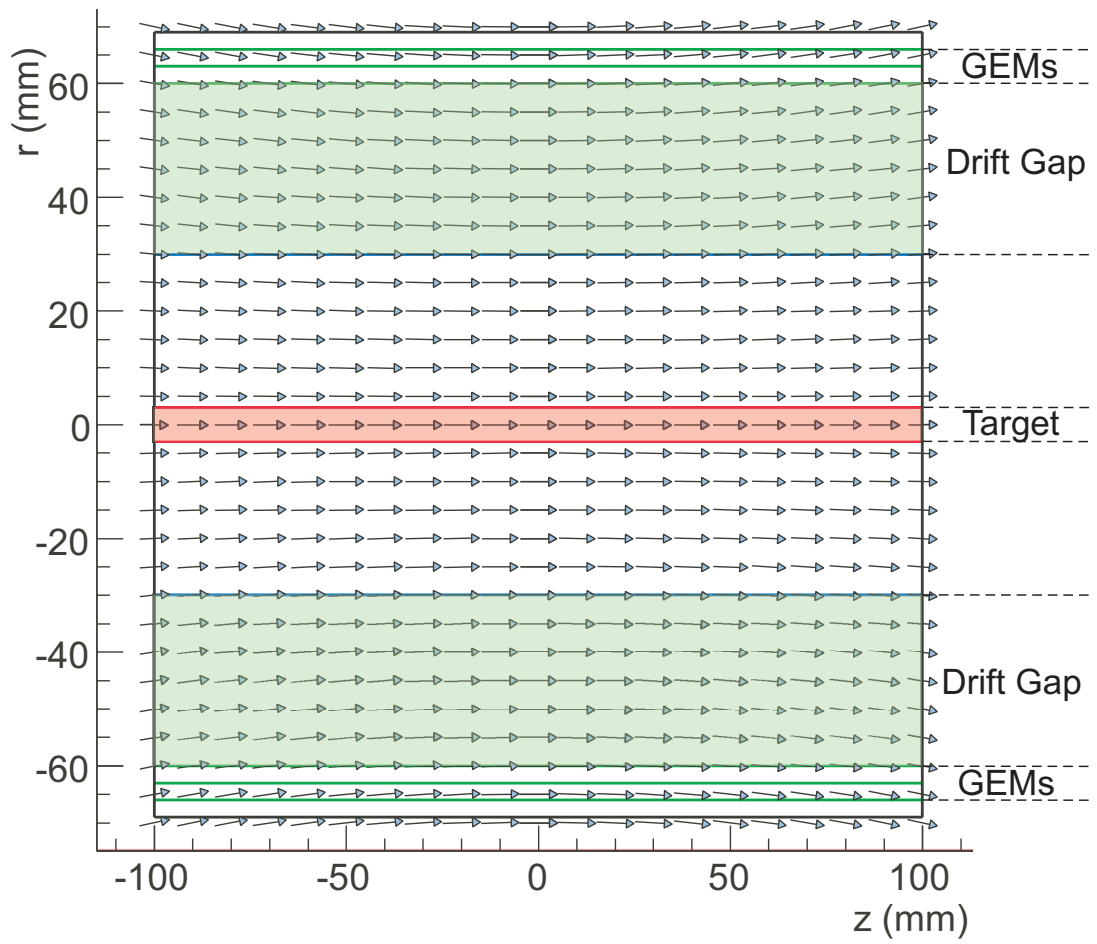


Figure 5.2: Solenoid magnetic field vectors in the  $r - z$  plane, with the various RTPC region locations indicated.

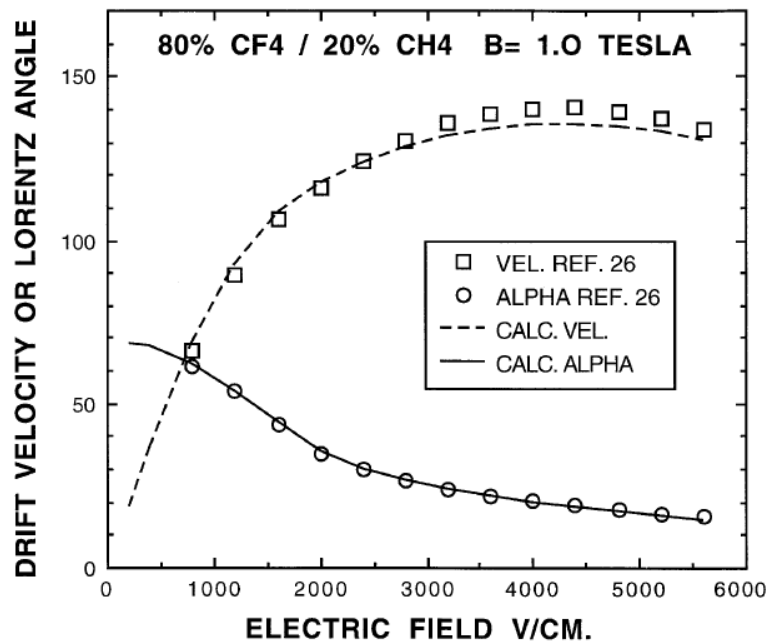


Figure 5.3: A typical MAGBOLTZ simulation result (dashed and solid lines) compared with the experimental values (open circles and squares) [54].

motion can then be written:

$$\begin{aligned}
 x_1 &= x_0 + v_{x0}\delta t + 0.5e/mE_x\delta t^2, \\
 y_1 &= y_0 + 1/\omega[(v_{y0} - E_z\omega) \sin \Omega + v_{z0}(1 - \cos(\omega)) + E_z\delta t], \\
 z_1 &= z_0 + 1/\omega[v_{z0} \sin \Omega - (v_{y0} - E_z/\omega)(1 - \cos \Omega)], \\
 v_{x1} &= v_{x0} + e/mE_x\delta t, \\
 v_{y1} &= (v_{y0} - E_z/\omega) \cos \Omega + v_{z0} \sin \Omega + E_z/\Omega, \\
 v_{z1} &= v_{z0} \cos \Omega - (v_{y0} - E_z/\Omega) \sin \Omega.
 \end{aligned} \tag{5.8}$$

After the unknown value,  $\delta t$ , is found by a standard Monte Carlo collision technique, the motion of the electron can be found after iterating the procedure over a number of real collisions given by the user. Typically  $2 \times 10^7$  collisions were used for our drift gas. This is the lowest number suggested by the program for an inelastic gas (any gas that is not solely made up of a pure noble gas) to obtain 1% accuracy in the least amount of computation time.

MAGBOLTZ was used to find the drift velocity vector in 1 mm steps of radius from  $r = 20$

mm to the cathode at  $r = 30$  mm to the first GEM at  $r = 60$  mm then through each transfer gap and the induction gap and finally reaching the pad surface at  $r = 69$  mm. The mirror symmetry of the solenoid field along the  $z$  axis,  $\vec{B}(z) = \vec{B}(-z)$ , allowed us to run the simulation in 5 mm steps from  $0 \leq z \leq 100$  mm. Similarly, the azimuthal symmetry,  $\vec{B}(\phi) = \vec{B}(\phi + \Delta\phi)$ , allowed us to rotate in  $\phi$  the results of MAGBOLTZ along the line of  $\phi = 0^\circ$ , around the  $z$  axis. Not only did we run the simulation on this 2-dimensional  $50 \times 21$  grid, we also needed to know the drift velocity vectors when the current in the solenoid was 450 and 534A. Next, the  $\vec{E}$  fields in the RTPC varied throughout the run as we attempted to optimize the sensitivity to heavily ionizing tracks. Therefore MAGBOLTZ was run across 10 settings covering the range of fields we utilized. Finally, since the exact ratio of He/DME was not held constant with a sophisticated gas control system (our system failed just before production running commenced), the mixture also becomes an unknown parameter in the final electron paths. Seven mixtures were simulated covering He/DME = 75/25 - 85/15. In all, there are  $21 \times 50 \times 2 \times 10 \times 7 = 147,000$  drift velocity vectors to determine and parameterize. Clearly, extra software was necessary to rerun MAGBOLTZ efficiently for all of the different configurations. The extra software consisted of a series of scripts designed to efficiently run MAGBOLTZ for multiple settings.

Figs. 5.4 and 5.5 depict how the radial and azimuthal drift velocities vary as a function of  $r$  and  $z$ . The radial component is typically twice the magnitude of the velocity in the  $\phi$  direction, leading to a fairly constant Lorentz angle of  $27^\circ$ , even in the transfer and induction gaps. The drift velocities vary weakly with  $z$  because the radial component of the B field is small, but  $\vec{B}_z$  does increase with distance away from the solenoid center. Fig. 5.5 shows that, correspondingly, the radial drift speed is largest at the upstream and downstream chamber extremes. In our standard configuration, an electron liberated at the cathode would take  $6 \mu\text{s}$  to travel to the first GEM layer, sweeping out  $\approx 34^\circ$  in azimuth. The resulting avalanche electrons take an additional 450 ns to reach the readout board, being deflected by an additional  $5^\circ$ .

All of this discussion of drift velocity components neglects the electron's drift in  $z$  along the cylindrical axis. This component is so small that its effect on the electrons path is negligible given the RTPC's pad width is 5 mm in  $z$ . To support this statement let us consider the RTPC field configuration which gives the largest  $v_z$ . At  $\Delta V_{drift} = 1685V$  and the highest solenoid current of 534A, MAGBOLTZ returns a maximum  $v_z = 0.2251 \pm 0.1019 \mu\text{m/ns}$  at  $r = 30$  mm and  $v_z = 1.4720 \pm 0.1591 \mu\text{m/ns}$  at  $r = 65$  mm and at the extreme downstream end of the

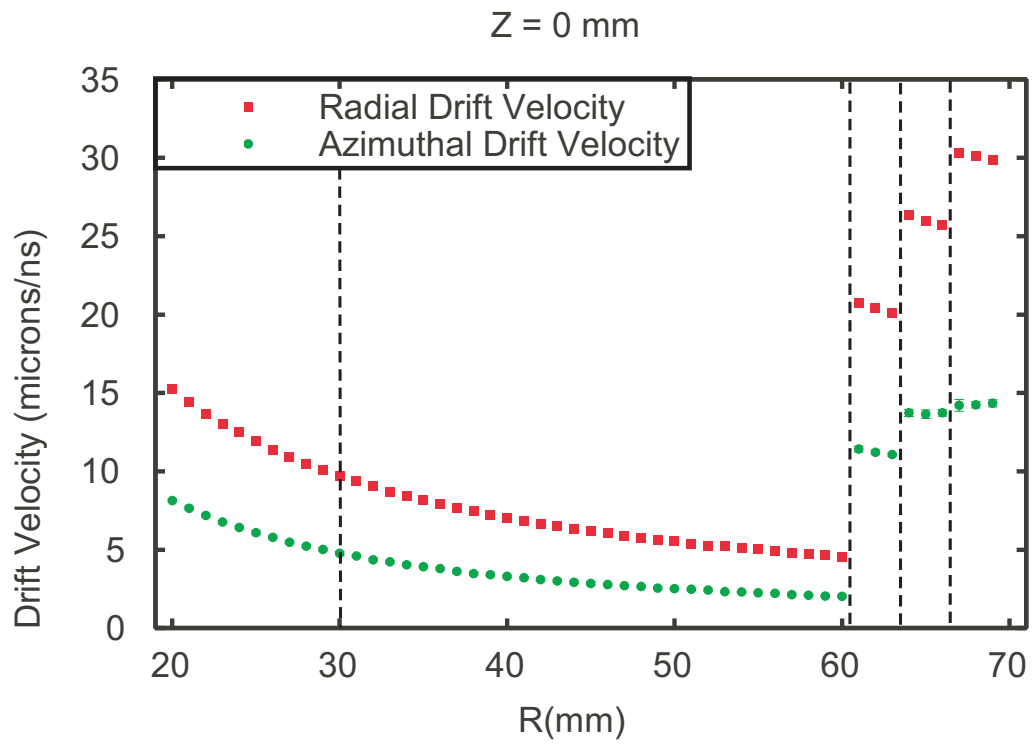


Figure 5.4: The dependence of the radial and azimuthal drift velocity on  $r$  for a given  $z$ . The dashed lines correspond to, from left to right, the cathode and the first, second and third GEMs.

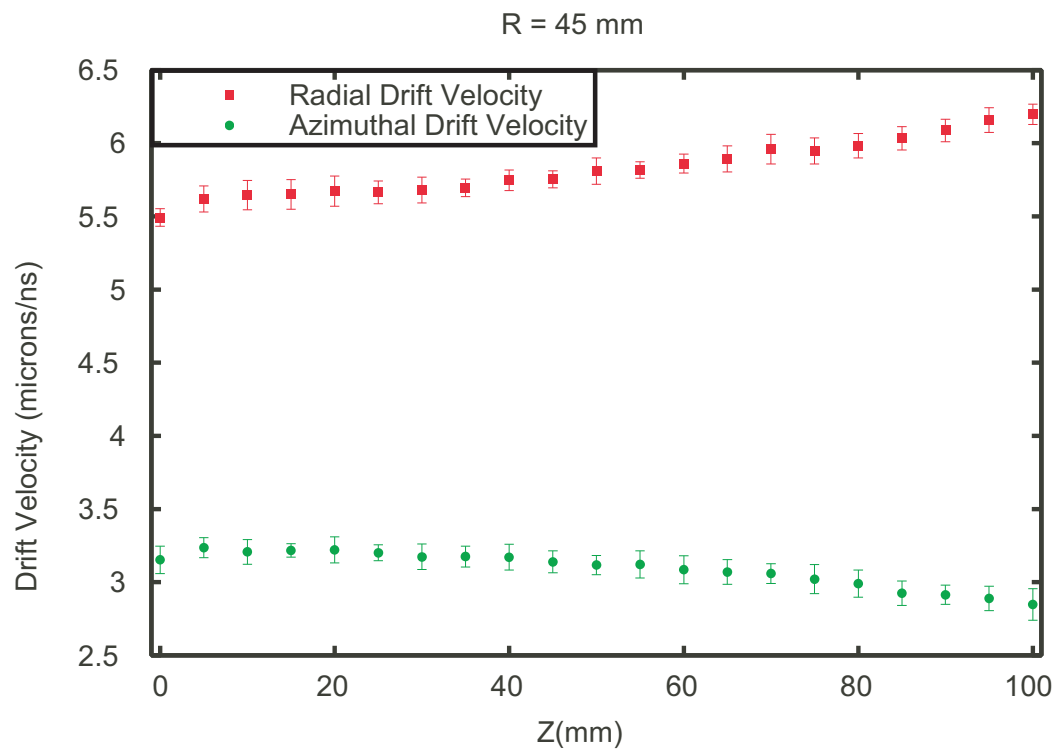


Figure 5.5: The dependence of the radial and azimuthal drift velocity on  $z$  for a given  $r$ .

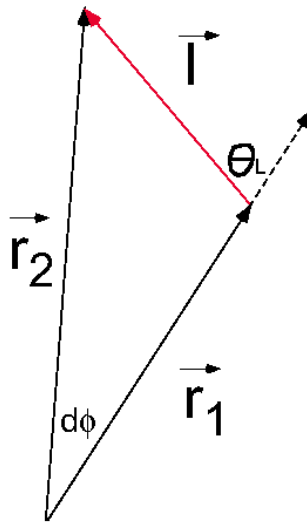


Figure 5.6: The definition of the Lorentz angle,  $\theta_L$ , position vectors and deflection angle,  $d\phi$ .

RTPC. Now let's assume the worst-case and take the upper end of both errors, 6000 ns drift time and 450 ns transfer time. This puts the maximum total drift distance in  $z$  at

$$z_{drift} = (0.327 \mu\text{m/ns} \times 6000 \text{ ns}) + (1.631 \mu\text{m/ns} \times 450 \text{ ns}) = 2700 \mu\text{m} = 2.7 \text{ mm}. \quad (5.9)$$

Even in this worst-case scenario, the maximum drift distance in  $z$  is approximately half of a pad width and can therefore be neglected in the reconstruction of tracks. Even if we were to somehow use the drift velocity along  $z$  it would take MAGBOLTZ an exorbitant amount of time to process enough collisions to reach an error commensurate with its magnitude.

### 5.1.3 Drift Electron Paths

MAGBOLTZ provides us with all of the drift velocity information that we need to determine the trajectory that an ionization electron will take after it is freed from its molecular parent. The case of an electron produced at the virtual cathode ( $r = 20 \text{ mm}$ ) is the only one which we need to consider because any electron produced at other radii will follow a segment of the path traced out by the electron which traverses the entire volume. This is true because thermal electrons reach terminal velocity almost immediately. The path of this one theoretical electron

will, however, be drastically altered depending on the potential difference in the drift gap, the particular region of solenoidal field, and gas mixture.

Let us define a “parent” electron path as one which starts at  $(r_0, \phi_0, z_0) = (20\text{mm}, 0^\circ, z_0)$  and ends at the first GEM. In the avalanche region, only the total time it takes the electrons to reach the pads and their  $\phi$  change from the first GEM to the pads are recorded. The next point on the path is determined by looking up the radial and azimuthal drift velocity components from MAGBOLTZ and using Eq. 5.10 to calculate where the electron will end up after 1 ns. If the initial position does not lie on a grid point we interpolate the drift velocity using the same interpolation scheme described in Sec. 5.1.1. Given a position vector,  $\vec{r}_1$ , we can find the subsequent path location,  $\vec{r}_2$ , if we know the Lorentz angle,  $\theta_L$ , and the length of the distance traveled,  $l$ . Inspection of Fig. 5.6 reveals the simple relationships:

$$\begin{aligned} \vec{r}_2 &= \vec{r}_1 + \vec{l}, \\ r_2^2 &= r_1^2 + l^2 + 2r_1l \cos \theta_L, \\ l^2 &= r_2^2 + r_1^2 - 2r_1r_2 \cos d\phi. \end{aligned} \quad (5.10)$$

where  $d\phi$  is the increment of azimuth that the electron sweeps out in 1 ns. Taking the drift velocity vector as  $\vec{w} = (w_r, w_\phi, w_z)$ , and again, setting  $w_z = 0$  we can find  $\theta_L$  and  $l$ ,

$$\theta_L = \arctan\left(\frac{w_\phi}{w_r}\right), \quad (5.11)$$

$$l = \Delta t \sqrt{w_\phi^2 + w_r^2}. \quad (5.12)$$

where we have chosen  $\Delta t = 1$  ns. Now we can find the coordinates of the next location on the path by combining the result of Eqs. 5.10 and 5.12

$$d\phi = \arccos \frac{l^2 - r_2^2 - r_1^2}{-2r_1l}, \quad (5.13)$$

$$\phi_2 = \phi_1 + d\phi. \quad (5.14)$$

When the avalanche electrons approach the pad plane we need to be sure not to project the next path step past  $r = 69$  mm. If the electron cloud will strike the pads in the next nanosecond we find the distance from  $r_1$  to the pad surface by taking the positive solution of Eq. 5.10 and

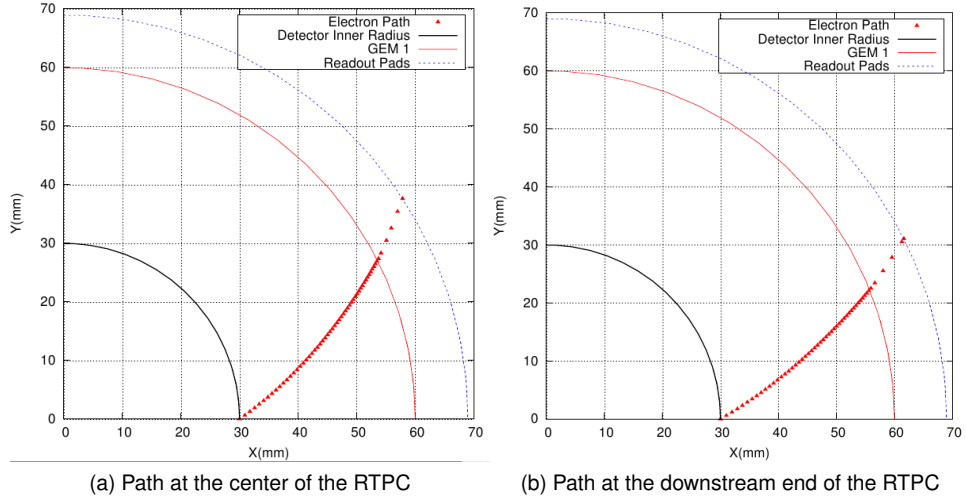


Figure 5.7: Two drift electron paths at different  $z$  positions, shown starting at the cathode and ending on the readout pads. The red points shown are in steps of 100 ns. Note the effect of the Lorentz angle on the total azimuthal angle swept out by the paths.

substituting  $r_2 = 69$  mm. We use  $l = -r_1 \cos \theta_L + \sqrt{r_1^2 \cos^2 \theta_L - (r_1^2 - 69^2)}$  to find the final  $d\phi$ .

Fig. 5.7 depicts a typical electron's path in the drift, transfer and induction region when produced at two different locations along the RTPC's central axis. In all three regions,  $\Delta V$  and the gas mixture are held constant so the larger path curvature in the center of the chamber can be attributed directly to the smaller  $B_\phi$  in the solenoid's center. As we introduce variations in  $\Delta V_{drift}$  and gas mixture, the complexity of dependencies for the "parent" electron paths, which we will use later to project signals, leads us to create a system of parameterizations. Multidimensional equations of the form

$$r_{hit} = A(t + B)^C \quad (5.15)$$

and

$$\phi_{hit} = D + F \log(t + G) \quad (5.16)$$

were fit to the paths using the standard function minimization program MINUIT [55]. The values of A, B, C, D, F and G are dependent on  $\Delta V_{drift}$ , gas mixture and  $z_{pad}$ . The magnetic field effects are accounted for by running the electron path generator at each individual pad's  $z$

position. A power law and logarithmic form for the radial and azimuthal dependence on time gave the best convergence to the drift electron path simulation while maintaining a smooth behavior outside of the fit range. Initially, fifth order polynomials in time were chosen but, as high order polynomials are wont to do, they fluctuated wildly outside the regions containing data. This could cause a problem when attempting to use the fit result to calibrate the data. A smooth curve is preferable. After the forms in Eqs. 5.15 and 5.16 were decided upon, further study revealed that the coefficients could all be adequately described by a quadratic polynomial in  $H$  (where  $H$  is the percentage of helium in the given mixture), a fourth order even polynomial in  $z_{pad}$  (due to the symmetry of the magnetic field across  $z = 0$  mm) and a linear polynomial in  $\Delta V_{drift}$ .

$$\begin{aligned}
A &= (\alpha_0 + \alpha_1 H + \alpha_2 H^2)(\alpha_3 + \alpha_4 z_{pad}^2 + \alpha_5 z_{pad}^4)(\alpha_6 + \alpha_7 \Delta V_{drift}), \\
B &= (\beta_0 + \beta_1 H + \beta_2 H^2)(\beta_3 + \beta_4 z_{pad}^2 + \beta_5 z_{pad}^4)(\beta_6 + \beta_7 \Delta V_{drift}), \\
C &= (\kappa_0 + \kappa_1 H + \kappa_2 H^2)(\kappa_3 + \kappa_4 z_{pad}^2 + \kappa_5 z_{pad}^4)(\kappa_6 + \kappa_7 \Delta V_{drift}), \\
D &= (\delta_0 + \delta_1 H + \delta_2 H^2)(\delta_3 + \delta_4 z_{pad}^2 + \delta_5 z_{pad}^4)(\delta_6 + \delta_7 \Delta V_{drift}), \\
F &= (\eta_0 + \eta_1 H + \eta_2 H^2)(\eta_3 + \eta_4 z_{pad}^2 + \eta_5 z_{pad}^4)(\eta_6 + \eta_7 \Delta V_{drift}), \\
G &= (\gamma_0 + \gamma_1 H + \gamma_2 H^2)(\gamma_3 + \gamma_4 z_{pad}^2 + \gamma_5 z_{pad}^4)(\gamma_6 + \gamma_7 \Delta V_{drift})
\end{aligned}
\tag{5.17}$$

Each group of coefficients was found using values of  $\Delta V_{drift} = 1718, 1703, 1688, 1674,$  and  $1659$  V,  $H = 75, 80, 85\%$ , and the full range of  $z_{pad}$  from  $-100$  to  $100$  mm. These values were chosen to fully cover the range of detector conditions thought to be present during the entire run period. Table 5.1 shows the final values for each parameter and Figs. 5.8 and 5.9 show the result of the fitting, with two of the middle values of  $\Delta V_{drift}$  suppressed in order to show more clearly the miniscule splitting that the changing electric field produces. Clearly the radial and azimuthal components of the electron drift paths are primarily sensitive to the drift gas mixture. The parameterization could do a better job of describing the  $\phi$  coordinate's time dependence on  $\Delta V_{drift}$ , especially at the largest drift time (furthest away from the cathode). However, the error on  $\phi$  is only  $\approx 1^\circ$ , which is easily corrected in later calibrations of the BoNuS detector.

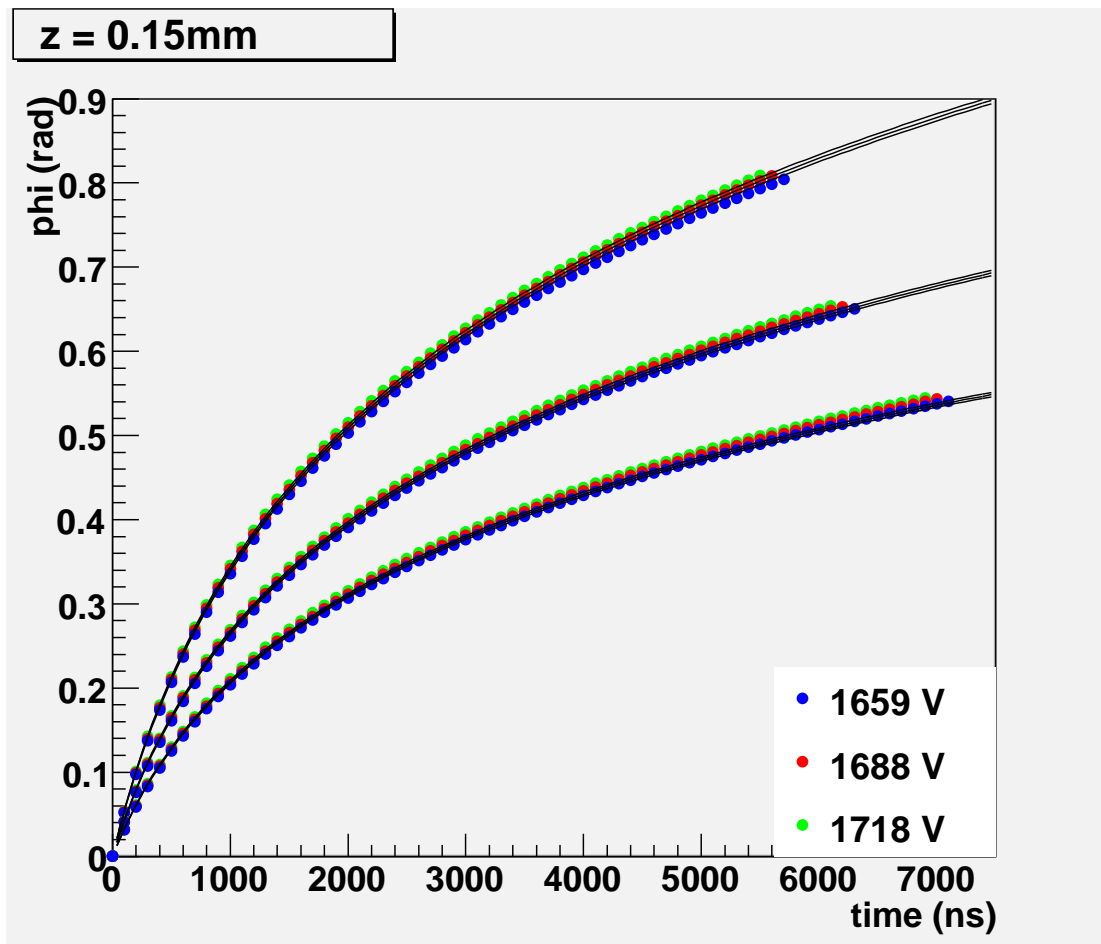


Figure 5.8: Azimuthal angle swept out by drift electrons in time  $t$  for different configurations of gas mixture and electric field at a fixed  $z$ .

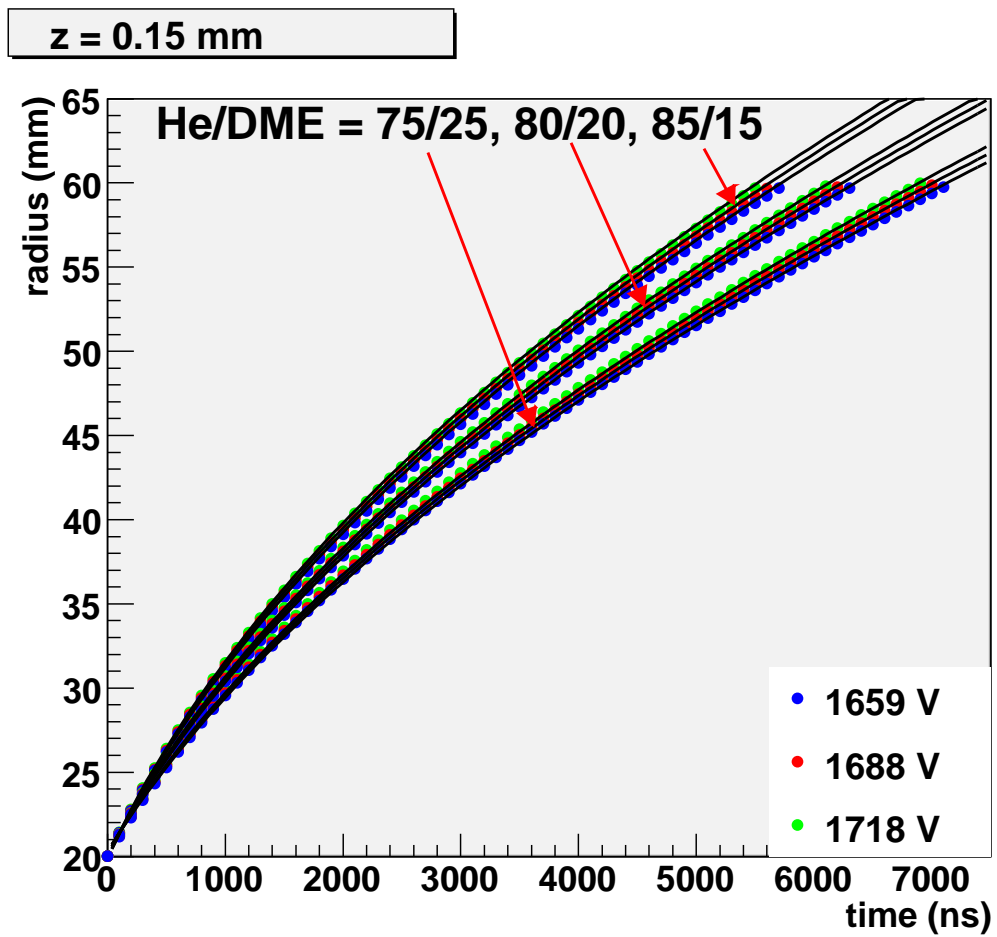


Figure 5.9: The radial coordinate of drift electrons versus time for different configurations of gas mixture and electric field at a fixed  $z$ .

| index | $\alpha$                | $\beta$                 | $\kappa$                |
|-------|-------------------------|-------------------------|-------------------------|
| 0     | $-1.73 \times 10^{+00}$ | $4.13 \times 10^{+03}$  | $6.03 \times 10^{-01}$  |
| 1     | $5.45 \times 10^{-02}$  | $-7.47 \times 10^{+01}$ | $-2.91 \times 10^{-03}$ |
| 2     | $-1.68 \times 10^{-04}$ | $3.69 \times 10^{-01}$  | $1.37 \times 10^{-05}$  |
| 3     | $5.20 \times 10^{-01}$  | $1.43 \times 10^{+00}$  | $1.06 \times 10^{+00}$  |
| 4     | $1.50 \times 10^{-05}$  | $-3.73 \times 10^{-05}$ | $-5.61 \times 10^{-06}$ |
| 5     | $5.30 \times 10^{-11}$  | $6.41 \times 10^{-10}$  | $3.21 \times 10^{-11}$  |
| 6     | $2.37 \times 10^{-01}$  | $2.19 \times 10^{+00}$  | $1.06 \times 10^{+00}$  |
| 7     | $4.51 \times 10^{-04}$  | $-7.07 \times 10^{-04}$ | $-3.59 \times 10^{-05}$ |
| index | $\delta$                | $\eta$                  | $\gamma$                |
| 0     | $-2.21 \times 10^{+01}$ | $3.05 \times 10^{+00}$  | $7.08 \times 10^{+03}$  |
| 1     | $5.95 \times 10^{-01}$  | $-8.29 \times 10^{-02}$ | $-1.61 \times 10^{+02}$ |
| 2     | $-4.23 \times 10^{-03}$ | $5.98 \times 10^{-04}$  | $1.00 \times 10^{+00}$  |
| 3     | $9.80 \times 10^{-01}$  | $1.08 \times 10^{+00}$  | $7.25 \times 10^{-01}$  |
| 4     | $-1.58 \times 10^{-05}$ | $-1.62 \times 10^{-05}$ | $-1.46 \times 10^{-06}$ |
| 5     | $9.25 \times 10^{-11}$  | $9.46 \times 10^{-11}$  | $-1.14 \times 10^{-11}$ |
| 6     | $1.19 \times 10^{+00}$  | $1.01 \times 10^{+00}$  | $2.45 \times 10^{+00}$  |
| 7     | $-8.73 \times 10^{-05}$ | $-8.91 \times 10^{-06}$ | $-6.44 \times 10^{-04}$ |

Table 5.1: Final Drift Electron Path Parameters to use in Eq. 5.17. They reproduce  $r$  in mm and  $\phi$  in radians.

#### 5.1.4 Offset Corrections

When the initial ionization electron reaches the amplification stage ( $r \geq 60$  mm) we no longer have information about where in  $r - \phi$  space it travels. What we do need to realize, however, is that when we register the first hit on pad  $i$  at time  $t_0$  we cannot simply assign  $\phi_0 = \phi_i$  and  $r_0 = 60$  mm to this hit because the electron cloud travels with finite speed and continues to receive a kick in the  $\phi$  direction (see Fig. 5.4). It is important to correctly quantify this time and angle offset since the time it takes the cloud to reach the readout pads can be larger than the width of four time bins and can cover more than  $5^\circ$ . Neither of the offsets is constant. Like the drift electrons, they are dependent on the mixture and the  $E$ - $B$  field. Therefore we use a similar MINUIT fitting procedure to obtain equations that can describe the offsets which will be used in calibrations to give the best track representations. Unlike for the drift electrons, the offset functions must be treated separately for the two halves of the chamber. The induction and transfer fields are calculated from the resistors placed between each GEM layer (see Sec. 4.1.5). Each chamber half is a completely independent circuit and must be treated as such. We use the voltage on the outside of GEM<sub>1</sub> as the only voltage variable in the fit functions, but the offsets which

| index | $p$                     | $c$                     |
|-------|-------------------------|-------------------------|
| 0     | $3.55 \times 10^{-08}$  | $-1.26 \times 10^{-03}$ |
| 1     | $-5.09 \times 10^{-04}$ | $9.38 \times 10^{-02}$  |
| 2     | $3.11 \times 10^{+00}$  | $-4.65 \times 10^{-06}$ |
| 3     | $-4.69 \times 10^{-09}$ | $2.07 \times 10^{-04}$  |
| 4     | $8.72 \times 10^{-05}$  | $1.04 \times 10^{-10}$  |
| 5     | $-2.29 \times 10^{-01}$ | $-5.81 \times 10^{-09}$ |
| 6     | $4.53 \times 10^{-11}$  | $2.20 \times 10^{+00}$  |
| 7     | $-1.18 \times 10^{-06}$ | $-1.58 \times 10^{+02}$ |
| 8     | $5.64 \times 10^{-03}$  |                         |
| 9     | $2.74 \times 10^{-12}$  |                         |
| 10    | $-5.81 \times 10^{-05}$ |                         |
| 11    | $6.14 \times 10^{+02}$  |                         |
| 12    | $-2.94 \times 10^{-16}$ |                         |
| 13    | $7.50 \times 10^{-09}$  |                         |
| 14    | $-7.35 \times 10^{-02}$ |                         |
| 15    | $2.08 \times 10^{-17}$  |                         |
| 16    | $-4.34 \times 10^{-10}$ |                         |
| 17    | $1.82 \times 10^{-03}$  |                         |

Table 5.2: Final Offset Parameters for RTPC Left

are calculated in the electron path generator use the full knowledge of the velocity vector in each region. We need only to know one voltage value for each half chamber since the rest of the circuit is fixed and the resistor values were measured. The best agreement to the offset functions came when using equations of the form:

$$\begin{aligned}
t_{off} = & (p_0 H^4 + p_1 H^2 + p_2)(p_9 V G_1^4 + p_{10} V G_1^2 + p_{11}) + \\
& [(p_3 H^4 + p_4 H^2 + p_5)(p_{12} V G_1^4 + p_{13} V G_1^2 + p_{14})] z_{pad}^2 + \\
& [(p_6 H^4 + p_7 H^2 + p_8)(p_{15} V G_1^4 + p_{16} V G_1^2 + p_{17})] z_{pad}^4, \\
\phi_{off} = & (c_0 H + c_1) V G_1 + (c_2 H + c_3) z_{pad}^2 + (c_4 H + c_5) z_{pad}^4 + (c_6 H + c_7) \quad (5.18)
\end{aligned}$$

where, again,  $H$  is the percentage of helium in the drift gas and  $V G_1$  is the voltage on the outside of  $GEM_1$ . The parameters that we found are given in Tables 5.2. and 5.3

The offset correction function parameters were found using a simulated data set that included the same values of  $H$  and  $z_{pad}$  as the drift electron paths but two different sets of  $V G_1$  values. On the left we simulated  $VGL_1 = 2242, 2411, 2579, 2747, \text{ and } 2915$  V and for the right side circuit we used  $VGR_1 = 2209, 2375, 2540, 2706, \text{ and } 2871$  V. Again, these voltages were

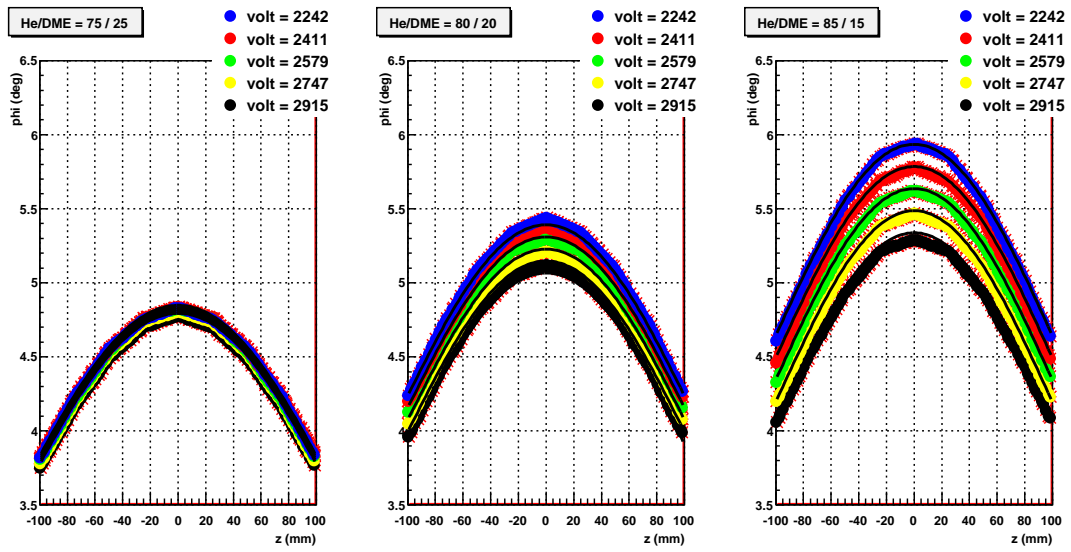
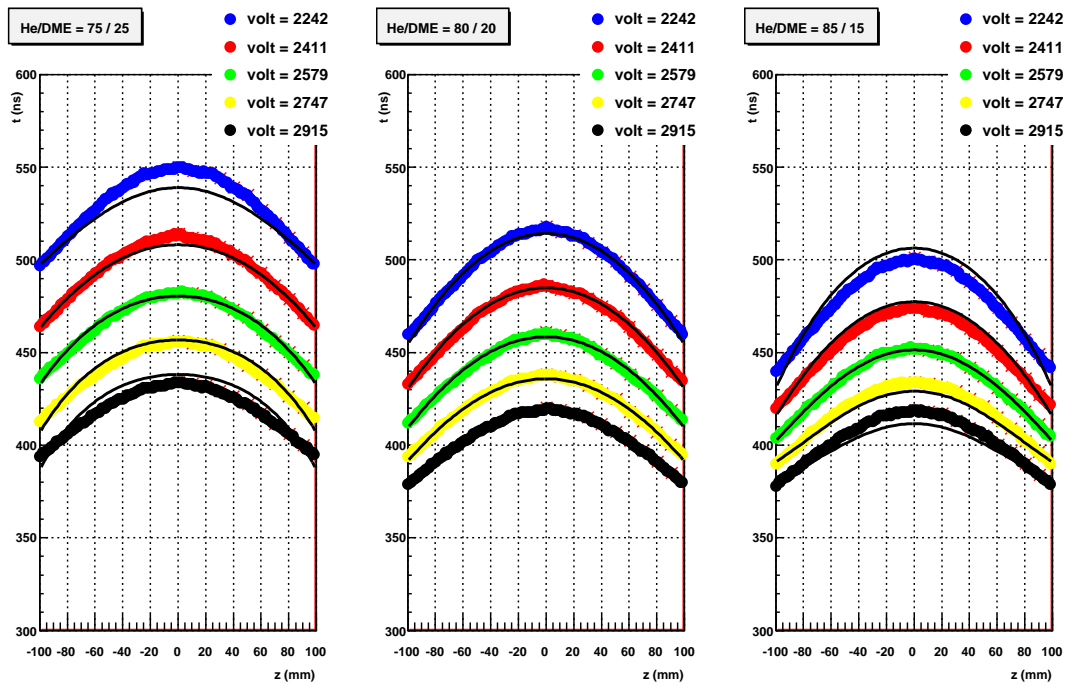
| index | $p$                     | $c$                     |
|-------|-------------------------|-------------------------|
| 0     | $3.53 \times 10^{-08}$  | $-1.09 \times 10^{-03}$ |
| 1     | $-5.08 \times 10^{-04}$ | $8.18 \times 10^{-02}$  |
| 2     | $3.14 \times 10^{+00}$  | $-4.89 \times 10^{-06}$ |
| 3     | $-4.84 \times 10^{-09}$ | $2.24 \times 10^{-04}$  |
| 4     | $8.58 \times 10^{-05}$  | $1.04 \times 10^{-10}$  |
| 5     | $-2.46 \times 10^{-01}$ | $-5.73 \times 10^{-09}$ |
| 6     | $4.29 \times 10^{-11}$  | $1.96 \times 10^{+00}$  |
| 7     | $-1.17 \times 10^{-06}$ | $-1.41 \times 10^{+02}$ |
| 8     | $5.62 \times 10^{-03}$  |                         |
| 9     | $2.85 \times 10^{-12}$  |                         |
| 10    | $-5.94 \times 10^{-05}$ |                         |
| 11    | $6.13 \times 10^{+02}$  |                         |
| 12    | $-9.48 \times 10^{-17}$ |                         |
| 13    | $5.77 \times 10^{-09}$  |                         |
| 14    | $-8.31 \times 10^{-02}$ |                         |
| 15    | $2.07 \times 10^{-17}$  |                         |
| 16    | $-4.28 \times 10^{-10}$ |                         |
| 17    | $1.72 \times 10^{-03}$  |                         |

Table 5.3: Final Offset Parameters for RTPC Right

chosen to fully cover the range of real settings on the power supplies that were used during the run. Figs. 5.10 and 5.11 depict the results of these fits on the left side of the RTPC. The discrepancy between the fit functions and the simulated data, which are  $< 10$  ns and  $< 0.1^\circ$ , are insignificant compared to our time and angular resolution.

### 5.1.5 Reconstructing Hits

The proceeding sections have outlined the framework for converting each channel's TDC (time to digital converter on the ALTRO chip) information to a position three vector locating the initial ionization. When a charge above threshold is recorded at time  $t_{TDC}$  on channel  $i$ , Eqs. 5.15, 5.16 and 5.18 can be combined to assign a  $(r, \phi)$  coordinate to the hit (again,  $z_{hit} = z_{pad}$  as proven in Eq. 5.9). One detail that we need to address is that the time recorded by the TDC is relative to the trigger. That is, a larger TDC value corresponds to charge which originated closer to the cathode. On the other hand, the value  $t$  in the pertinent equations is actually the elapsed time it took a "parent" electron to travel from the cathode to its current position. Therefore, the signal time from the TDC must be subtracted from the total time it takes

Figure 5.10: The  $\phi$  offset versus  $z$  for RTPC leftFigure 5.11: The time offset versus  $z$  for RTPC left

the proper “parent” electron to travel from the cathode to the first GEM in order to use the parameterization of time to distance conversion. Setting  $r_{hit} = 60$  mm in Eq. 5.15 and solving for  $t$  tells us the time it takes the “parent” electron to travel from the cathode to the first GEM. The drift time from the cathode to the first GEM,  $t_{K2G} = (60/A)^{1/C} - B$ , is obtained from Eq. 5.15 using the GEM location of 60 mm. The time  $t$  to use in Eqs. 5.15 and 5.16 can be calculated from

$$\begin{aligned} t_{K2G} + t_{off} &= t + (t_{TDC} - T_0) \\ t &= t_{K2G} + t_{off} + T_0 - t_{TDC} \end{aligned} \quad (5.19)$$

where  $t_{off}$  is given by Eq. 5.18 and  $T_0$  is the RTPC’s start time, explained in the previous chapter and found during the RTPC calibration procedure outlined in Sec. 5.2. The subtraction of  $T_0$  from the TDC time accounts for the pretrigger. The variables  $t$ ,  $t_{K2G}$ , and  $t_{off}$  are in units of nanoseconds but  $t_{TDC}$  and  $T_0$  are in discrete time bin units and must be properly converted to nanoseconds using 114 ns / time bin. This conversion is also described in Sec. 5.2. Fig. 5.12 shows the relative positions of each individual timing variable on the event time window scale starting at  $T = 0$  with time increasing from bottom to top.

The correct use of Eq. 5.16 entails keeping track of angular references in a similar way to how we kept track of timing references in the previous paragraph. Let us define  $\phi_{K2G}$  as the amount of azimuth that a given channel’s “parent” electron will sweep out as it travels on a full path from the virtual cathode to the first GEM. Inserting the channel’s value of  $t_{K2G}$  into Eq. 5.16 yields  $\phi_{K2G}$ . The value for  $t$  found in Eq. 5.19 can be used in Eq. 5.16 to tell us the angle the “parent” electron sweeps in  $\phi$  in time  $t$  with respect to the projected path’s  $\phi$  coordinate at the cathode. We’ll call that angle  $\phi_0 = D + F \log(t + G)$ . The  $\phi$  coordinate of the hit at time  $t_{TDC}$  is given by Eq. 5.20.

$$\phi_{hit} = \phi_{pad} + \phi_{K2G} + \phi_{off} - \phi_0. \quad (5.20)$$

The drift electrons are deflected in the negative  $\phi$  direction so  $\phi_{K2G}$  and  $\phi_{off}$  are added to the pad’s  $\phi$  coordinate. Fig. 5.13 shows how the  $\phi$  variables are related to each other.

Putting this all together, one can see a view of a typical track in four different views in Fig. 5.14 after calculating the  $r$  and  $\phi$  coordinates of the hits from the timing data and the  $z$

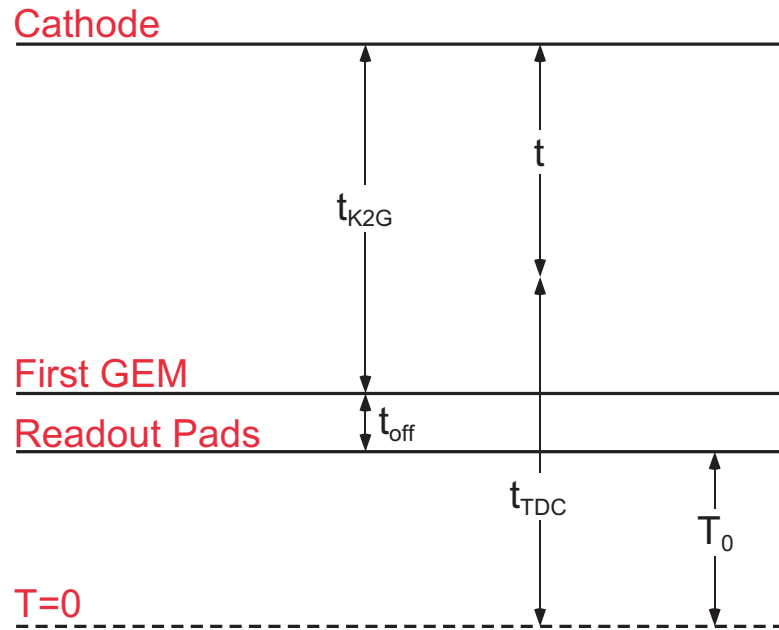


Figure 5.12: Schematic of various times needed to determine the proper time,  $t$ , for use in Eqs. 5.15 and 5.16. See the text for the definitions of the various time variables.

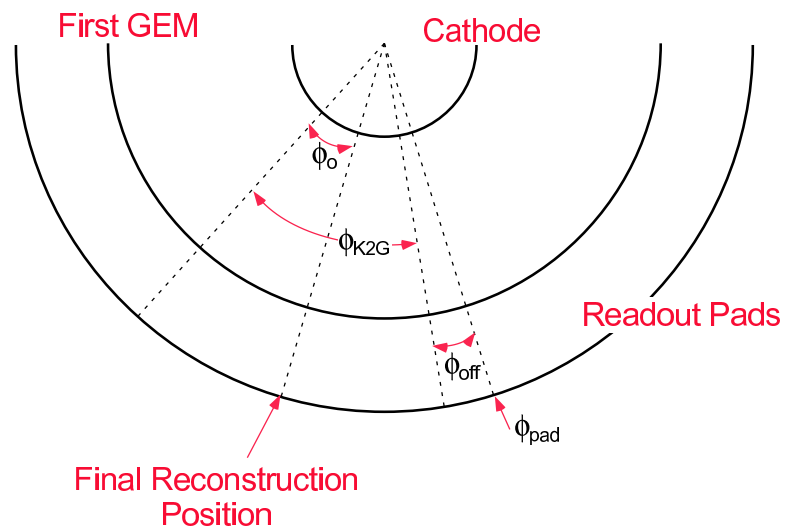


Figure 5.13: Determining the reconstructed  $\phi$  coordinate. See the text for the definitions of the various angular variables.

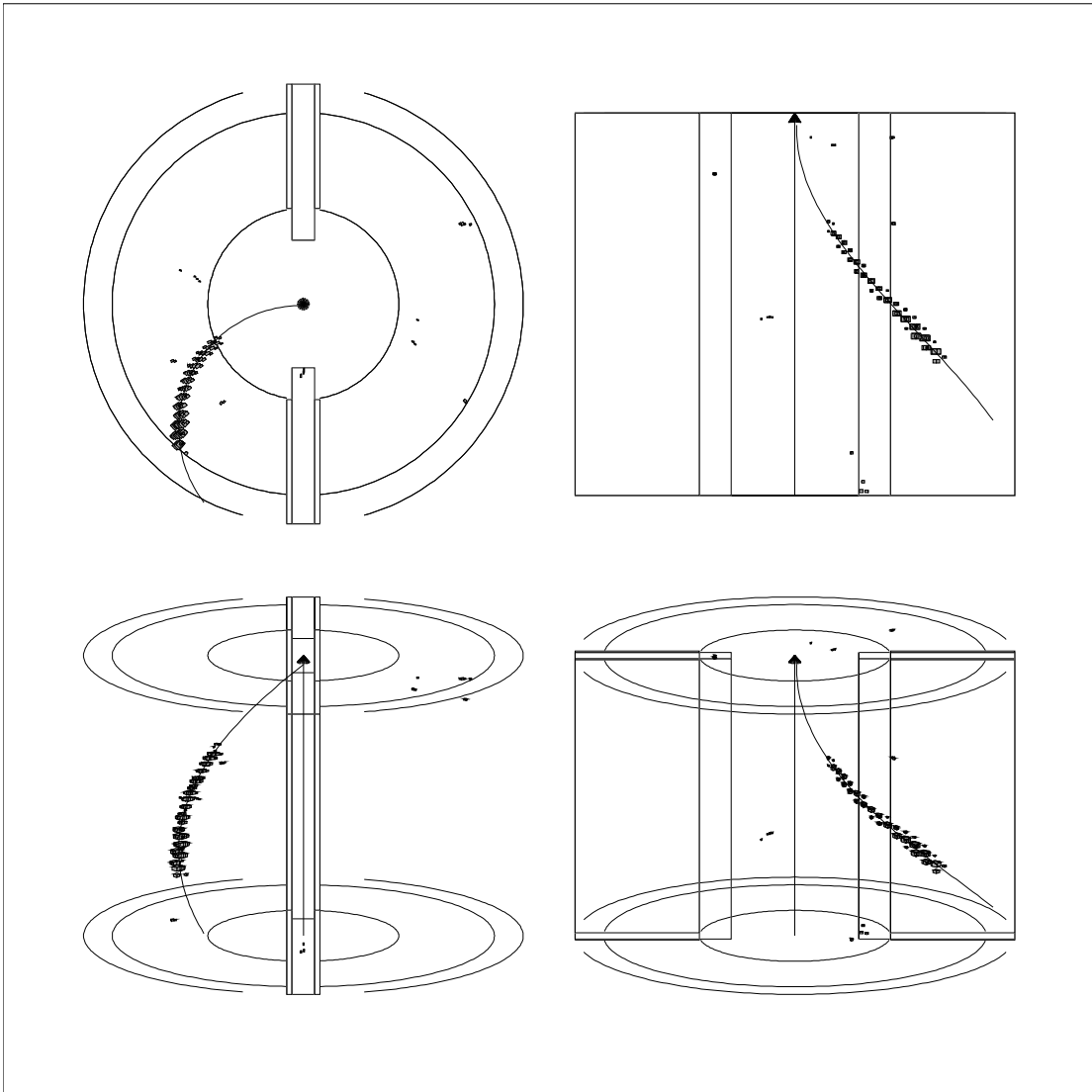


Figure 5.14: Online display of an ionization trail after properly reconstructing the locations of each hit in the tracking region. The box size for each hit is proportional to the pulse height. The four panels represent different views of the same event. The arrow in the center of the RTPC points in the direction of the electron beam.

given by the pad which registered the hit. The hits appear in the drift volume only and some spurious hits not forming a track cluster are visible. This illustrates the need for some pattern recognition software to locate charge clusters. The line drawn through the hits is the result of the helix fit described in Sec. 5.1.7. The particle appears to project back to the beam line close to the downstream end of the target.

### 5.1.6 Chain Linking

Pattern recognition software was developed to link together hits that are close to each other in space into a chain. The algorithm starts by using every possible hit in the TPC as the “seed” from which a possible chain may grow. These chains are fit to a helix if the number of links in the chain is longer than 10. The maximum total separation between two adjacent voxels is 8.3 mm. A voxel is defined as the complete volume that maps to one time interval for one pad. In the  $x - y$  plane the maximum separation between adjacent voxels is 2.28 mm. This occurs where the radial drift velocity is the fastest (near the cathode). Even though the arc length between two adjacent hits increases with radius, the slowing drift speed compensates for this and ends up reducing the distance between points. The maximum separation in the  $z - r$  plane is 8 mm and occurs at the first GEM.

Voxels are marked as adjacent to each other if their separation is less than 11.5 mm in order to jump possible gaps in the track that occur because of a dead preamplifier. This length was chosen rather loosely, but outliers from a track are removed at a later stage. Fig. 5.15 shows the regular peaks which occur every 5 mm from hits that are on the same pad row but not necessarily on the same track. A measurement of the number of RTPC tracks that have a similar vertex to the CLAS track ( $\Delta z$ ) was performed. The number of events that lie outside of the coincident peak (see the ratio in Fig. 5.16 labeled “outside/total”) appears to be dependent on the link separation. The separation cut was chosen as 11.5 mm because it does not significantly increase the level of spurious tracks (see Fig. 5.16) and, because it enables us to jump longer gaps from dead areas, it actually increases the number of VIP candidates. Increasing the cut any further clusters together too many hits that don’t really belong together and reduces the number of tracks that pass the quality cuts (described in Sec. 5.5).

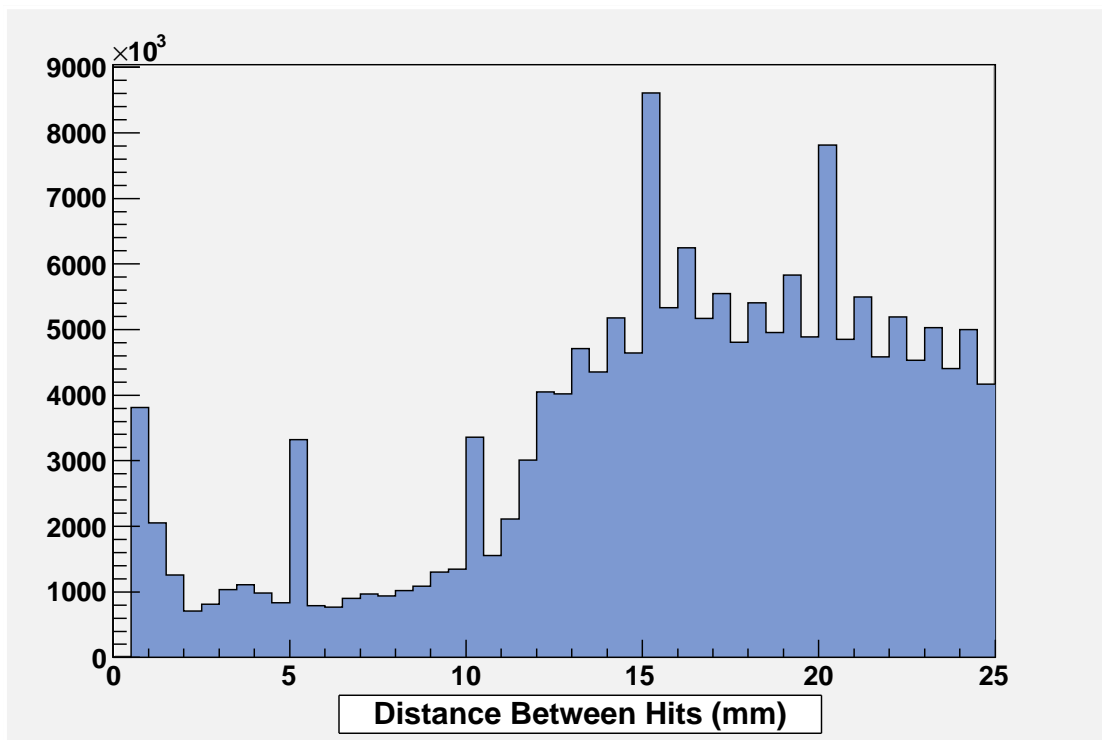


Figure 5.15: The distance that each point is separated from other link candidates. If two links are separated by less than 11.5 mm they are added to the same chain.

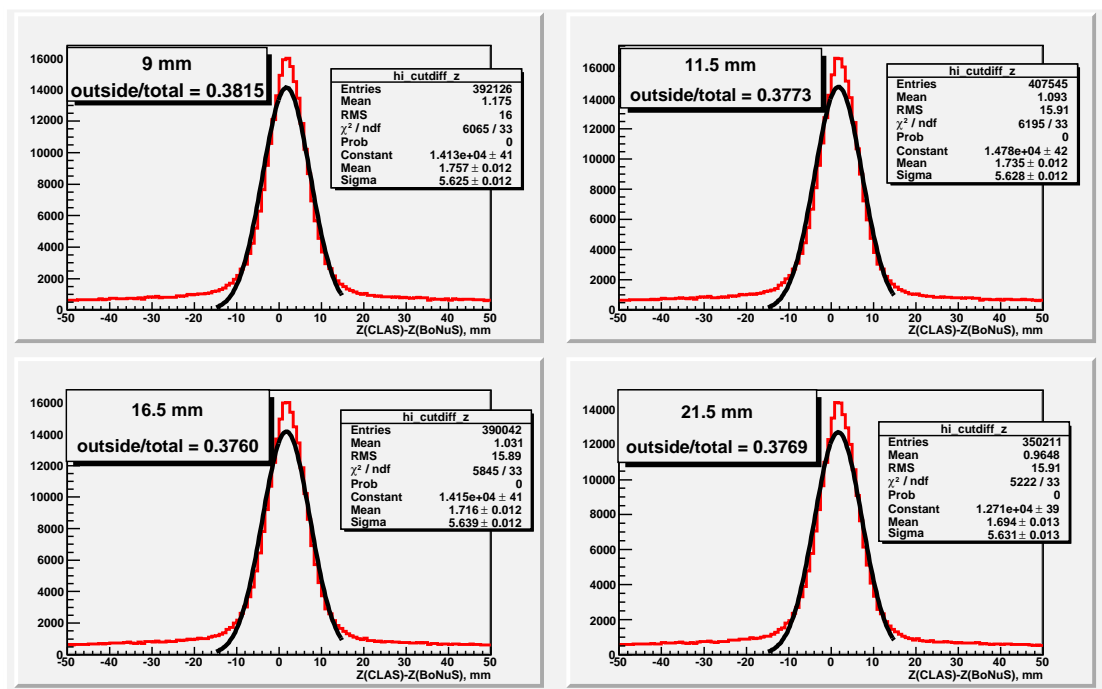


Figure 5.16: The difference between the RTPC particle's vertex and the CLAS electron vertex's ( $\Delta z$ 's) dependence on the chain link separation cut. Increasing the cut from 9 mm to 11.5 mm actually increases the proportion of events in the  $\Delta z$  peak region.

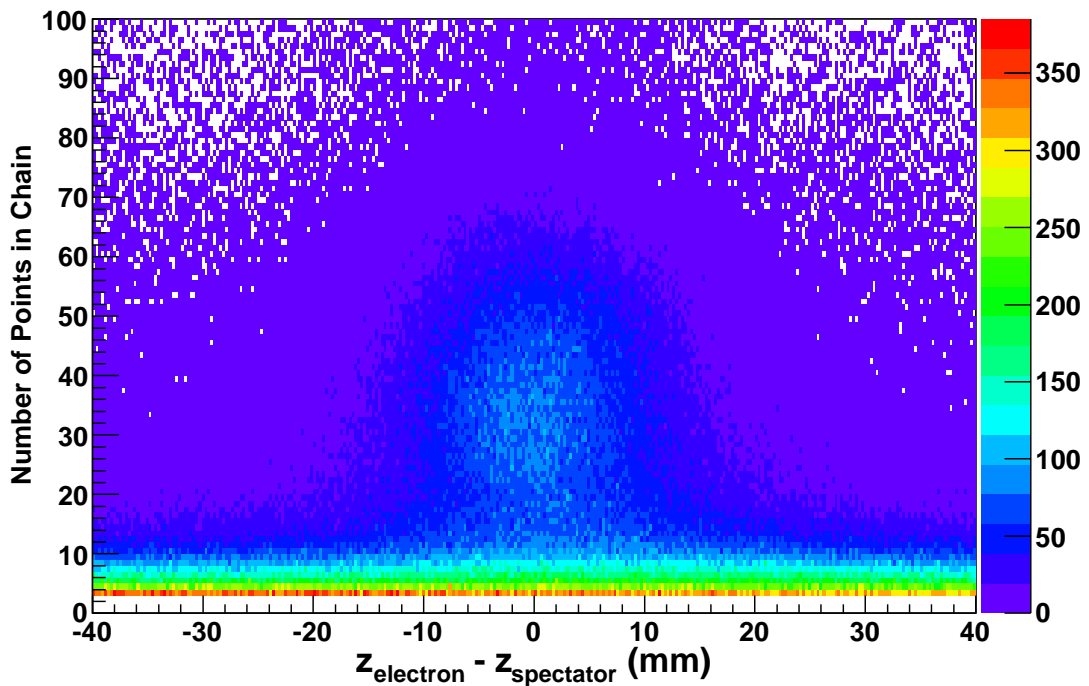


Figure 5.17: The number of points in a chain vs  $\Delta z$ . If the number of points is less than 10, no apparent correlation exists between the proton and electron  $z$  vertex.

### 5.1.7 Helix Fitting

Now that a pattern of hits is linked in a chain it can be fit to a helix. The criterion used to determine the minimum number of links is shown in Fig. 5.17. Below 10 links on a chain, there is virtually no correlation between the vertex of the trigger electron and the RTPC particle (no  $\Delta z$  peak at zero).

The helix fitting algorithm follows the prescription outlined in Ref. [56]. The first step is to fit a circle to the  $(x_i, y_i)$  coordinates of the chain's members

$$(x - a)^2 + (y - b)^2 = R^2,$$

where  $(a, b)$  is the location on the  $x - y$  plane of the circle's center and  $R$  is the radius of the circle that minimizes the mean square distance from the given points to this circle, thus

minimizing the functional

$$L(a, b, R) = \sum_{i=1}^n \rho_i^2, \quad (5.21)$$

where

$$\rho_i = \sqrt{(x - a)^2 + (y - b)^2} - R. \quad (5.22)$$

However the nonlinear dependence on  $\rho_i$  reduces the efficiency of applying the least squares method. A faster approach developed in Ref. [56] is to minimize the functional

$$K(a, b, R) = \sum_{i=1}^n \left( \frac{x_i^2 + y_i^2}{R} - 2\frac{a}{R}x_i - 2\frac{b}{R}y_i + \frac{a^2 + b^2 - R^2}{R} \right)^2. \quad (5.23)$$

We can find the normal equations by setting to zero the partial derivatives of Eq. 5.23 with respect to  $a, b, R$ :

$$\begin{aligned} Fa + Hb - a\gamma &= P, \\ Ha + Gb - b\gamma &= Q, \\ 2Pa + 2Qb + \gamma^2 &= T \end{aligned} \quad (5.24)$$

in which  $\gamma = R^2 - a^2 - b^2$ , which can later be used to find  $R$  when  $a$  and  $b$  are found. The coefficients of Eq. 5.24 are computed by summing various combinations of the  $(x, y)$  coordinates of the data points and their weights. The system of equations 5.24 can be manipulated to obtain a fourth degree polynomial in  $\gamma$  and solved via Newton's function minimization method. Once  $\gamma$  is obtained we can solve for  $a$  and  $b$  and find the distance of closest approach (DCA) to the beamline  $(x_{dca}, y_{dca})$ .

Each data point in the chain is assigned a weight according to its charge before the helix fit. The beam line point in the RTPC coordinate system  $(x, y) = (0, 0)$  is included in the first circle fit and is given a weight equal to the sum of the charge in the rest of the data points. The  $z$  coordinate of the beam line point is given zero weight so that it is not included in the subsequent line fit, described in the next paragraph.

The slope and  $z$ -intercept of a straight line fit to the points in  $s$ - $z$  ( $s$  given below by Eq. 5.25) space give the pitch ( $dz/ds$ ) of the helix and the  $z$ -coordinate of the point of closest approach to the beamline. The helix parameter  $s$  is defined as the distance from the DCA point to the point

$i$  along the projection of the circle on the  $x$ - $y$  plane. The DCA point is not necessarily the same as the interaction vertex point since the electron beamline does not lie directly on top of the RTPC's central axis. Let us transform to the coordinate system whose origin lies at the center of the circle and find the angles  $\alpha = \text{atan2}(y_{dca} - y_c, x_{dca} - x_c)$  and  $\beta_i = \text{atan2}(y_i - y_c, x_i - x_c)$ . The new  $x$  axis defines the position where  $\alpha = \beta_i = 0$  (see Fig. 5.18a). Now we compute the distance along the helix,  $s_i$ , according to

$$s_i = r_c(\beta_i - \alpha) \quad (5.25)$$

where  $(x_i, y_i)$ ,  $(x_c, y_c)$ , and  $(x_{dca}, y_{dca})$  are the cartesian coordinates of the data point, the center of the circle, and the DCA point, respectively. Here we must make use of the definition of the function  $\text{atan2}$ . For  $y \neq 0$ :

$$\text{atan2}(y, x) = \begin{cases} \varphi \cdot \text{sgn}(y) & x > 0 \\ \frac{\pi}{2} \cdot \text{sgn}(y) & x = 0 \\ (\pi - \varphi) \cdot \text{sgn}(y) & x < 0 \end{cases}$$

where  $\varphi$  is the angle in  $(0, \frac{\pi}{2})$  such that  $\tan(\varphi) = \left| \frac{y}{x} \right|$  and  $\text{sgn}$  is the sign function and:

$$\text{atan2}(0, x) = \begin{cases} 0 & x > 0 \\ \text{undefined} & x = 0 \\ \pi & x < 0 \end{cases}$$

This produces results in the range  $(-\pi, \pi)$ . We can then continue to fit a straight line in the  $s$ - $z$  plane to determine the pitch of the helix,  $dz/ds$  (Fig. 5.18b). The quantity in the parenthesis of Eq. 5.25 will be in the range  $(-2\pi, 2\pi)$ , depending on the particular quadrant of  $x$ - $y$  space that the points occupy. In order to make  $s_i$  represent the shortest arc around the circle to the given point, the following transformation is made: if the angle is  $< -\pi$ ,  $2\pi$  is added and if the angle is  $> \pi$ ,  $2\pi$  is subtracted. Clearly this will work if all points are on restricted to one half or the other of the circle, but breaks down when the cluster crosses the line at exactly  $180^\circ$  (see Fig. 5.18a). Luckily, this happens rarely for tracks which traverse the chamber volume from the

cathode to the first GEM. When it does occur we simply determine which point has the smallest absolute value of  $s$  and force all other points on the chain to have the same sign for  $s_i$ . This ensures that the track is not “broken” in  $s-z$  space and has the proper pitch. Also, for any good track, the point with the smallest  $s_i$  should have the largest drift time,  $t_{TDC}$ , and the smallest  $r$  coordinate.

After the full helix has been fit to the points, we calculate the residual of each point as the distance between the point’s center and the closest point to the hit on the helix. Hits that are on the chain but more than 5 mm away from the helix are removed (up to 4 points) and a new helix is fit to the chain without the outliers. The distribution of hit residuals after the first helix fit is shown in Fig. 5.19.

Since all tracks are forced to come from the apparent beam line, it is very important to have the  $(x, y)$  coordinate of the beam at a given  $z$  correct if we are to properly measure the track’s momentum from curvature. When the first pass of circle fitting is performed, the beam line is assumed to coincide with the origin. Once we have an estimation of the  $z$  vertex position, the real  $(x, y)_{beam}$  coordinates of the beam can be found using the results in Fig. 5.20 where  $y_{beam} = y_0 + b(z + 590)$  mm and  $x_{beam} = x_0 + a(z + 590)$  mm. These beam position fits and the subroutine which returns the position of the beam as a function of  $z$  are courtesy of J. Zhang. The technique uses the geometry found in Fig. 5.21 from elastic events to find the interaction point. The  $z$ -vertex,  $\theta$  and  $\phi$  of the elastic proton and electron measured in CLAS can be used with the equations in Fig. 5.21 to pinpoint the actual path of the beam through the target. Each parameter in the line fit is a function of the run number; the  $z$  offset of 590 mm just transforms from the CLAS coordinate system to the BoNuS system.

### 5.1.8 Track Parameters

The subroutine that performs the helix fit returns five parameters ( $\Delta_i$ ) which we subsequently convert into the track parameters. The first element of the returned data array is  $\Delta_1 = 1/rQ$  where  $r$  is the radius of curvature in the  $x-y$  plane and  $Q$  is the charge. The charge is positive (negative) if, when looking in the direction of the beam, the particle travels in a clockwise (counter-clockwise) direction around the helix. The next element is  $\Delta_2 = \tan \lambda = dz/ds$  where  $\lambda$  is the angle relative to the  $x-y$  plane or the pitch. The third element is an angle,  $\Delta_3 = \phi_0$ ,

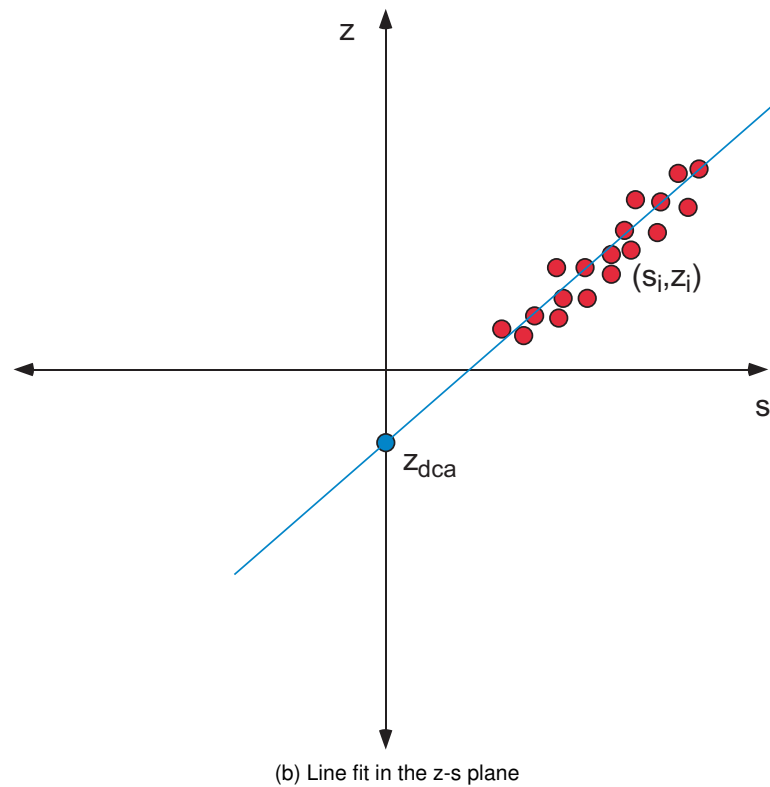
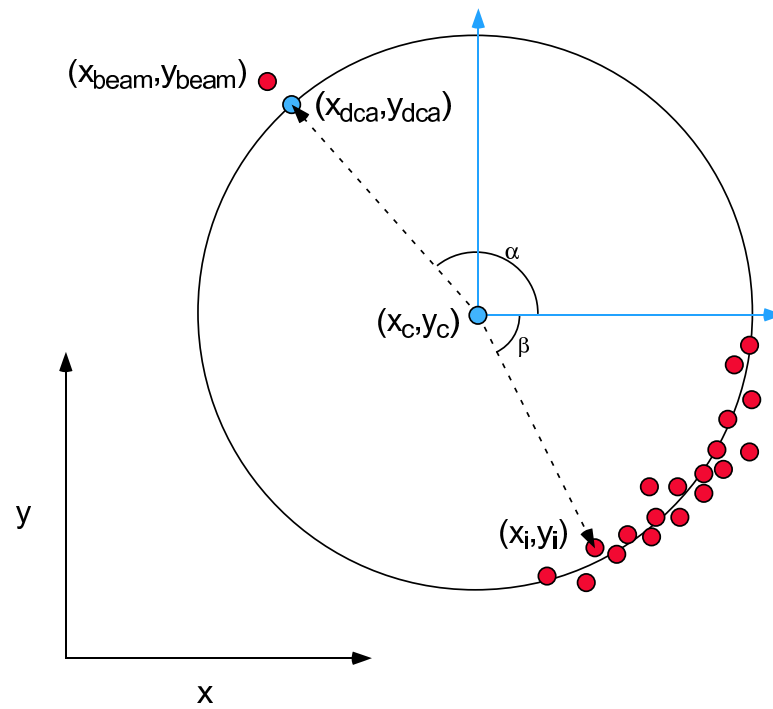


Figure 5.18: Track fits in two different coordinate spaces which, taken together, make up the helical track.

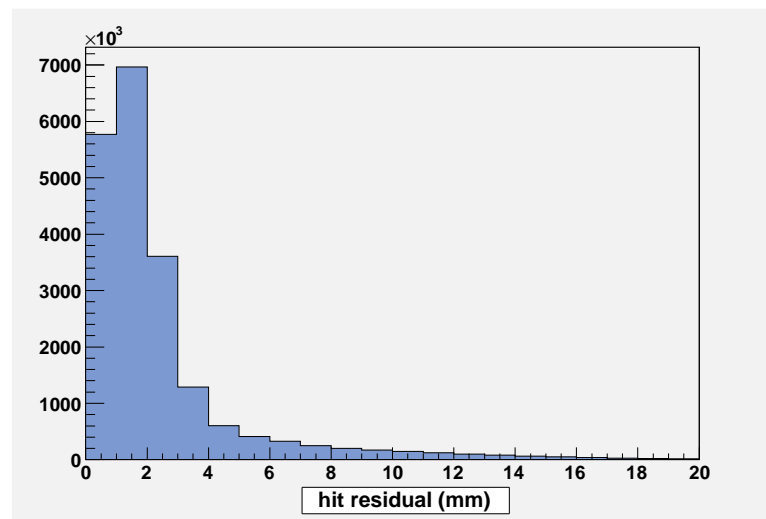


Figure 5.19: Hit Residuals after initial helix fit. Hits with residuals  $> 5$  mm are removed from the chain before refitting.

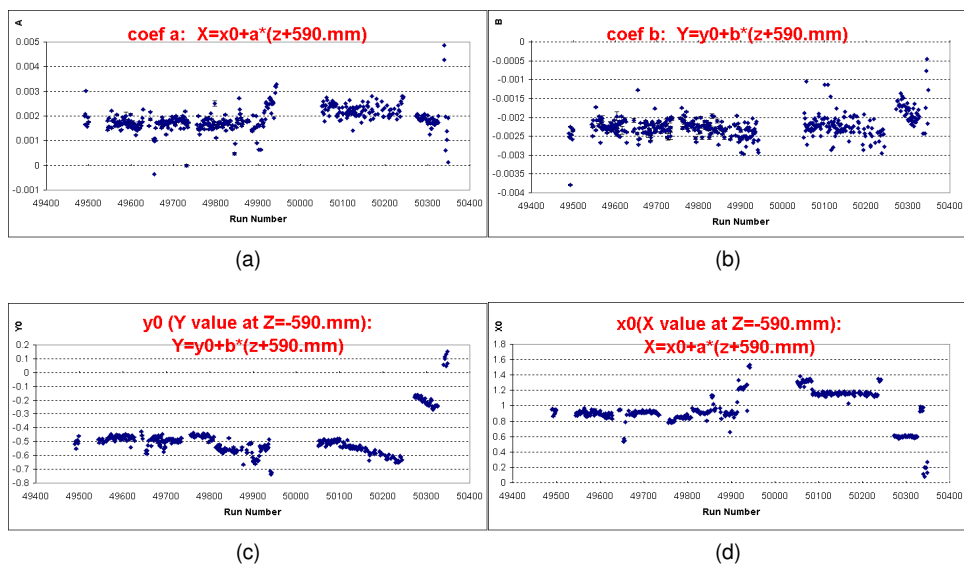


Figure 5.20: The slope and offset of the beam position as a function of run number. The vertical axis values for the offsets  $(x_0, y_0)$  are in mm. The quantity plotted in each panel is described by the text in red.

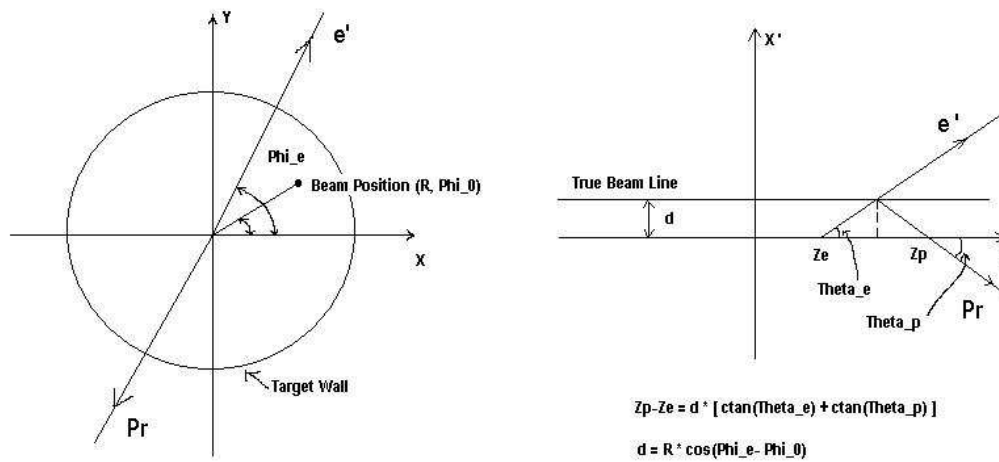


Illustration of Beam Position correction using  $e + p \rightarrow e' + p'$  elastic events (or any 2 tracks)

Figure 5.21: Kinematics for finding the CLAS beamline using elastic  $ep$  events. This is the technique devised by P. Bosted and implemented for this experiment by J. Zhang.

which represents the angle with respect to the  $x$ -axis at the position of closest approach to the  $z$ -axis. Next,  $\Delta_4 = d_0 \cdot \text{sign}$ , is the minimal distance to the  $z$ -axis multiplied by the sign ( $\pm 1$ ) that depends on whether or not the axis is encircled. And finally,  $\Delta_5 = z_{dca}$  is the  $z$  position at  $r = d_0$  and we mark this point as the  $z$  vertex point.

Conversion of the helix fit return values into track parameters represented in the RTPC coordinate system is necessary. The specific parameters that we extract directly from the helix fit values are  $\theta, \phi, r, x_0, y_0, x_{dca}, y_{dca}, z_{dca}$ :

$$\begin{aligned}
\theta &= \frac{\pi}{2} - \arctan \Delta_2 \\
\phi &= \Delta_3 \\
r &= -1/\Delta_1 \\
x_0 &= -(-\Delta_4 + |r|) \sin \phi \\
y_0 &= (-\Delta_4 + |r|) \cos \phi \\
x_{dca} &= (\Delta_4) \sin \phi \\
y_{dca} &= (-\Delta_4) \cos \phi \\
z_{dca} &= \Delta_5
\end{aligned} \tag{5.26}$$

Now, armed with these values for a track, we can find  $p_{perp} = (0.3)(B_z)(r)$ , which gives momentum in MeV/c as long as  $B_z$  is in Tesla and  $r$  is in meters and  $p_{para} = p_{perp}/\tan\theta$ . The value of  $B_z$  that we use is an average over the values of  $B_z$  that the particle encounters as it traverses the range in  $z$  from the initial hit on the track to the last hit.

The goodness of fit,  $\chi^2$ , of the track is given by,

$$\chi^2 = \frac{\sum_{i=1}^{N_{pts}} \frac{(r_i^{pt} - r_i^{helix})^2}{\sigma_r^2} + \frac{(\phi_i^{pt} - \phi_i^{helix})^2}{\sigma_\phi^2} + \frac{(z_i^{pt} - z_i^{helix})^2}{\sigma_z^2}}{N_{pts} - 4}, \tag{5.27}$$

where  $N_{pts}$  is the number of points in the chain,  $(r, \phi, z)_i^{pt}$  are the  $i^{th}$  point's cylindrical coordinates,  $(r, \phi, z)_i^{helix}$  are the cylindrical coordinates of the point on the helix closest to the  $i^{th}$  point,  $\sigma_{r,\phi,z}$  are the observed resolutions from *rms* variations for points fitted to a helix and they are found experimentally to be  $\sigma_r = 0.53$  mm,  $\sigma_\phi = 0.025$  radians, and  $\sigma_z = 1.2$  mm.

Two more important track parameters related to the timing are also calculated at this juncture. These quantities are known in the nomenclature of this experiment as the end distance (*edist*) and the start distance (*sdist*) of the visible track. The *sdist* (*edist*) is the length along the helix from the first (last) visible charge on the track to the closest intersection of the helix to a chamber boundary. For a typical good track which enters the drift volume at the cathode and exits at the first GEM, the *sdist* (*edist*) is the distance from the hit on the track with the smallest

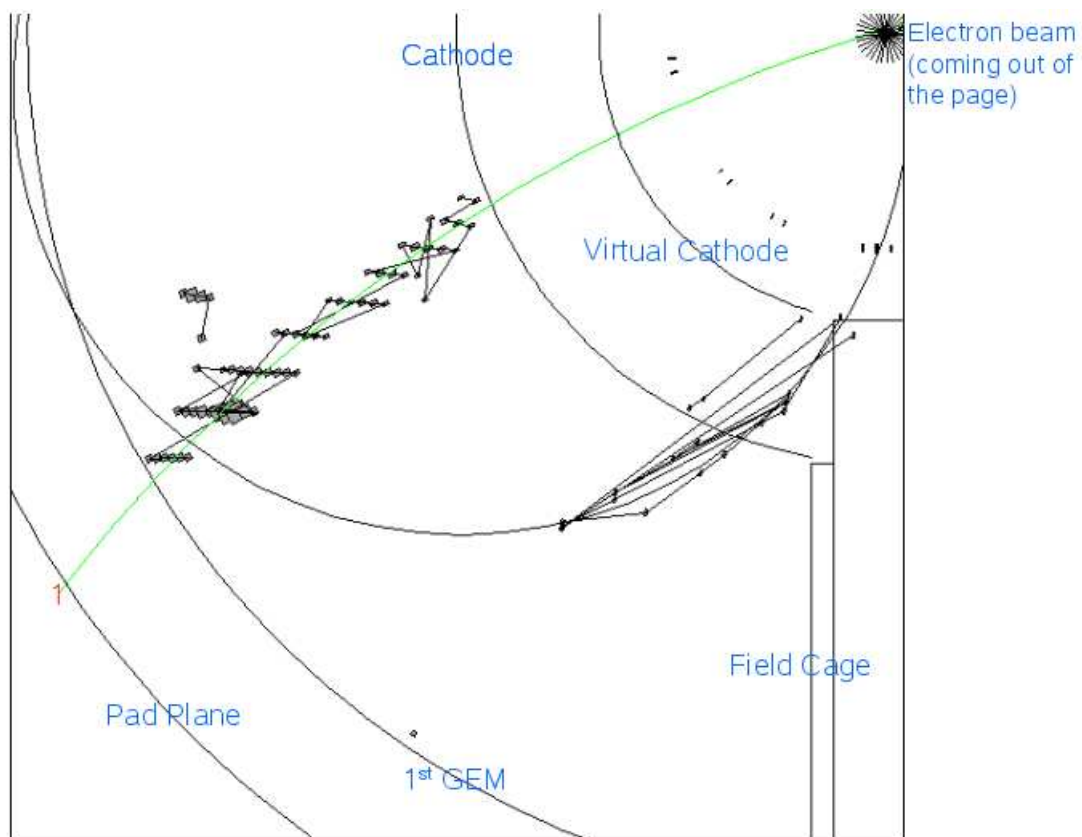


Figure 5.22: A typical “in-time” RTPC track seen looking upstream. The last and first visible charges in the track chain are projected very near the first GEM and the cathode. The green line is a helix fit to the chain. The lines drawn between each box indicate links on the same chain. The target cell is in the upper right corner. Some out-of-time charge can be seen projected in the space between the virtual and real cathode locations (helix fit in black) but this track will fail the *sdist* and *edist* cuts.

(largest)  $r$  to the cathode (first GEM). A negative value for *edist* or *sdist* indicates that the last or first charge lies outside of the physical chamber boundaries. An example of an “in-time” track and an “out-of-time” track occurring in the same event window can be seen in Fig. 5.22.

## 5.2 RTPC Calibration

### 5.2.1 Electron Drift Velocity

The RTPC analyzer uses the model of the electron drift paths described in Sec. 5.1.3 to project the location in space at which each observed hit originated. Despite our best efforts to simulate

and parameterize the paths on which drift electrons travel, a drift velocity calibration was still necessary. One difference between the simulation and reality stems from the failure of the RTPC's computer-controlled gas handling system. This failure led to a large uncertainty in the ratio of helium to DME in the drift volume. The RTPC expert on shift was tasked with regulating the flow from the bottles manually every half hour, keeping the rates at He/DME = 320/80 scfh. These values could easily deviate as much as 10 scfh during each 30 minute increment, depending on the environmental variables of any given day.

The calibration constants that we have available to us are the He/DME ratio, the voltage settings on the power supplies that regulate the left and right cathode and GEM circuits, the overall  $\phi$  rotation of the left and right chamber halves, the ALTRO start time  $T_0$ , and the  $(x,y)$  location of the center of the RTPC. The overall  $\phi$  rotation can compensate for errors in the  $\phi$  offset functions. Kirchoff's circuit laws are used to calculate the actual electric fields between the drift, transfer and induction gaps (see Sec. 4.1.5). As you can see from Eq. 4.1 the actual potential difference between the inside of the first GEM and ground is dependent on the voltage setting of the power supply that regulates the drift field, as well as its own power supply. Therefore, during the calibration procedure, only voltage on the drift circuit was varied to account for uncertainties in the resistor values.

The  $\phi_{off}$  and  $t_{off}$  offsets in the data (see Sec. 5.1.4) are accounted for by allowing the ALTRO start time and the overall  $\phi$  rotation to be variable during the calibration. The final calibration constants are the  $(x,y)$  coordinate of the center of the RTPC in CLAS coordinates. Tracks *should* originate from the beamline, therefore the  $\phi$  measurement of a track in BoNuS is very sensitive to the presumed location of the interaction point. Using the set of  $\phi$  measurements from BoNuS and the corresponding results from the CLAS track fits, one can figure out the relative displacement of the CLAS and BoNuS axes. This position does not effect the drift paths directly but it does have a major impact on the helix fit to the RTPC tracks since the beamline point is included on the track.

The trajectory of an identified electron measured in the CLAS drift chambers can be compared with the corresponding electron's ionization trail in the RTPC, if the RTPC gain is increased so that the detector becomes reasonably efficient for minimum ionizing particles. A comparison of the observed and predicted hit locations indicates that CLAS and BoNuS are not consistently calibrated for tracking using the unperturbed RTPC drift electron paths from

the previous sections. The final part of the BoNuS run period consisted of calibration data taken with electrons which only took a single pass around the accelerator. For these calibration runs, the GEM and cathode circuits on both sides of the RTPC had their high voltage increased by 400V so that the chamber would be sensitive to higher momentum and minimum ionizing tracks. The optimal drift velocity parameters are found by matching the trigger electron in CLAS with a track in the RTPC. The 1 GeV beam energy was chosen for this study because it is absolutely crucial that the production vertex and momentum vector of the electron are both well-measured by CLAS. The uncertainty on the measured electron momentum,  $\sigma_p$ , and vertex,  $\sigma_z$ , are proportional to beam energy, and the 1 GeV electron data are the easiest to calibrate (and require the smallest electron momentum corrections). This direct comparison can only be accomplished during the high-gain calibration runs, but one hopes that the extracted calibration constants can be applied to normal runs as well. The detailed procedure follows.

After finalizing the CLAS calibration, a list was compiled of electrons that are candidates to leave a track in the RTPC. The CLAS global event ID was used to match these candidates with tracks in the RTPC. Even with the increase in high voltage, a matching track was not seen 100% of the time due to the persistent inefficiency in measuring minimum ionizing tracks with high momentum. The  $(x, y, z)$  coordinate of each point on the electron track was calculated in steps of 0.1 mm as the particle was swum through the magnetic field. The path was determined from the interaction vertex in the target through the entire mass of the RTPC, however electron energy lost in the material could be neglected.

Each RTPC track's reconstructed parameters ( $z_{vtx}$ ,  $\theta$ , and  $\phi$ ), starting with our default calibration values, were compared to the CLAS track. If they passed our "similarity cuts" ( $|d\phi|$  and  $|d\theta| < 20^\circ$ ,  $|dz| < 15$  mm), then the CLAS track was anchored so that its  $z$ -intercept with the inside of the first GEM matched the  $z$  of the outermost hit in BoNuS. There is less uncertainty in the drift velocity at large  $r$  so we forced the tracks to match at the first GEM. The CLAS track's path was used to determine on which pad and at what time the charges should have shown up in the RTPC. The CLAS track can be seen in Figs. 5.23a and 5.23b in black, overlaid on the hits from the RTPC. The CLAS track is translated in  $z$  so that the last registered hit on the RTPC track matches the predicted position from the translated track (the new CLAS track is indicated as a red dotted line in Fig. 5.23b). The pad number and time bin of the registered hit and the  $\phi$  and  $r$  of the swum track is recorded. A separate software package written by H. Fenker used

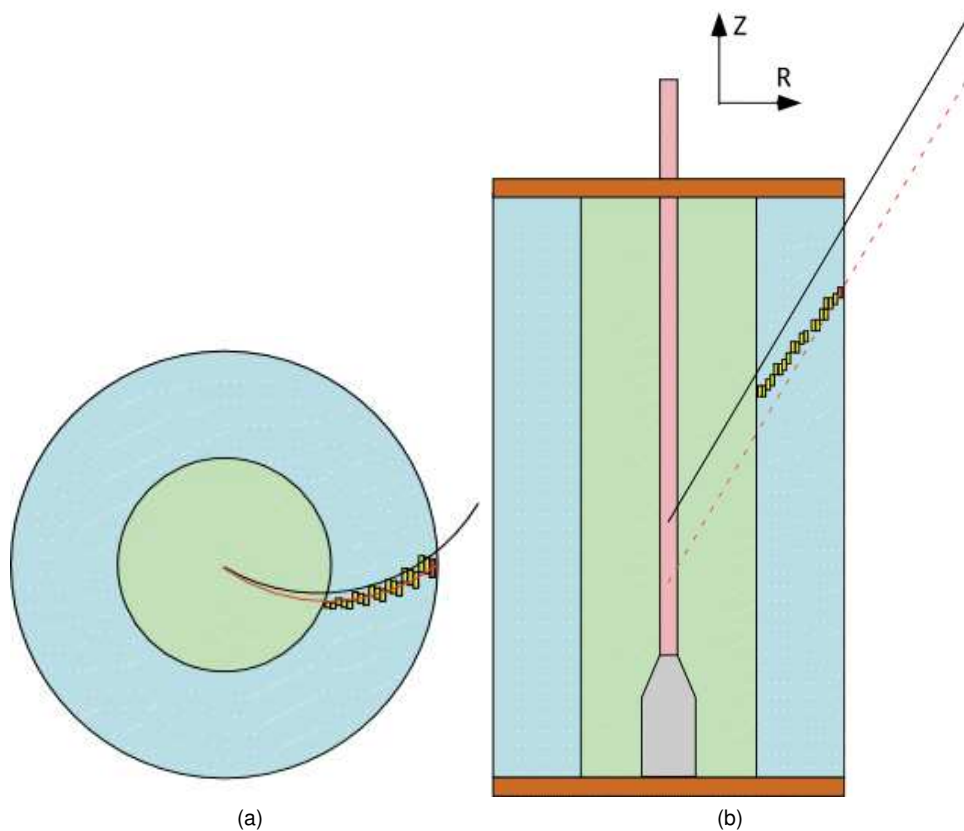


Figure 5.23: Comparing the reconstructed RTPC hit positions to the CLAS electron track's path.

the predicted hit locations together with MINUIT to manipulate the path parameters in order to minimize the sum over hits of the square of the distance from the CLAS-projected hit position minus the hit position obtained from the MAGBOLTZ paths. The width of this distribution was used in order to reject the outliers. The path generator in the minimization routines uses the same code as found in the BoNuS analyzer. The set of calibration constants which best matched the reconstructed RTPC hits to the predicted hit positions from the CLAS track were then applied to the entire data set.

Figs. 5.24, 5.25, 5.26, 5.27, and 5.28 show how well the resulting key track parameters  $z$ ,  $\theta$ ,  $\phi$ ,  $edist$ , and  $sdist$  match with the CLAS predicted paths before and after the drift velocity

calibrations. The final set of drift velocity calibration constants are as follows:

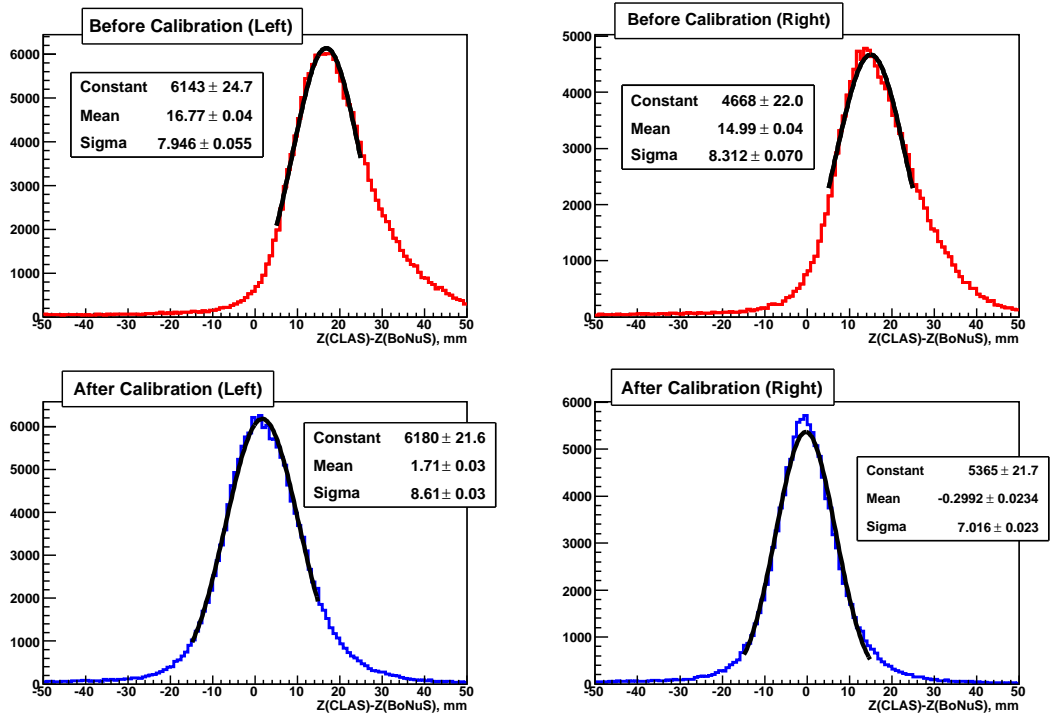
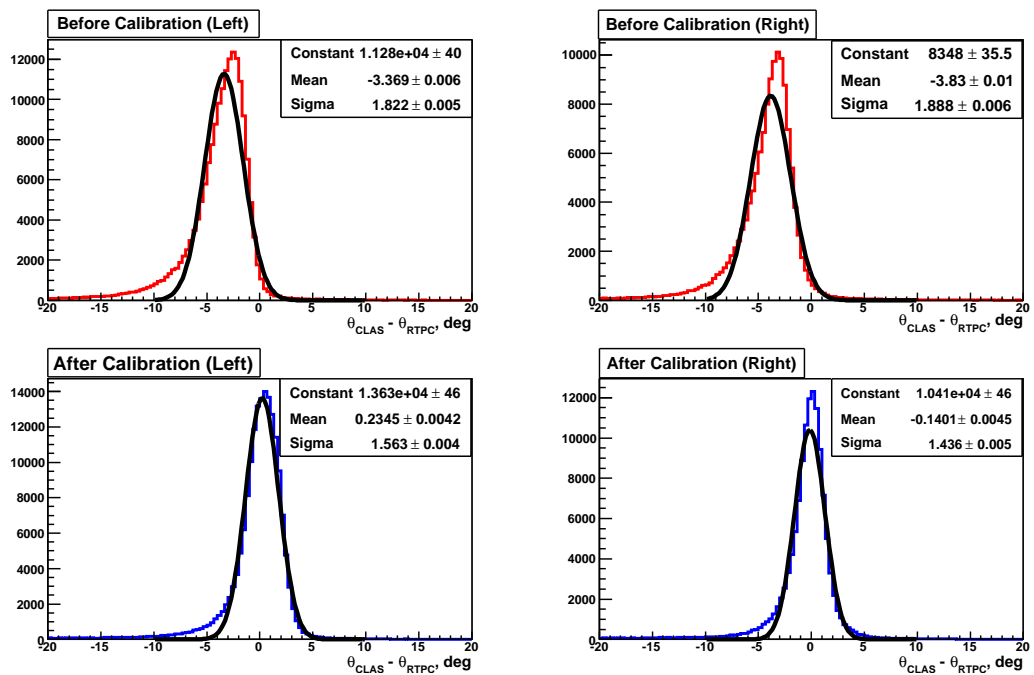
$$\begin{aligned}
 \%He &= 83.25\% \\
 \Delta_{VKL} &= -203.6 \text{ V} \\
 \Delta_{VKR} &= -196.1 \text{ V} \\
 \phi_{off}^L &= -0.0189 \text{ rad} \\
 \phi_{off}^R &= 0.0235 \text{ rad} \\
 T_0 &= 10.95 \text{ bins} \\
 x_B &= -0.197 \text{ mm} \\
 y_B &= -0.059 \text{ mm}
 \end{aligned}$$

Here %He is the percentage of helium to use in the drift electron path functions that generate tracks,  $\Delta_{VKL, VKR}$  are the amounts to change the power supply voltage settings on the left and right cathodes,  $\phi_{off}^{L,R}$  are the amounts of overall azimuthal rotation for the left and right chamber halves,  $T_0$  is the (now variable) ALTRO start time, and  $(x_B, y_B)$  is the offset of the center of the RTPC with respect to the ideal CLAS central axis.

### 5.2.2 Channel by Channel Gain Parameters

The main goal of the BoNuS experiment was to use the RTPC to identify spectator protons. However several kinds of particles make tracks with heavy ionization trails in the RTPC. We are forced to make a particle identification based on  $dE/dx$ , the amount of energy the particle loses to the drift gas per unit distance traversed. We were not sensitive, in production running, to particles with minimum ionization trails because the high voltage was turned down far enough that they would not make a dense enough ionization trail to be linked together for the tracking algorithm. The proton has the smallest mass of all particles that could make a dense track therefore particles with  $A > 1$  produce good tracks as well. As a consequence, we observe tracks from deuterons, tritons,  $^3\text{He}$ , and  $^4\text{He}$  from target contamination, FSI, and knockout of nuclei from the buffer gas.

Fig. 5.29 shows the raw distribution of  $dQ/dx$  vs.  $p/z$  where  $z$  is the charge of the nucleus. The measured quantity  $dQ/dx$  is the sum of the pulse-heights of all of the hits included on a

Figure 5.24: Comparing  $\Delta z$  before and after RTPC drift velocity calibrations.Figure 5.25: Comparing  $\Delta\theta$  before and after RTPC drift velocity calibrations.

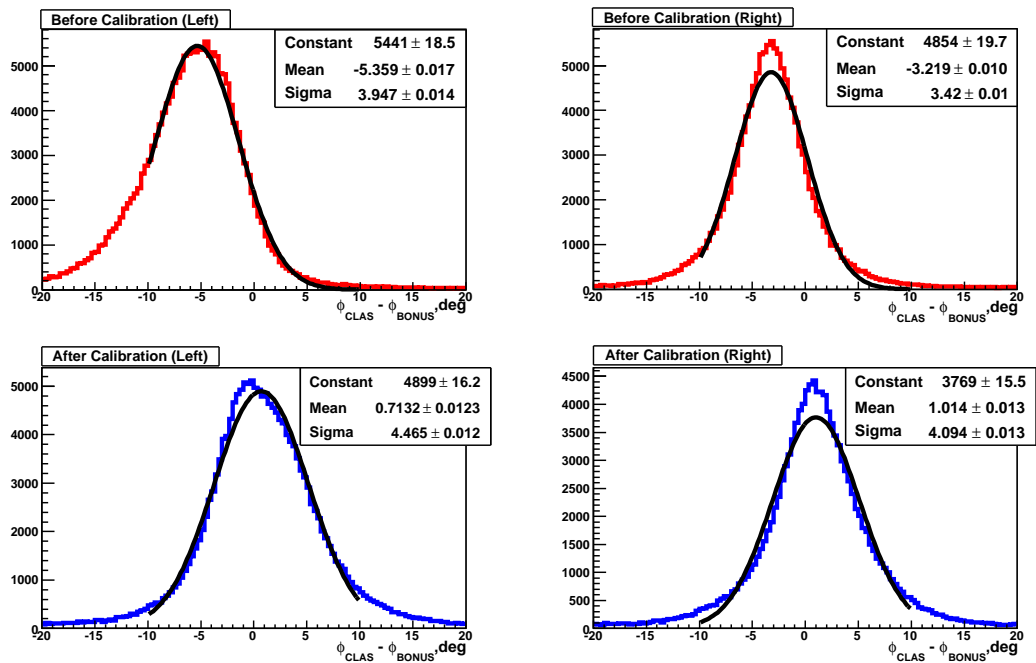


Figure 5.26: Comparing  $\Delta\phi$  before and after RTPC drift velocity calibrations.

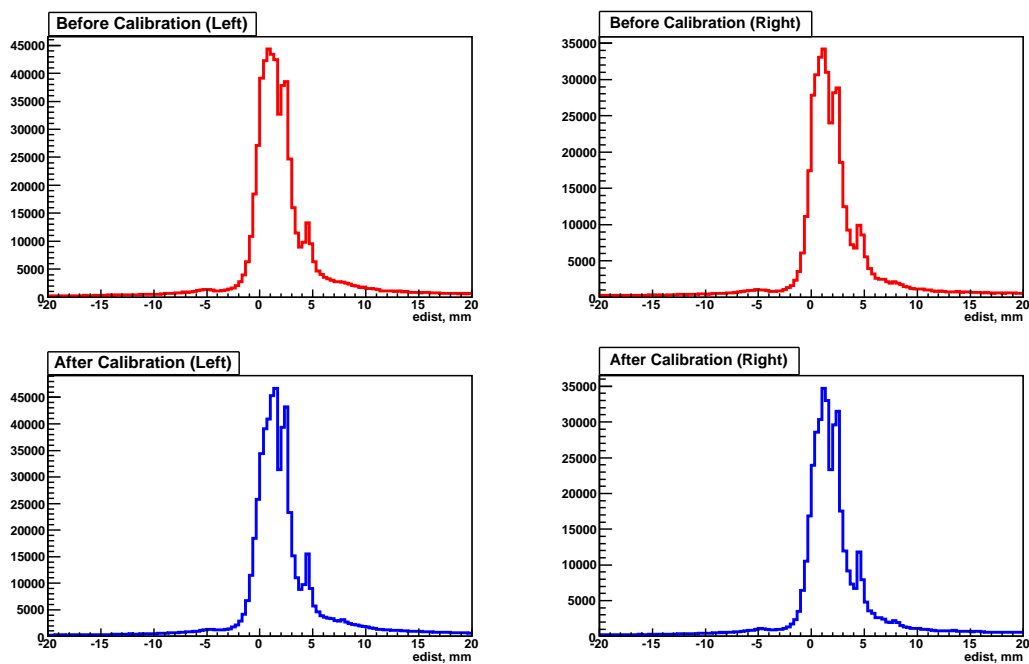


Figure 5.27: Comparing *edist* before and after RTPC drift velocity calibrations.

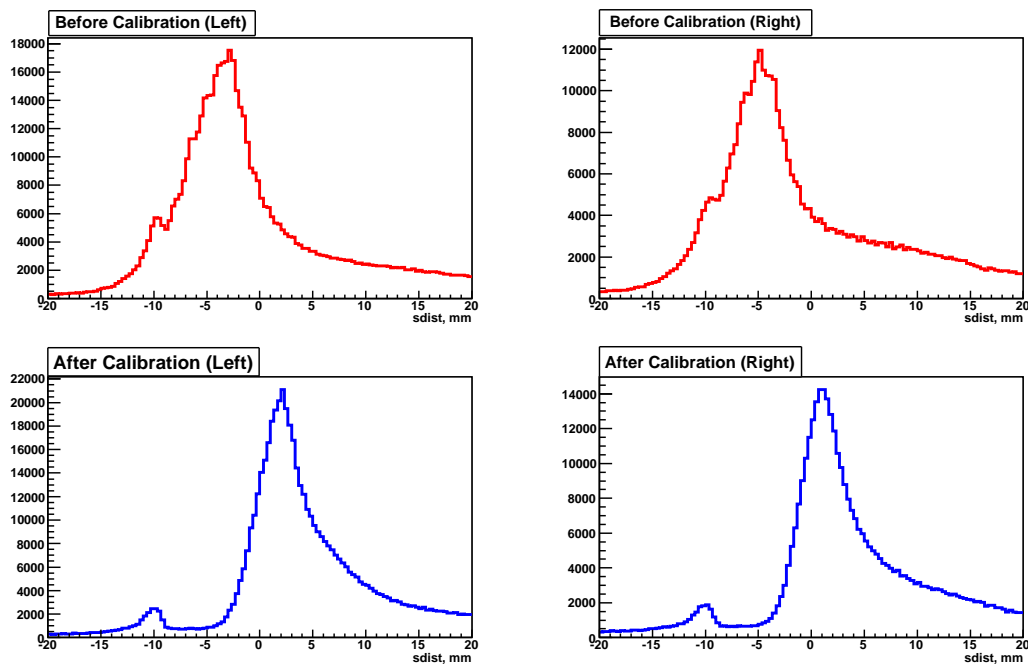


Figure 5.28: Comparing  $sdist$  before and after RTPC drift velocity calibrations. The hump at -10 mm comes from late tracks.

track divided by the visible length of the track (distance along a helix from first hit to last hit). Since the electric charge of the particle cannot be known a priori,  $p/z$  is the momentum from curvature of the track determined from a helix which was fit to the hit cluster and the beamline point. There is no clear band in the figure surrounding any of the Bethe-Bloch curves for the different species.

Two things can confuse our extraction of meaningful energy loss information — the electronic response of each channel (this was found to not vary by more than 10% from channel to channel) and the non-uniform gain over the surface of the GEMs. The overall gain varies quite a bit over the surface of the detector, despite the relative stability of the electronics channels, perhaps due to the GEM gain variations across different regions because of wrinkles, local flux of ionization electrons contributing to some rate-dependent effect, or some non-uniformity produced by the GEM structure itself. Given our time/man-power constraints, we lacked any reliable external gain calibration system such as a laser fired in the drift gas, parallel to the RTPC central axis, that could scan the azimuth and would have enabled a simple gain and drift

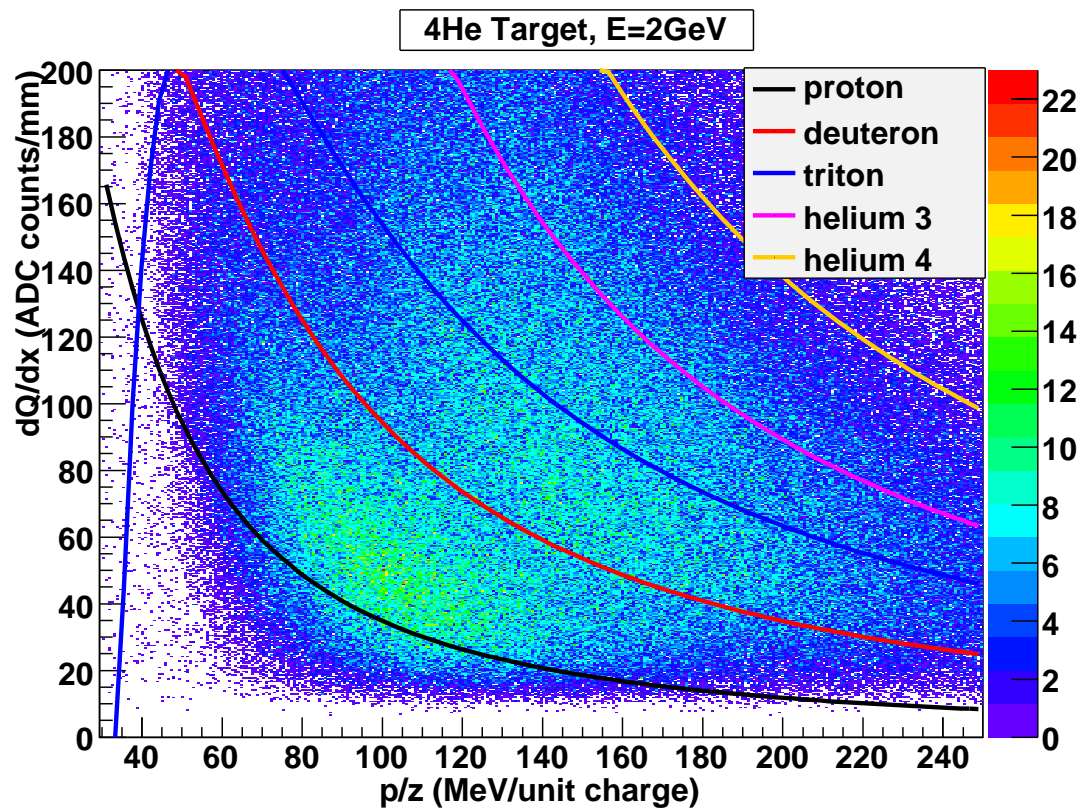


Figure 5.29:  $dQ/dx$  vs.  $p/z$  before RTPC gain calibrations. The lines represent the predictions from the Bethe-Bloch equation for different particles.

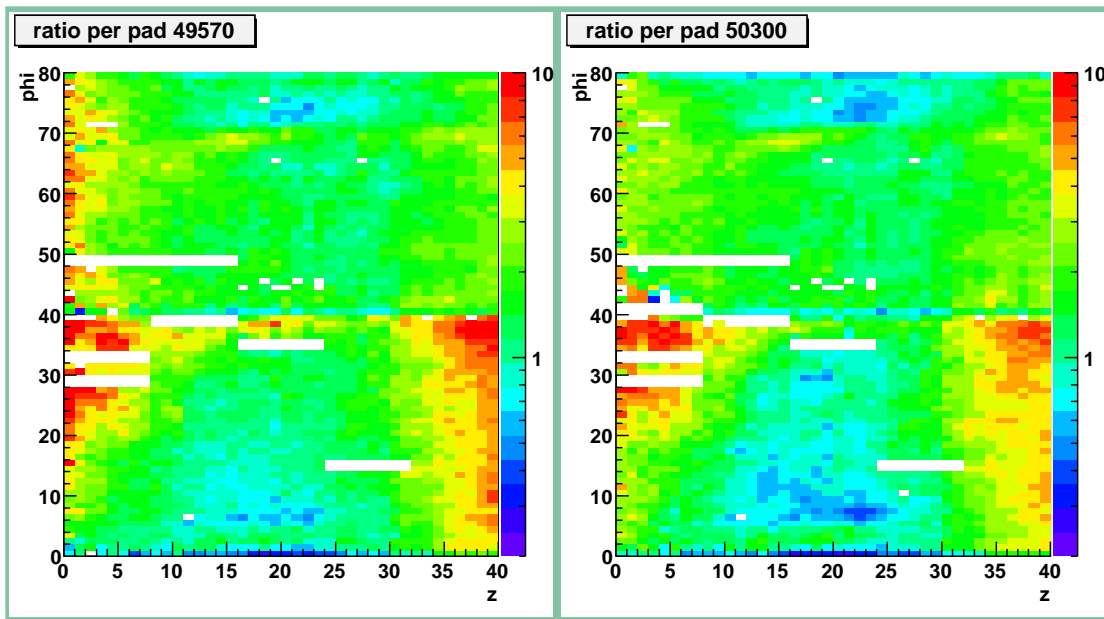


Figure 5.30: The gain calibration constants for every pad determined independently in two separate data runs. Each box represents one pad and white boxes indicate dead or manually turned off preamplifiers. The  $z$  and  $\phi$  coordinates are in channel number. The top half is the right side of the RTPC and the bottom half is the left side.

velocity calibration. Instead, a procedure was developed by H. Fenker [57] to use heavily ionizing tracks to self-calibrate the detector. After a final drift velocity calibration was determined from the technique in the previous section, track segments were projected onto the readout pad surface. Only pads that subtend more than 2 mm of track length were used. The amount of charge on each pad was compared with the prediction of  $dE/dx$  from the Bethe-Bloch [5] formula. This yields a set of scale factors, one per channel. The channel-by-channel gain factor determination goes through another iteration that excludes any tracks whose  $dE/dx$  is inconsistent with protons, giving us a set of gain factors optimized for the identification of protons. The two plots in Fig. 5.30 show the values of the gain scale factors for two different runs. The white rectangular sections are pads that are dead or have been turned off because the signals were oscillating wildly (hot pads). Each pixel in the plot corresponds to one readout pad. Clearly significant variations exist in the Triple-GEM gains, possibly caused by the aforementioned irregularities.

The gain calibration factors presented below come from repeated analysis of the same

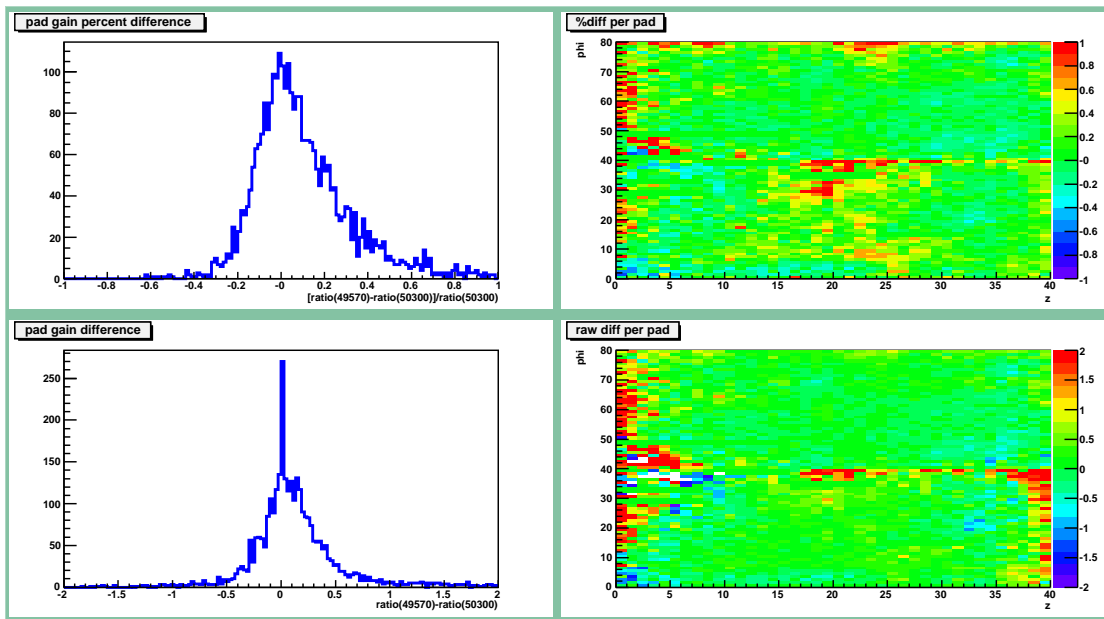


Figure 5.31: The difference in gain calibration constants between the same two runs as in Fig. 5.30. Each box in the right column represents the fractional difference between the two runs for every pad (top) and the absolute difference (bottom). The left column shows a distribution of the values in the right column as a 1-D histogram. The  $z$  and  $\phi$  coordinates are in channel number. The top half is the right side of the RTPC and the bottom half is the left side.

data file. Fig. 5.31 proves that this is a legitimate practice. It shows a comparison, channel-by-channel, of the results obtained from the two independent set of data in Fig. 5.30. These two data sets come from vastly different run conditions. They were taken 2 months apart, have different beam energies, and differing numbers of high mass particles tracked in the RTPC. The similarity of the results is evidence that the gain correction factors can be applied successfully to data sets other than the one used to obtain them. The variation near the edges is most likely due to less frequent use of these pads in useful tracks (see Fig. 5.32, for example).

The result of the final application of the gain correction factors can be seen in Fig. 5.33 for the same group of helium target runs shown in Fig. 5.29. Now clear bands surround the predictions for the proton, triton and deuteron with a lingering shadow below the  $^3\text{He}$  and  $^4\text{He}$  lines. Fig. 5.34 depicts the same BB plot for the deuterium target runs taken during the highest energy run period ( $E_{beam} = 5.262$  GeV). Only the proton band is visible and it is somewhat wider than the same band in the smaller sample of helium runs. This fluctuation in width will be addressed in Sec. 5.5.3.

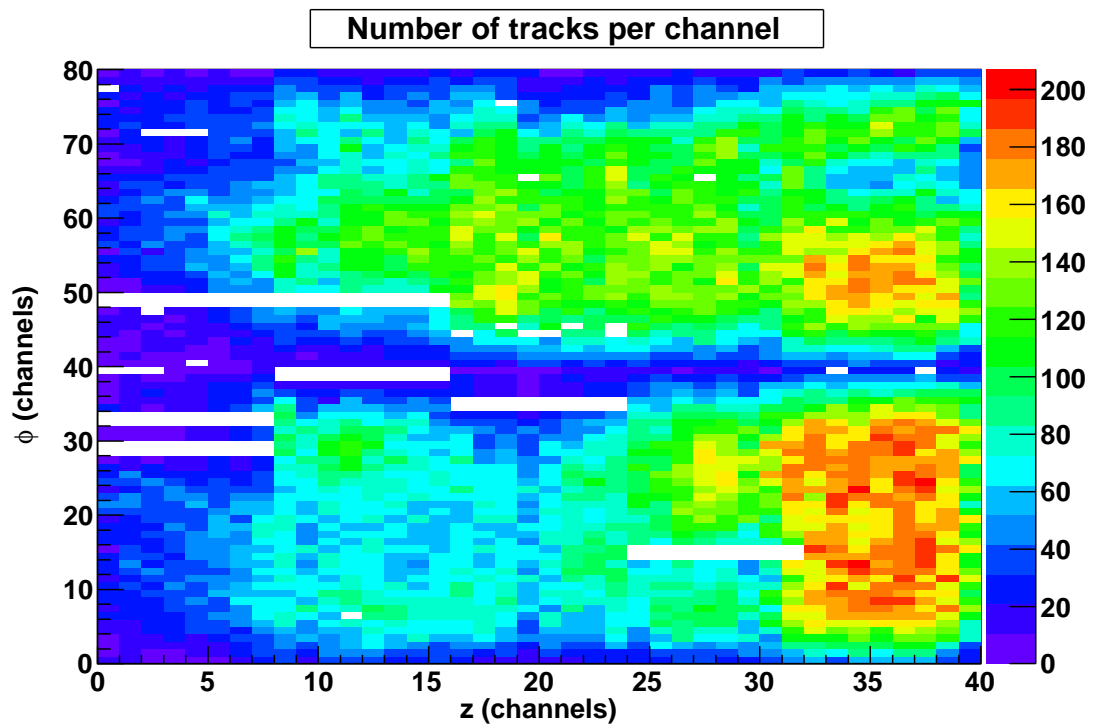


Figure 5.32: The number of times a given pad was used on a track in a typical run. The  $z$  and  $\phi$  coordinates are in channel number. The top half is the right side of the RTPC and the bottom half is the left side. The cold regions correspond to the location of the upstream aluminum target shroud. The apparent hot region in the lower right hand corner is probably due to a non-uniformity in the GEM gain increasing the likelihood that a given pad will have a signal not necessarily associated with the track.

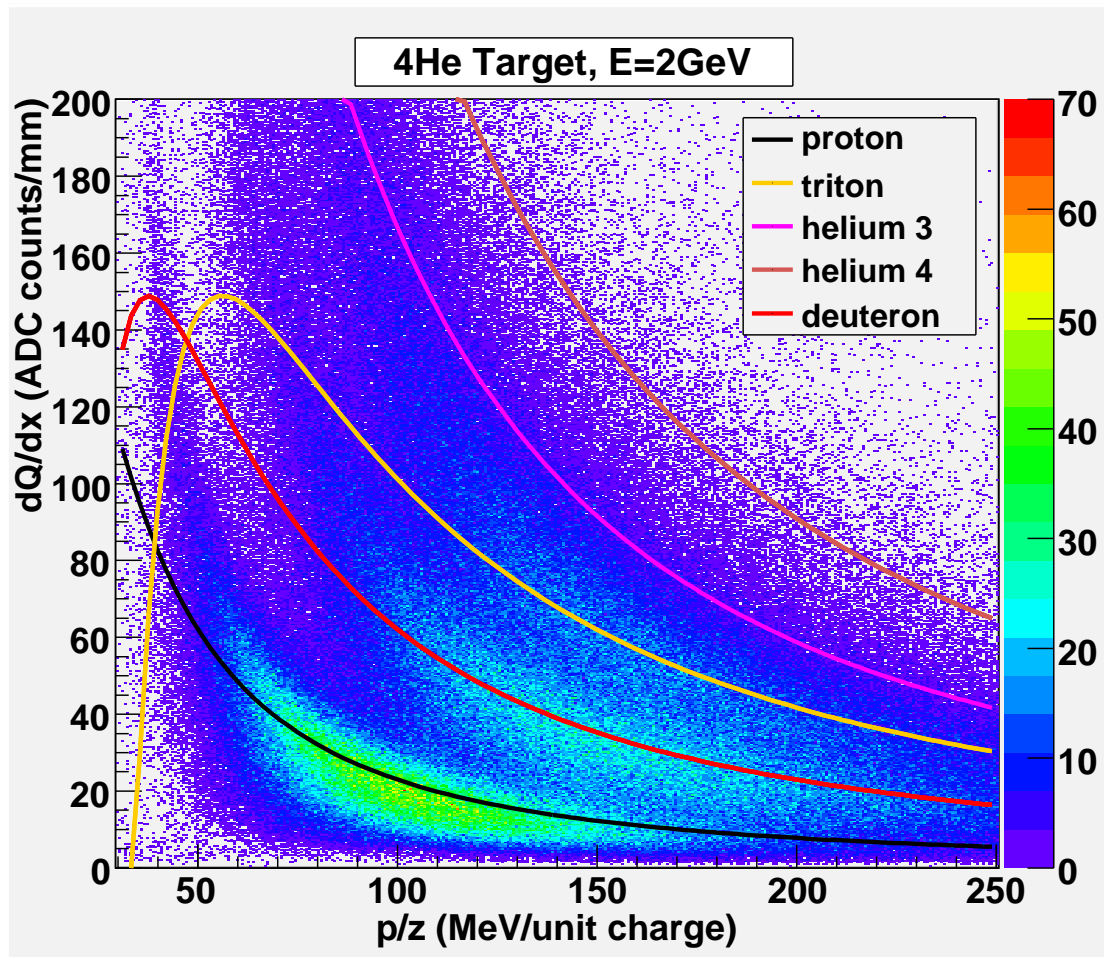


Figure 5.33:  $dQ/dx$  vs.  $p/z$  after RTPC gain calibrations. This should be directly compared with Fig. 5.29. The lines represent the predictions from the Bethe-Bloch equation for different particles.

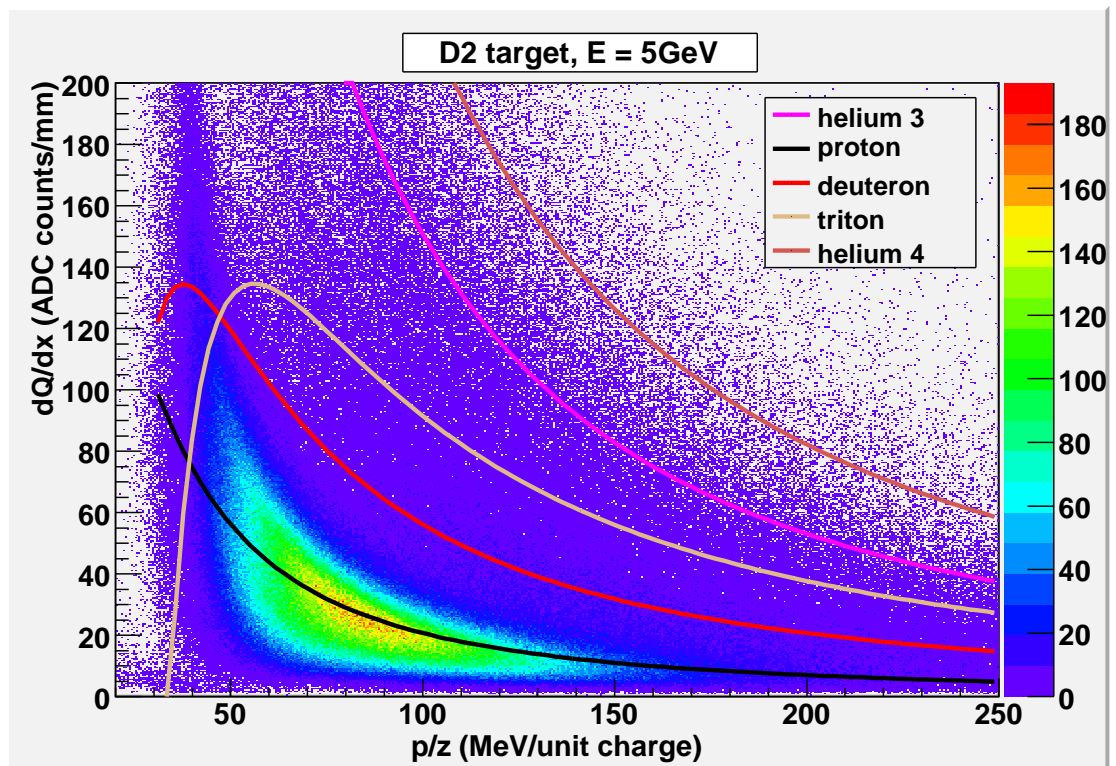


Figure 5.34:  $dQ/dx$  vs.  $p/z$  after RTPC gain calibrations for a deuterium data set. The lines represent the predictions from the Bethe-Bloch equation for different particles.

## 5.3 Data File Selection

### 5.3.1 Electrons per Charge Measured

The BoNuS experiment recorded nearly 860 data runs. However, not all of these were used in this analysis. Many problems can occur during a single run which may lead us to eliminate part of the run or its entire contents. Hardware problems which were most likely to occur included drift chamber and RTPC HV trips due to a current overage. Problems with the CLAS data acquisition system were also quite common and led to many short test runs that needed to be identified and eliminated by referencing the experiment's online logbook. In order to identify those runs which have a low number of reconstructed electrons per charge accumulated, a table is created which contains the ratio of the number of good scattered electrons to the total charge,  $N_{el}/\text{Charge}$ , for each run [58]. This table is grouped according to the beam energy, target, and the beam stopper in/out status. Next, a 1D histogram is filled with  $N_{el}/\text{Charge}$  and fit with a gaussian function to get the mean and sigma values. If a run lies outside of  $3\sigma$  it is marked as bad and removed from the sample. Fig. 5.35 shows the ratio  $N_{el}/\text{Charge}$  for the entire run period, the main variation comes from the fact that a beam stopper was put in place when the beam current exceeded 30 nA. Runs were also removed if the paper or electronic logbook indicated that they were non-standard.

### 5.3.2 High Mass ( $A > 1$ ) Background in the RTPC

The RTPC can also be used to select runs which have problems and need not be considered in the good data sample. One way to do this is to look at the number of VIPs and high mass background per electron trigger for each run. This technique can be used only after a valid RTPC particle identification (PID) cut has been established (see Sec. 5.5.3). Fig. 5.36 shows that the deuterium target runs starting at 49670 have a stable or steadily increasing RTPC proton per CLAS electron ratio. The golden track cuts refer to choosing a proton candidate in the RTPC based on the timing, vertex location, etc. and they will be explained in more detail in Sec. 5.5.

The increase may be due to a long-term charge up effect in the RTPC or helium contamination entering the target cell since the increase is also apparent in the ratio of higher mass

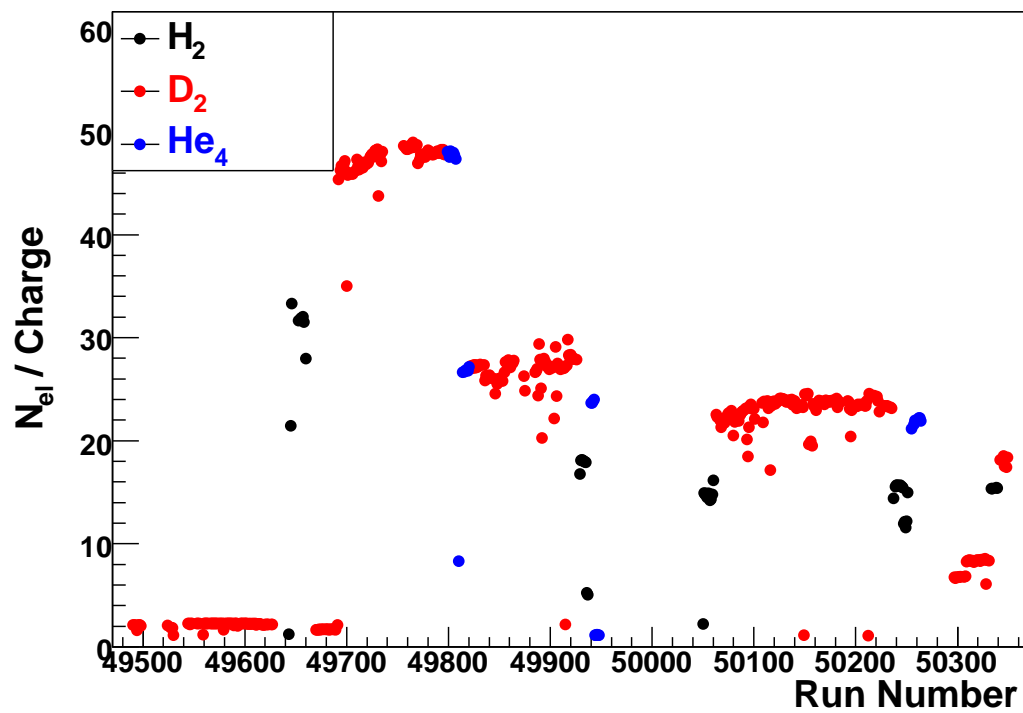


Figure 5.35: The ratio of the number of good scattered electrons to the total charge for all data runs. The value varies with changes to beam energy, target gas, stopper in/out, beam tuning, and trigger configuration.

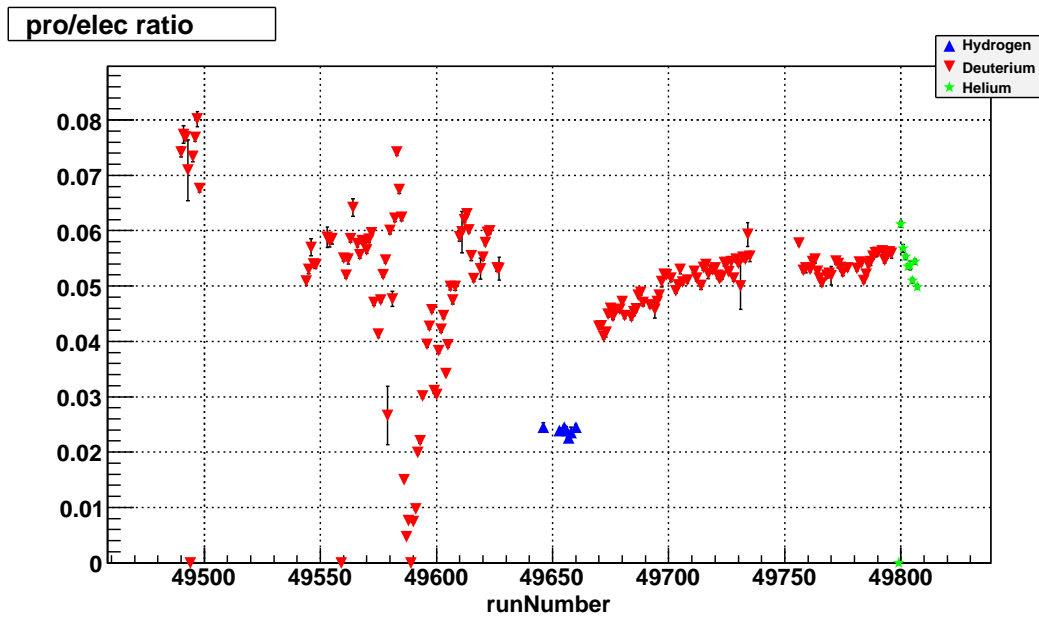


Figure 5.36: The number of RTPC particles per electron which pass the golden track cuts and the  $dQ/dx$  cut. The beam energy is 4.2 GeV.

background in the RTPC to CLAS electron. However if one looks at the number of mass number,  $A > 1$  background in the RTPC per CLAS electron in the period before run 49640 (Fig. 5.37) this was significantly higher and extremely erratic compared to later runs. There are three possible explanations for this behavior: (1) The DME bottle used for the RTPC drift gas during this section of the experiment was running very low and causing an unknown gas mixture. This can cause huge errors in the momentum and  $dQ/dx$  measurements reported by the RTPC. (2) There may have been a large fraction of helium contamination in the target during this section of the experiment due to a poorly regulated target gas purity. Or (3) the deuterium target gas bottle was nearly empty and possibly contaminated with air.

No matter what caused this phenomenon, the collaboration decided that all data before run 49640 was suspect and not useful for any physics analysis. The sudden drop in high mass background around run 49770 corresponds directly to a target recharge which occurred during that run. The fact that the same kink does not exist in the proton/electron ratio at that point indicates that the usage of the RTPC PID cut virtually eliminates the need to subtract the high mass background contamination fraction in the target from the proton data.

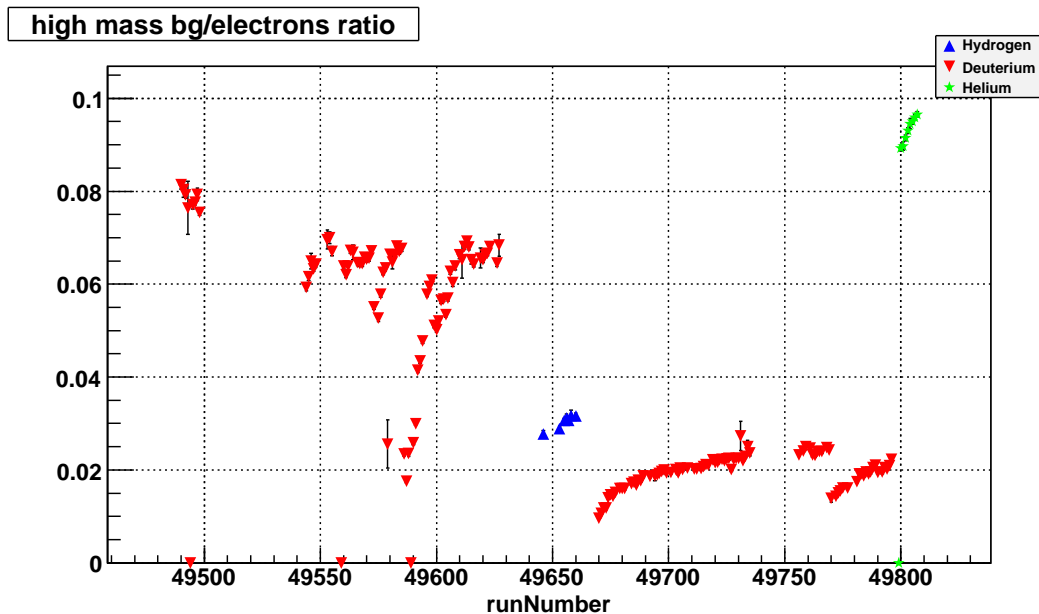


Figure 5.37: The number of RTPC particles per electron which pass the golden track cuts but fail the  $dQ/dx$  cut. The beam energy is 4.2 GeV. All  $D_2$  target runs before 49640 are removed from the data sample (see text for possible explanations).

## 5.4 Electron Identification in CLAS

The single scattered electron must be selected from among the particles ejected from an interaction in the target. Electrons are identified by the signal in a Cherenkov counter (CC) and a characteristic shower in the electromagnetic calorimeter (EC). However, there is one particle though that consistently plagues the electron sample — the negative pion. It is difficult to distinguish  $\pi^-$  from electrons simply based on their trajectory and flight time because their time-of-flight distributions overlap, especially at forward scattering angles. Fortunately, the interaction of pions with matter differs significantly from that of electrons and most of the discussion in this section discusses the removal of negative pion backgrounds by taking advantage of that fact.

### 5.4.1 Cherenkov Detector Fiducial Cuts

The Cherenkov counter can easily distinguish pions from electrons up to 2.7 GeV/c, but above this threshold the pion begins to emit Cherenkov light. When the particle momentum is larger than 2.7 GeV/c we must rely exclusively on an EC cut to remove the negative pion background

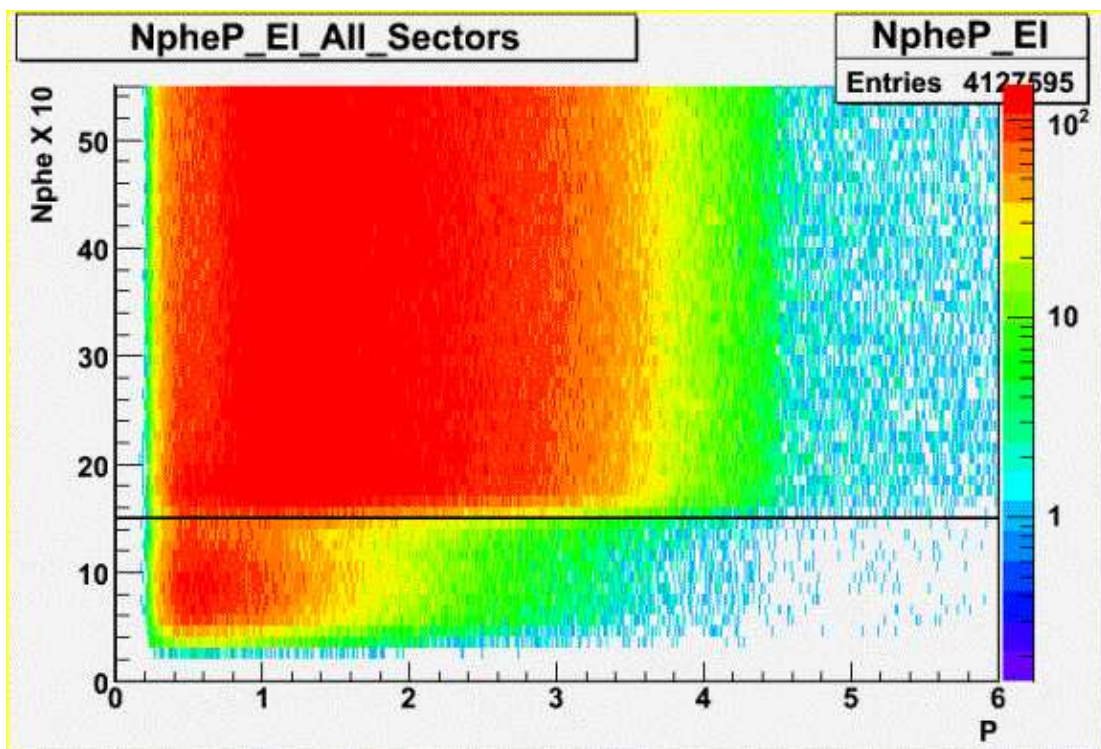


Figure 5.38: Number of photoelectrons (times ten) in the CC vs. the momentum of the particle. Events which fall below the line at 15 are removed if their momentum is below 3.0 GeV/c.

from the electron signal. The Cherenkov counters have a large inefficiency in some regions which needs to be removed from the data set in order to ensure that the systematic errors are small. To reduce the amount of pion contamination of the raw data set, the trigger threshold was set to 150 mV (or 75 mV, depending on the run period), which corresponds to 1.5 photoelectrons registered by the PMT. This value is somewhat higher than in other run periods (E6, for example, used 100 mV). Based on Fig. 5.38, a cut was chosen such that if the momentum is below 3.0 GeV/c, we require the number of photoelectrons to be larger than 1.5; otherwise we require the number of photoelectrons to be larger than 1.0. Furthermore, Fig. 5.39 leads us to require  $0 < cc_{c2} < 0.08$ , where  $cc_{c2}$  is the quality measure of geometrical matching in the Cherenkov counter, i.e. the angle (in rad) between the CC hit and the nearest hit in the scintillation counter (SC).

The CC fiducial cut parameterization, which removes inefficient edges of the CC acceptance, uses the scheme devised initially by V. Burkert for the E1 experiment. The function depends on particle momentum, scattering angle, and magnetic field in the detector volume.

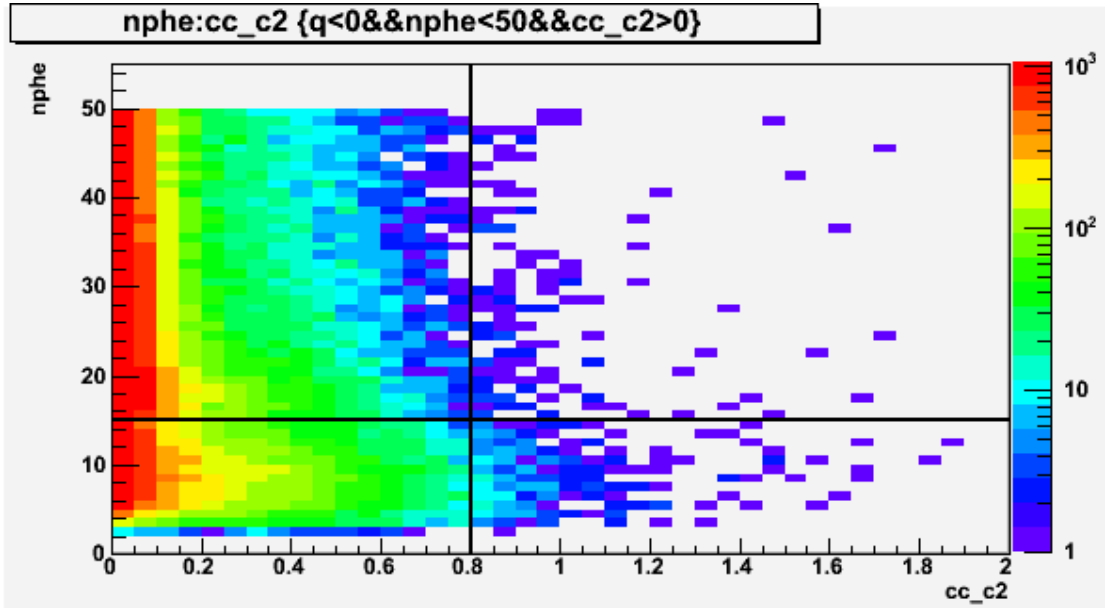


Figure 5.39: Number of photoelectrons vs.  $cc_{c2}$  for negative particles. The value  $cc_{c2}$  is the angle (in radians) between the CC hit and the nearest SC hit.

This is the functional form:

$$\theta_{cut}(P_{el}) = \alpha(P_{el}, I_{torus}) + \frac{16.7I_{torus}}{3375(P_{el} + 0.06)} \quad (5.28)$$

where  $I_{torus}$  is the torus current in amps and  $P_{el}$  is the electron's momentum in GeV/c. The quantity  $\alpha$  is a parameter dependent on the torus current and electron momentum determined by V. Tvaskis for this experiment.

Once  $\theta_{cut}$  is found, the parameters of the azimuthal acceptance  $\Delta\psi(\theta, P_{el})$  were fixed:

$$\Delta\psi = 36 \sin((\theta - \theta_{cut})\pi/180)^\xi \quad (5.29)$$

$$\xi = 0.28(3375P_{el}/I_{torus})^{0.3} \quad (5.30)$$

where  $\theta$  is the polar angle of the electron and  $\Delta\psi$  is acceptance in azimuthal angle for the given sector. Figs. 5.40 and 5.41 show the final results of this cut.

Another cut which is aimed at removing pions from the data sample is the so-called ‘‘Osipenko’’ Cut, developed by M. Osipenko [59]. Most of the pion background results from indeterminate track matching of the Cherenkov counter photomultipliers to the DC and SC-determined

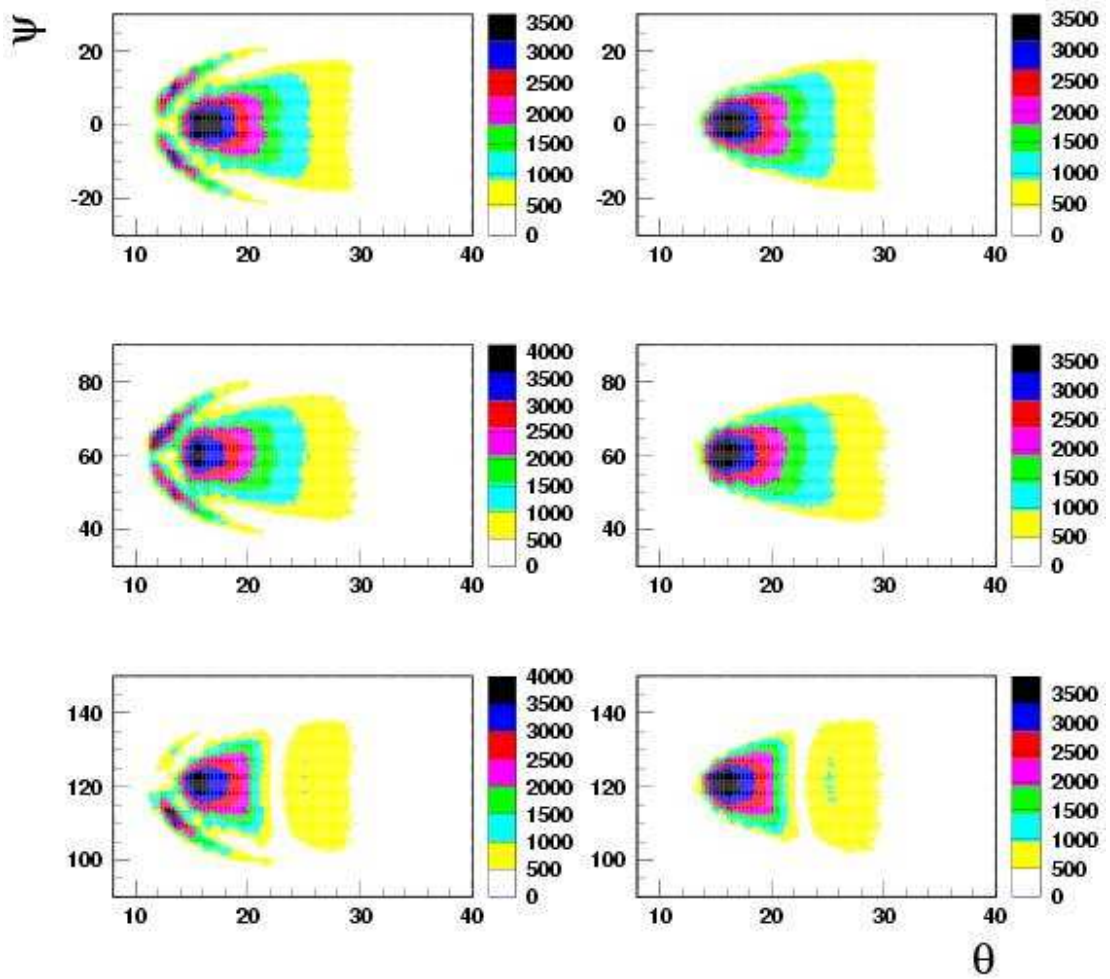


Figure 5.40: The result of the CC fiducial cut for Sectors 1 (top two plots), 2 (middle two plots), and 3 (bottom two plots). The column on the left shows the occupancy before the cut in  $\psi - \theta$  space, where  $\psi$  and  $\theta$  are the azimuthal and polar angles, respectively. The right hand column shows those regions which are not removed by the fiducial cut.

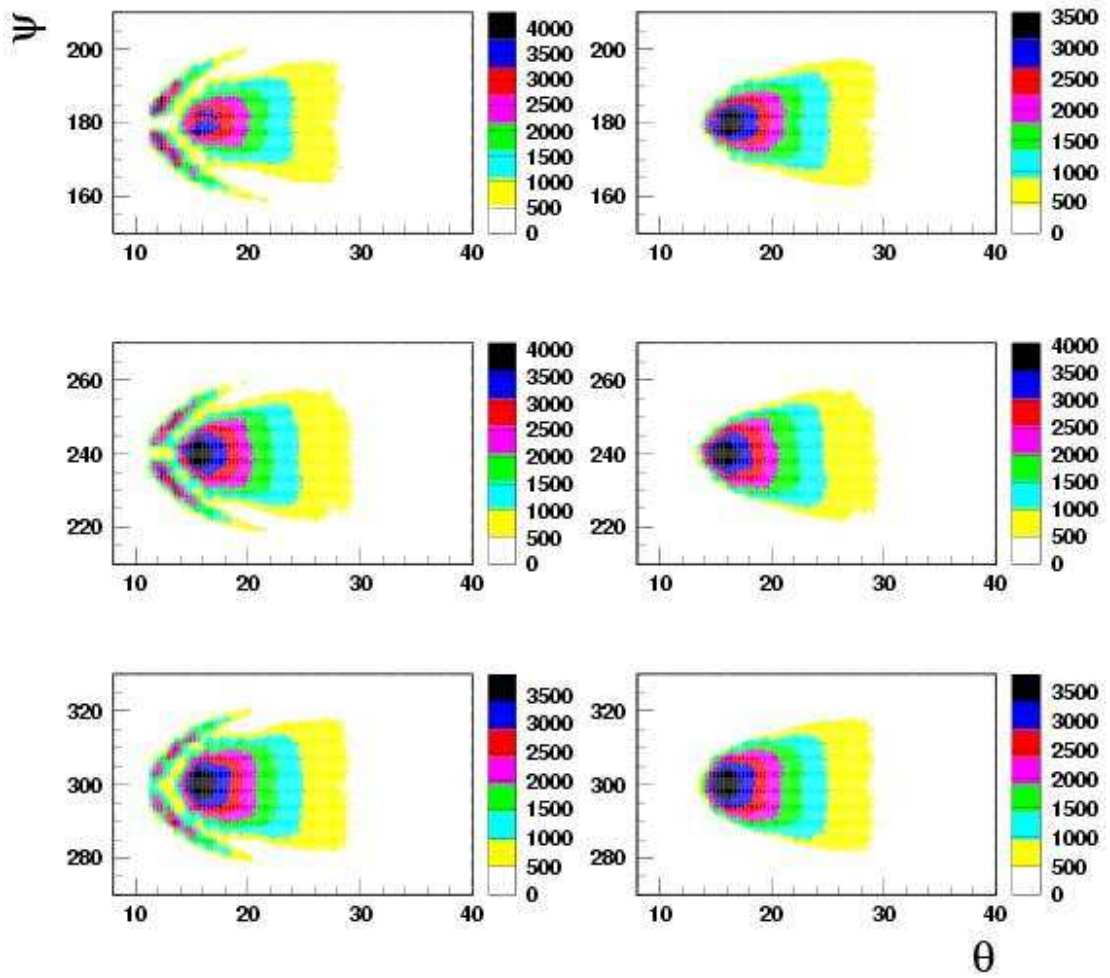


Figure 5.41: Same as Fig. 5.40 except for Sectors 4 (top two plots), 5 (middle two plots), and 6 (bottom two plots).

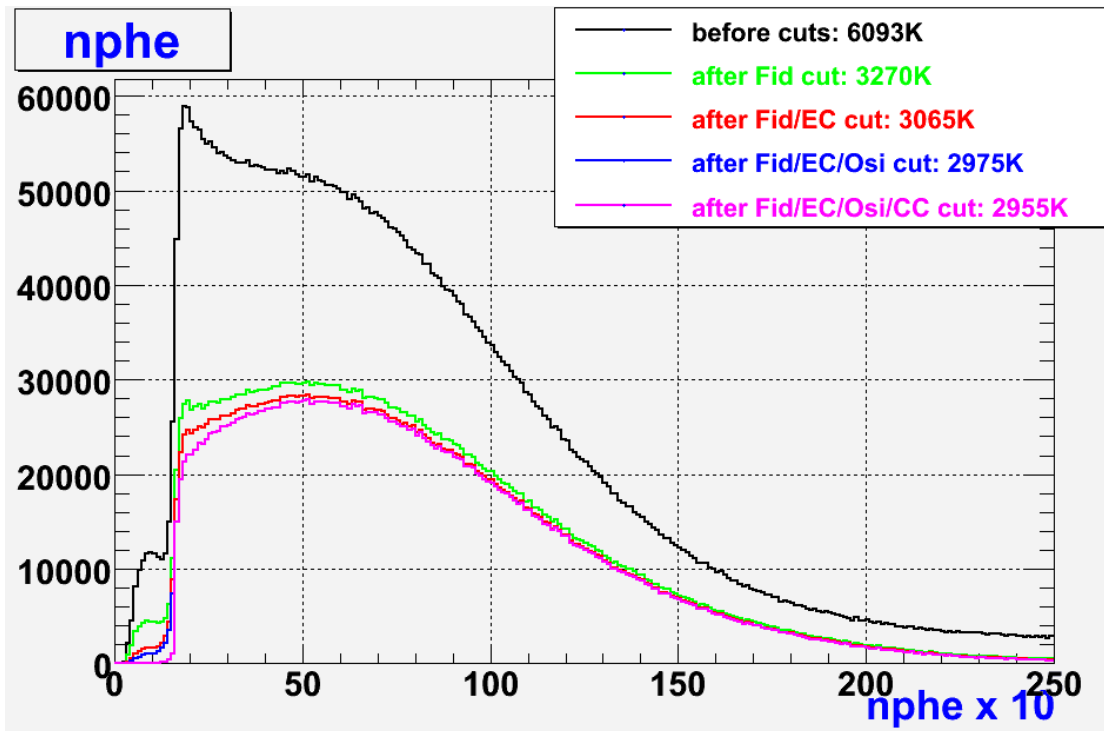


Figure 5.42: The impact of the combined pion background removal cuts on the photoelectron distribution of the CC.

track path and timing, allowing internal PMT noise to correlate with the particle. By applying restrictions to the geometry and trigger timing in the CC, the overwhelming majority of remaining pion background can be removed. The result of the application of this cut can be found in Fig. 5.42, which shows the amount of pion background removed from the original sample.

### 5.4.2 Electromagnetic Calorimeter Cuts

The Cherenkov counter cannot separate electrons from pions when the momentum is larger than 2.7 GeV/c, so the EC is used to distinguish high momentum particles, and provide a cross check with the CC for particles of all momenta. The primary energy loss mechanism in the EC for electrons is pair production and subsequent showering reactions, while pions lose most of their energy through ionization. Therefore, we can use the energy deposited in the inner layers (first 5 layers of the total 13 layers) and the total energy deposited in all the layers to separate pions from electrons. The EC energy cut requires the energy deposited in the inner layer ( $E_{inner}$ ) and the ratio of the total deposited energy in the EC to the momentum ( $E_{total}/P$ )

to satisfy

$$E_{inner} > 0.06 \quad (5.31)$$

$$0.016P + 0.15 < E_{total}/P < 0.34 \quad (5.32)$$

Fig. 5.43 shows the  $E_{inner}$  vs.  $E_{total}/P$  distribution of all negatively charged particles (top), for just electrons (middle) and pions (bottom). Pions predominately deposit less than 60 MeV in the inner calorimeter, while electrons deposit substantially more energy. The remaining pions above 60 MeV are removed via the  $P$  dependent cut in Eq. 5.32. This cut was generated by selecting the electrons in the red region in the center plot of Fig. 5.44. The remaining pions are removed by the CC because they have low momentum. The tiny fraction which still remains after the CC, PID, fiducial cuts, “Osipenko” cuts, and the EC energy cuts are removed with the procedure discussed in Sec. 5.6.5.

### 5.4.3 Solenoid $\theta - z$ Cut

In order to eliminate electrons that travel through any part of the solenoid magnet itself, a cut is made on the maximum electron polar angle. The  $\theta_{max}$  cut is, of course,  $z$  dependent and follows simply from the geometry of the magnet. The cut was developed for this experiment by S. Tkachenko. Table 5.4 shows the final number of electrons that pass all of the electron cuts mentioned in this section, along with the total raw triggers, for each beam energy and target.

## 5.5 RTPC Proton Identification

### 5.5.1 Timing Cuts

The time window of the RTPC is approximately  $11.4 \mu\text{s}$  wide. Once CLAS identifies a possible trigger electron, it sends a signal to the RTPC. The ALTRO records the charge in the time bins during the pretrigger (known as “early” charge) but since it only takes around 6-7  $\mu\text{s}$  for an ionization electron liberated at the cathode to traverse the drift volume, there is usually a significant amount of “late” charge as well. After all charge in the time window is reconstructed to a spatial position using the methods outlined earlier in this chapter, and a helix fit is made

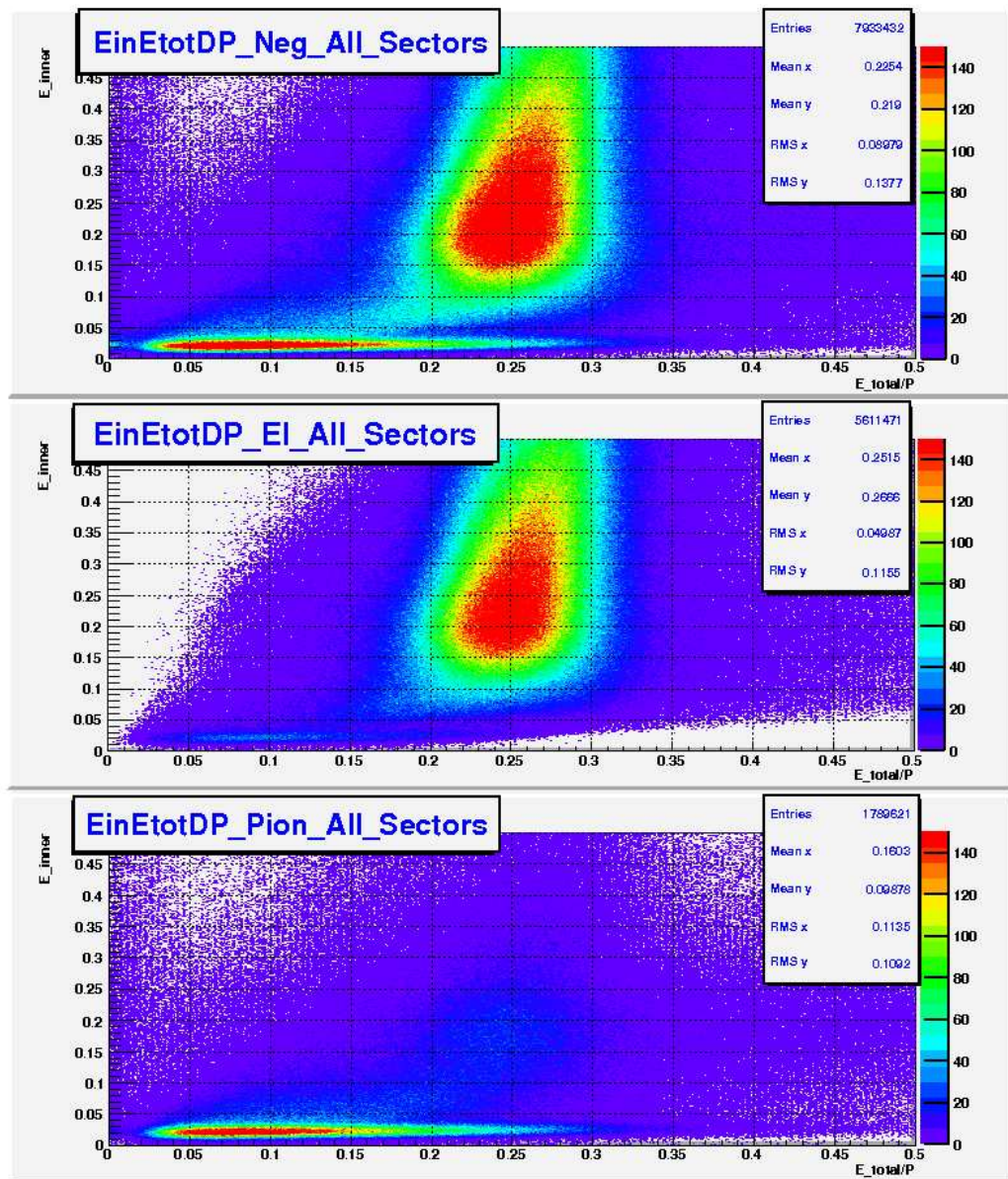


Figure 5.43: The energy deposited in the inner layer of the EC versus the total energy deposited in the EC divided by the momentum for all negative particles (top), for only electrons (middle) and for only pions (bottom).

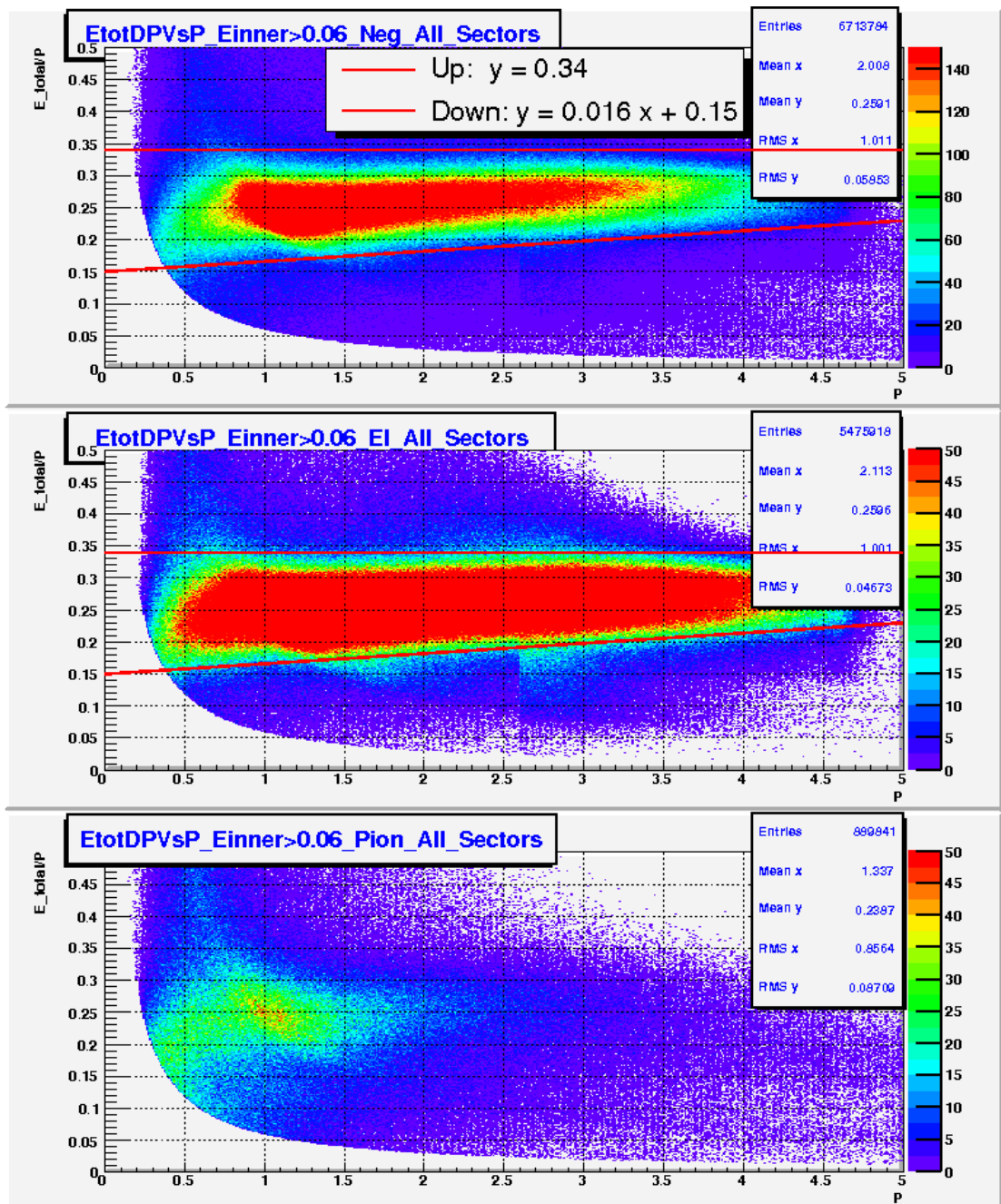


Figure 5.44: The total energy deposited in the EC divided by the momentum versus the particle's momentum for all negative particles (top), for only electrons (middle) and for only pions (bottom).

| Beam Energy (GeV) | Target Gas | Raw Triggers ( $\times 10^3$ ) | Pass Good $e^-$ Cuts ( $\times 10^3$ ) |
|-------------------|------------|--------------------------------|--|
| 1.099             | Helium     | 0                              | -                                      |
|                   | Hydrogen   | 4,990                          | 1,291                                  |
|                   | Deuterium  | 7,593                          | 1,969                                  |
| 2.140             | Helium     | 22,870                         | 5,085                                  |
|                   | Hydrogen   | 14,740                         | 3,111                                  |
|                   | Deuterium  | 91,170                         | 18,380                                 |
| 4.223             | Helium     | 22,400                         | 1,917                                  |
|                   | Hydrogen   | 11,010                         | 632.2                                  |
|                   | Deuterium  | 296,400                        | 25,170                                 |
| 5.262             | Helium     | 63,690                         | 2,242                                  |
|                   | Hydrogen   | 94,650                         | 2,781                                  |
|                   | Deuterium  | 465,100                        | 28,300                                 |

Table 5.4: Triggers and good electrons in BoNuS. For each beam energy and target material, the number of raw triggers, and the number of events which pass all the electron ID cuts are given.

to the track, the two key timing quantities mentioned previously  $edist$  and  $sdist$  are calculated. The “early” and “late” tracks are removed from the RTPC track sample by requiring that the  $edist$  and  $sdist$  of each track is within the range  $[-3,8]$  after the drift velocity calibration is performed. The peaks at  $-5$  mm in Fig. 5.45 and at  $-10$  mm in Fig. 5.46 are due to our truncation of the possible reconstructed position of early hits at  $r = 65$  mm and late hits at the virtual cathode ( $r = 20$  mm). They correspond to the maximum distance outside the physical chamber boundary that a hit can be projected before being completely discarded. The tails on either end are simply due to track stubs — those chains that are long enough for a helix fit but are just electronic noise or tracks whose charge fell on a dead pad group.

Charge is allowed to be projected outside the physical volume in order to assist in our calibration procedures. It is clear from these definitions and a look at Fig. 5.47 that a significant portion of tracks pass both the  $edist$  and  $sdist$  cuts at the same time - these are flagged as our “in-time” tracks. The “bullseye” seen in Fig. 5.48 further supports the notion of “in-time” tracks being coincident with the CLAS electron. The color axis of this plot shows the difference between the CLAS electron and the RTPC track, in millimeters. The blue spot in the middle shows that the “in-time” tracks also have the best agreement with the CLAS vertex, thus defining the region in  $edist-sdist-\Delta z$  space that we mark as spectator proton candidates.

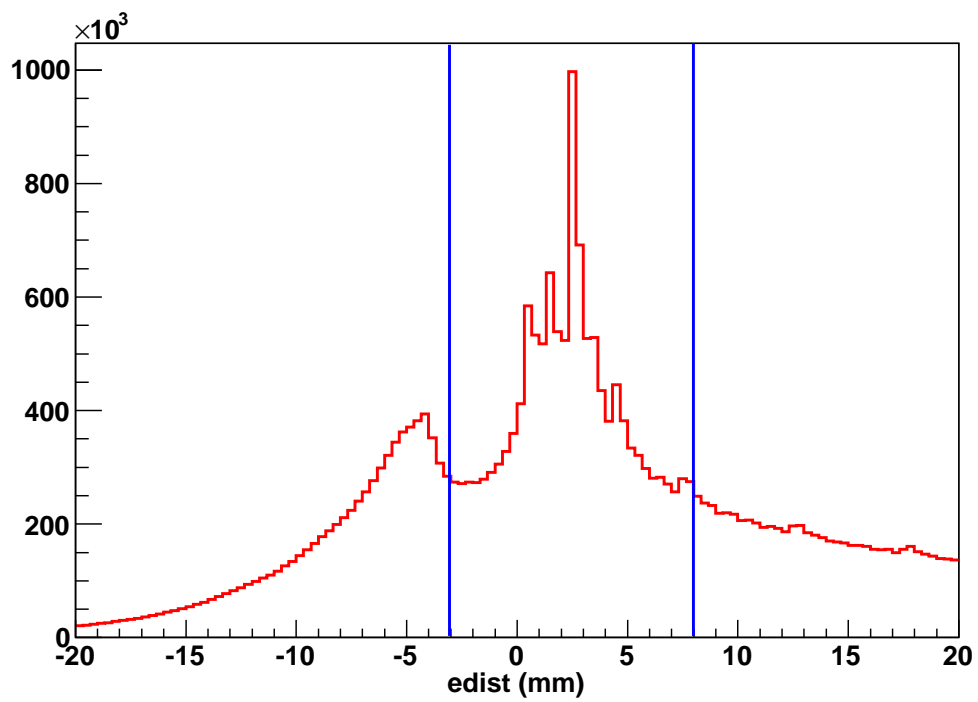


Figure 5.45: The cut on the track's *edist* is shown; we select tracks between the two vertical lines. An attempt is made to isolate the positive peak, the negative peak corresponds to out-of-time charge on the track.

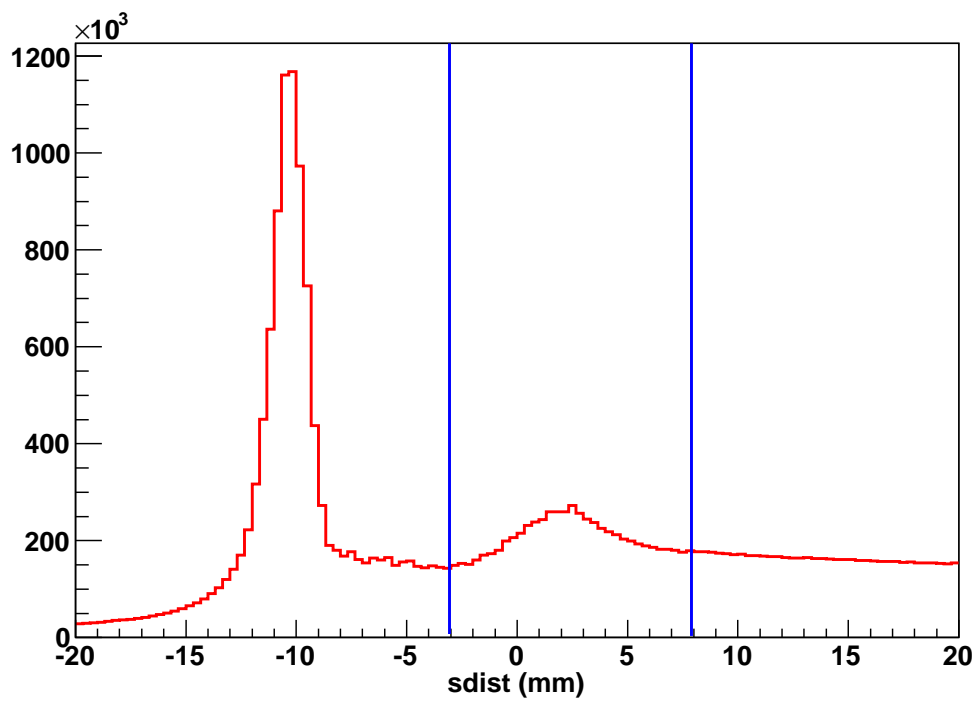


Figure 5.46: The cut on the track's  $sdist$  is shown; we select tracks between the two vertical lines. An attempt is made to isolate the positive hump, the negative peak corresponds to out-of-time charge on the track.

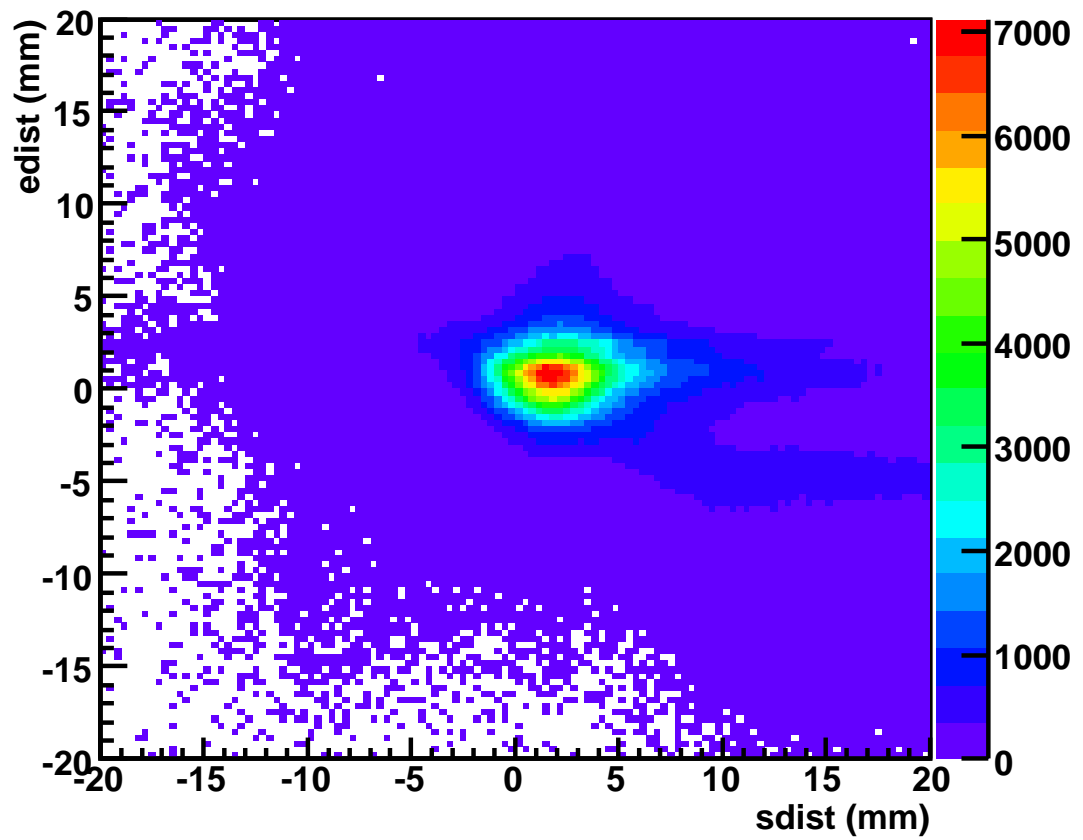


Figure 5.47: The track parameters  $edist$  versus  $sdist$ . The region around (0,0) corresponds to tracks that travel from the cathode to the first GEM (“in-time” tracks)

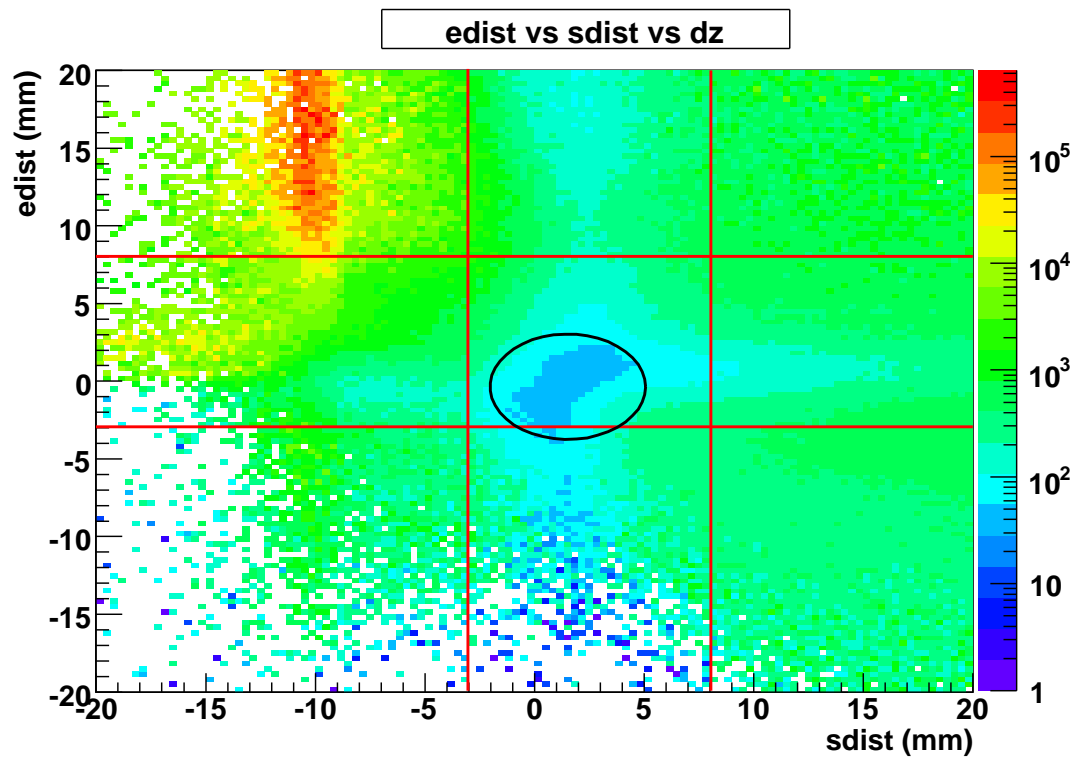


Figure 5.48: The track parameters  $edist$  versus  $sdist$ , with the color scale representing the average  $\Delta z$  (difference of the RTPC track vertex and the CLAS track) in the given bin. The circled blue spot highlights tracks that are marked as spectator proton candidates. The color scale is in units of mm. The hot area in the upper left corner is caused by out-of-time tracks that have no correlation with the trigger electron.

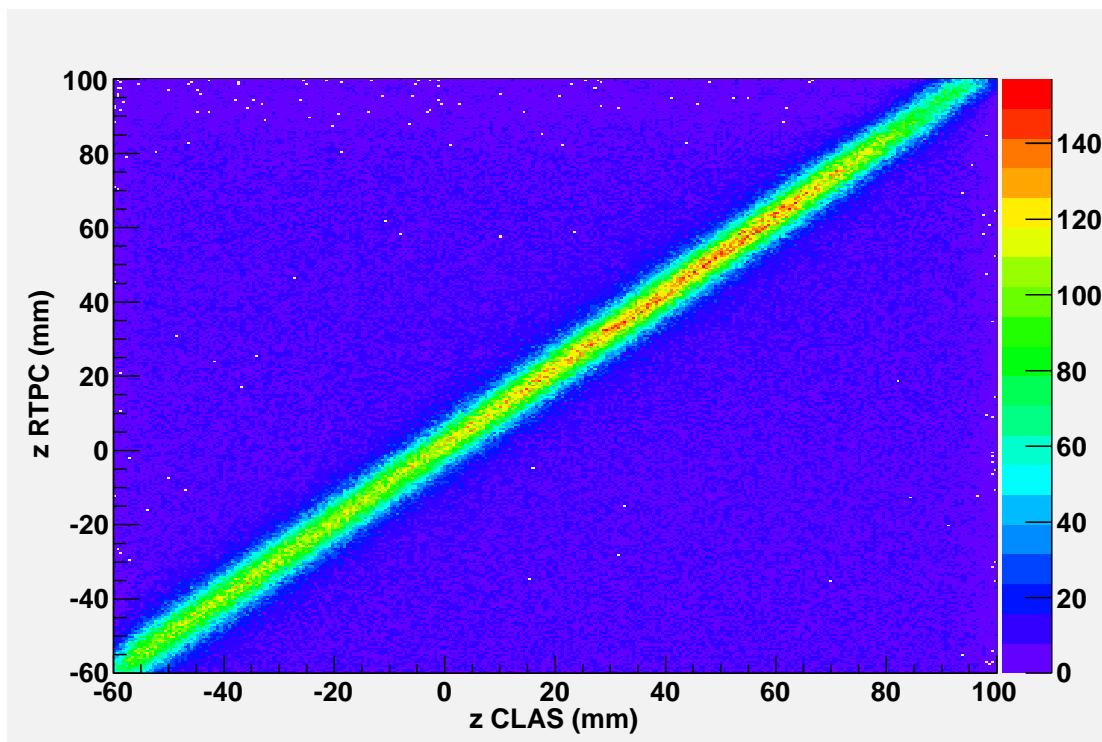


Figure 5.49: The  $z$  of the vertex of the particle measured in the RTPC vs. the  $z$  of the vertex of the electron measured in CLAS.

### 5.5.2 Vertex Cut and Background Subtraction

There is a clear correlation between the vertex position for particles measured in the RTPC and in CLAS. This defines our coincident tracks (Fig. 5.49). To insure that the spectator proton and the trigger electron came from the same interaction point, the difference between the  $z$  vertex measured for each particle is calculated. If that value  $\Delta z = z_e - z_p$  is outside the cut  $z_{mean} - 15mm < \Delta z < z_{mean} + 15mm$  (see Fig. 5.50), the event is thrown away from the good event sample, but it is kept in an array of background events to be subtracted later from the good sample. The accidental coincidences in the wings of Fig. 5.50 are subtracted from the number of good *tagged* events by evaluating the area underneath the coincident peak (all events inside the previously mentioned cut) and removing that fraction from the good sample. Let the area (counts over a particular  $\Delta z$  interval) of the background be  $A = A_1 + A_2 + A_3$  where  $A_3$  is the background under the coincident peak (shaded blue in Fig. 5.50), and  $A_1$  ( $A_2$ ) is the area in the left (right) wing (shaded peach in Fig. 5.50). The background shape is a convolution of two flat

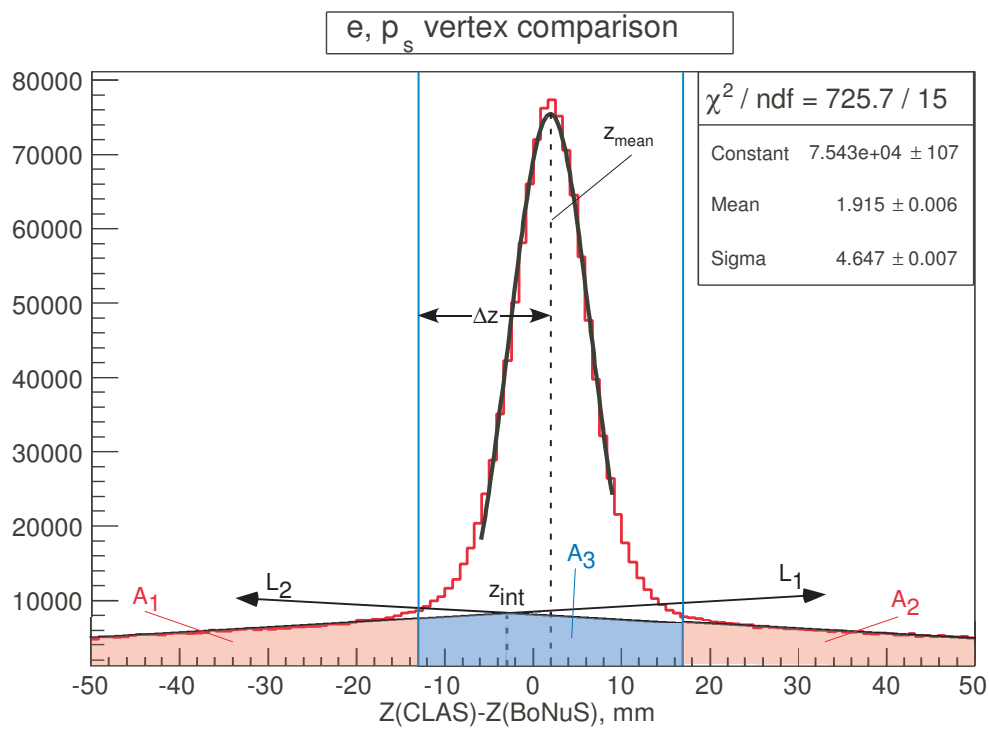


Figure 5.50: The difference between the electron vertex and the spectator proton vertex. All events outside of the blue vertical lines are removed from the *tagged* sample, and the area shaded blue is subtracted from the events in the coincidence peak.

distributions, which is triangular. Next we have to find the  $z$  coordinate of the intersection ( $z_{int}$ ) of the two lines  $L_1$  and  $L_2$  fit to the background in the wings. Clearly,  $z_{int} = \frac{b_2 - b_1}{m_1 - m_2}$  where  $b_n$  and  $m_n$  are the  $y$  intercept and slope of line  $L_n$ . Simple geometry shows that the areas can be found by,

$$A_1 + A_2 + A_3 = \frac{1}{2}(m_2 z_{int} + b_2) \left| b_2/m_2 + 2z_{int} + b_1/m_1 \right| \quad (5.33)$$

$$A_2 = \frac{1}{2} \left| b_2/m_2 + z_{mean} + \Delta z \right| [m_2(z_{mean} + \Delta z) + b_2] \quad (5.34)$$

$$A_1 = \frac{1}{2} \left| b_1/m_1 + z_{mean} + \Delta z \right| [m_1(z_{mean} + \Delta z) + b_1]. \quad (5.35)$$

Now the area of  $A_3$  can be found from Eqs. 5.33, 5.34, and 5.35 and the ratio  $R_{bg} = A_3/(A_1 + A_2)$  is multiplied by the number of counts in the wings and subtracted from the good *tagged* counts. The corrected counts is then

$$N_{corr}(W^*, Q^2) = N_{raw}(W^*, Q^2) - R_{bg} N_{bg}(W^*, Q^2) \quad (5.36)$$

where  $N_{corr}$  is the number of background subtracted counts,  $N_{raw}$  is the original number of counts and  $N_{bg}$  is the total number of counts falling outside of the  $\Delta z$  cut. The counts are binned in  $W^*$  and  $Q^2$ .

### 5.5.3 $dQ/dx$ vs. $p/z$ Cut

Only a very rudimentary particle identification is necessary for the BoNuS experiment. Simply put, we only have to decide if the particle is a proton or not (before checking if it is a VIP). This goal is accomplished by comparing the post-gain-calibration  $dQ/dx$  measurement of the track to the predicted  $dE/dx$  from the Bethe-Bloch function in the low-energy regime. The ratio of measured  $dQ/dx$  to predicted is recorded for every run. This ratio is not necessarily centered at 1.0 because of the arbitrary conversion from ADC units to energy. This conversion factor varies from run to run due to fluctuations in gas mixture, temperature and pressure. Instead of calibrating, run by run, we simply measure the centroid and width of the ratio and make  $\pm 2\sigma$  cuts, run by run. The Bethe-Bloch function has the form:

$$-\frac{dE}{dx} = \frac{\Gamma}{\beta^2} F(\beta) \quad (5.37)$$

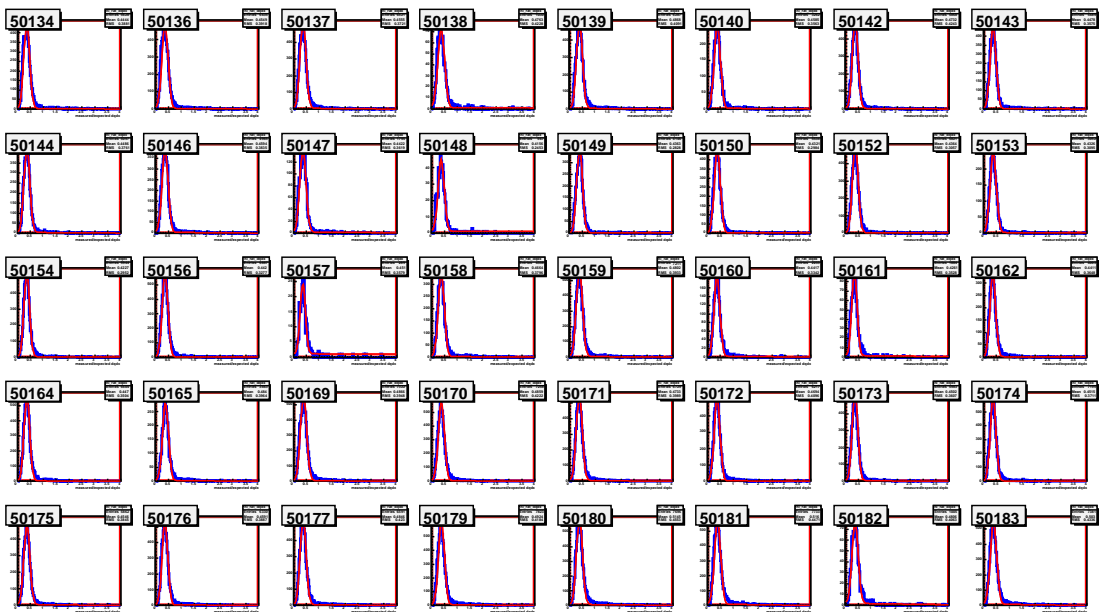


Figure 5.51: Ratio of measured to predicted  $dQ/dx$  for a sample of 40 deuterium target runs. The gaussian fit with a linear background is shown in red.

where  $\Gamma = Kz^2Z/A$ ,  $z$  is the charge of the incident particle,  $Z$  is the atomic number of the absorber,  $A$  is the atomic mass of the absorber and  $F(\beta)$  represents the rest of the Bethe-Bloch function that is  $\beta$  dependent. Here we use the values from the Particle Data Group [5]:  $K/A = 0.307075/4.003$  MeV cm<sup>2</sup>/gram (for a pure helium absorber),  $z^2 = 1$  for the proton,  $Z = 2$  for helium leading to a value of the scale factor,  $\Gamma = 0.1534$  MeV cm<sup>2</sup>/gram.

The measured to predicted  $dQ/dx$  ratio is fit to a gaussian plus a linear background. Fig. 5.51 shows the result of this fit for a subset of runs. Note the uniformity in the shape of the distribution. Fig. 5.52 shows the centroid and width of the fitted gaussian as a function of run number, for the entire experiment. Some runs had small statistics or unstable fit results. Since the variations in peak centroid and width were small and roughly linear with run number, each clear subgroup of runs was fit to a straight line (the black lines in Fig. 5.52). This fit was used in the PID cut for runs without a reliable mean and width. In the end we have a run-dependent proton PID cut.

The ratio of measured to predicted  $dQ/dx$  also shows that we are dominated by higher mass particles with momenta above 200 MeV/c. There is no distinguishable proton peak in Fig. 5.53 above that momentum threshold. For deuterium runs taken before 49640, a large amount of

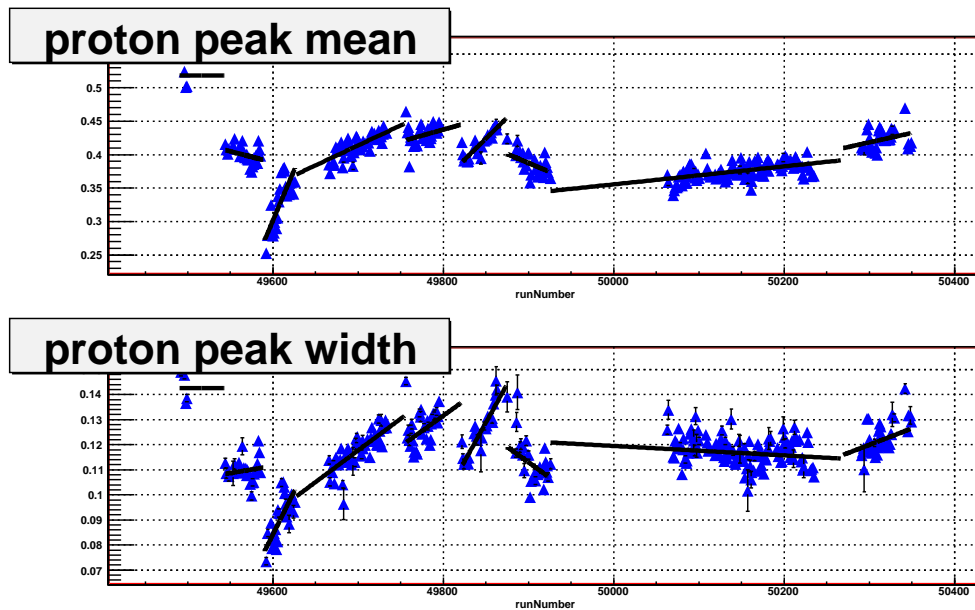


Figure 5.52: The mean and width of the gaussian fit to the ratio distribution of Fig. 5.51 as a function of run number, for the entire experiment. The straight lines are fits to segments of runs whose values drift linearly with time.

high mass background is clearly present in all momentum bins, giving more evidence that the data for that period were corrupted.

The tables holding the proton peak mean and sigma were used to make a PID cut of  $\pm 2\sigma$  around the peak. We considered removing the low  $\sigma$  part of this cut since it is virtually impossible to track pions in the RTPC with typical settings, but it makes very little difference to this analysis. One can see the result of the cut in Fig. 5.54a where the proton band is shown in color. The figure includes every run at 2 GeV beam energy, so there is no sharp cut-off between the proton band and the higher mass background because of the run by run variations in the proton band's location. As one would expect, the peaks in the invariant mass distribution of the struck nucleon,  $W^*$ , calculated from spectator kinematics for events that pass the proton PID cut are much sharper than for events that fail the proton PID cut (Fig. 5.54b).

#### 5.5.4 Other RTPC Track Quality Cuts

There are three track quality cuts in addition to the  $z$  vertex cuts, the timing cuts and the PID cuts. The first requires  $\chi^2 < 4$  in the helix fit (given by Eq. 5.27). This cut is very liberal and

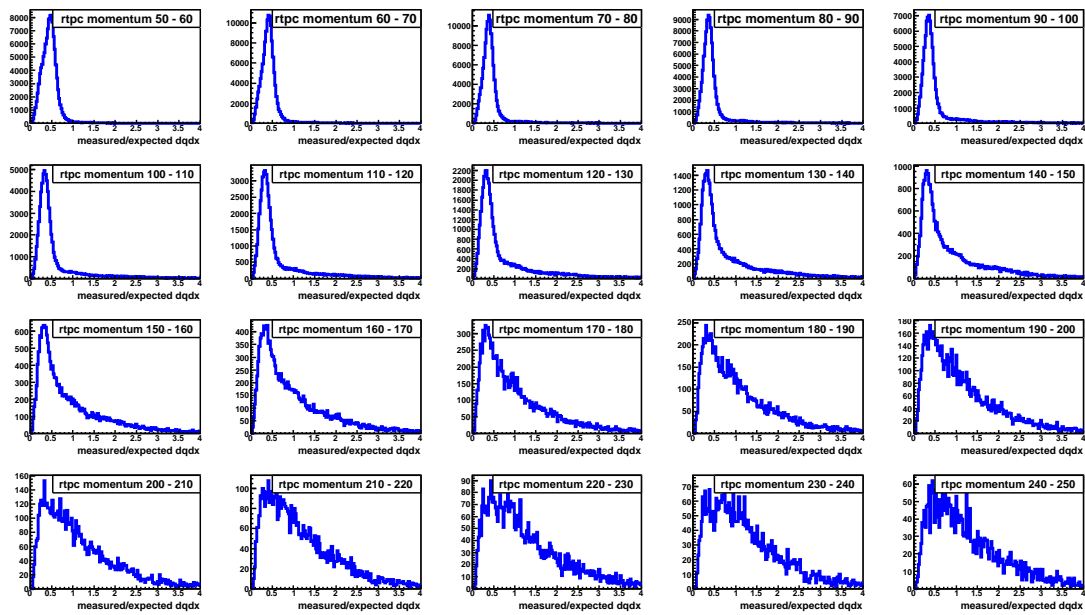


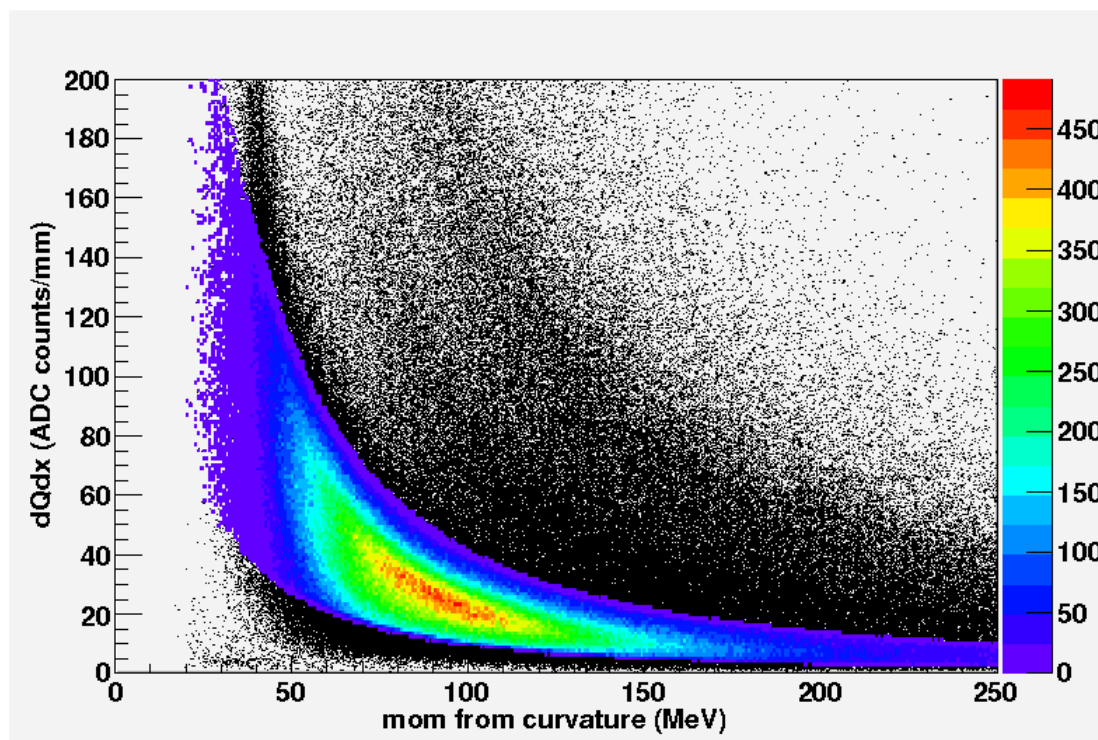
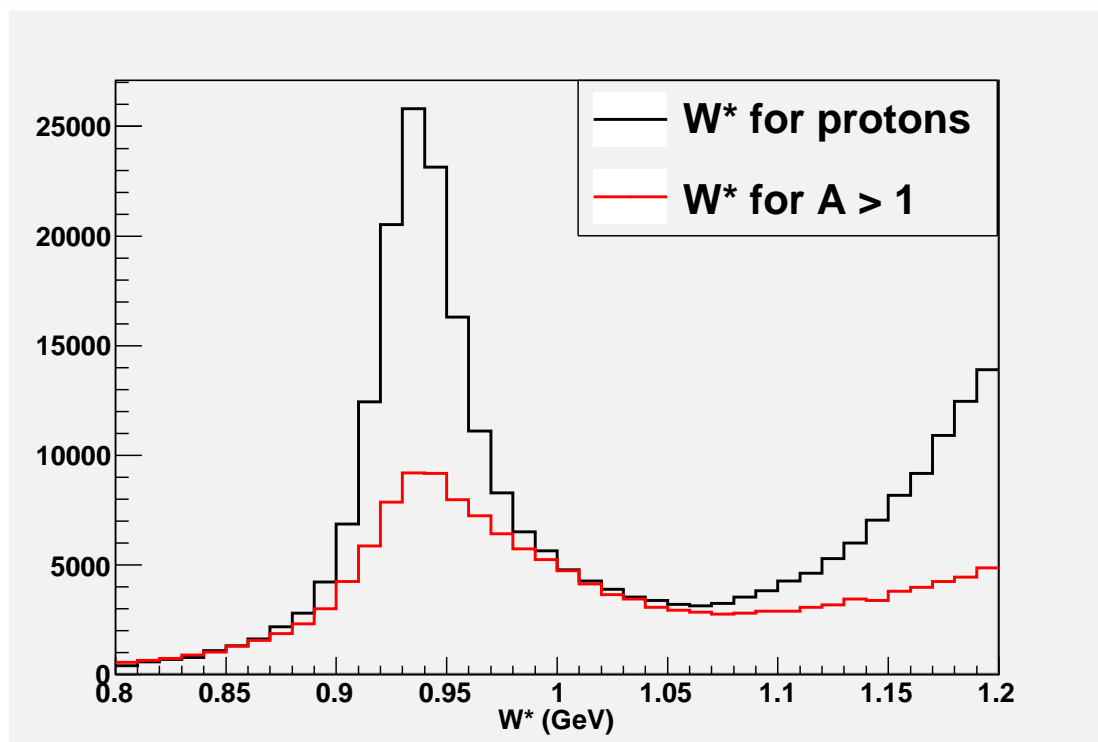
Figure 5.53: The measured  $dQ/dx$  divided by the calculated  $dQ/dx$  in bins of increasing particle momentum. This is deuterium target data, helium target data shows peaks corresponding to the bands in Fig. 5.33.

that eliminates only 12% of the tracks (see Fig. 5.55). The next cut is simply on the electric charge of the particle. We eliminate tracks that travel on a clockwise path after being ejected from the target (when looking upstream as in Fig. 5.22) because they have negative charge. Fig. 5.56 shows that about 57% of all tracks correspond to positive charged particles. The final cut requires 5 or more unique pads to fire. This number comes from a detailed study of the simulation by J. Zhang (see Sec. 5.6.2). Fig. 5.57 displays the real and simulated frequency histogram of the number of unique pads in a track — about 75% pass our cut.

## 5.6 Corrections

### 5.6.1 Electron Momentum, Angle, and Vertex

The CLAS electron momentum determination is inaccurate because of uncertainties in the drift chamber position and an imprecise knowledge of the magnetic field of the torus and solenoid magnets. A correction to the CLAS momentum can be made by isolating exclusive events and taking advantage of four-momentum conservation. S. Kuhn and A. Klimenko initially devised

(a)  $dQ/dx$  vs.  $p/z$ 

(b) Invariant mass

Figure 5.54: Comparing RTPC particles which pass/fail the PID cuts. (a) Events which pass the proton PID cut are in color, those that fail are shown as a black shadow. (b) The invariant mass spectrum for events which pass the proton PID cut (black curve) and for all those that fail (red curve). The elastic scattering peak centered at  $W^* = 938$  GeV is much narrower in the black distribution.

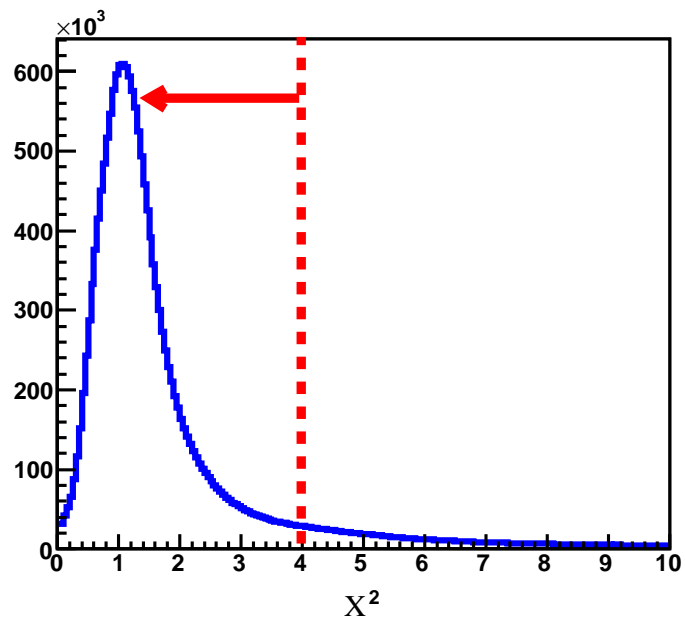


Figure 5.55: The  $\chi^2$  distribution of RTPC tracks. Any track with a  $\chi^2 > 4$  was not considered a spectator proton candidate.

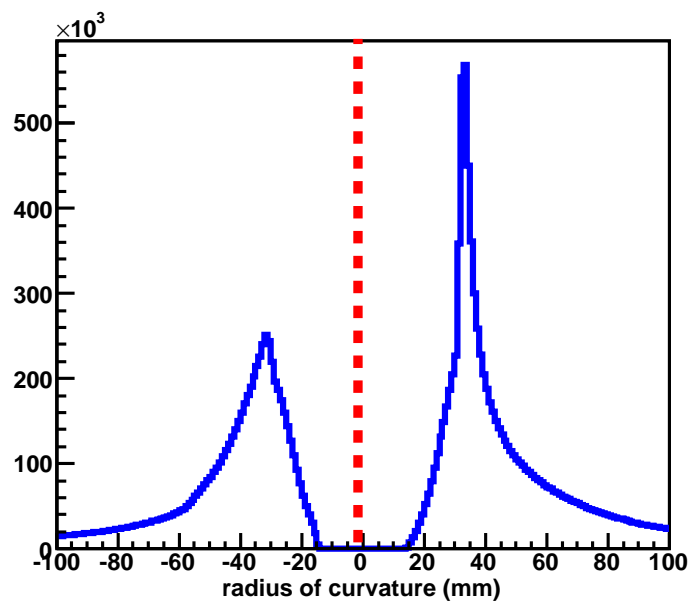


Figure 5.56: The raw distribution of radius of curvature measurements for RTPC tracks. All tracks with a negative radius of curvature, corresponding to negative charges, are removed.

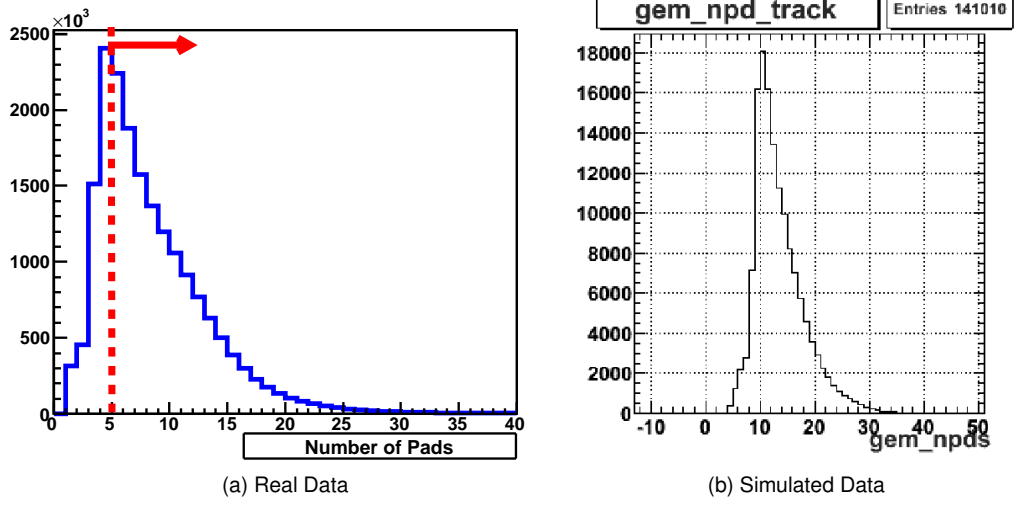


Figure 5.57: The real and simulated distributions of the number of unique pads that fired to produce an RTPC track. The cut required this number to be 5 or more.

the prescription for momentum corrections in Ref. [60]. These corrections were performed for this experiment by S. Tkachenko. The correction to the reconstructed scattering angle of the particle is parameterized as a function of the reconstructed azimuthal and polar angles:

$$d\theta = (c_1 + c_2\phi_{rec}) \frac{\cos \theta_{rec}}{\cos \phi_{rec}} + (c_3 + c_4\phi_{rec}) \sin \theta_{rec} \quad (5.38)$$

$$\theta_{cor} = \theta_{rec} + d\theta$$

where  $c_1, c_2, c_3, c_4$  are fit parameters,  $\theta_{rec}$  is the polar angle of the particle as reconstructed by the tracking software,  $\phi_{rec}$  is the reconstructed azimuthal angle of the particle and  $\theta_{cor}$  is the polar angle of the particle after correction. The correction to the momentum has the form:

$$dp = \left\{ (c_5 + c_6\phi_{rec}) \frac{\cos \theta_{cor}}{\cos \phi_{rec}} + (c_7 + c_8\phi_{rec}) \sin \theta_{cor} \right\} \frac{p_{rec}}{qB_{torus}} + c_9 + c_{10}\phi_{rec} + c_{11}\phi_{rec}^2$$

$$+ (c_{12} + c_{13}\phi_{rec} + c_{14}\phi_{rec}^2) \sin \theta_{cor} + (c_{15} + c_{16}\phi_{rec}) \cos \theta_{cor} \quad (5.39)$$

$$p_{cor} = p_{rec} + dp$$

where  $c_{5...16}$  are fit parameters,  $p_{rec}$  is the reconstructed momentum,  $q$  is the charge of the particle in units of elementary charge,  $p_{cor}$  is the momentum of the particle after correction,  $B_{torus}$  is the idealized  $\int B \cdot dl$  along the path of the track. The parameters attempt to take

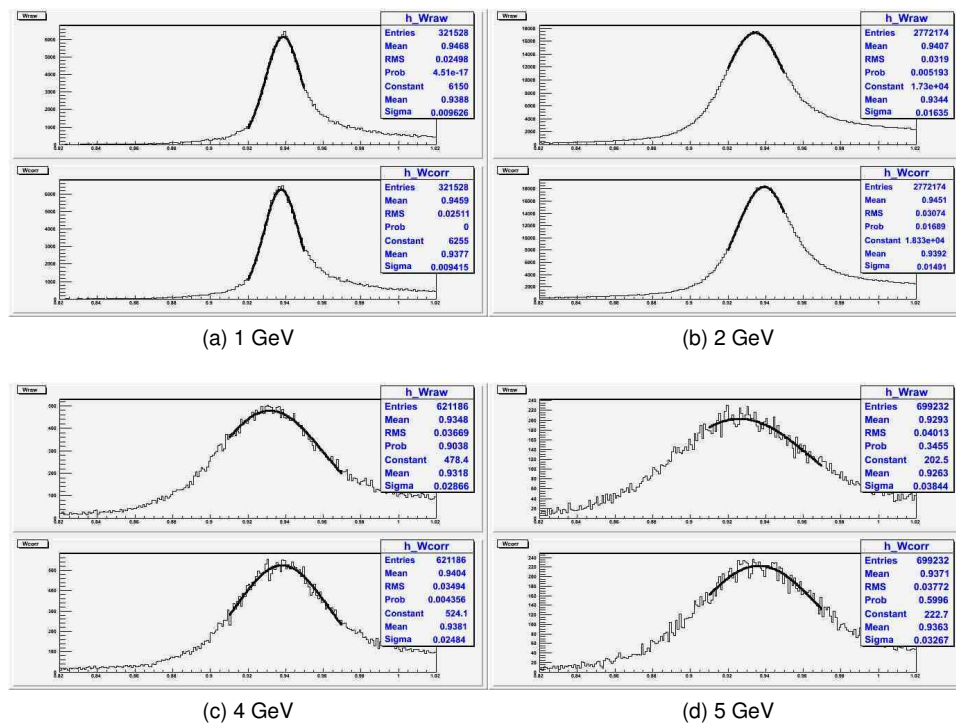


Figure 5.58: The invariant mass of the final state in the process  $H(e, e')p$  before (top) and after (bottom) the trigger electron momentum corrections for the four beam energies. The mean and the width of the elastic peak has improved in every case.

into account the drift chamber displacements and rotations (still present even after applying the alignment procedure from Sec. 3.2.2) and uncertainties in the magnitudes of the magnetic fields which the particles encounter. The reactions used to determine the fit parameters were elastic scattering on hydrogen ( $ep \rightarrow e'p$ ), two-pion production on hydrogen ( $ep \rightarrow e'p\pi^+\pi^-$ ), and pion production on deuterium ( $ed \rightarrow e'pp\pi^-$ ). The software package MINUIT was used to minimize the weighted sum of squared deviations of the total 4-momentum difference from zero ( $p_{initial}^\mu - p_{final}^\mu$ ). After application of the momentum corrections the elastic peak resolution improvement ranged from  $\sim 0.02\%$  for the 1 GeV beam energy to  $\sim 0.12\%$  for the 5 GeV run period. In addition, the corrected elastic peak locations are more consistent with the proton mass. Fig. 5.58 contains a sample of these results.

The CLAS tracking reports an inaccurate  $z$  vertex if the beam delivered to the Hall does not travel down the center of the target. This was the case in our experiment as was previously discussed in Sec. 5.1.7. The left plot in Fig. 5.59 shows clearly that the reconstructed  $z$  position

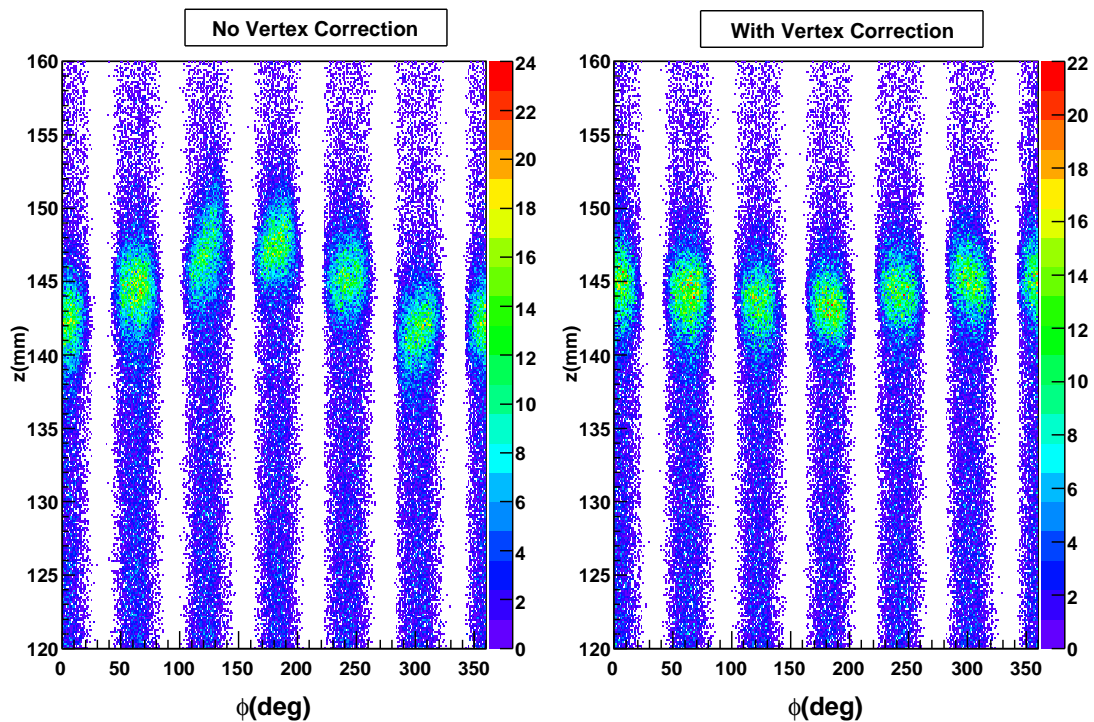


Figure 5.59: The reconstructed  $z$  position of the downstream target endcap before and after the trigger electron energy loss corrections were applied. After correction, each of the six sectors report nearly the same  $z$  for the endcap.

of the downstream target exit window (nominally at  $z = 145$  mm in the RTPC coordinate system) is sector-dependent. The vertex of the electron will be shifted in the negative direction for the sector which lies in the direction of beam offset and vice versa for sectors on the opposite side of the offset. Knowledge of the beam's true  $(x, y)$  position as a function of  $z$  from the beam position monitors can be combined with the vertex measurements in multi-particle, exclusive events to correct the electron vertex. The right side of Fig. 5.59 shows how the vertex reconstruction improves after this correction.

### 5.6.2 RTPC Simulation and Proton Energy Loss Correction

In order to reconstruct the spectator proton's momentum at the vertex, an energy-loss correction must be applied. The energy loss of the spectator proton was simulated by J. Zhang [61], using a detailed model of the BoNuS detector in GEANT4. This package was included in a software chain with the standard CLAS simulation, GSIM, which is based on GEANT3. For the

energy-loss correction of the spectator proton only the RTPC simulation is relevant since these particles are stopped before reaching CLAS.

A typical 70 MeV/c spectator proton at laboratory scattering angle  $\theta = 90^\circ$  loses roughly 1 MeV/c as it traverses the target, 17 MeV/c in the target wall, 1 MeV/c in the helium buffer gas, 3 MeV/c in the ground plane, 2 MeV/c in the second buffer gas, 4 MeV/c in the cathode, and finally 10 MeV/c in the tracking region. Fig. 5.60 shows how these values will change with different starting spectator energies.

The momentum distribution of spectator protons generated by the simulation is shown in Fig. 5.61. The scattered electron detected in CLAS and the spectator proton in the RTPC from the semi-inclusive reaction  $d(e, e' p_s) X$  are generated via an event generator based on code, initially written by S. Stepanyan, known as “fpack” which produces a scattered electron using user-specified  $W$  and  $Q^2$  distributions and a flat  $\phi$  distribution. The Fermi motion of the initial neutron is modeled using the deuteron momentum distribution obtained from the Bonn potential [62] with a bin width of 10 MeV/c. This leads to the step function seen in the “true” distribution of events in Fig. 5.61. Once the simulated spectator is swum through the detector with energy loss and multiple scattering taken into account, it enters the tracking volume. Here, the same tracking code and cuts used to reconstruct the real data is used. The black line in Fig. 5.61 represents the measured momentum in the simulation. Then a correction is applied to make the corrected momentum agree with the thrown momentum. The bottom plot of Fig. 5.61 shows the difference in reconstructed momentum before and after this correction is applied. One can also see the result of applying the correction to real data in Fig. 5.62.

It is very important to make sure that we are measuring the spectator momentum correctly in the RTPC. This is not a trivial task since there is no other detector which measures the spectator — it stops in the outer edge of the RTPC. Although we have calibrated the RTPC by matching straight tracks in CLAS and the RTPC, there is no guarantee that this works for spectator protons. However we can cross-check using exclusive events in CLAS. The reaction  $d(e, e' p \pi^-) p_s$  can be used to infer the momentum of the spectator when all other final state particles are detected in CLAS. There is a large uncertainty (perhaps 20-30 MeV/c) on this prediction because we are taking the difference of large values to find a much smaller missing momentum. The bottom right plot of Fig. 5.63 shows the best we might hope to do with this

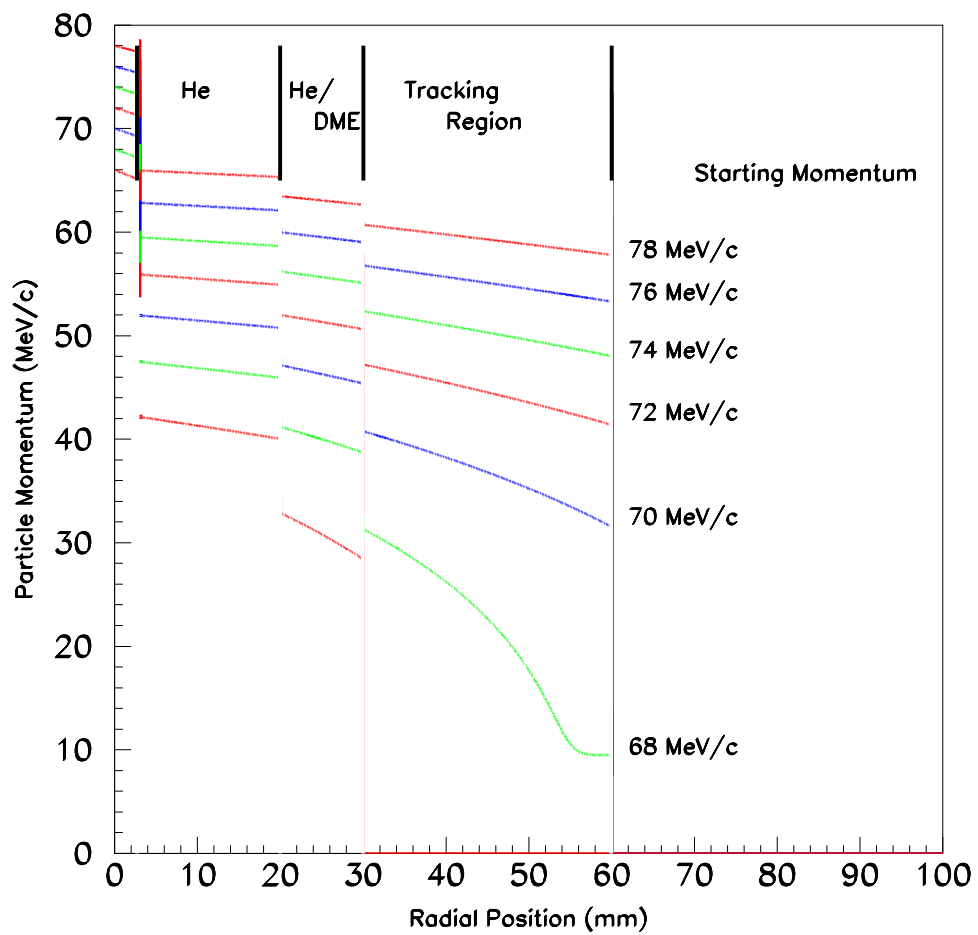


Figure 5.60: Spectator proton's momentum vs. the radial distance traveled for  $\theta = 90^\circ$  and a range of initial momentum. Here,  $R = 0$  corresponds to the center of the target.

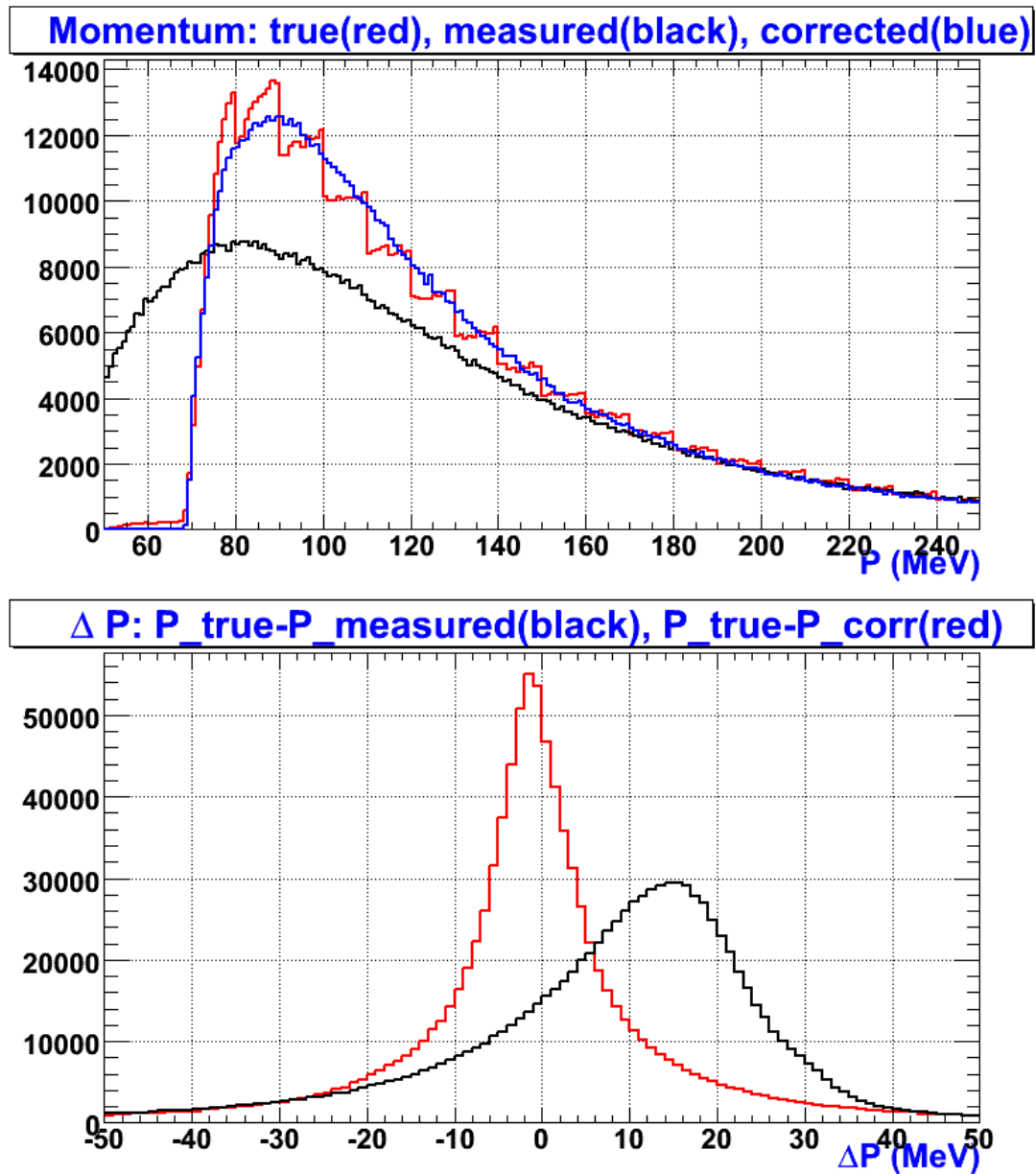


Figure 5.61: RTPC simulation results [61]. The top plot shows the thrown (red), measured (black) and corrected (blue) distributions. The bottom plot shows the difference between the thrown and measured momentum before (black) and after (red) correction.

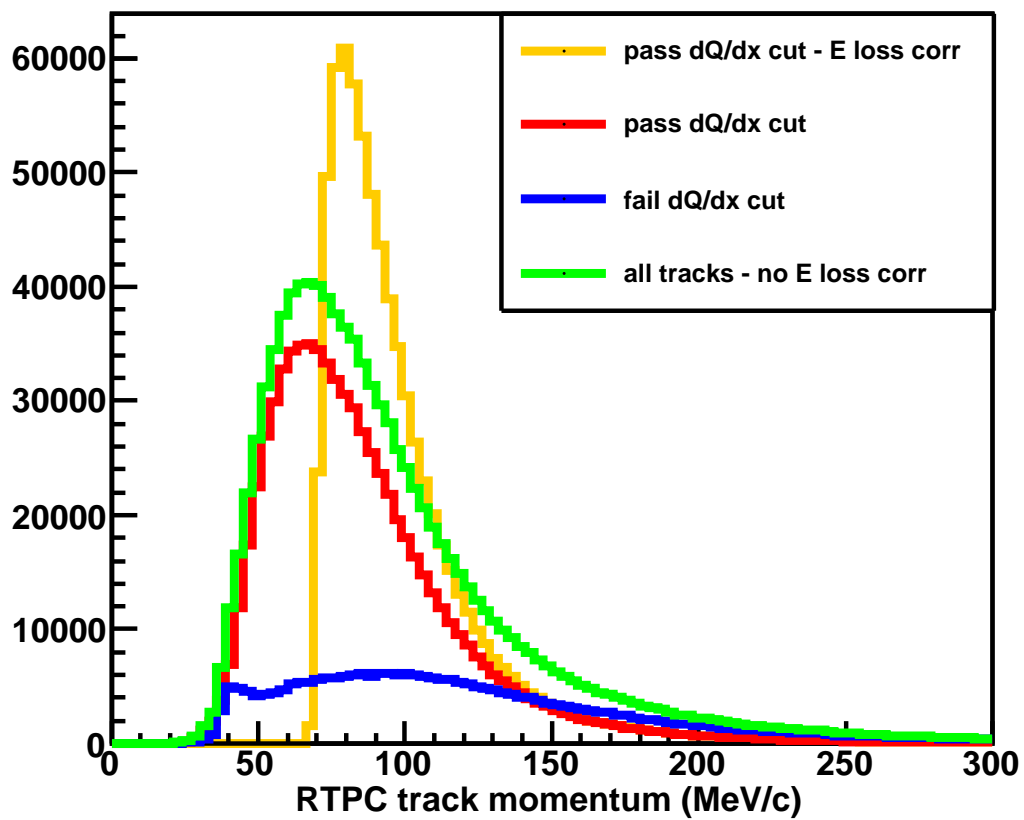


Figure 5.62: Comparison of the momentum distribution before RTPC  $dQ/dx$  cut (green), after  $dQ/dx$  cut (red) and after energy loss corrections have been applied (yellow). The blue line shows those events which fail the  $dQ/dx$  cut. See Sec. 5.5.3 for more details on the  $dQ/dx$  cut.

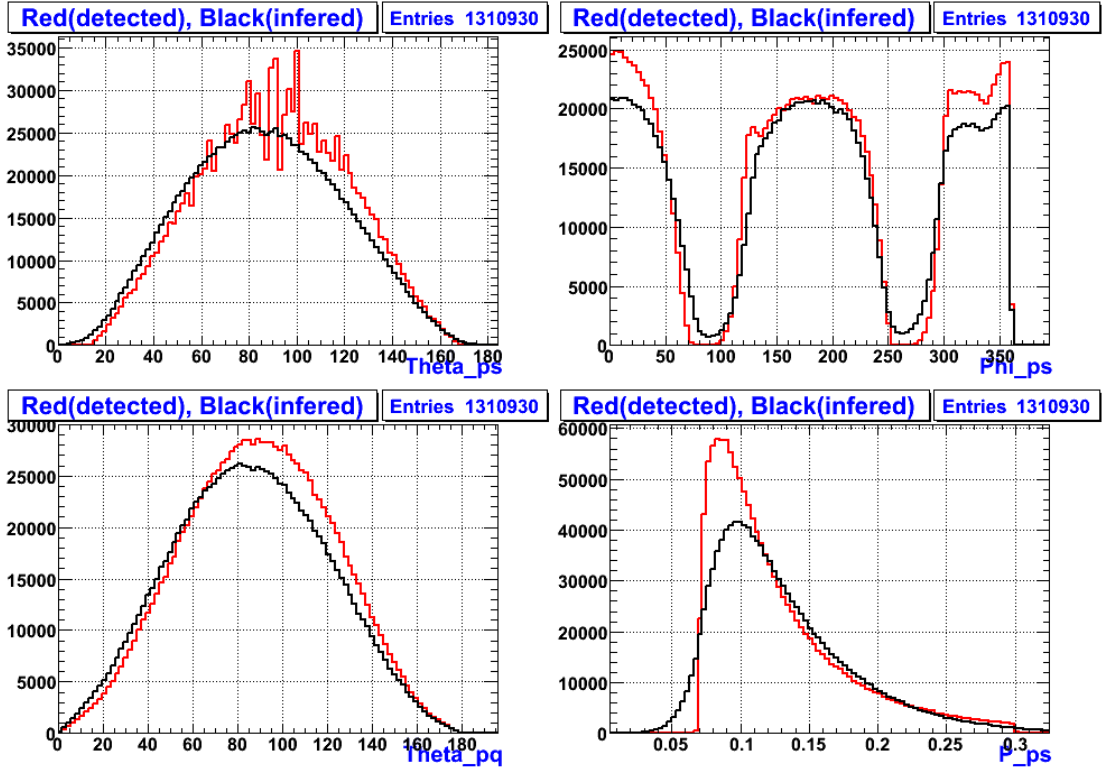


Figure 5.63: The full simulation's result for the inferred angles and momentum of the spectator calculated from exclusive CLAS events overlaid on the reconstructed angles and momentum.

method. The following equations are used to calculate  $p_{miss}$ , the missing spectator momentum.

$$E_{miss} = E + M_d - p_e - \sqrt{p_p^2 + M_N^2} - \sqrt{p_\pi^2 + M_\pi^2} \quad (5.40)$$

$$p_{miss}^z = E - p_e^z - p_p^z - p_\pi^z$$

$$p_{miss}^x = -(p_e^x + p_p^x + p_\pi^x)$$

$$p_{miss}^y = -(p_e^y + p_p^y + p_\pi^y)$$

$$p_{miss}^2 = (p_{miss}^x)^2 + (p_{miss}^y)^2 + (p_{miss}^z)^2$$

$$m_{miss}^2 = E_{miss}^2 - p_{miss}^2$$

where  $(E, p^x, p^y, p^z)_{miss,e,p,\pi}$  are the missing, electron, proton and pion momentum four vectors,  $E$  is the beam energy,  $M_d$  is the deuteron mass,  $M_N$  is the nucleon mass, and  $M_\pi$  is the pion mass.

If the squared missing mass of an event is consistent with the nucleon mass, we check

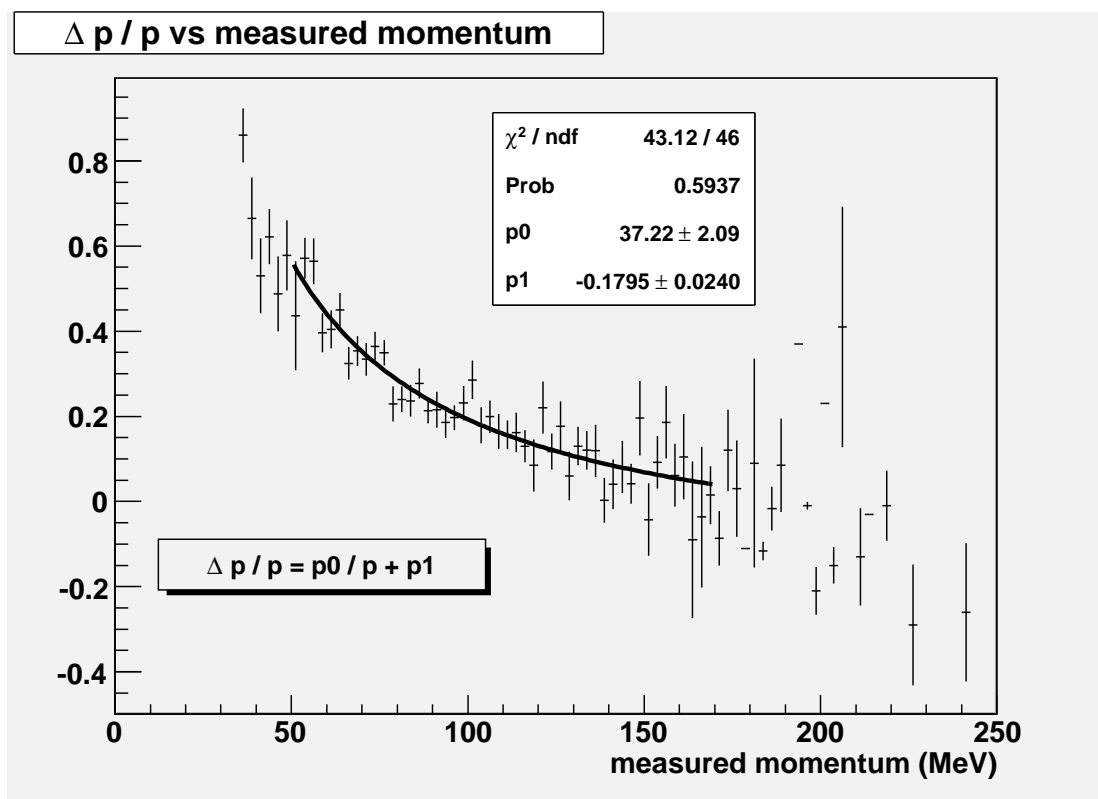


Figure 5.64: A plot of raw  $\Delta p/p_s$  versus measured  $p_s$  where  $\Delta p$  is the difference between the inferred and measured momentum in real data. The fit has the form  $\Delta p/p_s = p_0/p_s + p_1$  and the values of the parameters are noted in the figure.

for a particle in the RTPC that passes all of our standard track quality cuts and compare the CLAS and RTPC momentum of the spectator proton. The result of this comparison, after applying the energy-loss correction to the RTPC spectator proton, can be viewed in the plots in Figs. 5.65a and 5.65c. Here the combined CLAS-RTPC momentum resolution of 17% is quite good. However on average the inferred momentum is 7.8% larger than the measured momentum. Furthermore, the shape of the corrected  $p_s$  is wrong — it does not match the spectator momentum distribution model expected from the Bonn potential.

If we instead ignore the simulated energy-loss correction and simply make a linear fit to  $\Delta p = p_{miss} - p_{RTPC}$  versus  $p_{RTPC}$ , where  $p_{RTPC}$  is the uncorrected momentum measured by the RTPC (see Fig. 5.64) we do a much better job of measuring  $p_s$ . This technique shows promise because the resulting shape of the momentum distribution matches the expected shape from a realistic model, and the offset of the mean between the measured and expected

$p_s$  is consistent with zero (Figs. 5.65b and 5.65d). One might consider simply applying the empirical correction only. However, when the empirical correction was applied to all events with a spectator proton, the mean of the quasi-elastic peak's invariant mass (should be the neutron mass) differed from the expected value of 940 MeV (see Figs. 5.65e and 5.65f). Therefore, because (1) the energy loss correction fully takes into account the actual detector system and (2) the correction from simulation is a function of reconstructed  $\theta$ ,  $z$  and  $r$  of the spectator (not just the measured raw momentum) this analysis will use the energy loss correction from the simulation, despite the apparent misrepresentation of measured momentum.

One could also envision using the predicted spectator momentum to extract calibration constants for the drift velocity in the RTPC. This technique was attempted but the result obtained could not match the quality of the procedure outlined in Sec. 5.2. This study needs more time to develop and may yield a better calibration for future analysis projects.

### 5.6.3 Radiative Corrections

The cross section in Eq. 2.9 is only an approximation of the actual physical processes which occur during lepton-nucleon scattering. The one photon exchange (OPE) approximation is the lowest order Feynman diagram and is known as a *tree-level* diagram because it contains no loops (Fig. 5.66a). Higher order contributions need to be taken into account in order to calculate the measured (radiated) cross section and compare it to the OPE (also known as the Born) approximation. The next orders in perturbation theory (order  $\alpha$ ) include (in Figs. 5.66b, c, and d) *vacuum polarization* (modification to photon structure by a virtual  $e^+e^-$  pair), *vertex correction* (a virtual photon is emitted, then reabsorbed by the lepton), and *internal Bremsstrahlung* (where a real photon is emitted before or after the interaction vertex). The higher order process *multi-photon emission* (more than one bremsstrahlung process occurs) is shown in Fig. 5.66e. The radiative effects can take place either internally (at the scattering vertex) or externally (in the target material, before or after the interaction takes place). These processes lead to an energy change to the incoming or outgoing electron. For example, if an electron radiates a photon before interacting with a nucleon, an elastic scatter is more likely to occur [63].

Radiated and Born cross section models were generated by the code of P. Bosted [64] and E. Christy [65], with a treatment of radiative corrections detailed in Ref. [66]. We determined the

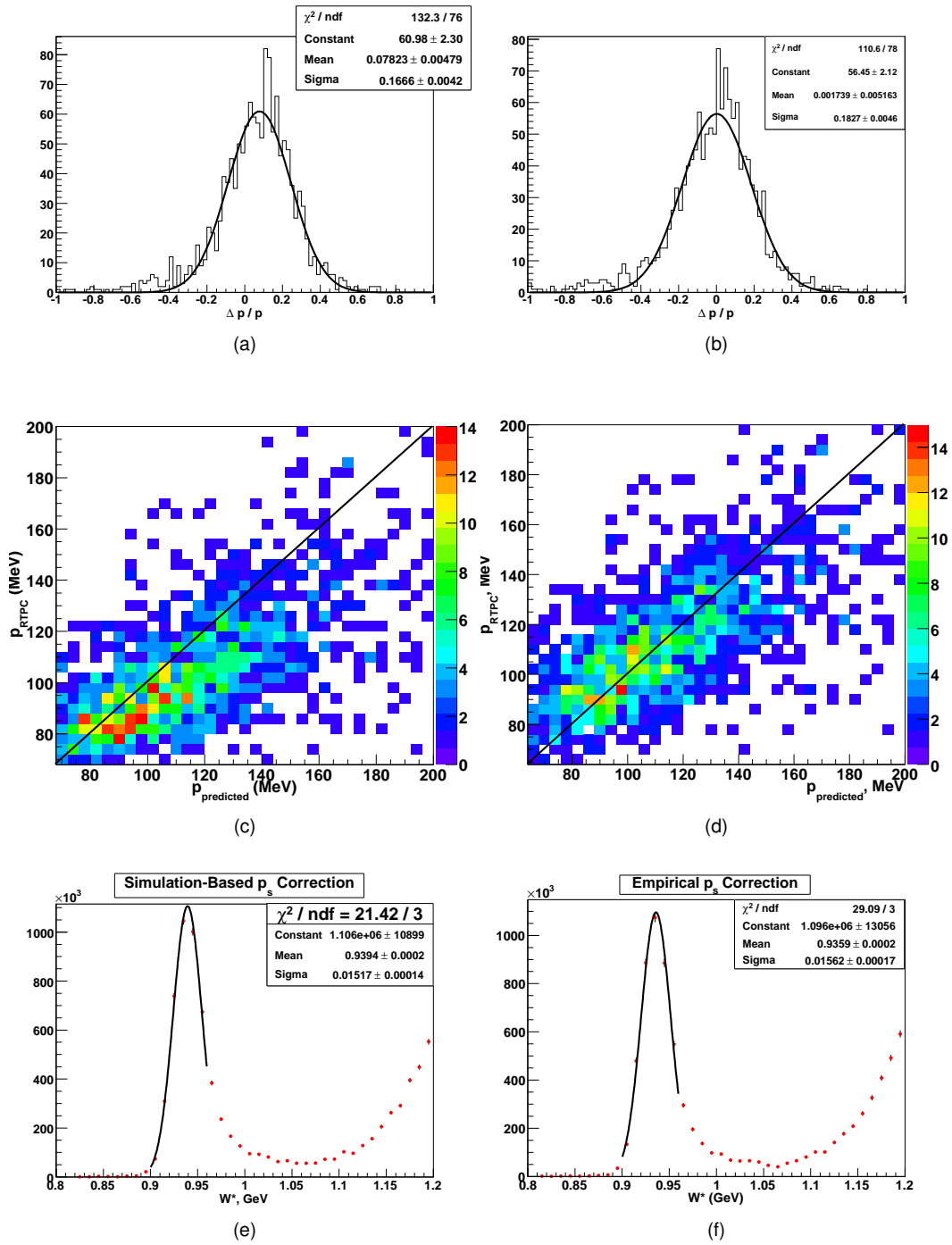


Figure 5.65: Left column is the spectator momentum correction derived from the RTPC simulation. The right column is the empirical momentum correction using the formula in Fig. 5.64. (a) and (b) show the percent difference between the predicted and measured spectator momentum. (c) and (d) show the measured momentum versus the predicted momentum. (e) and (f) show the invariant mass of the final state hadron,  $W^*$ .

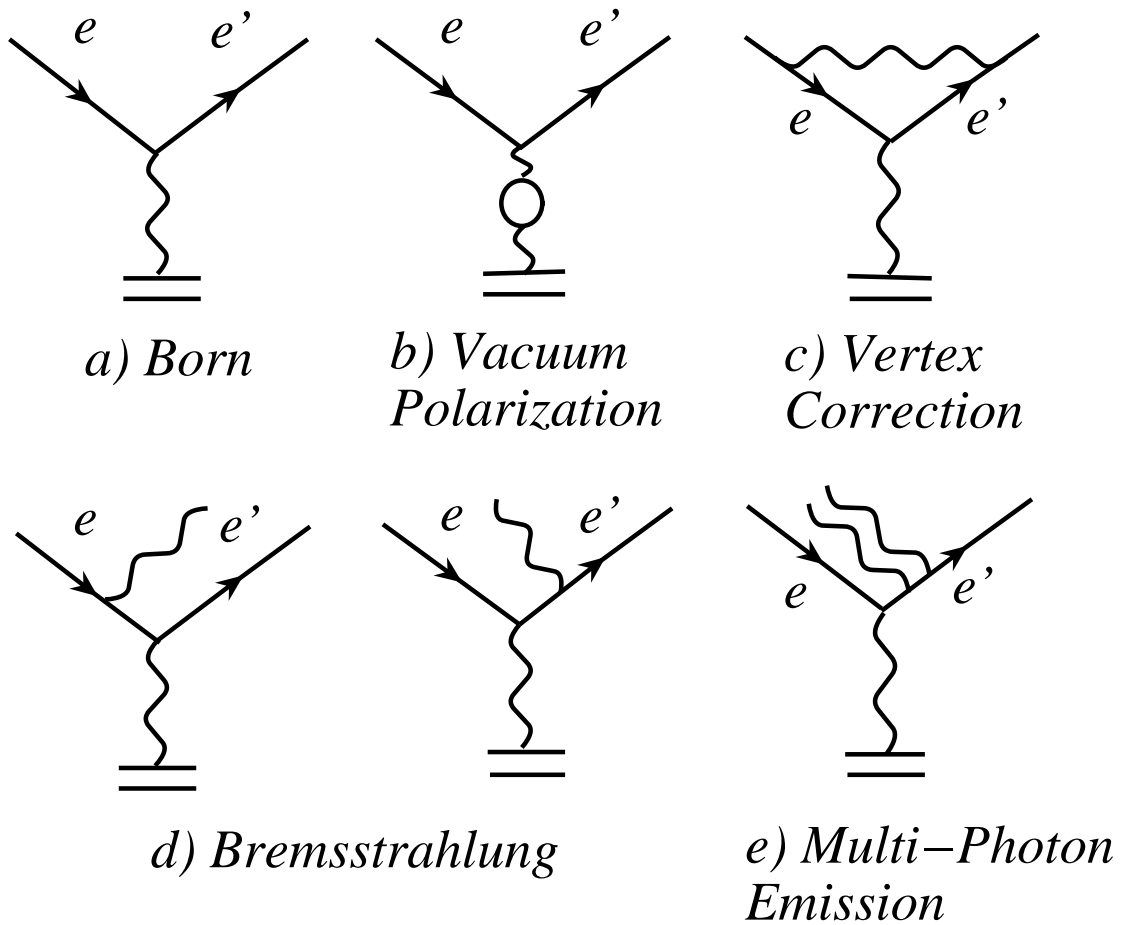


Figure 5.66: a) One Photon Exchange approximation b)-e) Additional Feynman diagrams depicting internal and external processes that need to be taken into account.

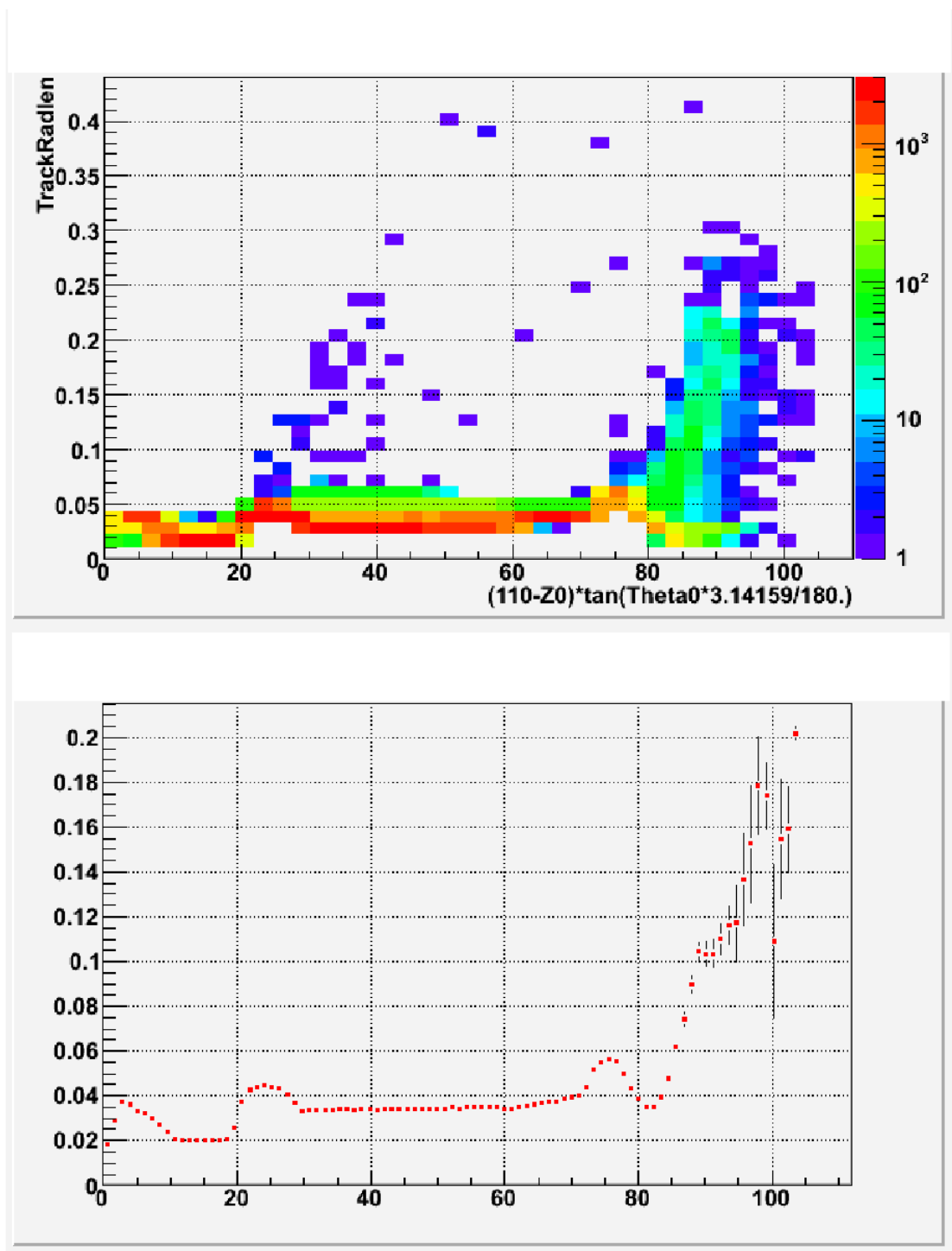


Figure 5.67: The simulated radiation length as a function of the radial position where the electron exits the cylinder defining the RTPC simulation region. A typical forward electron travels through  $\sim 0.04$  radiation lengths in the target.

number of radiation lengths that a scattered electron sees in the target (0.04 - see Fig. 5.67), and the radiated and Born cross sections were generated in the same bins of  $W$  and  $Q^2$  that we bin our *tagged/untagged* ratio. The unpolarized cross section models also provide us the fraction of  $\sigma_r^{n,d}$  coming from the elastic tail in a particular bin. We took care to avoid regions where this fraction was greater than 10%. The radiative correction is expressed as a super ratio to minimize systematic errors. Hence, we can apply a multiplicative correction to the *tagged/untagged* measurement:

$$r_{rc} = \frac{\sigma_{Born}^n / \sigma_r^n}{\sigma_{Born}^d / \sigma_r^d} \quad (5.41)$$

A sample of the super ratio correction ( $1/r_{rc}$ ) is plotted in Figs. 5.68 and 5.69 for the 4 and 5 GeV beam energies. The different curves cover different  $Q^2$  bins. No radiative corrections are applied to our data below  $W = 1.1$  GeV because of the difficulty in getting resolution smearing to work correctly for the neutron elastic peak.

#### 5.6.4 Acceptance and Efficiency

The correction for CLAS electron acceptance was determined as follows: A radiated model of the world's data for inclusive electron scattering on deuterium was provided by P. Bosted [64] and E. Christy [65] (some details of this model were mentioned in the previous section). The first step was to run the analysis code to obtain inclusive  $d(e, e')X$  events binned in  $Q^2$  and  $W$ . Next, we divided these events by the model calculated for the same kinematics, which produced a relative electron efficiency,  $\epsilon(W, Q^2)$  for CLAS. The last row of Fig. 5.70 shows the ratio's dependence on  $W$  for a few  $Q^2$  bins.

Now, for each *tagged*  $d(e, e'p_s)X$  event within the spectator proton cuts both  $W^*$  (proper invariant mass) and  $W$  (nominal invariant mass for a stationary target) were calculated. The variables  $W^*$  and  $Q^2$  define which bin to increment in the  $N_{tag}(W^*, Q^2)$  table of *tagged* events. The calculated  $W$  and  $Q^2$  determine the efficiency to use. Events are accumulated by adding  $1/\epsilon(W, Q^2)$  to the  $(W^*, Q^2)$  bin in the *tagged* table. The corrected ratio of *tagged/untagged*

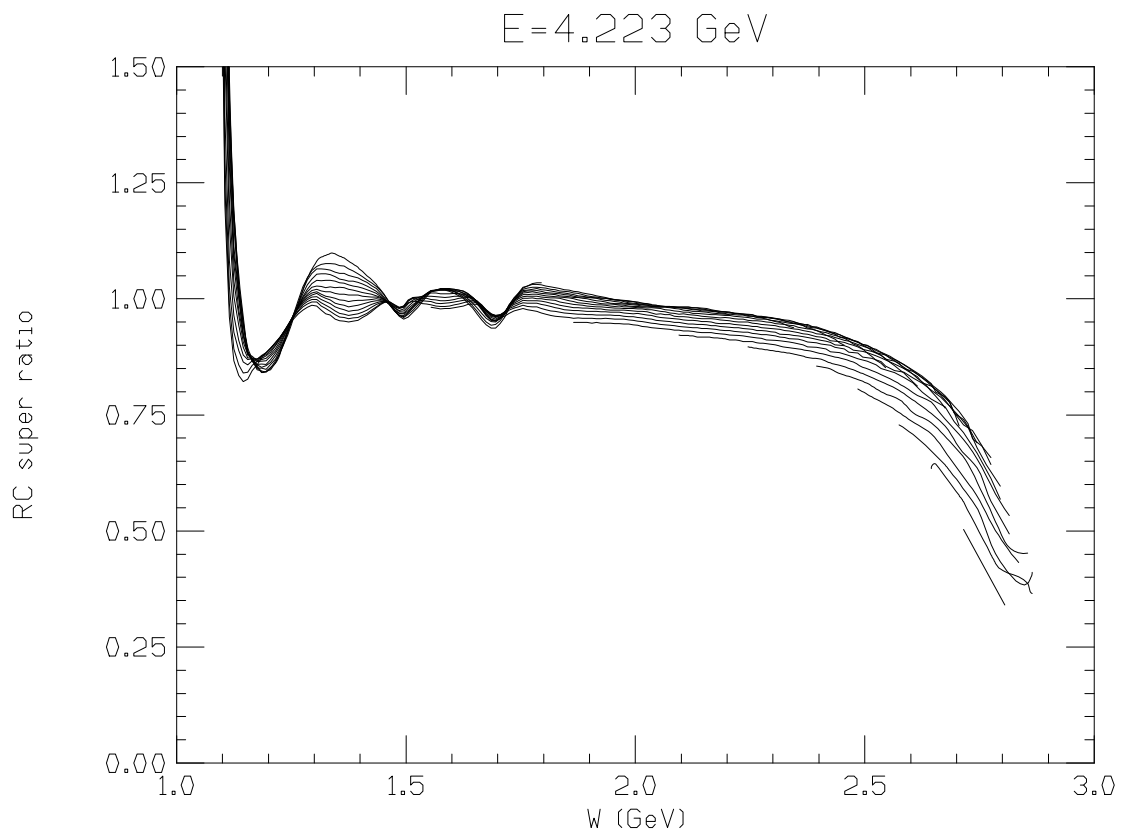


Figure 5.68: The inverse of the super ratio  $r_{rc}$  for  $E_{beam} = 4.223$  GeV. The curves that start at higher  $W$  correspond to lowest  $Q^2$ .

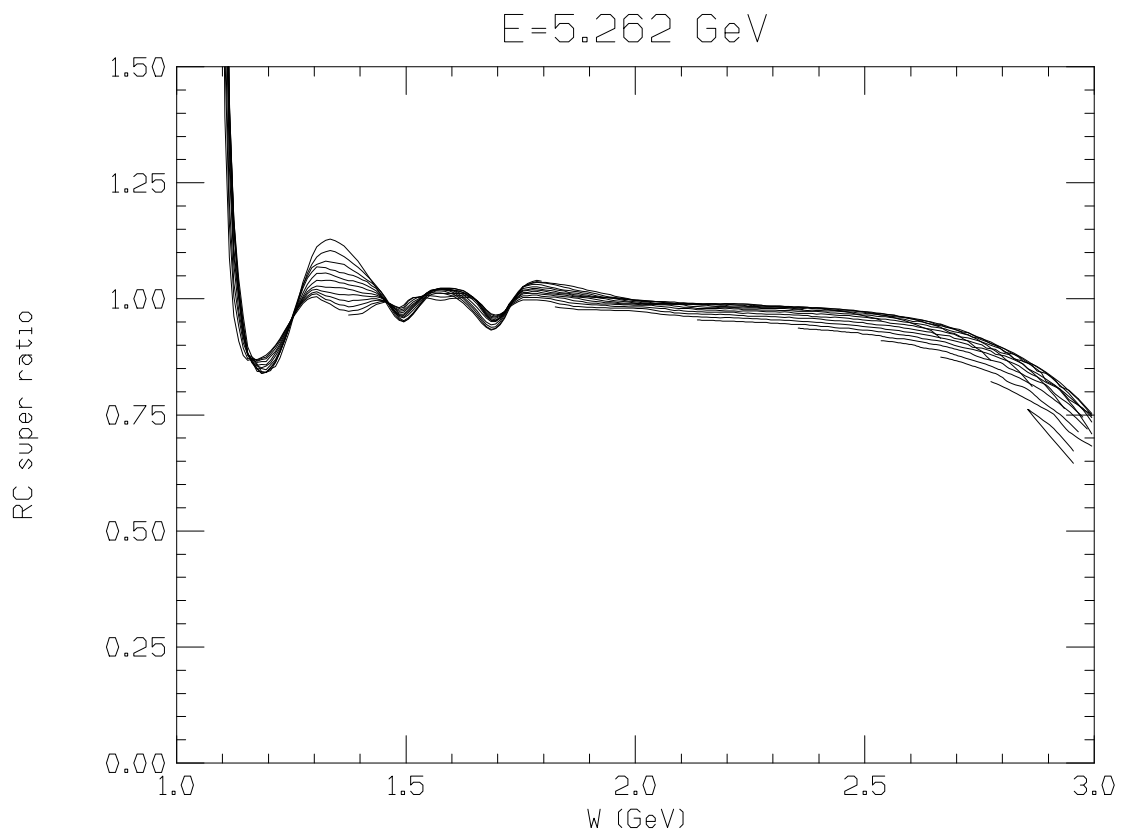


Figure 5.69: The inverse of the super ratio  $r_{rc}$  for  $E_{beam} = 5.262$  GeV. The curves that start at higher  $W$  correspond to lowest  $Q^2$ .

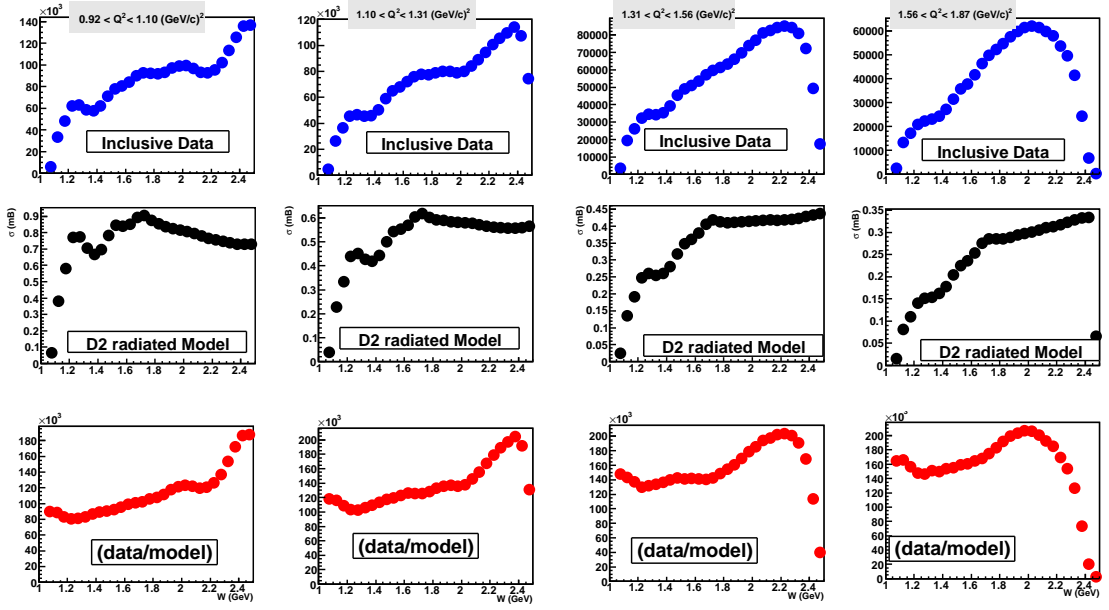


Figure 5.70: The total inclusive electron scattering counts for deuterium (top row), the total radiated deuteron cross section model provided by P. Bosted [64] and E. Christy [65] (middle row) and the ratio of data to model. The plots are all versus invariant mass,  $W$ . Each column corresponds to a different  $Q^2$  bin (only the  $E_{beam} = 4$  GeV data are shown).

counts (with the proper subtraction of accidental backgrounds) becomes:

$$R_{corr} = \frac{\sum_{i=1}^{N_{tag}(W^*, Q^2)} \frac{1}{\epsilon_i(W, Q^2)} - R_{bg} \sum_{j=1}^{N_{bg}(W^*, Q^2)} \frac{1}{\epsilon_j(W, Q^2)}}{\sum_{k=1}^{N_{untag}(W, Q^2)} \frac{1}{\epsilon_k(W, Q^2)}} \quad (5.42)$$

In this way, we properly account for the fact that there are many possible bins in  $W$  that can contribute to a given  $W^*$  bin.

This treatment does not account for the efficiency of the RTPC. J. Zhang's RTPC simulation provides us an acceptance value that is a function of  $W^*$ ,  $Q^2$ , and the spectator kinematics  $p_s$  and  $\theta_{pq}$  (the angle between the spectator proton and the direction of momentum transfer). Unfortunately, at this point, the application of the RTPC acceptance correction to this analysis does not yet give consistently reliable results and will not be used in this analysis. Instead, we have devised a way to correct for the RTPC efficiency by normalizing our ratio of *tagged/untagged* events to the world's cross section ratio data in a kinematical region where  $\sigma_n$  can be extracted

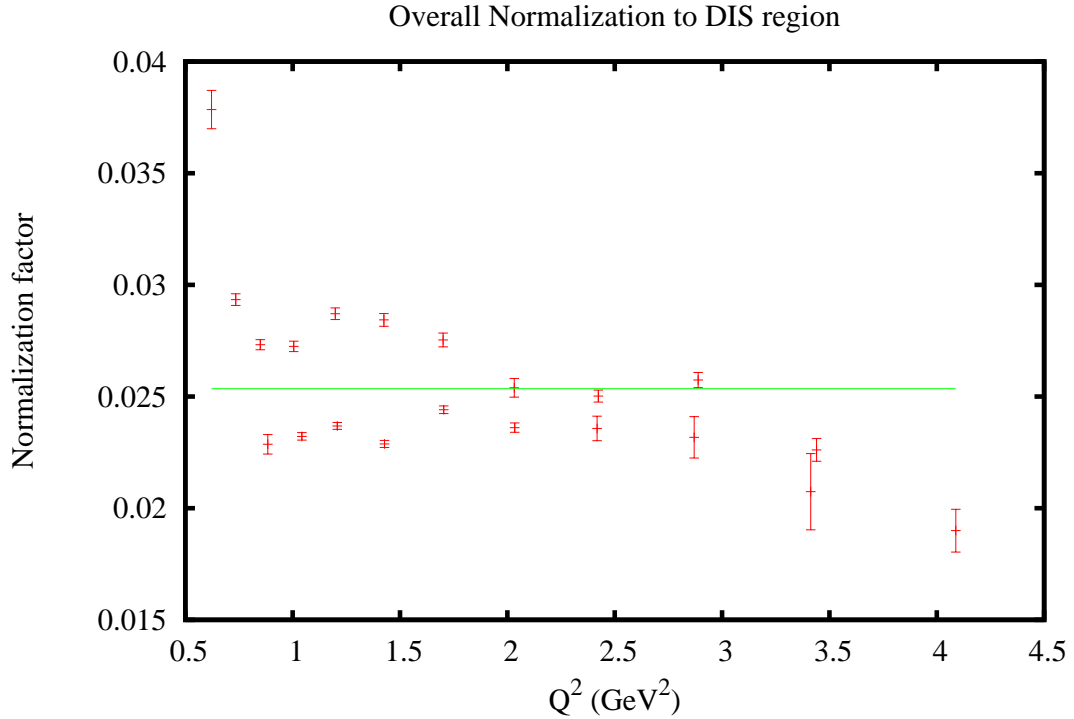


Figure 5.71: The inverse of the overall normalization,  $n$ , as a function of  $Q^2$ . The green line shows the average value used for the final data set. The plot shows the normalization for the  $E = 4.223$  and  $5.262$  GeV data sets, which is why there are two points for some of the  $Q^2$  values.

from deuteron data without a large dependence on model corrections. We have chosen the section of the DIS region at  $x_b = 0.35$ ,  $W > 2.0$  GeV and  $Q^2 > 1.0$  GeV<sup>2</sup>. The normalization, simply referred to from now on as  $n$ , is found to be  $n = 1/0.02535 \pm 3.37\%$ , where the error corresponds to the rms variation of  $n$  for the multiple  $Q^2$  bins. This was the average value of  $n$  obtained from an analysis of the  $E_{beam} = 4.223$  and  $5.262$  GeV data sets. Fig. 5.71 suggests that  $n$  may have a slight  $Q^2$  dependence, but it appears to be small and can be added into the systematic error on the *tagged/untagged* ratio as a 5% normalization error.

### 5.6.5 Pion and Charge Symmetric Background Contamination

This section describes the correction procedure for pion background and pair symmetric contamination using the CLAS EG1B parameterizations of N. Guler [67]. We assume that the EG1B  $\pi^-/e^-$  and  $e^+/e^-$  ratios are similar to those of the BoNuS experiment. We use N.

Guler's routine to calculate the amount of contamination for each beam energy. We interpolate to our beam energies and use a weighted average of the two ratios  $r_{NH_3}$  and  $r_{ND_3}$ , for ammonia and deuterated ammonia targets that allows us to extract ratios for the neutron and deuteron. The superscript  $X$  represents either  $\pi^-$  or  $e^+$  events, depending on which background we're interested in. The quantity  $\sigma_t^X$  stands for the probability of detecting particle  $X$  emerging from target  $t$ .

The 10 protons and 8 neutrons in  $NH_3$  and the 10 protons and 11 neutrons in  $ND_3$  lead to the following definitions:

$$r_{NH_3} \equiv \frac{\sigma_{NH_3}^X}{\sigma_{NH_3}^e} = \frac{10\sigma_p^X + 8\sigma_n^X}{10\sigma_p^e + 8\sigma_n^e}, \quad (5.43)$$

$$r_{ND_3} \equiv \frac{\sigma_{ND_3}^X}{\sigma_{ND_3}^e} = \frac{10\sigma_p^X + 11\sigma_n^X}{10\sigma_p^e + 11\sigma_n^e}. \quad (5.44)$$

For the BoNuS case, we are interested in the contamination ratios for a neutron target ( $r_n$ ), a deuteron target ( $r_d$ ), or a proton target ( $r_p$ ). We use the estimation here that  $\sigma_n$  inside a nucleus equals  $\sigma_n$  for a free neutron. Now we make the following definitions:

$$r_n \equiv \frac{\sigma_n^X}{\sigma_n^e}, r_p \equiv \frac{\sigma_p^X}{\sigma_p^e} \quad (5.45)$$

$$r_d \equiv \frac{\sigma_d^X}{\sigma_d^e} = \frac{\sigma_n^X + \sigma_p^X}{\sigma_n^e + \sigma_p^e} = \frac{Rr_n + r_p}{R + 1} \quad (5.46)$$

We've defined  $R = \sigma_n^e/\sigma_p^e$  and we use the value for  $R$  from P. Bosted's published parameterization of the world's data ([64] and [65]). We can rewrite Eqs. 5.43 and 5.44 as

$$r_{NH_3} = \frac{10\sigma_p^X + 8\sigma_n^X}{(10/R + 8)\sigma_n^e} = \frac{10\sigma_p^X + 8\sigma_n^X}{(10 + 8R)\sigma_p^e}, \quad (5.47)$$

$$r_{ND_3} = \frac{10\sigma_p^X + 11\sigma_n^X}{(10/R + 11)\sigma_n^e} = \frac{10\sigma_p^X + 11\sigma_n^X}{(10 + 11R)\sigma_p^e}. \quad (5.48)$$

The quantities necessary for BoNuS,  $r_n$  and  $r_p$ , can be expressed as the following linear combinations of the EG1B ratios,

$$r_n = \frac{1}{3}(- (10/R + 8)r_{NH_3} + (10/R + 11)r_{ND_3}) \quad (5.49)$$

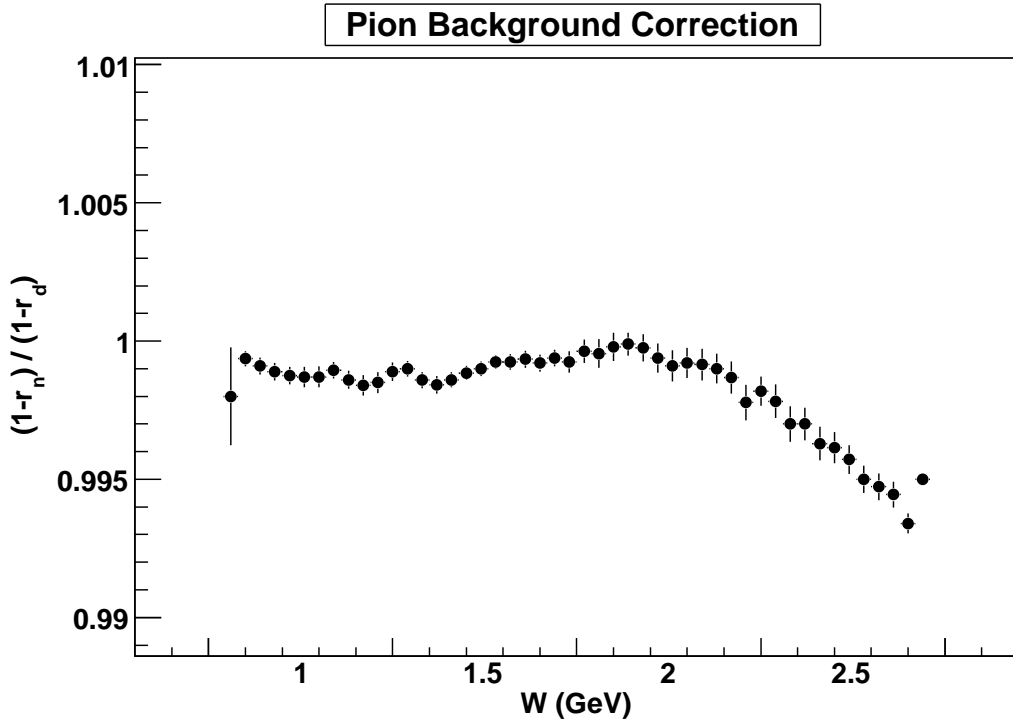


Figure 5.72: The correction to the *tagged/untagged* ratio due to  $\pi^-$  contamination.

$$r_p = \left(\frac{10}{8} - \frac{10}{11}\right)^{-1} \left(\frac{1}{8}(10 + 8R)r_{NH_3} + \frac{1}{11}(10 + 11R)r_{ND_3}\right) \quad (5.50)$$

Now the correction to the BoNuS measured *tagged/untagged* count ratio is,

$$R_{\text{raw}} = \frac{\text{tagged}}{\text{untagged}} = \frac{\sigma_n}{\sigma_d} \quad (5.51)$$

$$R_{\text{corr}} = \frac{(1 - r_n)\sigma_n}{(1 - r_d)\sigma_d} = C_X R_{\text{raw}} \quad (5.52)$$

where, as before,  $X = \pi$  or  $e^+$ . The correction factor,  $C_X$ , extracted from EG1B's result for the ratio of  $\pi/e$  is plotted in Fig. 5.72. The correction factor extracted from EG1B's result for the ratio of  $e^+/e^-$  is plotted in Fig. 5.73. An attempt was made to estimate just how sensitive the ratio is to the amount of contamination by multiplying  $r_n$  and  $r_p$  by a factor of 10 and recalculating the correction (Figs. 5.74 and 5.75). The error bars are larger for these figures because they were run over fewer statistics. Even in the extreme case where the contamination from  $\pi^-$  and electron's from  $e^+e^-$  pairs is 10 times worse than for the EG1B experiment, it still only

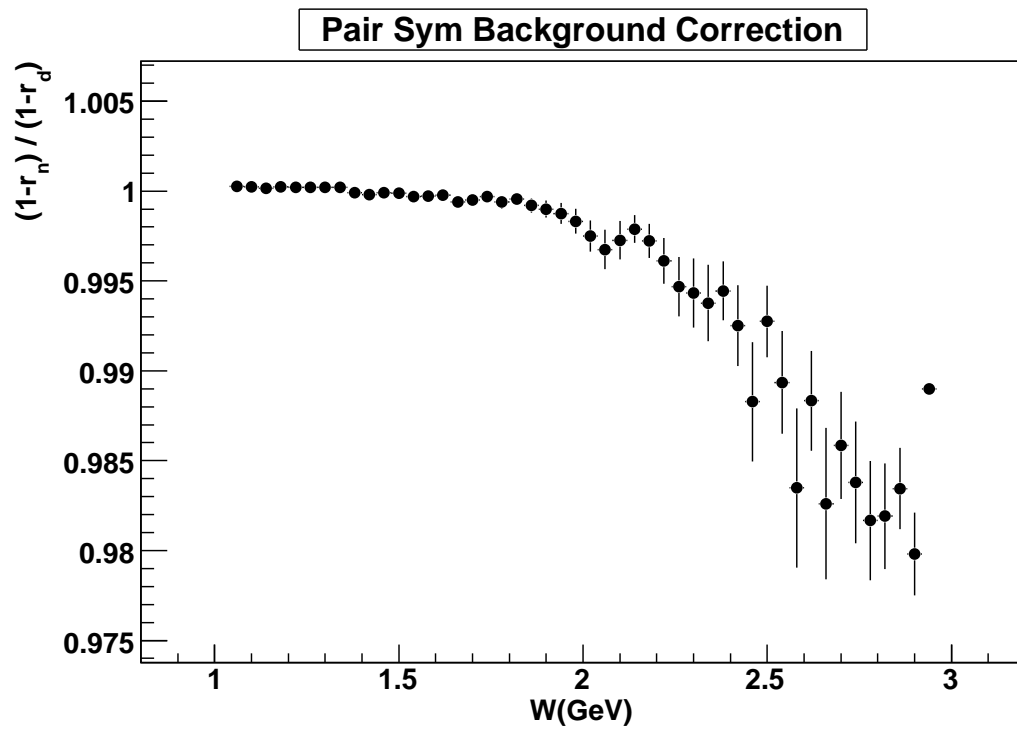


Figure 5.73: The correction to the *tagged/untagged* ratio due to pair symmetric background contamination.

introduces a 5% difference in the *tagged/untagged* ratio at the worst, and in most cases, is less than 1%.

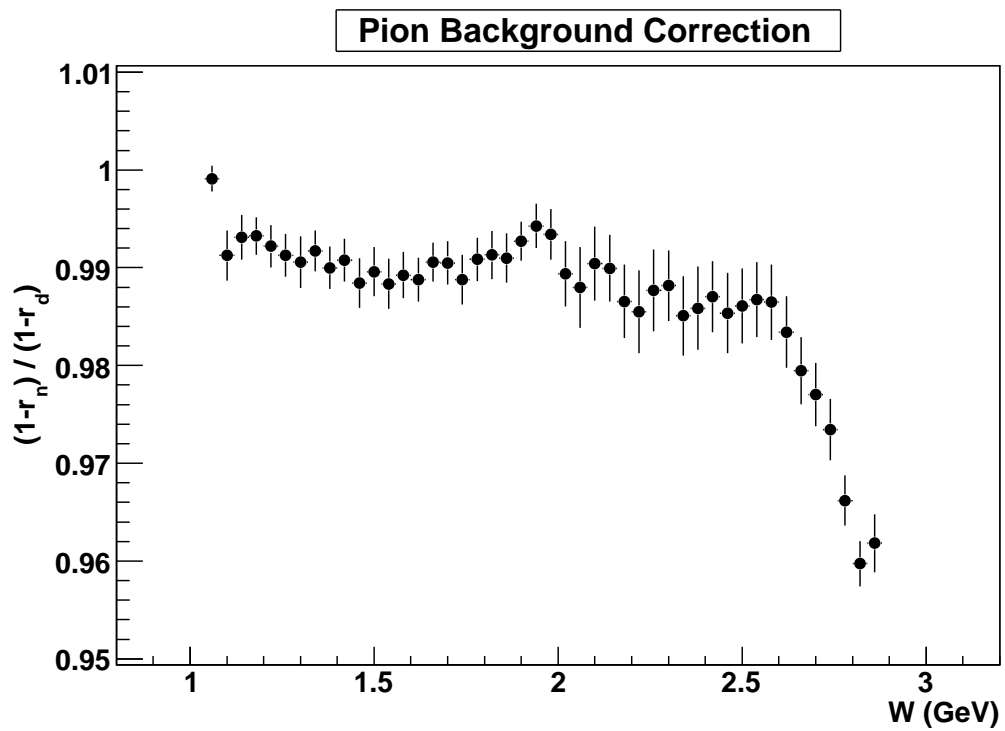


Figure 5.74: The correction to the *tagged/untagged* ratio due to  $\pi^-$  contamination. The factors  $r_n$  and  $r_p$  extracted from EG1B have both been multiplied by a factor of ten

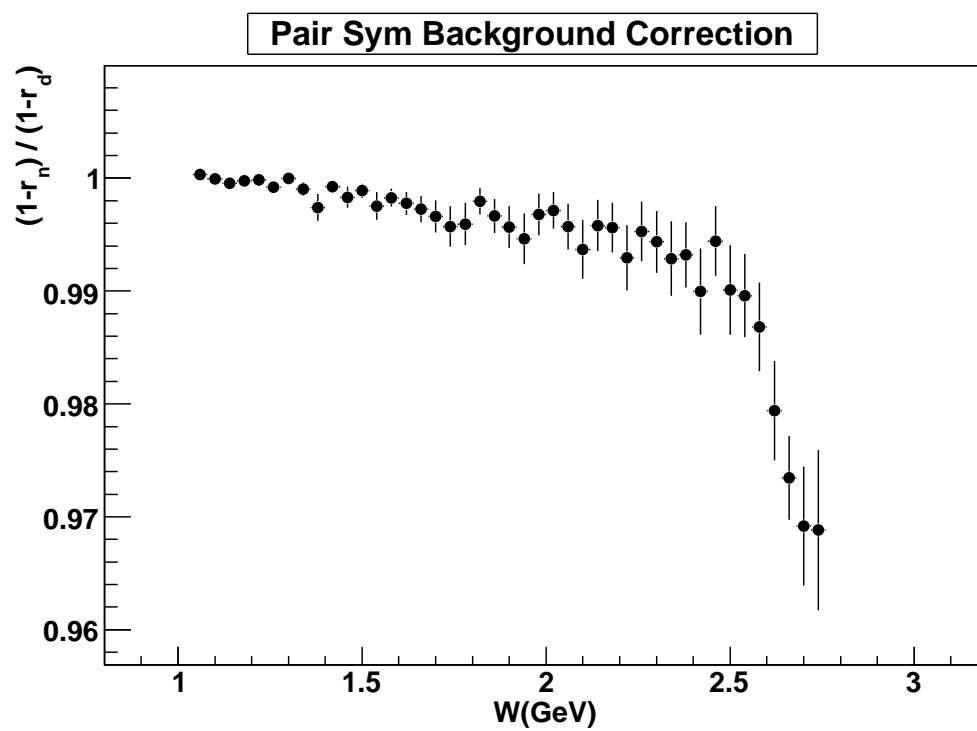


Figure 5.75: The correction to the *tagged/untagged* ratio due to pair symmetric background contamination. The factors  $r_n$  and  $r_p$  extracted from EG1B have both been multiplied by a factor of ten

# Chapter 6

## RESULTS AND CONCLUSIONS

### 6.1 Introduction

This chapter presents the results of the data analysis after applying the corrections outlined in Chapter 5. The technique for the extraction of structure function ratios from the corrected counts is first outlined. A very cursory discussion of the error analysis is presented next. The final section shows our key result for the model independent  $F_2^n/F_2^p$  compared with different treatments of SLAC's measurement of this ratio. Also included is a presentation of a simple extraction of  $d/u$  and a set of  $F_2$  ratios versus  $W$  and  $x$ , compared with the phenomenological models from Refs. [64] and [65].

### 6.2 Structure Function Ratio Extraction

A sample of the *untagged* and *tagged* distributions can be seen in Fig. 6.1. Clearly the calculation of the proper invariant mass of the neutron,  $W^*$ , sharpens the quasi-elastic peak and the resonances begin to take shape as we would expect from inclusive scattering on a free nucleon. Once we have accumulated the corrected *tagged/untagged* counts in bins of  $W$  and  $Q^2$  (see Fig. 6.2 for our kinematic coverage), we can go on to our final step of extracting structure function ratios.

In order to extract  $F_2^n/F_2^p$  it is necessary to put together all the multiplicative corrections from Chapter 5. The background and acceptance corrected *tagged/untagged* ratio,  $R_{corr}$  is given by Eq. 5.42. This ratio is converted to  $F_2^n/F_2^d$  in the following way

$$\frac{F_2^n}{F_2^d} = (R_{corr})(C_{e^+})(C_\pi)(r_{rc})(n) \quad (6.1)$$

where  $n$  is the RTPC efficiency correction found in Sec. 5.6.4,  $C_{e^+}$  and  $C_\pi$  are the pion and pair

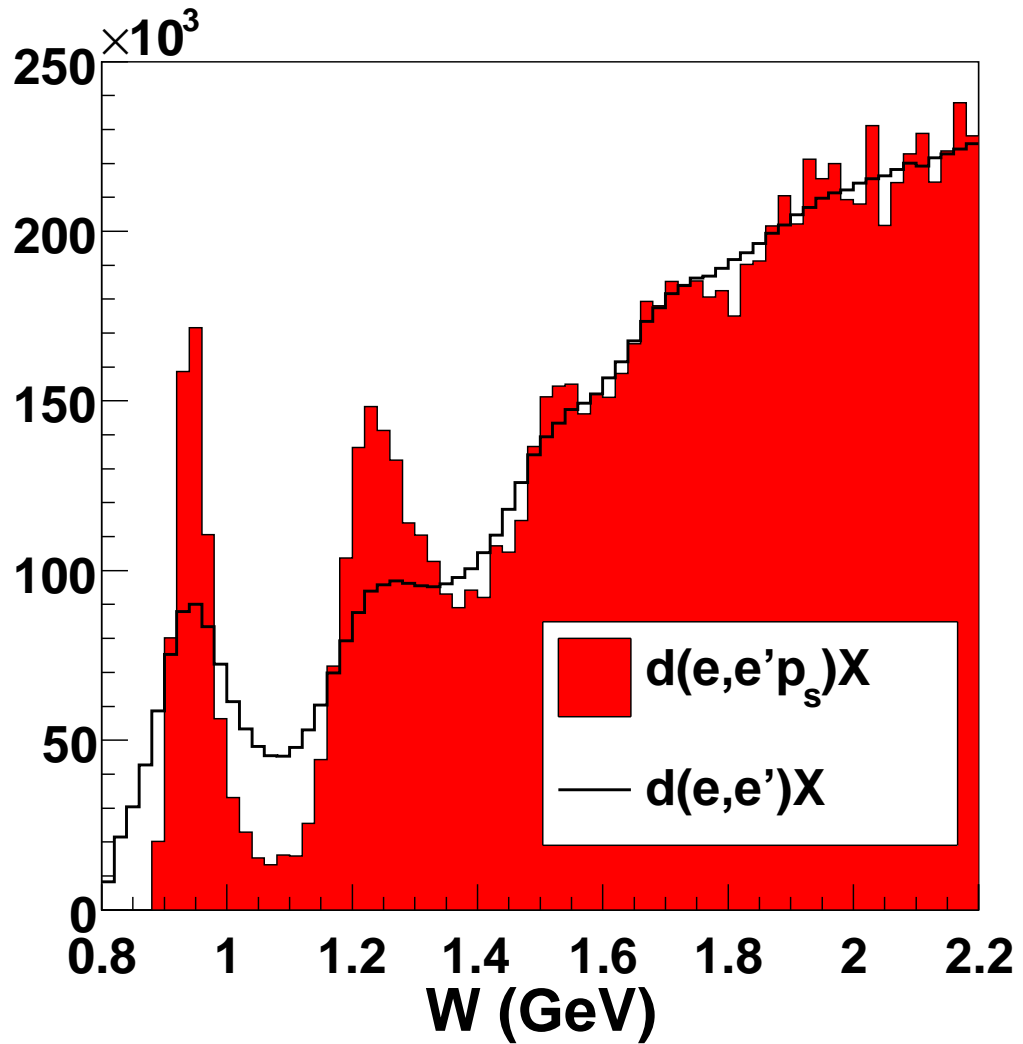


Figure 6.1: Inclusive scattering on deuterium (black line) representing our *untagged* data sample as a function of  $W$  and the corresponding *tagged* sample as a function of the corrected mass  $W^*$ . The data are normalized so that the area under the curves is equal.  $E_{beam} = 4.223$  GeV

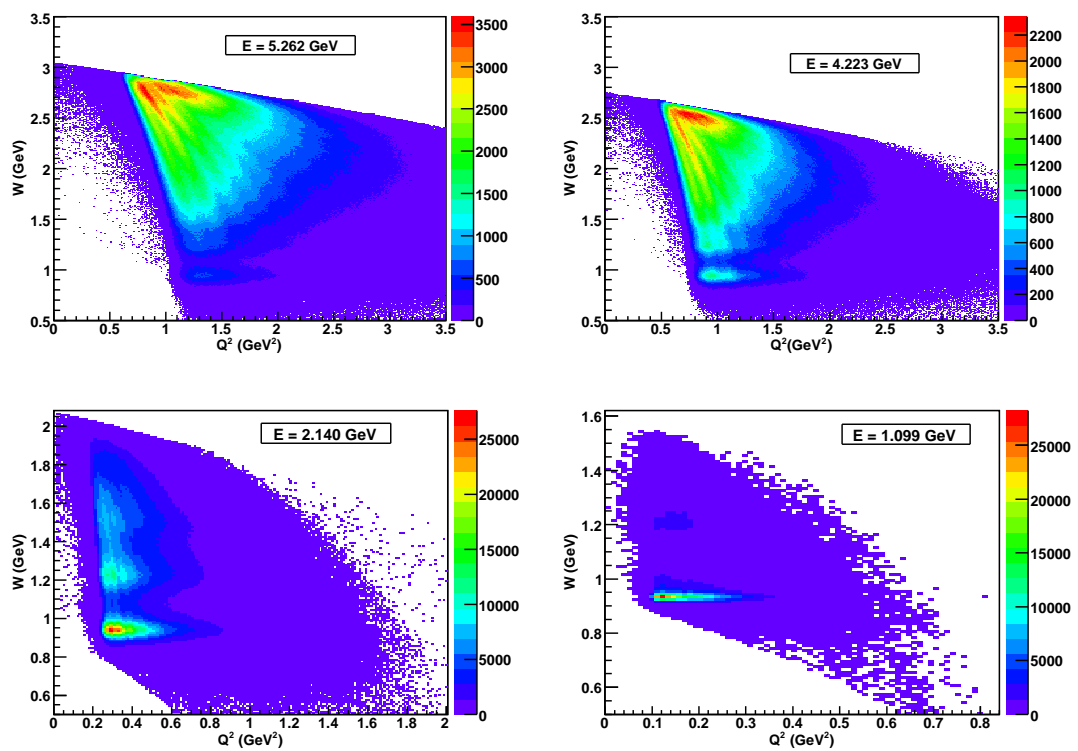


Figure 6.2: The invariant mass and momentum transfer coverage of the BoNuS experiment. This plot contains all deuteron data except for that taken at  $E_{beam} = 1.099$  GeV.

symmetric contamination corrections found by Eq. 5.52,  $r_{rc}$  is the radiative correction super ratio found in Eq. 5.41. Finally  $F_2^d/F_2^p$  is the well-measured and parameterized deuteron to proton structure function ratio,

$$\frac{F_2^n}{F_2^p} = \left( \frac{F_2^n}{F_2^d} \right) \left( \frac{F_2^d}{F_2^p} \right)_{\text{model}}. \quad (6.2)$$

Multiplying Eq. 6.2 by  $F_{2(\text{model})}^p$  provides an extraction of  $F_2^n$ . Also we can further extract a measurement of  $d/u$ , once we have the nucleon structure function ratio, by applying Eq. 2.33.

Since  $W^*$  is always less than  $W$  there is a steep fall off to the *tagged/untagged* ratio at the edge of the experiment's  $W$  acceptance. This is an unavoidable result of the kinematics and can be removed with a simple  $Q^2$ -dependent cut on the maximum invariant mass. This cut has been made on all of the ratio plots in this chapter.

### 6.3 Error Estimation

The statistical error on the acceptance corrected counts is simply  $\sqrt{\sum_{i=1}^N \frac{1}{\epsilon_i^2(W, Q^2)}}$  for each summation in the numerator and denominator, properly propagated through to give the total statistical error on  $R_{corr}$  in Eq. 5.42. The systematic error on each of the multipliers in Eq. 6.1 is given in Table 6.1.

The experimental technique used in this analysis has the advantage of canceling out some typical sources of systematic errors. These errors include, but are not limited to, the EC ID cut, the trigger efficiency, and CC efficiency. Presumably, the normalization error of 5% could be reduced at a later date upon the successful completion of the RTPC efficiency Monte Carlo simulations.

### 6.4 Ratios ( $F_2^n/F_2^d$ , $F_2^n/F_2^p$ , $d/u$ ) and $F_2^n$

This section contains the graphs of the results of the extraction of  $F_2^n/F_2^d$ ,  $F_2^n/F_2^p$ ,  $F_2^n$ , and  $d/u$  from the measured and corrected *tagged/untagged* ratio following the prescription of Eq. 6.1. The ratios in Fig. 6.3 and 6.4 have a cut of  $Q^2 > 1.0 \text{ GeV}^2$  and  $W > 1.6 \text{ GeV}$  applied, with the further requirement that  $Q^2 > 2.0 \text{ GeV}^2$  if  $W < 2.0 \text{ GeV}$  so that we make an extension in  $x$

| Correction Factor    | Estimated Systematic Error (%) | Explanation  |
|----------------------|--------------------------------|--|
| FSI                  | 5.0                            | The uncertainty coming from the effect of final state interactions at spectator kinematics. [31]   |
| Target Fragmentation | 1.0                            | The uncertainty coming from the effect of target fragmentation at spectator kinematics. [26]   |
| Off-Shell            | 1.0                            | The uncertainty coming from the effect of nucleon off-shellness at spectator kinematics. [27]  |
| $C_{e^+}$            | 1.0                            | Assuming our pair symmetric background contamination is less than 10 times than the amount in the EG1B experiment, Fig. 5.75 shows that amount of correction to the ratio is less than 1%. |
| $C_\pi$              | 1.0                            | Same argument as above, only reference Fig. 5.74.  |
| $r_{rc}$             | 2.0                            | Each value of $\sigma_b(E, W, Q^2)$ and $\sigma_r(E, W, Q^2)$ for the neutron and the deuteron has an uncertainty of 1% leading to a 2% error on the ratio.                                |
| $n$                  | 5.0                            | The approximate deviation from a flat normalization as seen in Fig. 5.71.  |
| $F_2^d/F_2^p$        | 4.2                            | The error quoted in [64] and [65] on the fits to the structure functions is 3% which leads to an error of 4.2% on our ratio.   |
| <b>Total Error</b>   | <b>8.7</b>                     | After adding all these errors in quadrature.   |

Table 6.1: The total systematic error on the ratio  $F_2^n/F_2^p$ . Each error is quoted in percentage of the ratio and the estimation explanation is found in the last column.

without much contribution from the resonances. The group of graphs from Fig. 6.5 through 6.22 contain the structure function ratios and  $F_2^n$  as a function of  $W$  and  $x$ , for bins in  $Q^2$  where there were enough counts to be statistically significant. The model of Refs. [64] and [65] that shares these plots is plagued by nuclear corrections so deviations are expected.

## 6.5 Conclusion and Summary

We have made the first measurement of the neutron structure function,  $F_2^n$ , using an almost free neutron target. An encouraging result can surely be seen in Fig. 6.3 for the behavior of the nucleon structure function ratio at moderate  $x$ . The data point at  $x = 0.65$  certainly seems to eliminate the possibility of a simple Fermi correction which fully describes the bound neutron. However, the large statistical error bar on the  $x = 0.75$  point, and the fact that we have extended into the resonance region to extract this result, virtually eliminates the possibility to say anything definitive about the  $d/u$  ratio at high  $x$ . In fact, a 0.5 GeV lower than promised maximum beam energy severely hampered our ability to reach a large  $x$  while staying in the DIS region. Another issue was a reduced data rate from an incompatibility between the CLAS and BoNuS RTPC electronics that was unable to be fixed by the time our experiment was scheduled to run. A repeat of this experiment approved to run after Jefferson Lab's beam is upgraded to 12 GeV will certainly have these two issues solved.

In fact, there are many improvements that can still be made to this analysis. One can continue to try to improve the measured RTPC momentum so that it agrees with predictions from exclusive events or with the shape of the spectator distribution predicted by the deuteron wave function. This is not terribly important for this analysis as can be seen from Fig. 6.1 where the neutron quasi-elastic and resonance structure are clearly visible. This would not be possible if the RTPC was completely mis-measuring the VIP momentum, but it may be that just identifying a VIP is enough to sharpen peak structure. There are still questions within the collaboration as to how to approach this issue. It is very important to have an accurate measurement of  $p_s$  if one wants to characterize the dependence of FSI or off-shell corrections on spectator kinematics and extrapolate down to  $p_s = 0$  MeV/c.

Other improvements that could be made include a proper treatment of the RTPC acceptance / efficiency, an accurate measurement of the pion and pair symmetric contaminations,

a characterization of the amount of helium contamination present in the deuterium target and a technique to subtract this contribution. Attempts were made to address all of these issues during the analysis of this experiment but the projects were not deemed final enough to be included in this dissertation. The next stage would be to extract absolute cross sections from the BoNuS data but this is a much more involved procedure to be completed at a later date. Two other extensions of the BoNuS analysis include a test of Quark Hadron Duality on the neutron and an extraction of the neutron resonance transition form factors.

There is no question that the construction and operation of the RTPC was a wild success. It is clear that the challenge of operating a TPC in the presence of crossed electric and magnetic fields was a daunting one, but not impossible to overcome. The tracking methods developed during this project enabled definite detection of VIPs and the main ideas and lessons learned will be the basis of the later experiments using a BoNuS-like RTPC.

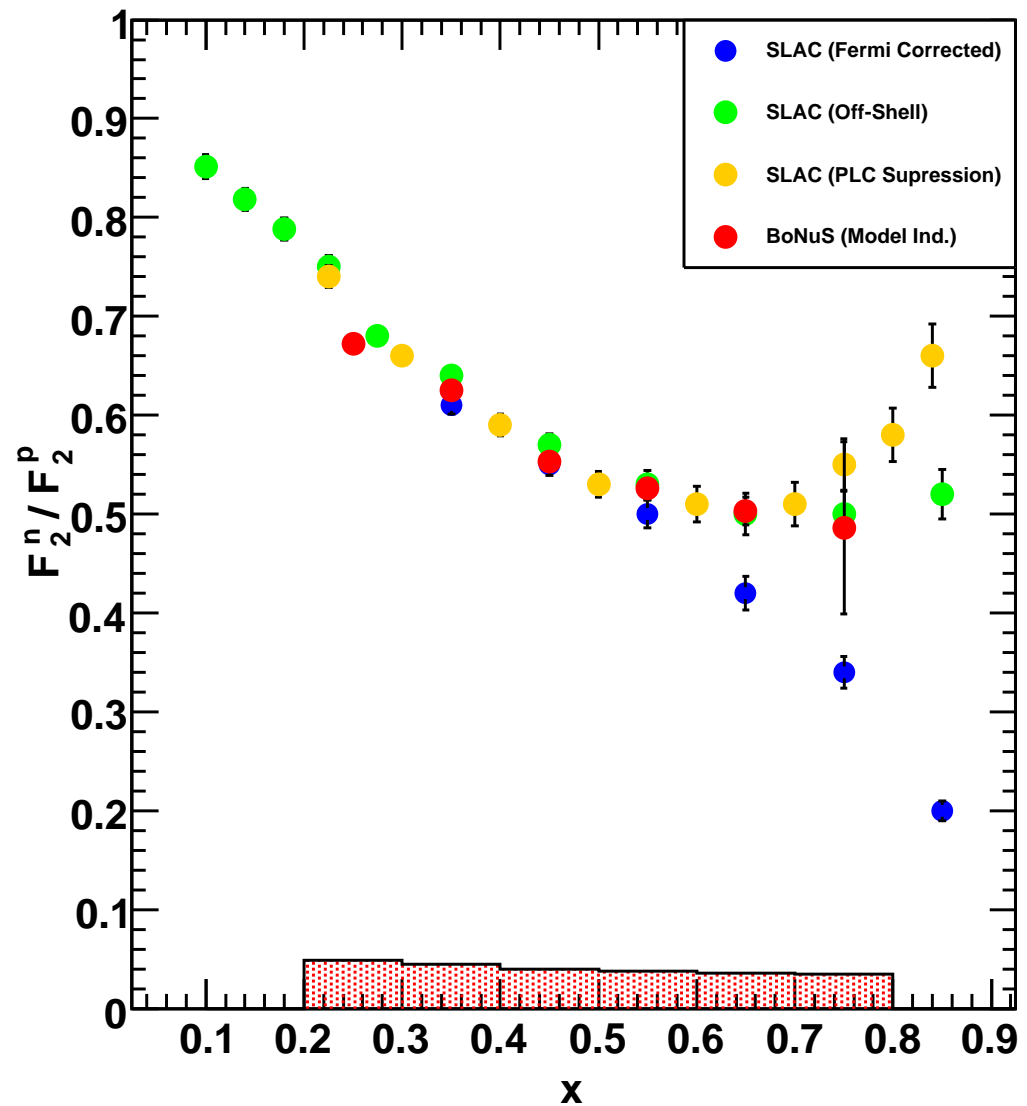


Figure 6.3: The ratio  $F_2^n / F_2^p$  from SLAC and from BoNuS. The SLAC data is from [20] and [21], with different corrections based on Ref. [19]. The BoNuS data (red points) is from the  $E_{beam} = 5.262$  GeV run period, with statistical error bars and total systematic uncertainty shown as an error band on the bottom of each plot.

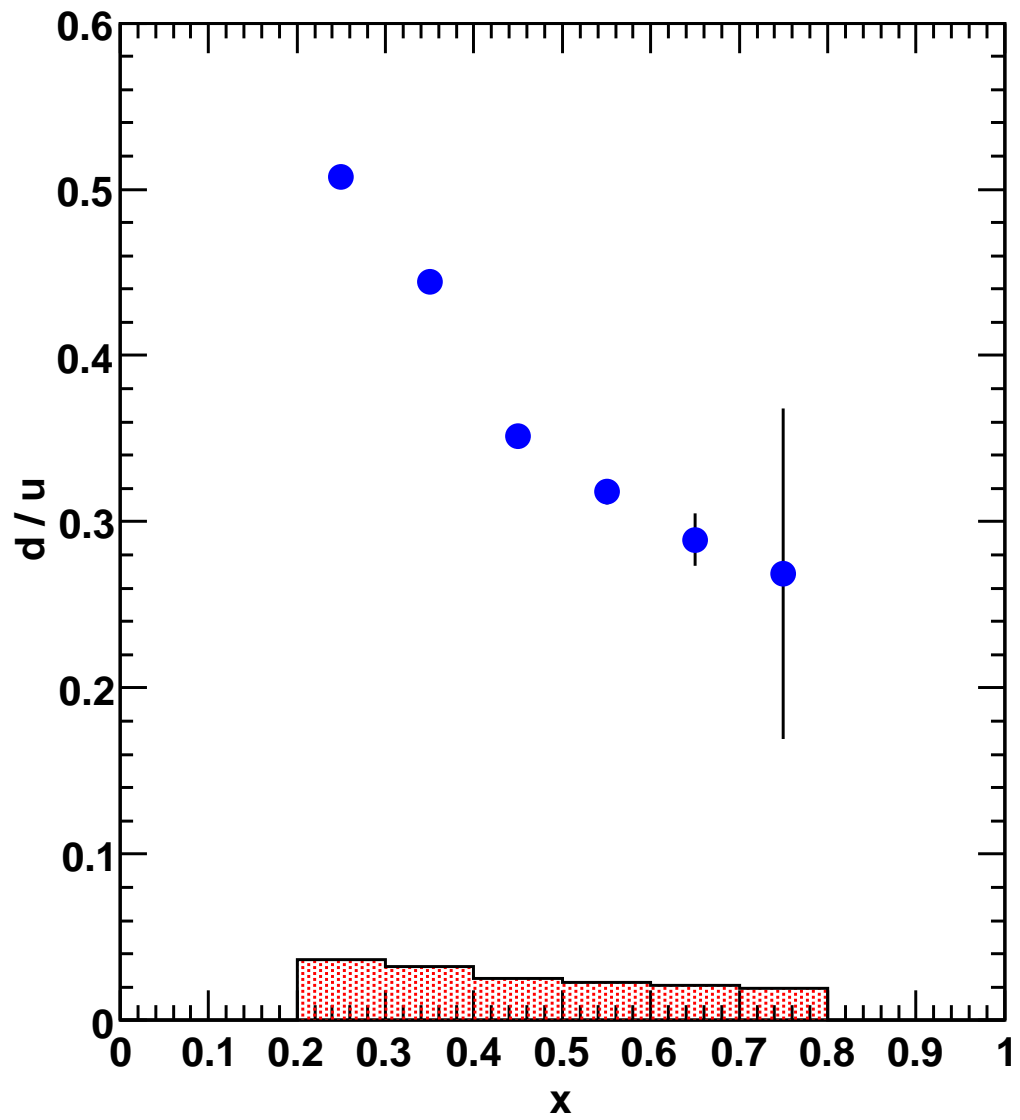


Figure 6.4: The ratio of  $d/u$  extracted from the nucleon structure function ratio, measured by BoNuS. The error bars are statistical and the error band shows the systematic error.

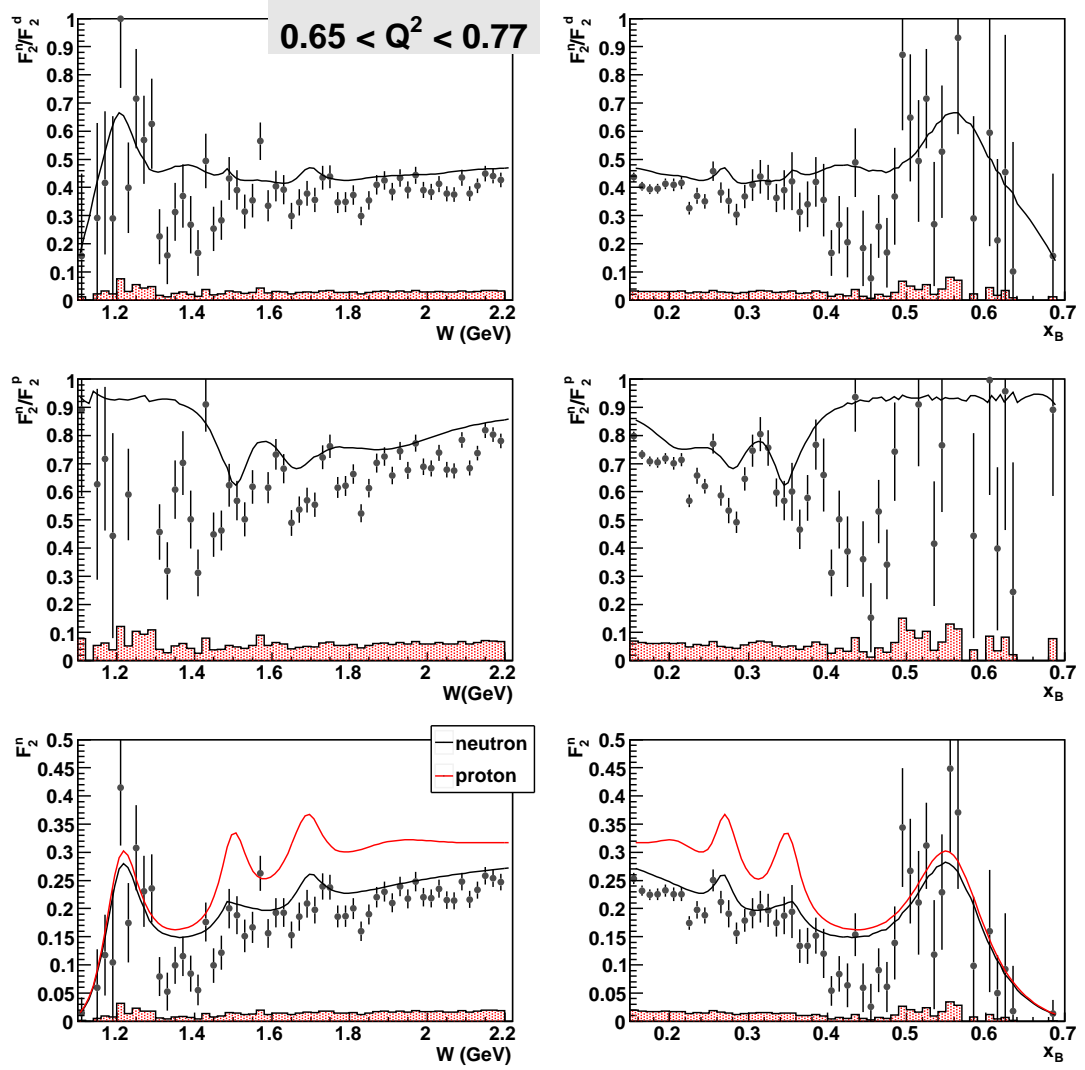


Figure 6.5:  $F_2^n/F_2^d$ ,  $F_2^n/F_2^p$ , and  $F_2^n$  versus  $W$  and  $x$  at  $0.65 < Q^2 < 0.77$  GeV<sup>2</sup>,  $E_{beam} = 4.223$  GeV. The neutron and proton lines are from the phenomenological model of Refs. [64] and [65].

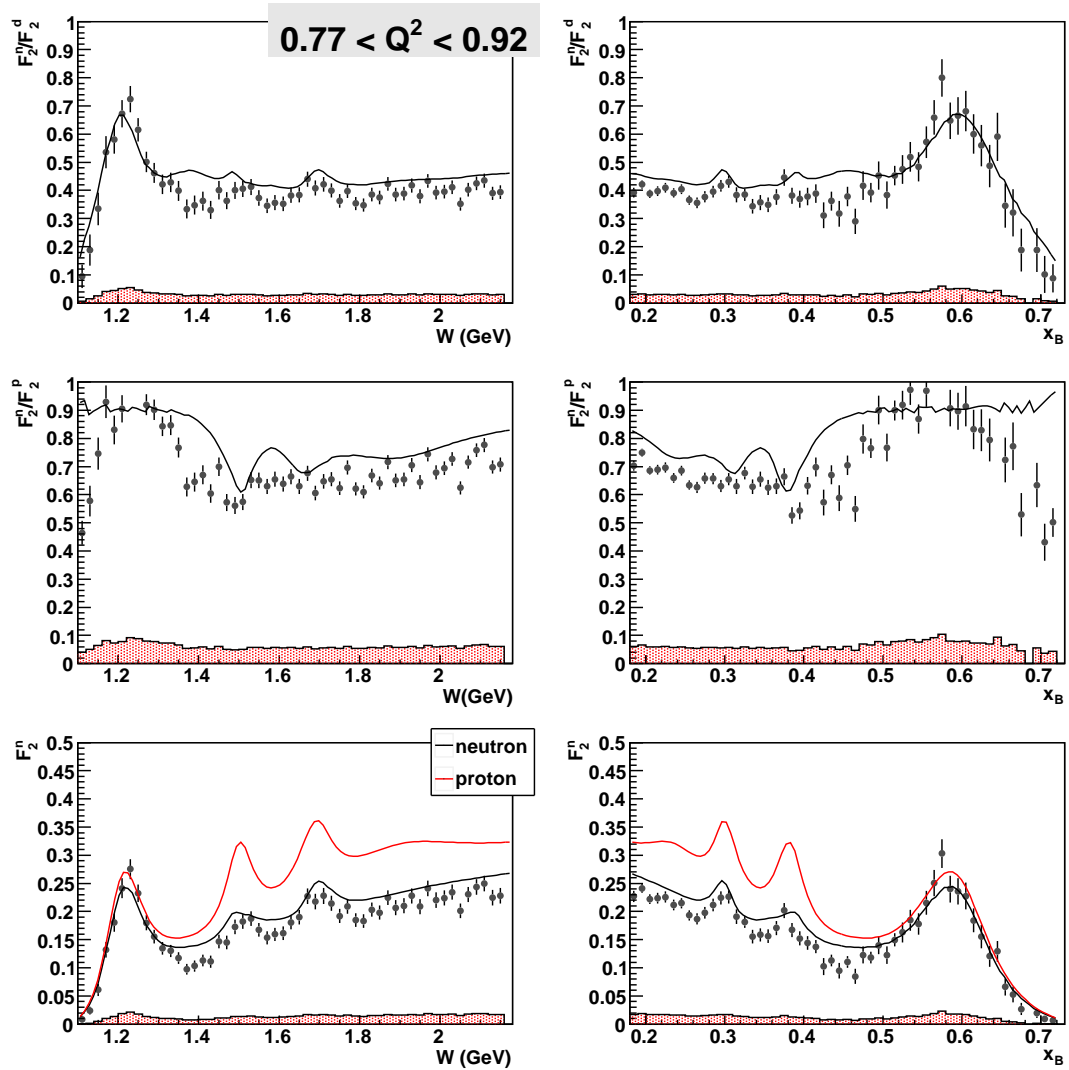


Figure 6.6: Same as Fig. 6.5 but at  $0.77 < Q^2 < 0.92 \text{ GeV}^2$ .

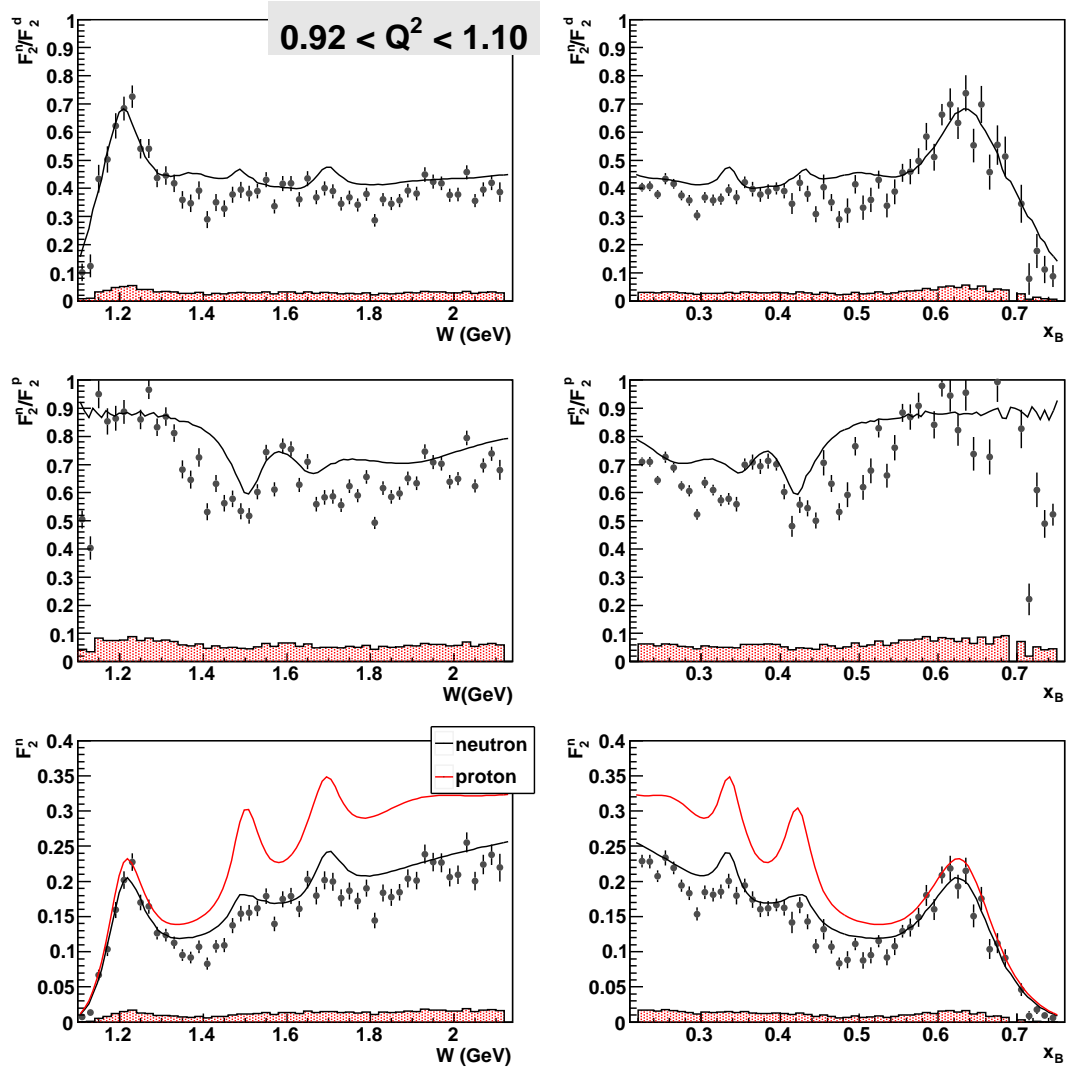


Figure 6.7: Same as Fig. 6.5 but at  $0.92 < Q^2 < 1.10 \text{ GeV}^2$ .

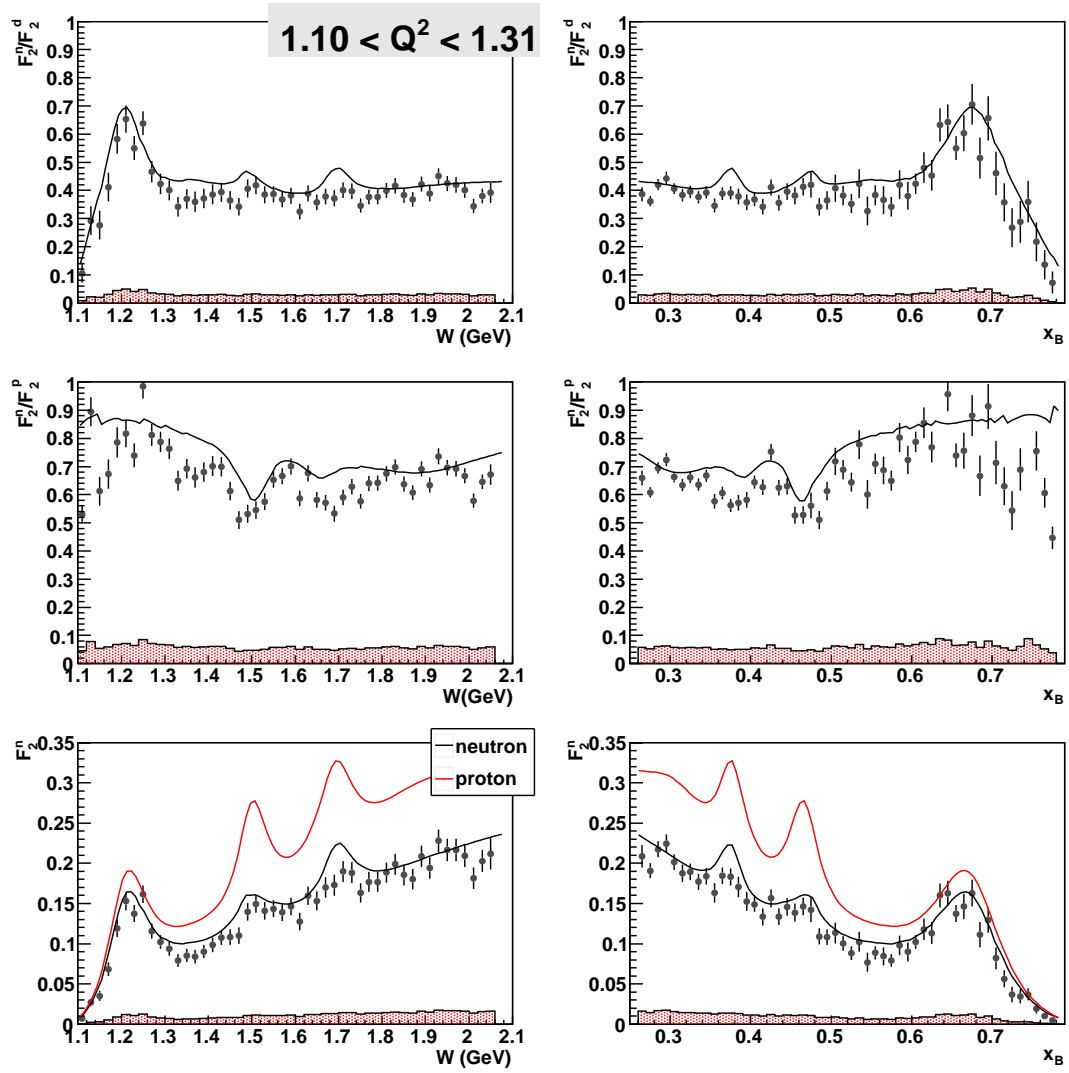


Figure 6.8: Same as Fig. 6.5 but at  $1.10 < Q^2 < 1.31 \text{ GeV}^2$ .

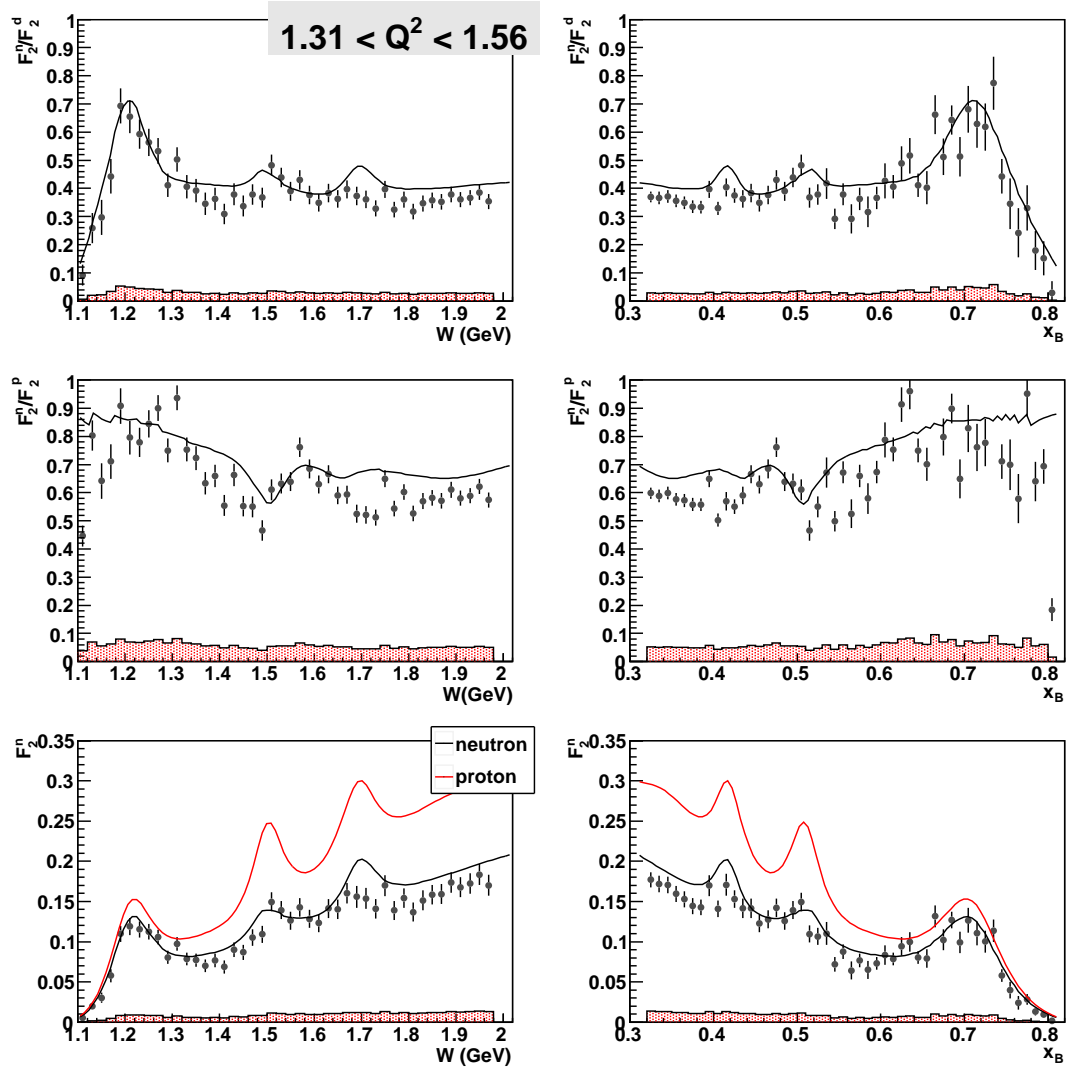


Figure 6.9: Same as Fig. 6.5 but at  $1.31 < Q^2 < 1.56 \text{ GeV}^2$ .

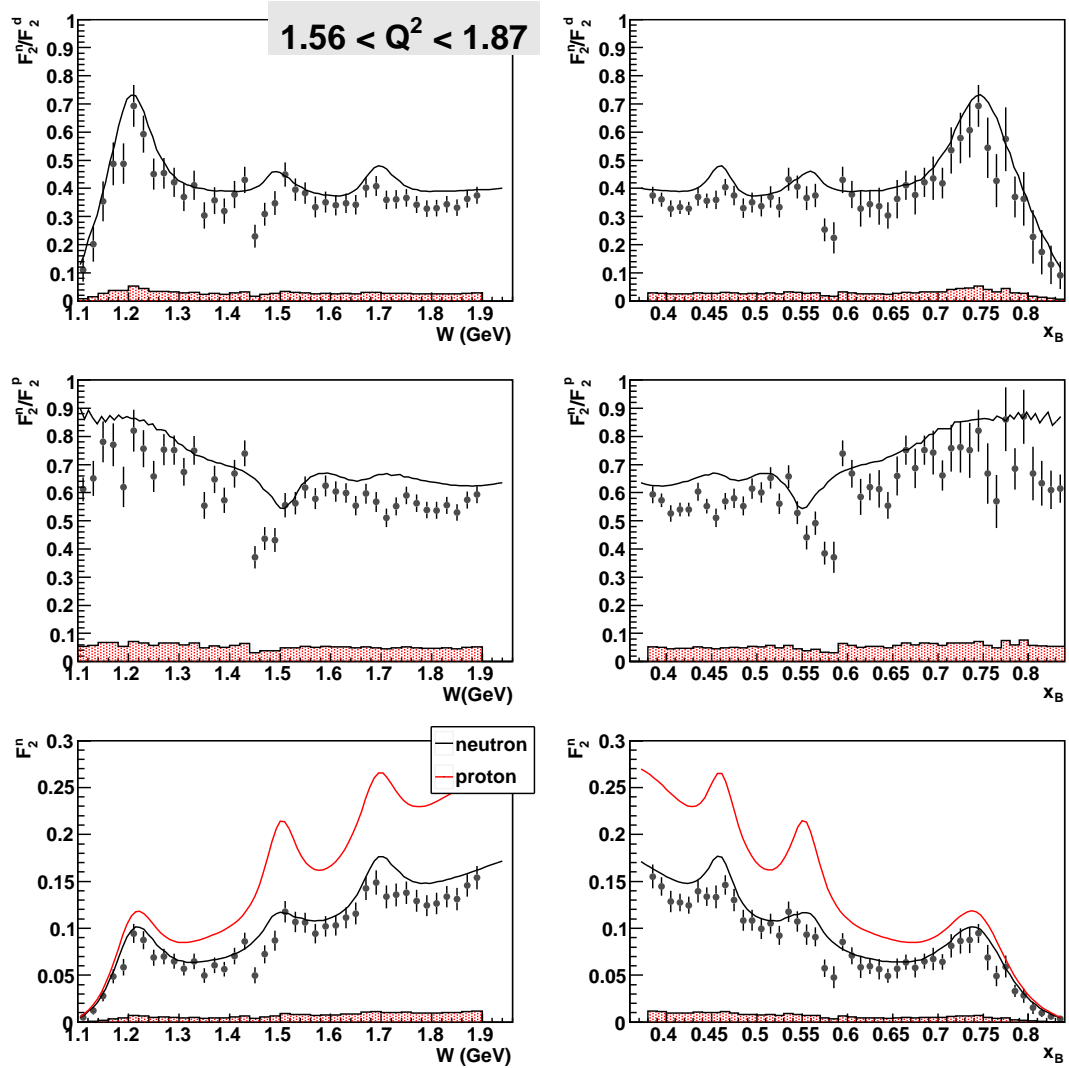


Figure 6.10: Same as Fig. 6.5 but at  $1.56 < Q^2 < 1.87$  GeV<sup>2</sup>.

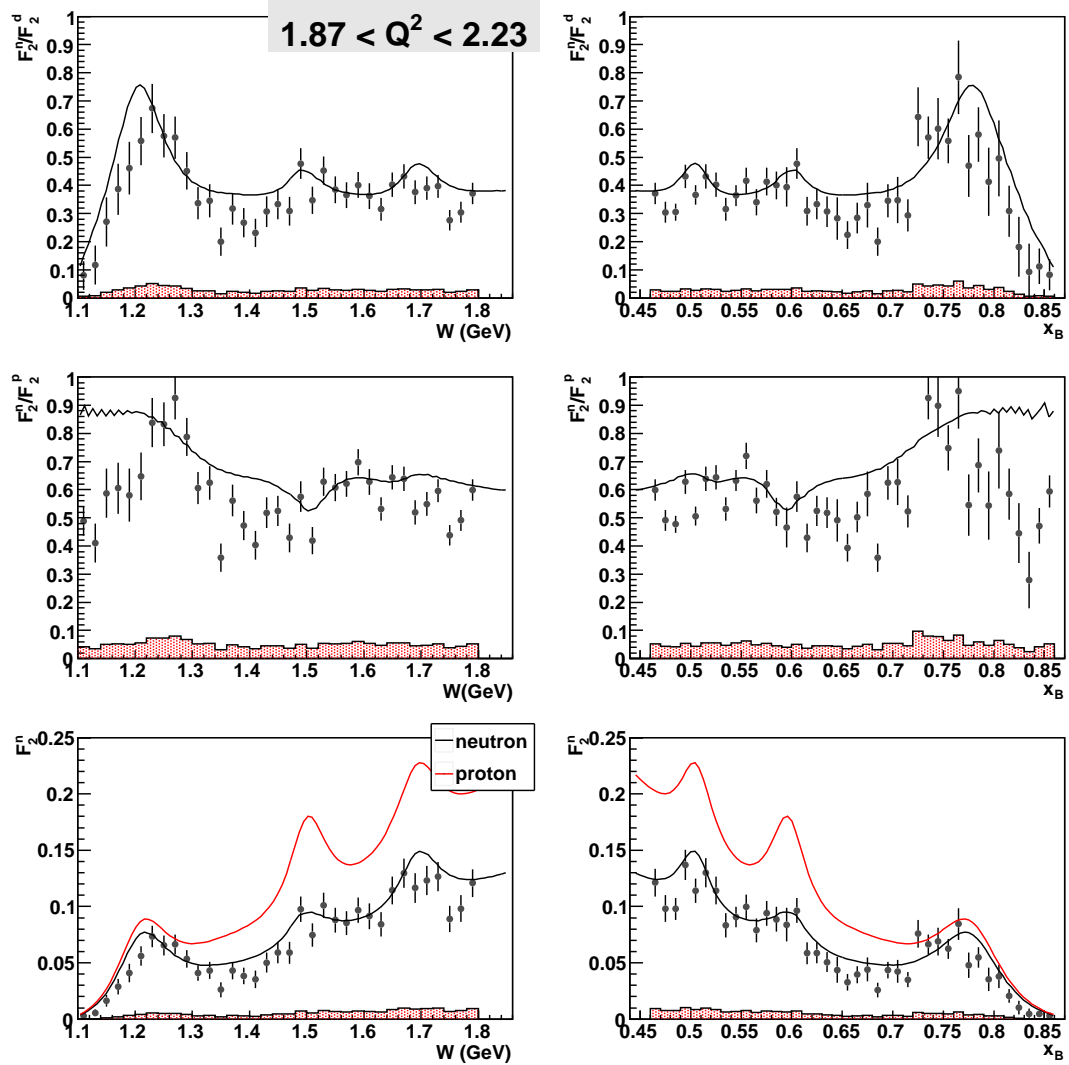


Figure 6.11: Same as Fig. 6.5 but at  $1.87 < Q^2 < 2.23 \text{ GeV}^2$ .

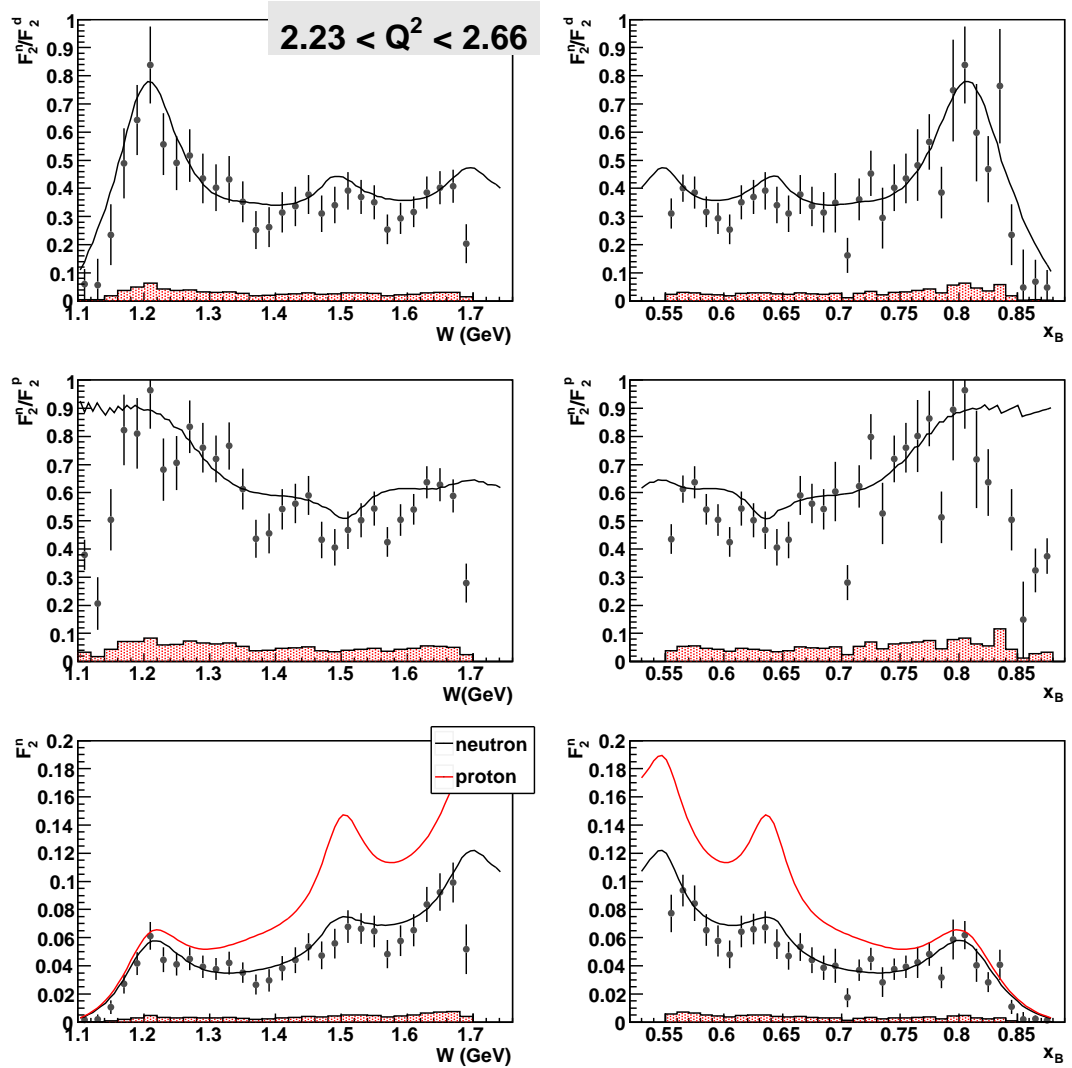


Figure 6.12: Same as Fig. 6.5 but at  $2.23 < Q^2 < 2.66 \text{ GeV}^2$ .

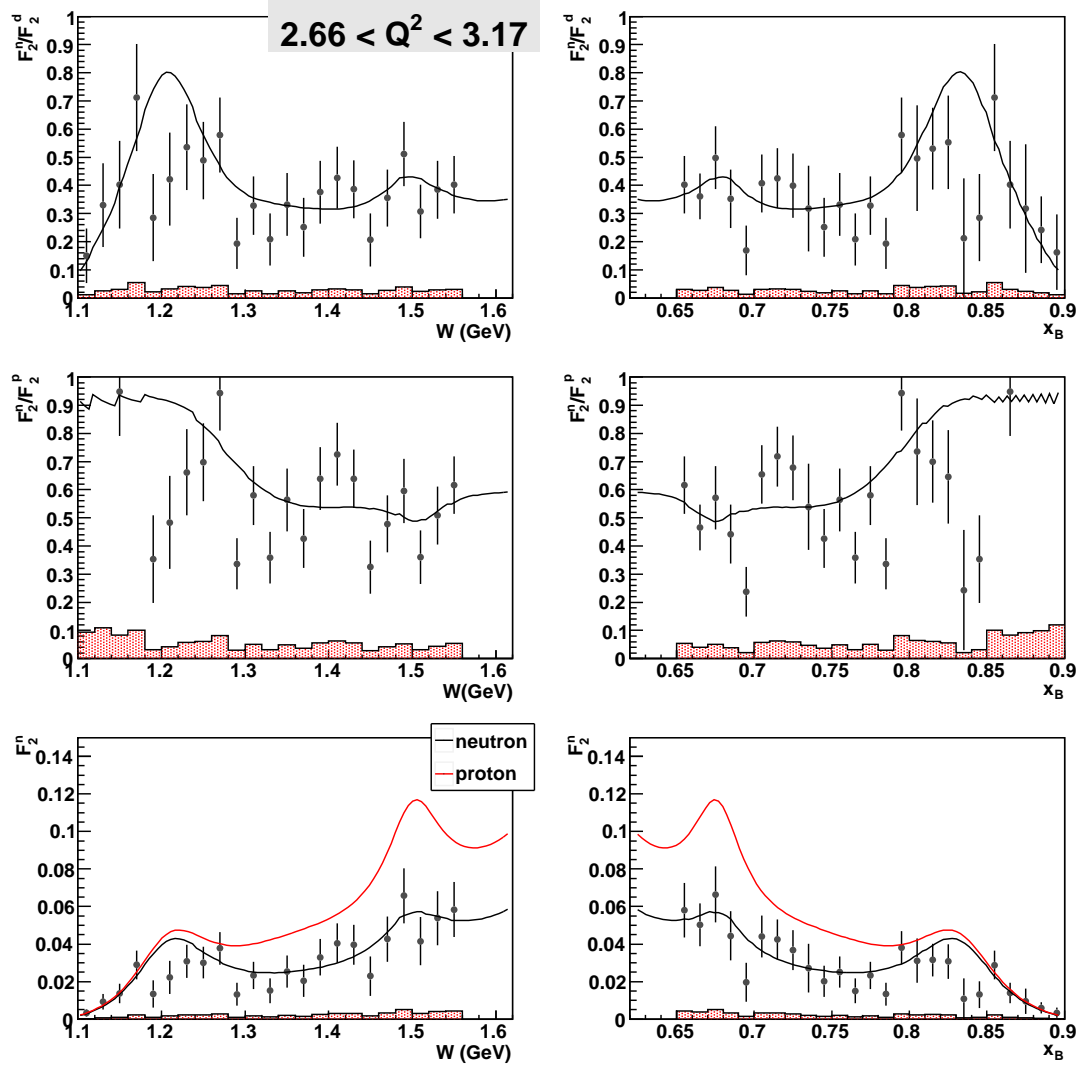


Figure 6.13: Same as Fig. 6.5 but at  $2.66 < Q^2 < 3.17$  GeV<sup>2</sup>.

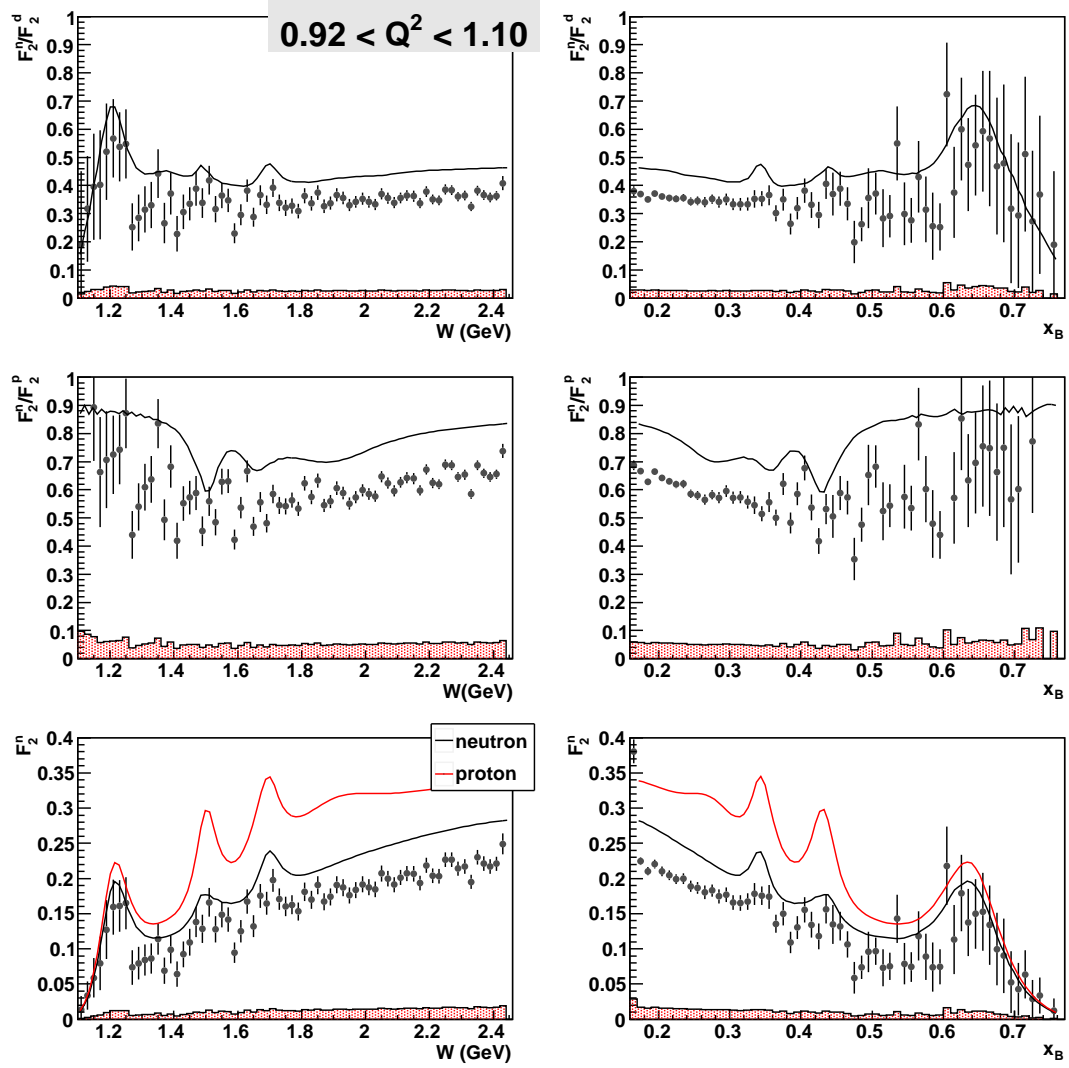


Figure 6.14:  $F_2^n/F_2^d$ ,  $F_2^n/F_2^p$ , and  $F_2^n$  versus  $W$  and  $x$  at  $0.92 < Q^2 < 1.10 \text{ GeV}^2$ ,  $E_{beam} = 5.262 \text{ GeV}$ . The neutron and proton lines are from the phenomenological model of Refs. [64] and [65].

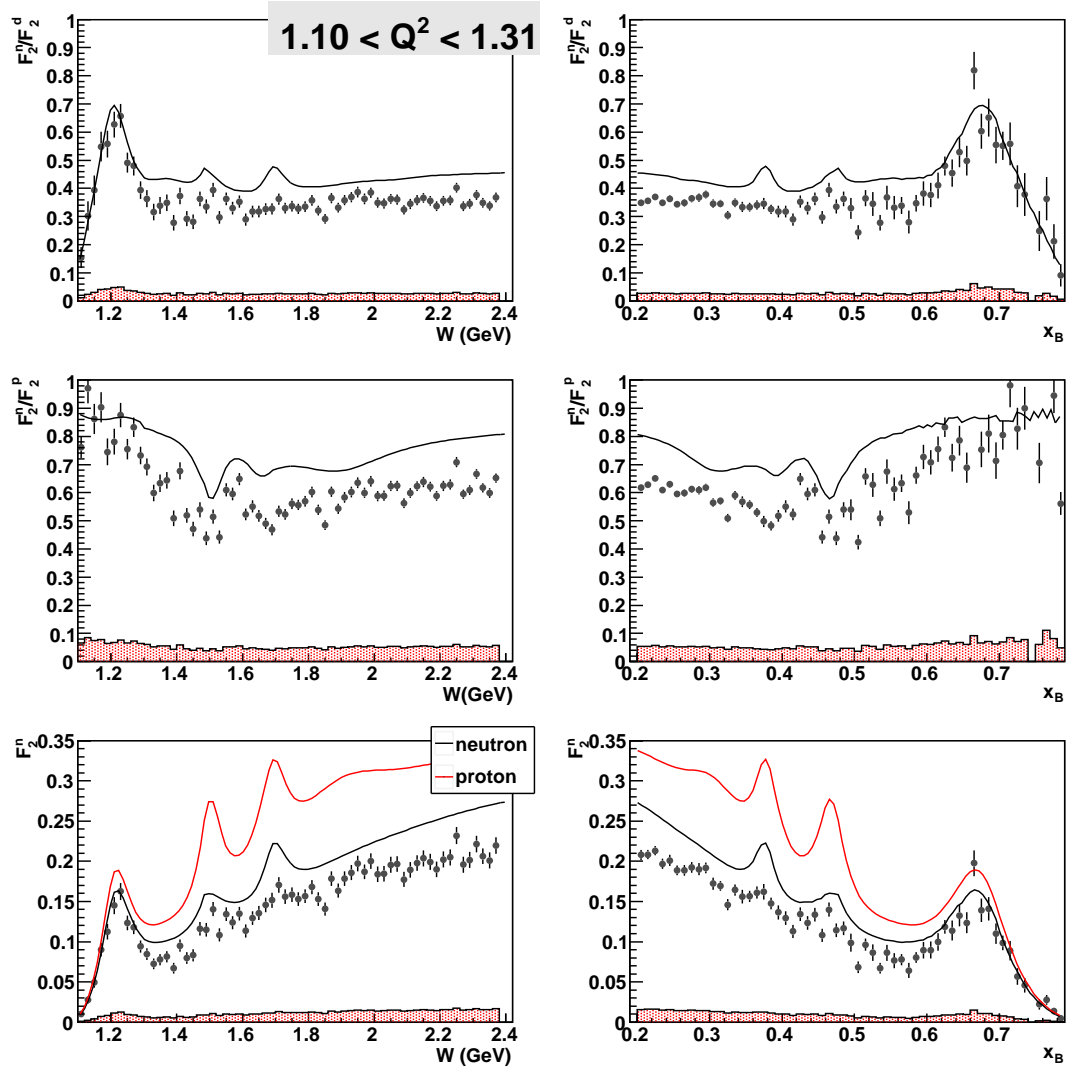


Figure 6.15: Same as Fig. 6.14 but at  $1.10 < Q^2 < 1.31 \text{ GeV}^2$ .

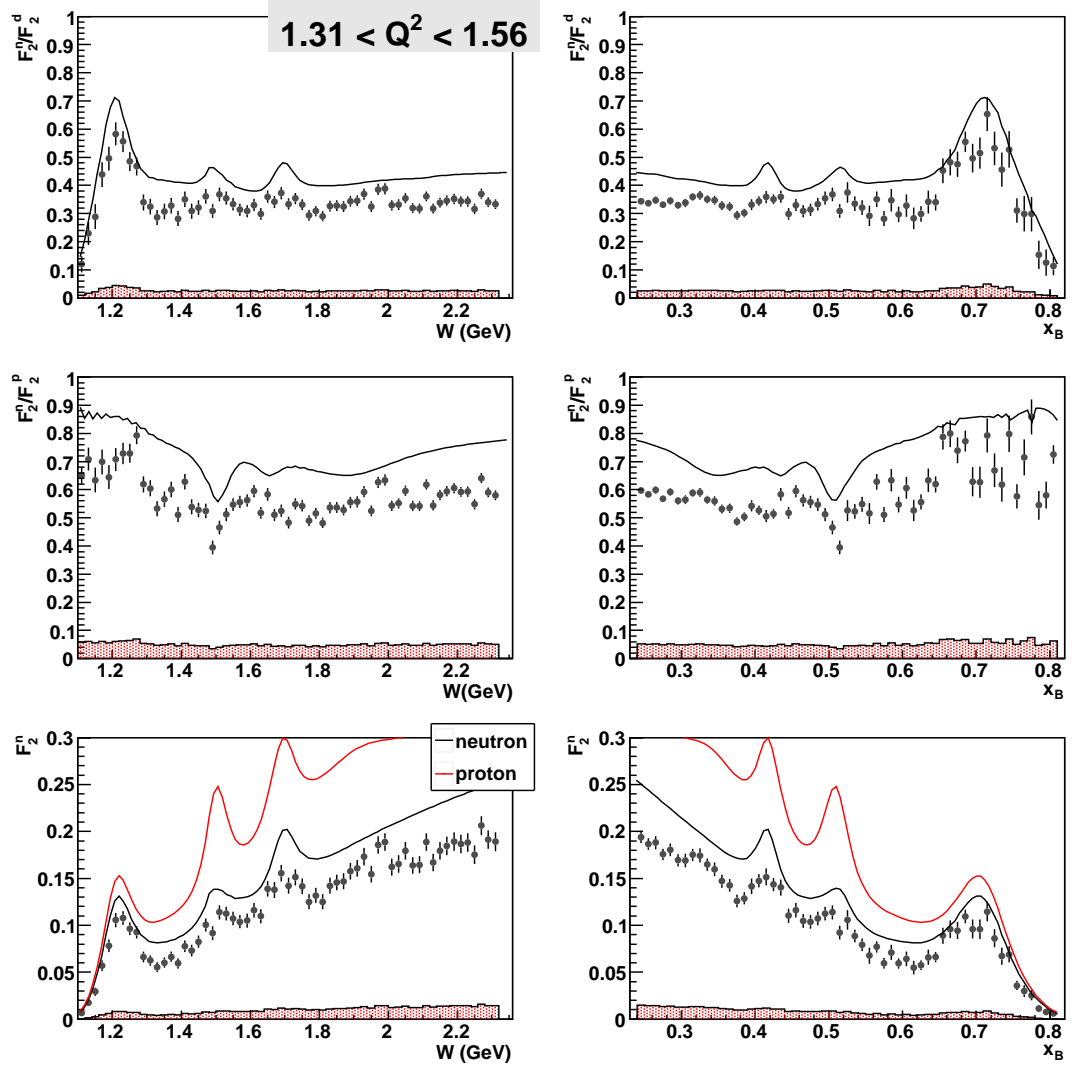


Figure 6.16: Same as Fig. 6.14 but at  $1.31 < Q^2 < 1.56$  GeV<sup>2</sup>.

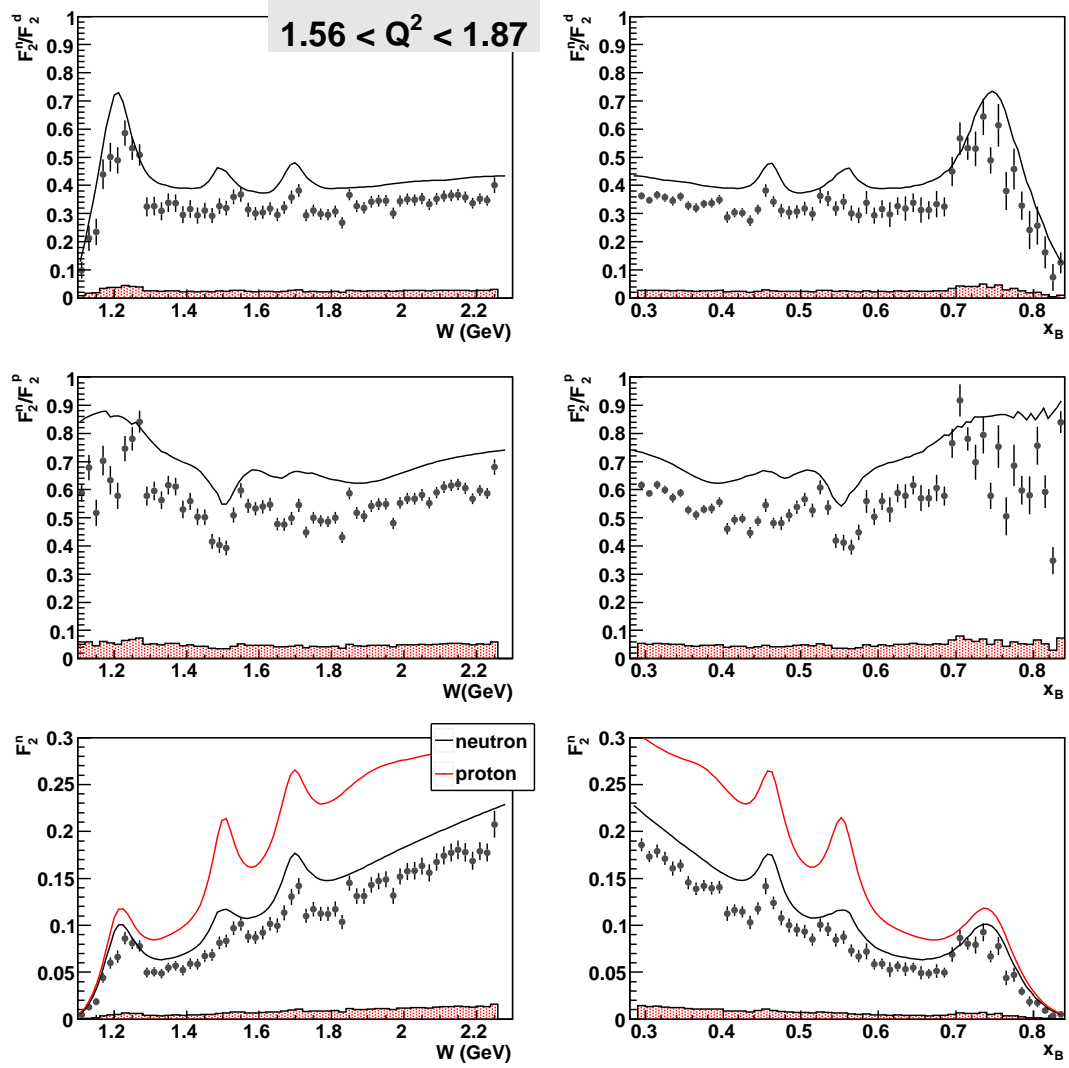


Figure 6.17: Same as Fig. 6.14 but at  $1.56 < Q^2 < 1.87 \text{ GeV}^2$ .

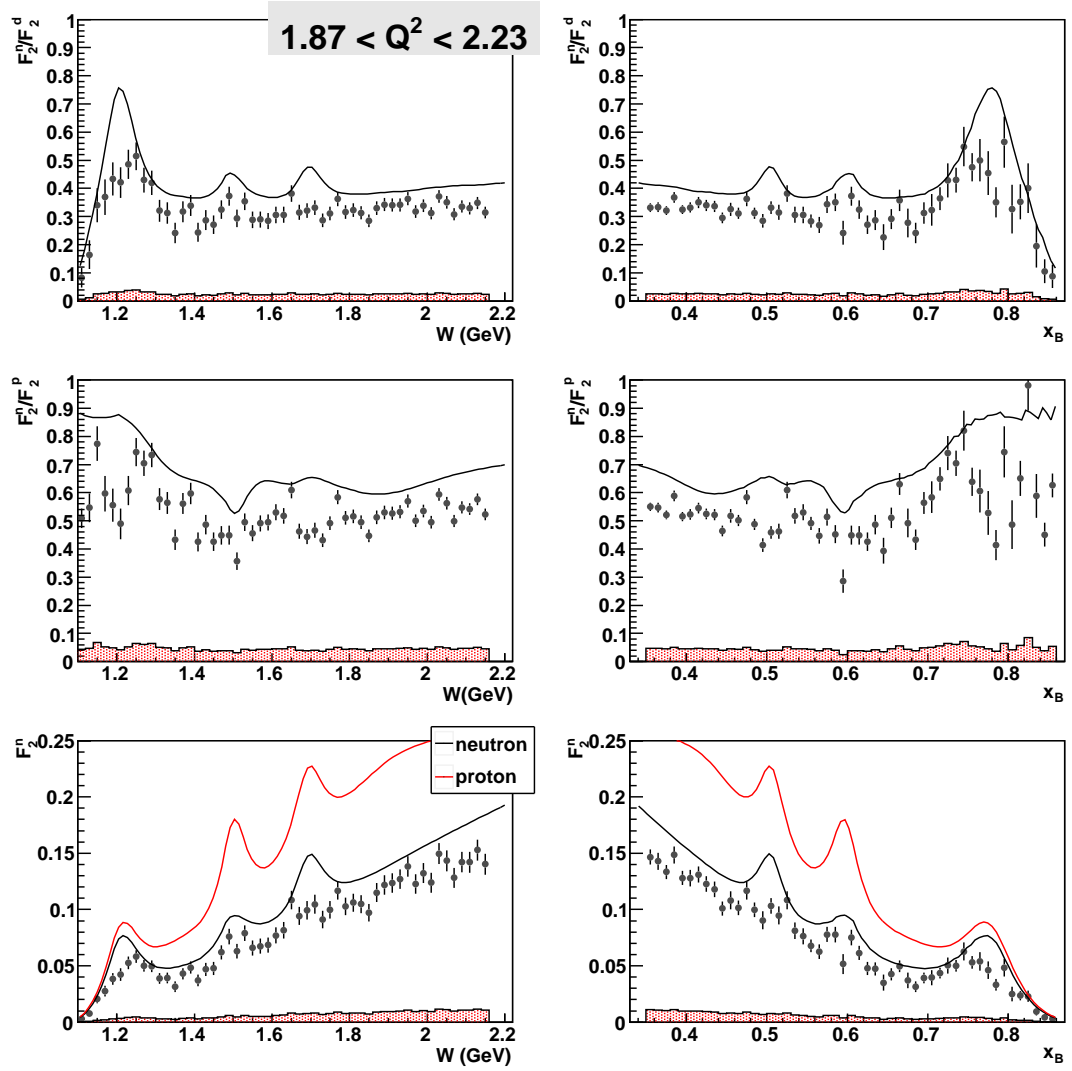


Figure 6.18: Same as Fig. 6.14 but at  $1.87 < Q^2 < 2.23 \text{ GeV}^2$ .

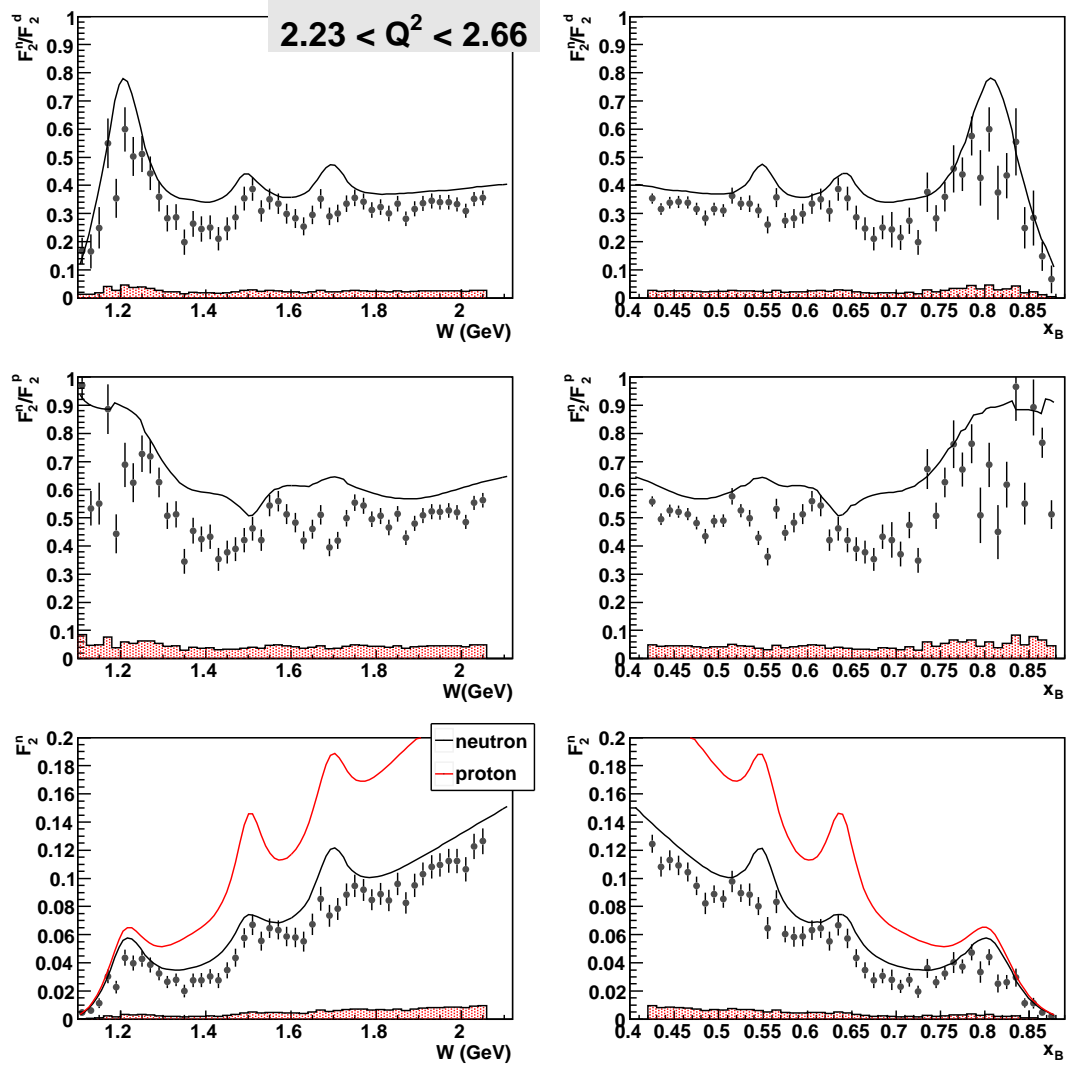


Figure 6.19: Same as Fig. 6.14 but at  $2.23 < Q^2 < 2.66$  GeV<sup>2</sup>.

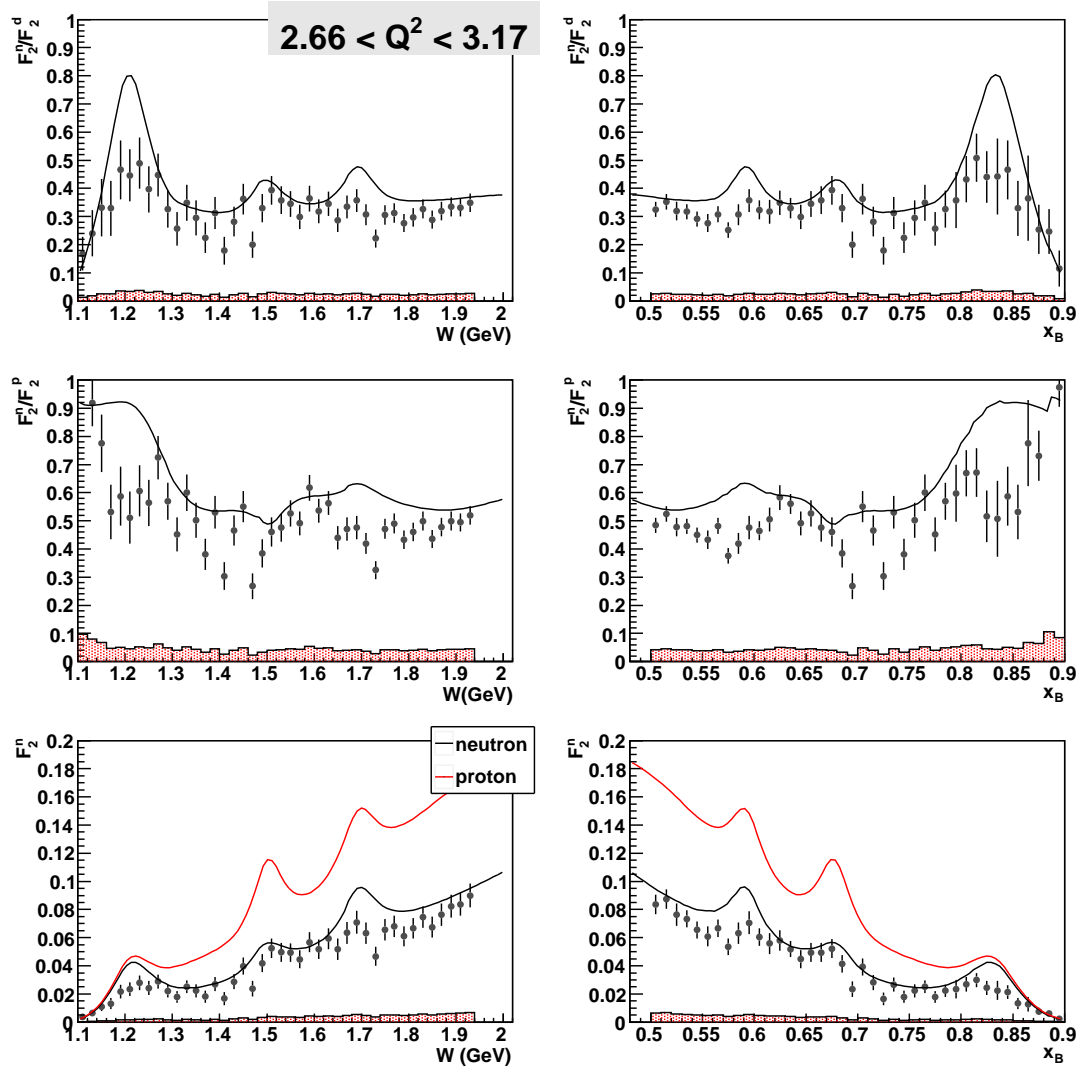


Figure 6.20: Same as Fig. 6.14 but at  $2.66 < Q^2 < 3.17 \text{ GeV}^2$ .

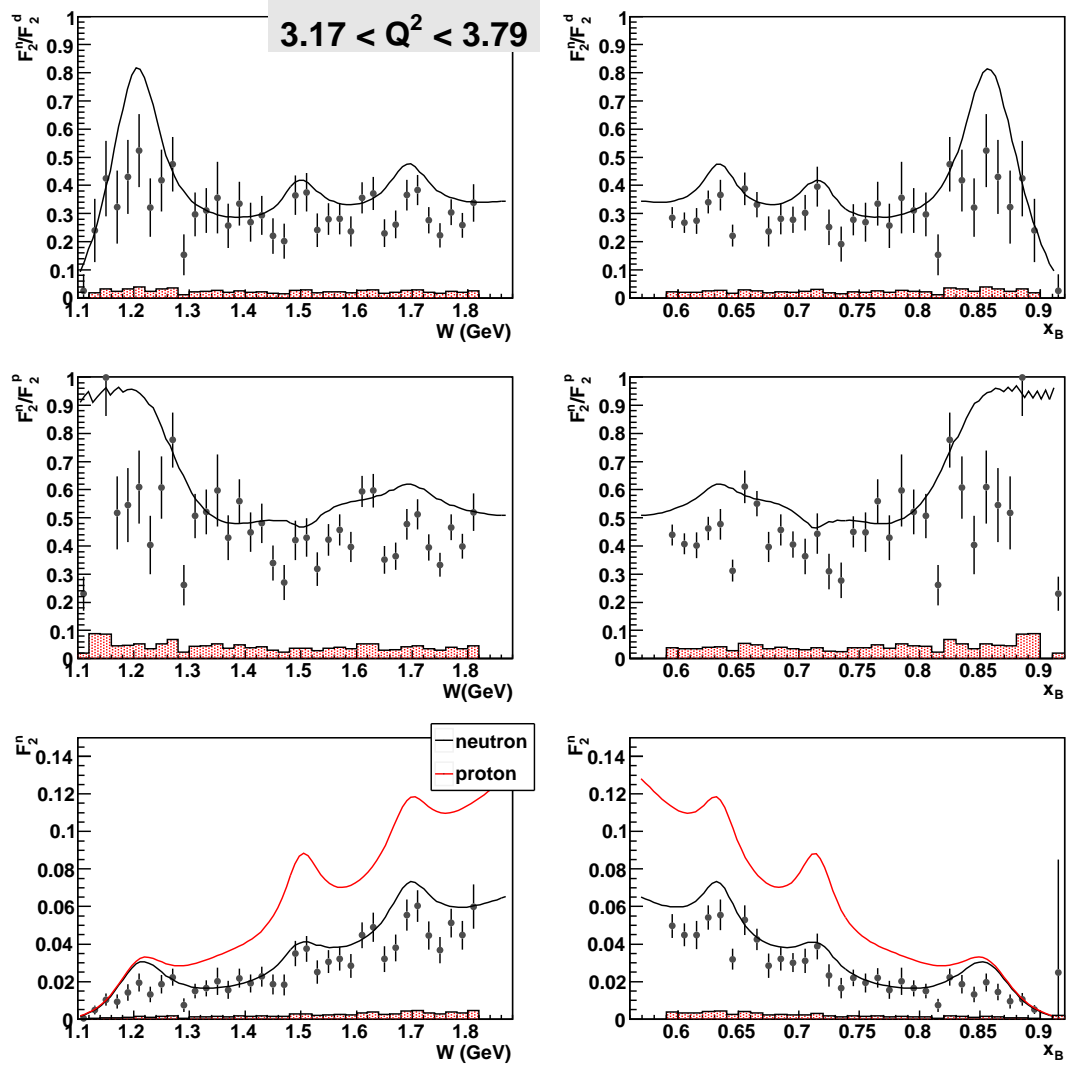


Figure 6.21: Same as Fig. 6.14 but at  $3.17 < Q^2 < 3.79$  GeV<sup>2</sup>.

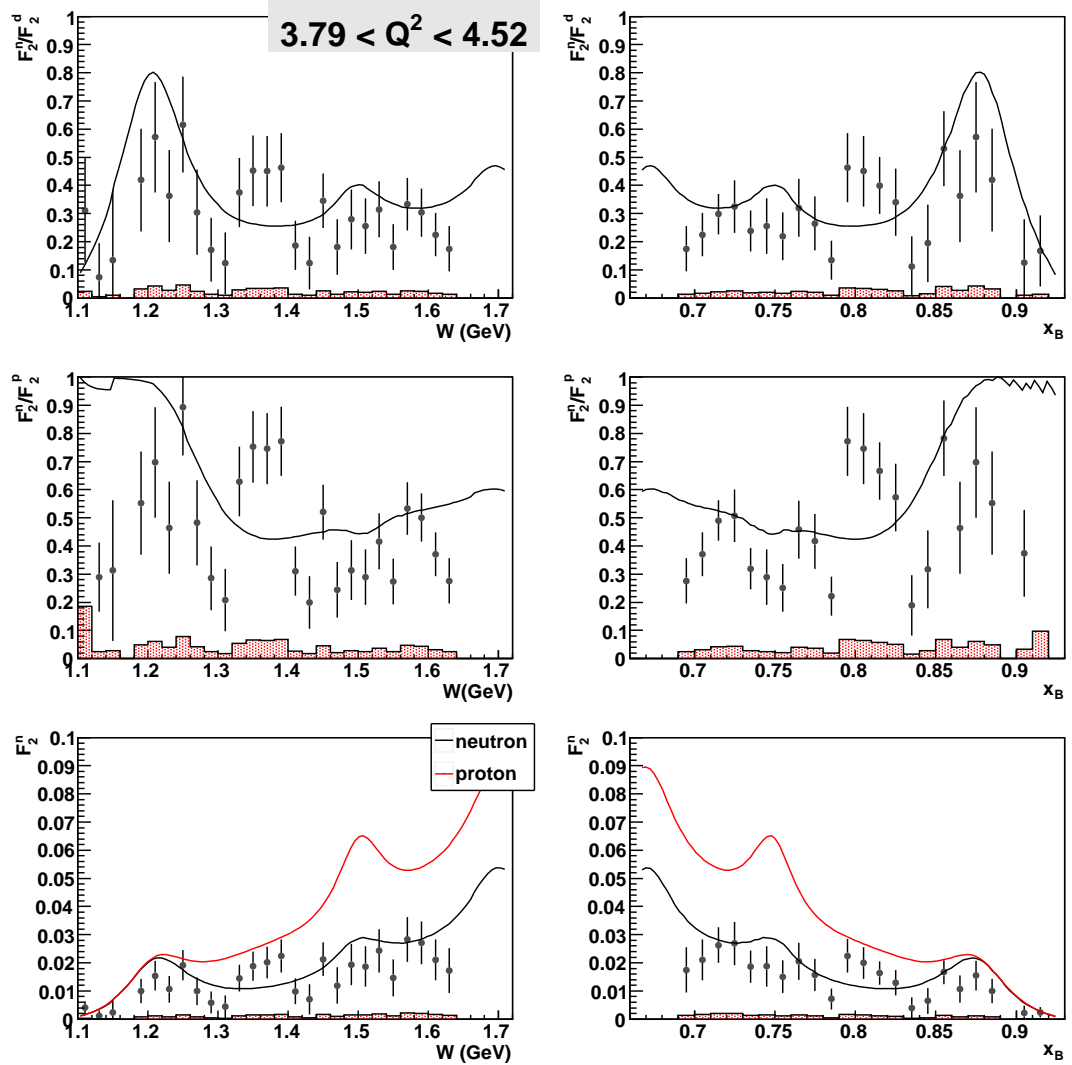


Figure 6.22: Same as Fig. 6.14 but at  $3.79 < Q^2 < 4.52 \text{ GeV}^2$ .

## BIBLIOGRAPHY

- [1] F. Halzen and A. Martin, *Quarks and Leptons: An Introductory Course in Modern Particle Physics*. New York: John Wiley and Sons, 1984.
- [2] F. Close, *An Introduction to Quarks and Partons*. New York: Academic Press, 1979.
- [3] J. Walecka, *Electron scattering for nuclear and nucleon structure*. New York: Cambridge University Press, 2001.
- [4] J. D. Bjorken, "Asymptotic sum rules at infinite momentum," *Phys. Rev.*, vol. 179, pp. 1547–1553, Mar 1969.
- [5] C. Amsler *et al.*, "Review of Particle Physics (Particle Data Group)," *Physics Letters B*, vol. 667, pp. 1–1340, 2008.
- [6] C. G. Callan and D. J. Gross, "High-energy electroproduction and the constitution of the electric current," *Phys. Rev. Lett.*, vol. 22, pp. 156–159, Jan 1969.
- [7] A. Thomas and W. Weise, *The Structure of the Nucleon*. New York: Wiley-VCH, 2001.
- [8] V. N. Gribov and L. N. Lipatov, "Deep inelastic e p scattering in perturbation theory," *Sov. J. Nucl. Phys.*, vol. 15, pp. 438–450, 1972.
- [9] Y. L. Dokshitzer, "Calculation of the Structure Functions for Deep Inelastic Scattering and e+ e- Annihilation by Perturbation Theory in Quantum Chromodynamics," *Sov. Phys. JETP*, vol. 46, pp. 641–653, 1977.
- [10] G. Altarelli and G. Parisi, "Asymptotic Freedom in Parton Language," *Nucl. Phys.*, vol. B126, p. 298, 1977.
- [11] F. E. Close, "Nu w(2) at small omega' and resonance form-factors in a quark model with broken su(6)," *Phys. Lett.*, vol. B43, pp. 422–426, 1973.
- [12] R. D. Carlitz, "SU(6) Symmetry Breaking Effects in Deep Inelastic Scattering," *Phys. Lett.*, vol. B58, p. 345, 1975.

- [13] F. E. Close and A. W. Thomas, "The Spin and Flavor Dependence of Parton Distribution Functions," *Phys. Lett.*, vol. B212, p. 227, 1988.
- [14] H. L. Lai *et al.*, "Global QCD analysis and the CTEQ parton distributions," *Phys. Rev.*, vol. D51, pp. 4763–4782, 1995.
- [15] N. Isgur, "Valence quark spin distribution functions," *Phys. Rev. D*, vol. 59, p. 034013, Jan 1999.
- [16] N. Isgur, G. Karl, and R. Koniuk, "Violations of  $su(6)$  selection rules from quark hyperfine interactions," *Phys. Rev. Lett.*, vol. 41, pp. 1269–1272, Nov 1978.
- [17] G. R. Farrar and D. R. Jackson, "Pion and Nucleon Structure Functions Near  $x=1$ ," *Phys. Rev. Lett.*, vol. 35, p. 1416, 1975.
- [18] S. J. Brodsky, M. Burkardt, and I. Schmidt, "Perturbative QCD constraints on the shape of polarized quark and gluon distributions," *Nucl. Phys.*, vol. B441, pp. 197–214, 1995.
- [19] W. Melnitchouk and A. W. Thomas, "Neutron / proton structure function ratio at large  $x$ ," *Phys. Lett.*, vol. B377, pp. 11–17, 1996.
- [20] L. Whitlow *et al.*, "Precise measurements of the proton and deuteron structure functions from a global analysis of the SLAC deep inelastic electron scattering cross sections," *Phys. Lett. B*, vol. 282, p. 475, 1992.
- [21] J. Gomez *et al.*, "Measurement of the  $a$  dependence of deep-inelastic electron scattering," *Phys. Rev. D*, vol. 49, pp. 4348–4372, May 1994.
- [22] M. Arneodo, "Nuclear effects in structure functions," *Phys. Rept.*, vol. 240, pp. 301–393, 1994.
- [23] D. F. Geesaman, K. Saito, and A. W. Thomas, "The nuclear EMC effect," *Ann. Rev. Nucl. Part. Sci.*, vol. 45, pp. 337–390, 1995.
- [24] L. L. Frankfurt and M. I. Strikman, "Point-Like Configurations in Hadrons and Nuclei and Deep Inelastic Reactions with Leptons: EMC and EMC-like Effects," *Nucl. Phys.*, vol. B250, pp. 143–176, 1985.

- [25] W. Melnitchouk, M. Sargsian, and M. I. Strikman, "Probing the origin of the EMC effect via tagged structure functions of the deuteron," *Z. Phys.*, vol. A359, pp. 99–109, 1997.
- [26] C. Ciofi degli Atti and S. Simula, "Slow proton production in semiinclusive deep inelastic lepton scattering off nuclei," *Phys. Lett.*, vol. B319, pp. 23–28, 1993.
- [27] W. Melnitchouk, A. W. Schreiber, and A. W. Thomas, "Relativistic deuteron structure function," *Phys. Lett.*, vol. B335, pp. 11–16, 1994.
- [28] F. Gross and S. Liuti, "Role of nuclear binding in the EMC effect," *Phys. Rev.*, vol. C45, pp. 1374–1381, 1992.
- [29] S. Liuti and F. Gross, "Extraction of the ratio of the neutron to proton structure functions from deep inelastic scattering," *Phys. Lett.*, vol. B356, pp. 157–162, 1995.
- [30] L. Heller and A. W. Thomas, "Structure Functions of Nuclei in the 'Instant' Form Dynamics," *Phys. Rev.*, vol. C41, pp. 2756–2763, 1990.
- [31] C. Ciofi degli Atti, L. P. Kaptari, and B. Z. Kopeliovich, "Hadronization and final state interaction effects in semi-exclusive deep inelastic scattering off nuclei," *Eur. Phys. J.*, vol. A19, pp. 133–137, 2004.
- [32] C. Leemann *et al.*, "The Continuous Electron Beam Accelerator Facility: CEBAF at the Jefferson Laboratory," *Annu. Rev. Nucl. Part. Sci.*, vol. 51, pp. 413–450, 2001.
- [33] E. Smith *et al.*, "Calibration of CLAS Time-of-Flight System," *CLAS-NOTE*, vol. 99-011, 1999.
- [34] D. Lawrence and M. Mestayer, "CLAS Drift Chamber Calibration Procedures," *CLAS-NOTE*, vol. 99-018, 1999.
- [35] A. Vlassov *et al.*, "CLAS Chrenkov Detector Calibration," *CLAS-NOTE*, vol. 99-005, 1999.
- [36] B. Mecking *et al.*, "The CEBAF large acceptance spectrometer (CLAS)," *Nuclear Instruments and Methods in Physics Research A*, vol. 503, pp. 513–553, 2003.
- [37] M. Mestayer, D. Carman, *et al.*, "The CLAS drift chamber system," *Nuclear Instruments and Methods in Physics Research A*, vol. 449, pp. 81–111, 2000.

- [38] G. Adams *et al.*, “The CLAS Cherenkov detector,” *Nuclear Instruments and Methods in Physics Research A*, vol. 465, pp. 414–427, 2001.
- [39] E. Smith *et al.*, “The time-of-flight system for CLAS,” *Nuclear Instruments and Methods in Physics Research A*, vol. 432, pp. 265–298, 1999.
- [40] M. Amarian *et al.*, “The CLAS forward electromagnetic calorimeter,” *Nuclear Instruments and Methods in Physics Research A*, vol. 460, pp. 239–265, 2001.
- [41] L. Quettier and J. Ball, “Magnetic Field Measurements of the DVCS-Solenoid,” *CLAS-NOTE*, vol. 2009-009, 2009.
- [42] W. Leo, *Techniques for Nuclear and Particle Physics Experiments*. New York: Springer Verlag, 1994.
- [43] D. R. Nygren, “The Time Projection Chamber: A New 4 pi Detector for Charged Particles,” *Berkeley 1974, Proceedings, Pep Summer Study*, pp. 58–78, 1976. PEP-0144.
- [44] F. Sauli, “GEM: A new concept for electron amplification in gas detectors,” *Nuclear Instruments and Methods in Physics Research A*, vol. 386, pp. 531–534, 1997.
- [45] F. Sauli *et al.*, “Electron Collection and Ion Feedback in GEM-based Detectors,” *IEEE Transactions on Nuclear Science*, vol. 50, pp. 803–808, 2003.
- [46] J. Benlloch *et al.*, “Development of the Gas Electron Multiplier (GEM),” *IEEE Transactions on Nuclear Science*, vol. 45, pp. 234–243, 1998.
- [47] F. Sauli, “Recent developments and applications of fast position-sensitive gas detectors,” *Nuclear Instruments and Methods in Physics Research A*, vol. 422, pp. 257–262, 1999.
- [48] F. Sauli, “Progress with the gas electron multiplier,” *Nucl. Instrum. Meth.*, vol. A522, pp. 93–98, 2004.
- [49] R. Veenhof, “GARFIELD, a drift chamber simulation program,” Prepared for International Conference on Programming and Mathematical Methods for Solving Physical Problems, Dubna, Russia, 14-19 Jun 1993.
- [50] H. Fenker *et al.*, “BoNuS: Development and use of a radial TPC using cylindrical GEMs,” *Nuclear Instruments and Methods in Physics Research A*, vol. 592, pp. 273–286, 2008.

- [51] B. Ketzer *et al.*, “Triple GEM tracking detectors for COMPASS,” *IEEE Transactions on Nuclear Science*, vol. 49, pp. 2403–2410, 2002.
- [52] R. Bosch *et al.*, “The ALTRO Chip: A 16-Channel A/D Converter and Digital Processor for Gas Detectors,” *IEEE Transactions on Nuclear Science*, vol. 50, pp. 2460–2469, 2003.
- [53] D. Cords *et al.*, “CLAS Event Format with BOS - Version 1.00,” *CLAS-NOTE*, vol. 94-012, 1994.
- [54] S. Biagi, “Monte Carlo simulation of electron drift and diffusion in counting gases under the influence of electric and magnetic fields,” *Nuclear Instruments and Methods in Physics Research A*, vol. 421, pp. 234–240, 1999.
- [55] F. James and M. Roos, “Minuit: A System for Function Minimization and Analysis of the Parameter Errors and Correlations,” *Comput. Phys. Commun.*, vol. 10, pp. 343–367, 1975.
- [56] N. Chernov, “Effective Algorithms for Circle Fitting,” *Computer Physics Communications*, vol. 33, pp. 329–333, 1984.
- [57] H. Fenker, “BoNuS RTPC Pad Gain Correction Factors and Tracking / Track-Finding Efficiency.” BoNuS technical note, 2007.
- [58] J. Zhang and G. Dodge, “Quality Check for BoNuS.” BoNuS technical note (*in progress*), 2009.
- [59] A. V. M. Osipenko and M. Taiuti, “Matching between the electron candidate track and the Cherenkov counter hit.,” *CLAS-NOTE*, vol. 2004-020, 2004.
- [60] S. Kuhn and A. Klimenko, “Momentum Corrections for E6,” *CLAS-NOTE*, vol. 03-005, 2003.
- [61] J. Zhang, “The Simulation of BoNuS.” BoNuS technical note (*in progress*), 2009.
- [62] R. Machleidt, K. Holinde, and C. Elster, “The Bonn Meson Exchange Model for the Nucleon Nucleon Interaction,” *Phys. Rept.*, vol. 149, pp. 1–89, 1987.
- [63] M. Peskin and D. Schroeder, *An Introduction to Quantum Field Theory*. Boulder, Colorado: Westview Press, 1995.

- [64] P. E. Bosted and M. E. Christy, "Empirical Fit to Inelastic Electron-Deuteron and Electron-Neutron Resonance Region Transverse Cross Sections," *Phys. Rev.*, vol. C77, p. 065206, 2008.
- [65] M. E. Christy and P. E. Bosted, "Empirical Fit to Precision Inclusive Electron-Proton Cross Sections in the Resonance Region," *arXiv:0712.3731*.
- [66] L. Mo and Y. Tsai, "Radiative Corrections to Elastic and Inelastic  $ep$  and  $\mu p$  Scattering," *Rev. Mod. Phys.*, vol. 41, p. 205, 1969.
- [67] N. Guler, "Pion and Pair Symmetric Contamination in the EG1B experiment." CLAS technical note (*in progress*), 2009.